Chapter 6
Earth Terminal Architectures

Keith E. Wilson, Abhijit Biswas, Andrew A. Gray, Victor A. Vilnrotter,
Chi-Wung Lau, Meera Srinivasan, and William H. Farr

6.1 Introduction
Keith E. Wilson

As Solar System exploration missions evolve from flybys to orbiters and landers, high resolution instruments will enable us to establish a virtual and real presence on other worlds. The data rates needed to support advanced high resolution instruments will increase orders of magnitude—to hundreds of megabits per second.

Higher carrier frequencies, larger antennas on spacecraft, larger antennas on the ground, increased receiver sensitivities, and higher efficiency modulation and coding schemes are all strategies that increase the signal-to-noise ratio (SNR) of the link. Yet within this, the trade space is constrained by the size, mass, and power limitations of spaceborne systems. Increasing the transmitted power requires that more power be generated on the spacecraft; a challenge for spacecraft that rely on solar energy to explore the outer planets where the solar intensity is low. Increasing the onboard antenna diameter, D, reduces the required transmitted power. However, higher carrier frequencies impose increasingly more stringent demands on the antenna pointing system to reduce pointing losses and maintain the often-required $\lambda/10D$ beam pointing accuracy, and they increase the losses due to weather. To reduce the impact of these demands on the onboard systems, the approach taken for deep space communications at radio frequency (RF) carrier frequencies has been to emphasize three areas of performance enhancements for closing the link. These

are receiver gain, receiver sensitivity, and coding and modulation efficiency. This paradigm is unchanged for deep space optical links.

Section 6.1.1 discusses the Earth-based optical receiver, the search for low-cost large aperture single telescopes, and the deployment strategies to mitigate the effects of cloud cover. This section also addresses high-power laser beam uplink transmission safety and established strategies to mitigate atmospheric scintillation effects on the uplink beam. It concludes with a series of JPL concept validation experiments performed in support of deep space optical communications.

The required receiver gain for the link can also be achieved by an array of smaller aperture telescopes with equivalent area to that of a single large telescope. An array has the advantage of tapping into established technology for building smaller telescopes, thereby expanding the number of potential suppliers. Also, using a large number of smaller array elements allows economies of scale to be realized. Stahl et al. have developed a parametric cost model for ground-based telescopes using multi-variable statistical analysis [1]. Their results, comparing primary mirror and not mount costs, show the cost advantage of an array of smaller telescopes. Whether this advantage is retained in the presence of operational conditions (including mount calibrations and pointing and alignment of the array elements) is yet to be determined. In Section 6.1.2 the array approach is discussed, and its performance characteristics are compared to those of an equivalent-area single aperture. The results show that the array is a viable alternative to the single aperture.

At the receiver, the downlink signal received by the telescope is focused onto a photosensitive surface that converts the detected signal intensity to an electric current. The efficiency of this statistical process of photon detection defines the quantum efficiency of the detector. Silicon and indium-gallium-arsenide (InGaAs) detectors are the optical communications detectors of choice because of their low noise characteristics are crucial for detecting the weak deep space downlinks. Yet because of its wider band-gap, the quantum efficiency of silicon detectors is low at near-infrared wavelengths. To compensate for this, developers have explored strategies to reduce the band gap of silicon thereby increasing its absorption at infrared wavelengths [2]. A plethora of detector architectures exists within the silicon-based technology. These range from hybrid photomultiplier tubes (PMTs) with silicon surfaces to linear and Geiger-mode avalanche photodiode detectors (APDs) and focal plane arrays and are discussed in Section 6.2. Some of these devices such as the Geiger-mode APDs and hybrid PMTs can operate in the photon-counting mode. Low signal level detection is key for the signal-starved deep space links. High-sensitivity low-noise-figure detectors not only enhance the link performance but also can provide adequate link margin in the presence of higher atmospheric attenuation; a feature that can affect the number of ground stations needed to achieve the required availability.

While telescopes, optical trains, and detectors constitute the front end of the receiver chain, the back end electronics for the deep space receiver are uniquely designed to match the higher order pulse-position modulation formats of the deep space optical link. Section 6.3 describes the advanced time synchronization and post detection filtering techniques required to demodulate the nanosecond pulse streams from the deep space link.

6.1.1 Single-Station Downlink Reception and Uplink Transmission
Keith E. Wilson

6.1.1.1 Introduction. This section addresses the transmitters and receivers for the deep space optical communications. In Section 6.1.1.2 we discuss the evolution of the JPL strategy for achieving the large 10-m receivers that have been shown to be the appropriate aperture size to support deep space optical links [3]. In Section 6.1.1.3, we describe the global required deployment of the Optical Deep Space Network (ODSN) stations to provide the needed coverage and the options on network concepts to mitigate the effects of cloud cover and provide the required availability. We also discuss the application of adaptive-optics technologies to reduce the effects of sky background on the optical link at small Sun angles. Airborne receivers located above the clouds so they can provide an assured link for low-rate engineering and science data on an emergency basis are discussed in Section 6.1.1.5 along with the results of space-based receiver studies. The most recent of these baselined the technologies of the James Webb Space Telescope (JWST) to realize significant cost savings on the development of the large space-based optical receiver.

For the uplink, the laser beam serves both as a reference beacon to signal ground station availability for links with short round-trip light times (RTLTs) and as a low-rate command uplink channel. In Section 6.1.1.6, we discuss the uplink laser requirements for both the command and beacon links. Atmospheric turbulence causes scintillation and wavefront tilt as the laser beam propagates through the atmosphere. Although aperture averaging and large aperture detectors mitigate these atmospheric effects of the direct detection downlink receiver, in the absence of clouds and aerosols, the uplink beam is most affected by clear-air atmospheric turbulence. The effect of atmospheric turbulence on the uplink and the multi-beam strategies to mitigate these effects are described in Section 6.1.1.7.

Ground-to-space laser beam propagation from United States territory is regulated by two Federal government agencies. The Federal Aviation Administration (FAA) regulates beam propagation in navigable air space. The United States Strategic Command (USSTRATCOM of the U.S. Air Force) Laser Clearinghouse (LCH) regulates propagation of laser beams into space for all Department of Defense (DoD) related programs. In Section 6.1.1.10, we describe a JPL three-tiered safety system for safe ground-to-space laser beam

propagation. In Section 6.1.1.11, we discuss a series of experiments conducted at JPL to validate deep space optical communications link concepts. In Section 6.1.1.11, we describe the 1968 laser link from Table Mountain Observatory to the Surveyor-VII camera on the Moon. This demonstration qualitatively showed the effects of atmospheric conditions and "seeing" on laser beam propagation. The 1992 Galileo Optical Experiment (GOPEX) described in Section 6.1.1.11.1 demonstrated a six–million-kilometer link, and quantified the effects of scintillation on single-uplink beam propagation. In addition, GOPEX demonstrated the benefits of ground-station site diversity.

The transmitted beam intensity is inversely proportional to the square of the beam divergence, and adaptive optics can allow the propagation of diffraction-limited beams through the atmosphere. In Section 6.1.1.11.2, we describe the 1994 joint JPL and Starfire Optical Range (SOR), Albuquerque, New Mexico demonstration of an atmosphere-compensated laser uplink to the Apollo 15 retro-reflectors on the Moon. Lessons on beam propagation learned from GOPEX were implemented in the Ground-to-Orbiter Lasercom Demonstration with the National Space Development Agency of Japan's (NASDA's) ETS-VI spacecraft where the first scintillation mitigation using multi-beam uplinks was demonstrated. This is discussed in Section 6.1.1.11.3. The Missile Defense Agency's lasercom terminal manufactured by AstroTerra Corp. of San Diego, California, was integrated onto the Space Technology Research Vehicle (STRV-2) instrument platform at JPL and launched on the Air Force TSX-5 spacecraft. Although a link was never established between the spacecraft and ground terminals, invaluable lessons were learned both about the design and materials selection for space-based terminals and about the design of transportable ground terminals.

6.1.1.2 Deep-Space Optical Ground Receivers. The 1994 Ground-based Advanced Technology Study (GBATS) report explored two deployment options and quantified the number of ground antennas needed to support a high-availability optical link in the presence of cloud cover [4]. The study evaluated two global subnets: (i) The Clustered Optical Subnet (COS) that consisted of groups of three receivers near the current DSN locations, and (ii) the Linearly Dispersed Optical Subnet (LDOS) receivers consisting of six to eight stations approximately equally separated in longitude. To reduce the overall cost of deploying six to nine Deep Space Optical Receiving Antenna (DSORA) stations globally, several designs were considered. Among them were instruments that are non-diffraction-limited at optical wavelengths (photon-buckets) [5]. Millimeter and submillimeter telescope receivers (such as the California Institute of Technology Sub-millimeter Observatory's (CSO) 10.4-m Leighton's dish, shown in Fig. 6-1, and the 3-m Kolner Observatory for Sub-Millimeter Astronomy (KOSMA) telescope at Zermatt, Switzerland, Fig. 6-2)

Fig. 6-1. Leighton Dish California Institute of Technology (Caltech) Sub-Millimeter Observatory (CSO), Mauna Kea, Hawaii.

Fig. 6-2. KOSMA 3-m sub-millimeter telescope in Zermatt, Switzerland, built by Vertex Antennentechnik.

were explored [6,7]. The design approach of the low cost 10-m Hobby-Ebberly telescope (Mount Fowlkes, Fort Davis, Texas) was also considered [8].

The CSO dish consists of 84 nominally 1-m hexagonal panels and is modular in design and easily assembled. The f/0.45 parabolic primary panels are made of aluminum front and back face sheets bonded to an aluminum honeycomb core for stiffness. As manufactured at the California Institute of Technology, the antenna had a surface figure of approximately 15 µm root mean square (RMS) Although low-cost and capable of supporting high

nighttime links in the absence of sky background, the surface roughness of the CSO could not support daytime operation at small Sun angles.

Strategies explored included an integral sunshade that consisted of a series of 1.11-m side hexagonal tubes approximately 12 m long integrated to the hexagonally segmented primary to prevent direct sunlight from being incident on the primary [9,10,11]. Analysis showed that the sunshade would enable pointing to as low as ~12 deg of the Sun without signal loss. A series of vanes arranged like an asterisk designed into each tube would allow pointing to within 6 deg of the Sun with only 3.6 percent signal loss.

The KOSMA telescope uses actuators to achieve the required panel-to-panel alignment, and it uses highly polished surfaces to achieve the required surface quality. The primary is made of 1–2 mm thick light-weighted aluminum panels that are 0.9 m × 0.8 m. The panels were micro-machined to better than 4 μm RMS surface roughness by the Laboratory for Micro-machining at the University of Bremen, Germany, to serve as a starting point. The modifications considered for the DSORA were first to nickel plate the panels to fill the grooves from the micro machining, and then inscribe the plated surface with micron-sized stress relief patterns to relieve any thermally induced stresses caused by the differential thermal expansion between the nickel and aluminum. An aluminum layer with an SiO_2 overcoat would then be deposited over the nickel to increase the surface reflectivity in the visible from the 50 percent of nickel to approximately 90 percent. The residual panel surface roughness expected by using this process is approximately 200 nm peak-to-valley [12].

A JPL study by Sandusky et al. analyzed the effects of sunlight scattered from the primary mirror into the focal plane in greater detail [13]. Their results showed that a telescope meeting the expected performance of the modified KOSMA antenna could support optical communications at much smaller Sun angles than the DSORA [14]. The Sandusky results were that machined panels with RMS surface roughness $\sigma \sim \lambda/10$ could support optical communications at a 1-deg Sun angle.

Other cost reduction approaches considered to achieve the desired surface quality have included glass fusion technology for making lightweight panels. This is shown in Fig. 6-3 [14]. Alternatively, a spherical rather than a parabolic primary, as was done in the Hobby-Ebberly, can take advantage of the economies of scale. More recently, an array of smaller telescopes of about 1-m diameter each has been considered for the Mars laser communications demonstration project.

6.1.1.3 Mitigating Cloud Cover and Sky Background Effects at the Receiver. Selection of optical deep space network (ODSN) sites to provide both nominal twenty-four hour coverage and weather availability requires the consideration of several factors. Among these are:

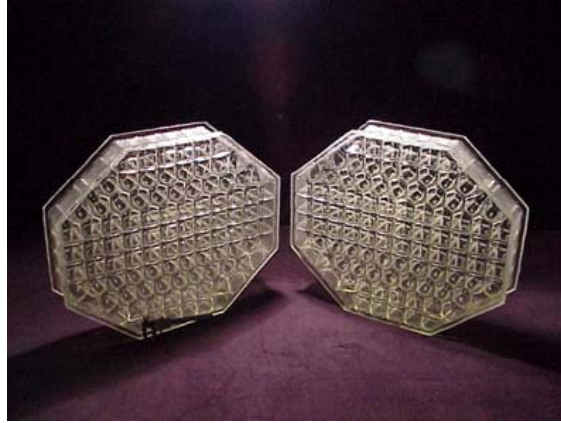1) Longitude of locations to achieve near twenty-four hour coverage

**Fig. 6-3. Candidate lightweight glass panels from HEXTEK
for making the primary for a 10-m receiver.**

2) Altitude and weather statistics of the site to mitigate effects of atmospheric turbulence and sky background.

3) Accessibility and infrastructure support including transportation, housing and telecommunications facilities.

4) Geopolitical: To protect NASA's investment and ensure long-term accessibility and security.

5) Environmental impact of construction at the site. Ignoring these impacts can result in cost overruns and significant schedule delays.

6) Security and access control: To protect the assets and ensure system integrity.

7) Aircraft avoidance: To prevent illumination of aircraft by high power uplink lasers.

Cloud cover data for sites in the United States Southwest show seasonal cloud cover ranging from 12 percent in the summer months to greater than 50 percent in the winter and fall months [15]. Table 6-1 gives the seasonal cloud cover variation during the night at Table Mountain Facility (TMF) observatory over the eleven-year period 1993 to 2003. The data show that the mean cloud cover ranges from 21 percent in the summer to 51 percent in the winter. For an array of n receivers located in independent weather cells in a region of cloud cover probability q, the weather availability p for is given by $p = (1 - q^n)$, when n stations are simultaneously visible to the spacecraft. For a three-station COS configuration located in a region of 20 percent to 50 percent cloud cover probability, the corresponding weather availability decreases from 99 percent to 88 percent. Currently, weather satellite data are being used to develop cloud-free line-of-sight statistics for a range of global sites [16].

The 1994 GBATS study considered a six-, seven-, and eight-station LDOS and a 3×3 and 3×4 COS located between +40 and –40 degrees latitude [4]. The locations of the 3×3 COS and the six-station LDOS shown in Fig. 6-4 were in the vicinity of existing DSN sites at Goldstone (California), Canberra (Australia), and Madrid (Spain) separated by 200 km to 500 km, the nominal size of a weather cell. For this configuration, the size of the weather cell

Table 6-1. Table Mountain, California, cloud statistics for 1993–2003.

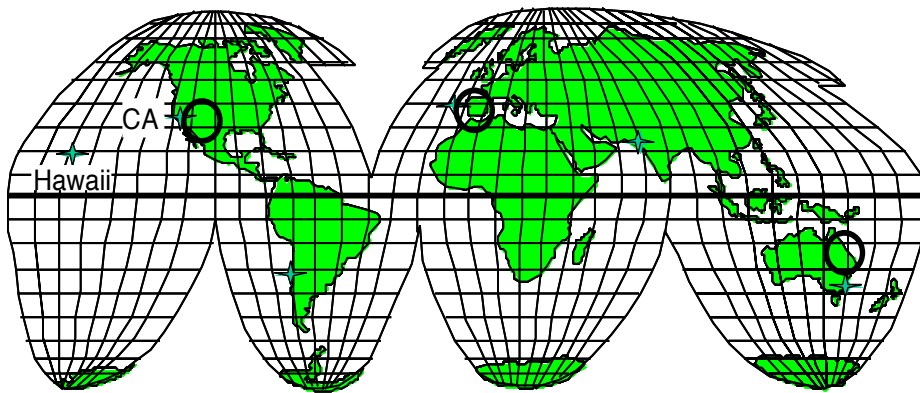| Year	Annual Avg. %Cloudy	Winter %Cloudy	Spring %Cloudy	Summer %Cloudy	Fall %Cloudy
1993	**27.5**	50.0	36.7	15.4	22.2
1994	**37.6**	56.5	40.5	32.5	17.7
1995	**26.6**	33.3	35.6	16.9	29.3
1996	**31.6**	80.0	39.5	11.1	13.8
1997	**22.1**	16.0	16.0	15.4	39.4
1998	**21.2**	52.6	22.2	8.5	20.0
1999	**27.3**	54.5	26.1	14.3	21.0
2000	**28.3**	57.1	27.6	26.3	27.1
2001	**39.6**	50.0	46.1	29.4	53.9
2002	**39.2**	57.1	12.0	23.5	55.7
2003	**39.1**	56.6	39.7	33.3	33.3
Seasonal average		**51.2**	**31.1**	**20.6**	**30.3**

Fig. 6-4. One realization of a COS 3 $\times$ 3 and a six-station LDOS deployment for global

establishes the minimum station separation. The maximum separation will be based on the mission operations concepts. In Fig. 6-4, the locations of the six-station LDOS were Mauna Kea (Hawaii), U.S. Southwest, Cerro Pachan (Chile), Calar Alto (Spain), Zairat (Pakistan), and Siding Spring (Australia); all clearly in independent weather cells.

A Mars-to-Earth link offers an excellent example of the impact of the mission's concept of operations on the ground station deployment for weather diversity. The large difference in range between conjunction and opposition (0.37 AU and 2.7 AU) in the Mars-to-Earth link allows a ready comparison of COS and LDOS operational scenarios.

At the two extreme ranges of the link, the footprints of the optical downlink beam of 3-µrad 3-dB beam width (a 30-cm transmitter operating at a 1-µm wavelength) are 166 km at opposition and 1200 km at solar conjunction. A maximum COS station separation of less than 1200 km would allow the downlink beam to simultaneously cover all stations in the region at conjunction. This approach is particularly advantageous for communications from ranges where the light time is so long (for this case, the one-way light time at conjunction is approximately 21 minutes) that threatening clouds at any one station could obscure the line of sight within the time it takes to send a command to the spacecraft. At opposition the beam footprint is small. However, the light time is short, approximately 3 minutes, and could support an operations scenario of re-pointing the beam from one station to the next to communicate through a cloud-free line of sight in patchy cloud sky, thereby increasing each station's availability.

These options do not apply to the LDOS configuration. In all cases station separation exceeds 1200-km, and for all ranges the spacecraft terminal would need to be re-pointed from one station to the next to avoid impending cloud cover. The selection of sites for a global ground network will be based on an optimization of several considerations including those listed above.

6.1.1.4 Daytime Sky Background Effects. Rayleigh scattering of sunlight by the atmosphere is the main source of optical background noise on the daytime optical link. The ability to point at small Sun angles increases the availability of the optical link around solar opposition. Mitigating the effects of sky background on the optical link requires the implementation of spatial and spectral filtering techniques coupled with higher order pulse position modulation (PPM). The optical noise is directly proportional to the slot width and can therefore be reduced by implementing higher order PPM schemes. Yet, the receiver complexity and the susceptibility of the link performance to pulse jitter increases with PPM order. Angstrom-wide Fabry-Perot optical filters further suppress sky background noise. However, when pointing as close as 3 deg to the Sun additional techniques are required. JPL has been exploring the application of adaptive optics methods to reduce the receiver field-of-view

(FOV) and thereby further mitigate the effects of sky background on the optical link. Preliminary analysis has shown that an adaptive optics system with 900 actuators per square meter adaptive optics techniques can realize as much as 6 dB increase in SNR for PPM-16 formats in the presence of high sky background noise [17]. Figure 6-5 illustrates improvement in SNR for different background levels realized by implementing adaptive optics across a 1-m aperture.

6.1.1.5 Earth-Orbiting and Airborne Receivers. Cloud cover, atmospheric turbulence, sky background, and high winds affect the optical availability and quality of the link to a ground receiver. Oceans and geopolitics are constraints on the availability of locations for deploying a ground stations. A space-based receiver offers the optimum availability for a single receiver, and an optical interplanetary crosslink between a geostationary receiver and the probe offers a high bandwidth link with high availability. Past studies of space-based receivers [18,19] have shown that the payload and launch costs drive the cost of the space–based receiver to approximately twice that of the 3×3 COS ground-based receiver network. The high payload cost was due to the pre-development technology needed to build and deploy large apertures in space. A 1998 study took advantage of the James Webb Space Telescope deployable apertures technology to achieve significant reductions in the payload costs. The result showed that the cost of the 7-m space-based receiver station was comparable to and within cost uncertainties of a 3×3 COS (10-m apertures) [20].

Concepts for airborne receivers are based on 2.7-m apertures such as the Stratospheric Observatory for Infrared Astronomy (SOFIA) telescope [21]. With advances in station keeping, balloon-borne receivers have been recently added to the list of approaches to mitigate atmospheric effects. Key advantages of this approach are: (i) The receivers are stationed above the cloud cover and the scintillation effects of the troposphere, (ii) they are above most of the atmosphere, and background sky scatter when pointing close to the Sun is minimal, (iii) deployment costs are low, (iv) they are serviceable, (v) they can be deployed globally over oceans and avoid geopolitical issues. Yet, because of their smaller apertures airborne receivers have been considered only to expand availability for the transmission of low-rate science and critical engineering data. This, however, is rapidly changing with the development of efficient photon-counting IR detectors at the infrared communications wavelength.

6.1.1.6 Uplink Beacon and Command. For bi-directional optical communications to a deep space probe out to Mars ranges, the uplink will not only serve as a carrier for transmitting commands to the spacecraft but also as a beacon to signal to the spacecraft identifying the ground station location with a cloud-free line of sight. Although hybrid concepts that use an RF uplink and an
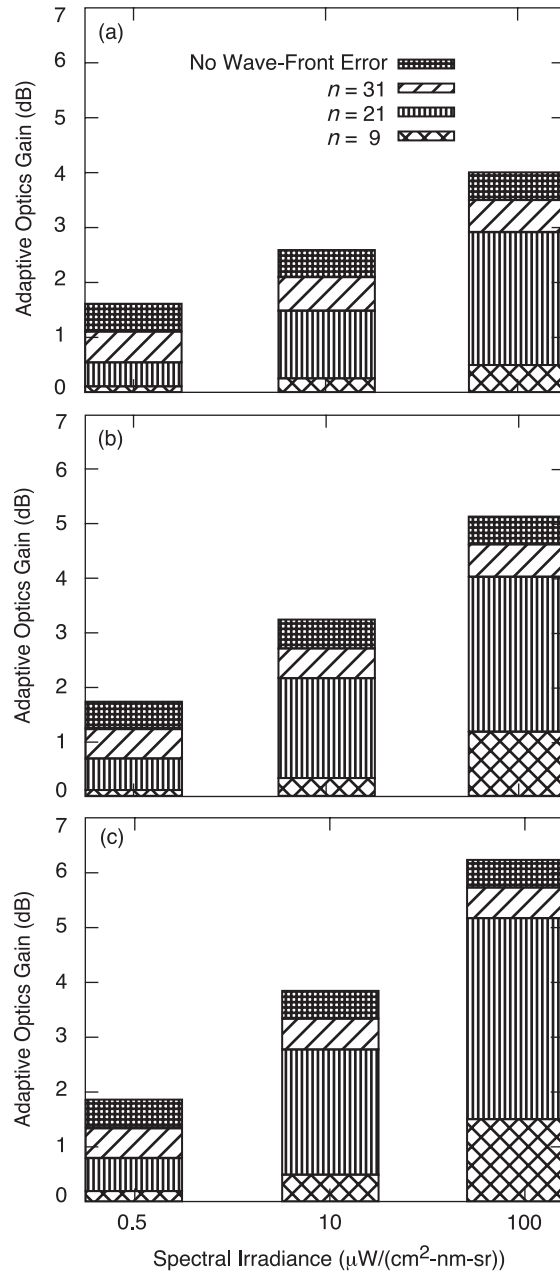
Fig. 6-5. Improvement in SNR for different background levels realized by implementing adaptive optics across a 1-m aperture: (a) 256-PPM, r_0 = 7 cm, probability of bit error (PBE) = 0.01, (b) 64-PPM, r_0 = 7 cm, PBE = 0.01, and (c) 16-PPM, r_0= 7 cm, PBE = 0.01.

optical downlink are an alternative approach, with such an approach, there is still a need for precision pointing of the narrow optical beam from the spacecraft to the ground. Proposed approaches for pointing the downlink from Mars, use an uplink beacon.

The required beacon power is determined from the requirements of the onboard acquisition and tracking sensors. For an onboard sensor requiring N signal photoelectrons per charged-couple device (CCD) frame, the uplink power is given by Eq. (6.1-1):

$$P_T = \frac{\dfrac{hc}{\lambda}}{G_T\left(\dfrac{\lambda}{4\pi R}\right)^2 G_R \eta_{QE} \eta_{atmos} \eta_{AT} \eta_{trans}} NF \qquad (6.1\text{-}1)$$

where h is Planck's constant; λ is the optical wavelength; F is the frame rate; and η_{QE}, η_{atmos}, η_{ATP}, and η_{trans} are the quantum efficiency, the atmospheric transmission, the optical transmission of the acquisition and tracking optical train, and the uplink transmitter efficiency, respectively.

An estimate of the required uplink power has been calculated for two scenarios, for a 30-cm receiver aperture at the spacecraft with the requirement that the downlink beam be stabilized to 1-µrad and 0.3-µrad, respectively [22]. Assuming a noise spectral density of the Olympus spacecraft, the required number of signal photoelectrons per CCD frame is 7,500 and 33,000 for the 1-µrad and 0.3-µrad stabilization requirements, respectively. The required uplink power over the link range 0.38 AU to 2.7 AU is given in Fig. 6-6 for these two cases, where $\lambda = 1064$ nm, $F = 10$ Hz, $\eta_{QE} = 0.4$, $\eta_{atmos} = 0.7$, $\eta_{ATP} = 0.25$, $\eta_{trans} = 0.5$, $G_T = 2.33 \times 10^{10}$ (5-cm uplink beam aperture), and $G_R = 8.37 \times 10^{11}$ (30-cm effective receiver aperture).

Strategies that use inertial sensors to measure spacecraft vibrations between camera frames allow for precision pointing at slower camera frame rates. This is an approach being considered at the farthest ends of the Mars link [23]. For ranges beyond Mars, plans call for a beacon-less approach that includes the use of an advanced system of well-calibrated and characterized onboard star trackers for precise pointing.

The optimum uplink transmitter gain is dictated by the atmospheric seeing conditions of the site. A plot of daytime atmospheric seeing measurements, θ_s, made at the Optical Communications Telescope Laboratory (OCTL) is shown in Fig. 6-7. Atmospheric seeing is a measure of the atmospheric turbulence and changes with time of day, atmospheric conditions, and season. The data in the figure were based on measurements using the star Polaris at a 94-deg Sun-angle. The flux incident on a CCD science camera at the OCTL focal plane was
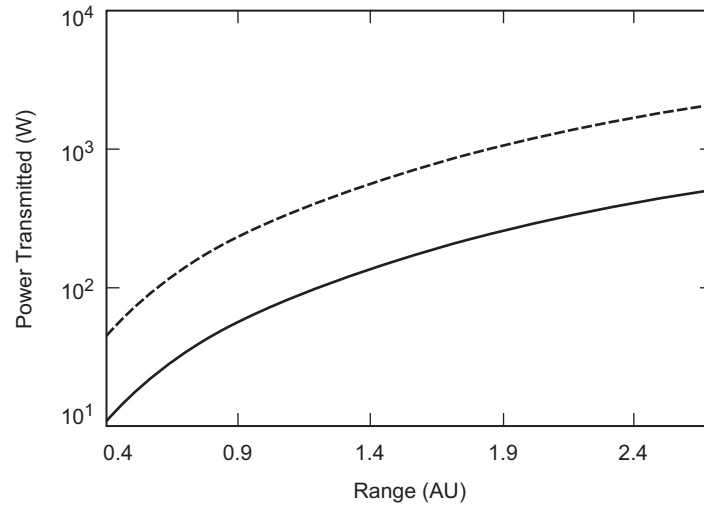
Fig. 6-6. Plot of required beacon power as a function of range for 7500 (solid) and 33,000 (dashed) signal photons per CCD frame.
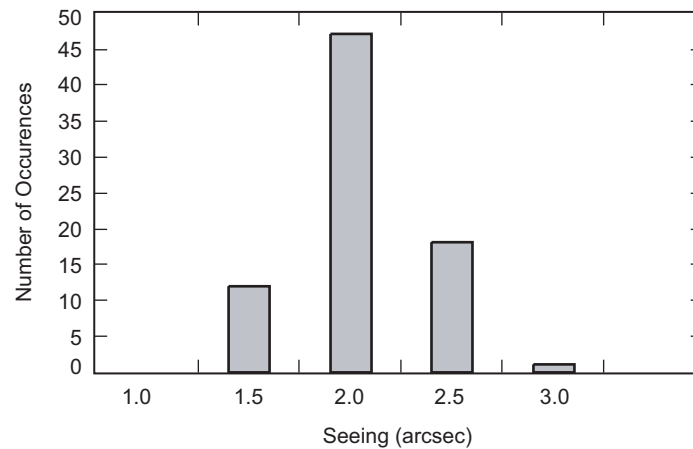

Fig. 6-7. Daytime atmospheric seeing measurements made through an 810-nm filter. Measurements were made in March 2004 using the 1-m OCTL telescope.

measured over a period of several seconds, and the full-width-at-half-maximum (FWHM) of the image calculated. Images were taken through a 10-nm wide optical filter centered at 810 nm. The mean seeing was 1.8 ±0.16 arc seconds.

Figure 6-8 shows the coherence length at 1064 nm. The results presented were corrected for the 34-deg zenith angle of Polaris as seen from the OCTL.
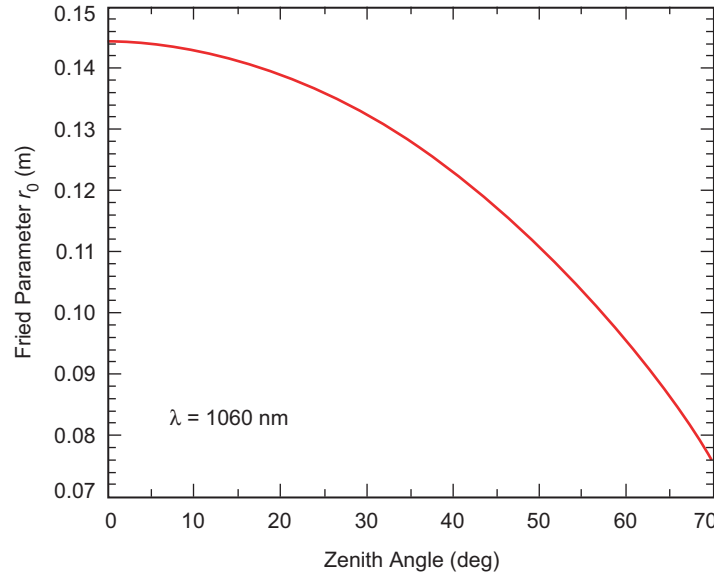
Fig. 6-8. Fried coherence length for range of zenith angles. Calculations are based on data taken at the JPL OCTL, Wrightwood, California.

Communications with deep space probes is highly asymmetric. Data rates for uplink commands are typically a few kilobits per second while downlinks from Mars will be in the tens to hundreds of megabits per second. Beam propagation strategies for the uplink optical command are the same as those for beacon transmission. At the low uplink data rates, the average optical power required for communications is much less than that required for the uplink beacon. However, because the higher pulse position modulation formats afford greater suppression of in-band optical noise, communications design considerations tend towards higher PPM orders. Yet, the peak power requirements will depend on the modulation format with the higher PPM orders requiring peak powers well in excess of those required for the beacon laser. The selection of a modulation format will be based on a systems trade of the modulation format required for background against the availability of lasers with the requisite average and peak power. For low-rate uplinks, on-off keying (OOK) or binary PPM formats are more consistent with the beacon laser requirements. In these modulation formats the peak-to-average power ratio is a factor of two.

The number of photons per bit required to close the link depend on receiver efficiencies, coding gains, and other factors. Modulating the beacon uplink in an OOK or binary PPM format is an operational scenario that would support the required beacon signal and a low rate communications uplink. Figure 6-9 plots the bits per photon received as a function of range for 20 W of optical
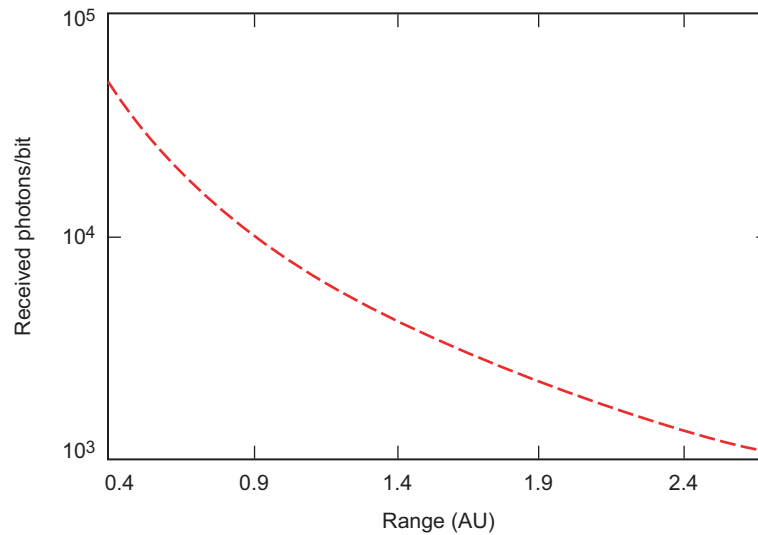
Fig. 6-9. Photons per bit received versus range for a 5-cm transmitter aperture emitting 20 W of power at 1064 nm.

power at 1064 nm. The beam is transmitted through a 5-cm aperture, corresponding to 20-µrad full-width-at-half-maximum beam divergence, and received by a 0.3-m aperture. The optical losses in the receiver and transmitter are 3 dB, and atmospheric transmission is 80 percent. Pointing losses correspond to 30 percent off-peak combined pointing bias and jitter. The data show that the received photons per bit ranges from 5.1×10^4 at 0.4 AU to 1.1×10^3 at 2.7 AU. The details of the link analysis are given in Table 6-2 for the 1-AU range.

Although a full-beacon power modulation is modeled above, it should be noted that other alternative approaches to integrating the command uplink and the beacon (such as wavelength or polarization diversity) are equally viable. In these approaches the command beam is shifted in wavelength or is orthogonal in polarization to the beacon and is then separated at the receiver by dichroic or polarizing beam splitters.

Over the years high power laser sources have been developed by industry for a variety of DoD applications. Boeing, Northrop Grumman, IPG Photonics, and other manufacturers build high power lasers in the 1000-nm to 1500-nm region that are useful for communications and beacon uplinks [24,25,26]. Unconstrained by size, mass, and power requirements of spaceborne systems, high power ground-based lasers satisfying kilobit per second uplink command links to probes in the Solar System are within the capabilities of the current state-of-the-art.

Table 6-2. Link analysis table for 10-bps uplink to spacecraft at 1 AU (5 percent of the transmitted power, i.e., 20 W, is diverted for the uplink command).

		dB
Gains		
Transmitted power, W	400	26.02
Effective transmitter aperture, m	5.00^{-2}	
Transmitter gain	2.18^{10}	103.38
Receiver aperture, m	3.00^{-1}	
Receiver gain	7.85^{11}	118.95
Losses		
Transmitter optical system	0.5	–3.01
Pointing loss		–1.55
Atmospheric transmission	8.00^{-1}	–0.97
Range, m	1.50^{11}	
Free space loss	3.19^{-37}	–364.97
Receiver optical system	0.5	–3.01
Loss to acquisition/tracking	0.05	–13.01
Signal Reception		
Received power, W	1.53^{-14}	–138.17
Energy/photon, J	1.87^{-19}	–187.29
Received number of photons/s	8.17^{4}	49.12
Bit rate	10	
Detection		
Detected photons/bit	8.17^{3}	

6.1.1.7 Techniques for Mitigating Atmospheric Effects. Scintillation and wavefront tip/tilt induces signal fades in an optical beam propagating through clear air turbulence. In this section we explore the impact of atmospheric turbulence and discuss mitigation strategies. On the downlink, the source of the disturbance is close to the receiver aperture, and using receiver apertures that are many atmospheric coherence cell sizes averages the scintillation and mitigates the effects of atmospheric turbulence. Discussions of aperture averaging effect are given by Fried and by Churnside [27,28]. Churnside's approximation for the aperture averaging is given in Eq. (6.1-2), where the aperture averaging factor A, is defined as the ratio of the intensity variance for an aperture D to that for a point detector $(\sigma_I(D)^2/\sigma_I(0)^2)$ for weak turbulence conditions. Churnside has shown that under weak turbulence conditions the aperture-averaging factor for large apertures can be approximated by

Eq. (6.1-2) for a plane wave A_{pw} and by Eq. (6.1-3) for a spherical wave A_{sw}. The wavenumber is k, and L is the optical path through the atmosphere.

$$A_{pw} = 0.932 \left(\frac{kD^2}{4L} \right)^{-7/6} \tag{6.1-2}$$

$$A_{sw} = \left(1 + 0.214 \left\{ \frac{kD^2}{4L} \right\}^{7/6} \right)^{-1} \tag{6.1-3}$$

Figure 6-10 shows the aperture averaging factor for both cases. The downlink from deep space is in the far field of the transmitter and corresponds to the plane wave case. The results show that for a 10-m class receiving aperture the intensity variance is reduced by approximately five orders of magnitude.

On the uplink the wavefront disturbance is close to the source, and the effects on the far-field intensity distribution are more severe. Aperture averaging is impractical, so alternative mitigation strategies are required. Adaptive-optics wavefront correction and multi-beam propagation are uplink strategies used to mitigate atmospheric turbulence effects.
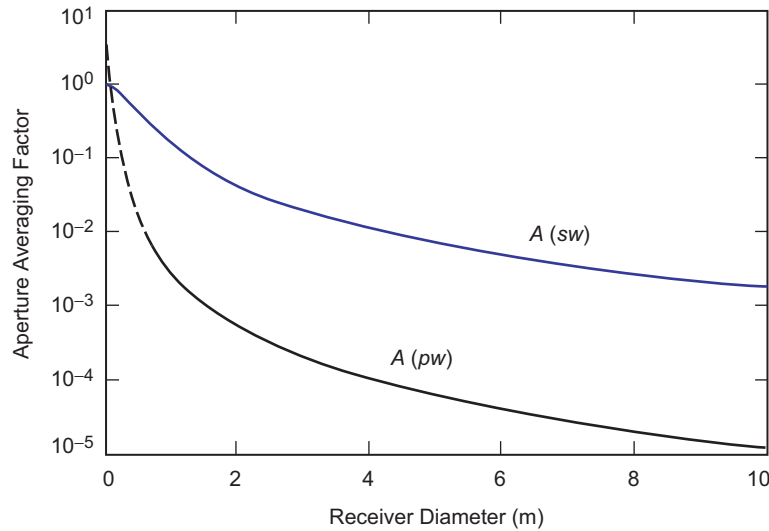

Fig. 6-10. Aperture averaging factor (the ratio of the intensity variance for an aperture D to that for a point detector versus receiver diameter). The upper trace is for a spherical wave and the lower for a plane wave, which is more indicative of optical links from deep space.

6.1.1.8 Adaptive Optics. The literature is replete with references on adaptive optics wavefront correction [29,30,31]. Rayleigh backscatter from copper vapor lasers focused 15 km to 18 km into the atmosphere have been used to correct higher order wavefront aberrations [32]. Sum frequency generation, using the 1064-nm and 1320-nm outputs from neodymium: yttrium aluminum garnet (Nd:YAG) lasers, and dye laser technologies have been used to generate a 589-nm probe beam for exciting the 90-km high mesospheric sodium layer [33,34]. Yet, laser guide stars allow for correction of higher order aberrations. Correcting lower order tip/tilt aberration requires the use of an exo-atmospheric beacon such as a natural guide star.

Figure 6-5 shows the gain that could be realized by adaptive optics in the deep-space channel. Yet, realizing this gain requires correction of both lower-order and higher-order aberrations. For deep-space communications where the spacecraft moves across the star field during interplanetary cruise and is in orbit around a planet during its mission, there is a paucity of stars bright enough for the lower-order tip/tilt correction. The planets are extended sources, and tip/tilt correction would require the use of a correlation tracker. Yet, for uplink beam propagation that uses the light from a planet or the downlink from the spacecraft as a reference beacon, the large point-ahead angles, given by Eq. (6.1-4), can exceed the isoplanatic angle θ_0, given by Eq. (6.1-5), and the uplink beam with such a reference can experience tilt errors greater than the beam divergence.

$$\theta_{pa} = 2\frac{V_{s/Earth}}{c} \qquad (6.1\text{-}4)$$

$V_{s/Earth}$ is the relative velocity between the spacecraft and Earth

$$\theta_0 = \left[2.914 \left(\frac{2\pi}{\lambda} \right)^2 (\sec(\xi))^{8/3} \int_h dh C_n^2(h) h^{5/3} \right]^{-3/5} \qquad (6.1\text{-}5)$$

for an estimated 5-km mean turbulence height the isoplanatic angle ranges from 7 µrad at zenith to 0.5 µrad at an 80-deg zenith angle.

Equation (6.1-6) gives the RMS atmospheric turbulence-induced wavefront tip/tilt across an aperture D. From the wavelength dependence of r_0 given in Chapter 3 and the r_0 dependence of the RMS tilt error in Eq. (6.1-6), the wavefront tilt is seen to be independent of wavelength. Figure 6-11 shows a plot of the RMS wavefront tilt as a function of zenith angle for three apertures of 5 cm, 10 cm, and 1 m. These apertures correspond to 3-dB beam widths of 22 µrad (4.4 arc-sec), 11 µrad (2.2 arc-sec) and 1.1 µrad (0.22 arc-sec), respectively. The RMS tilt error increases with zenith angle and is proportional to $D^{-1/6}$ [35]. Thus, the larger the aperture, the smaller the atmospheric tip/tilt.
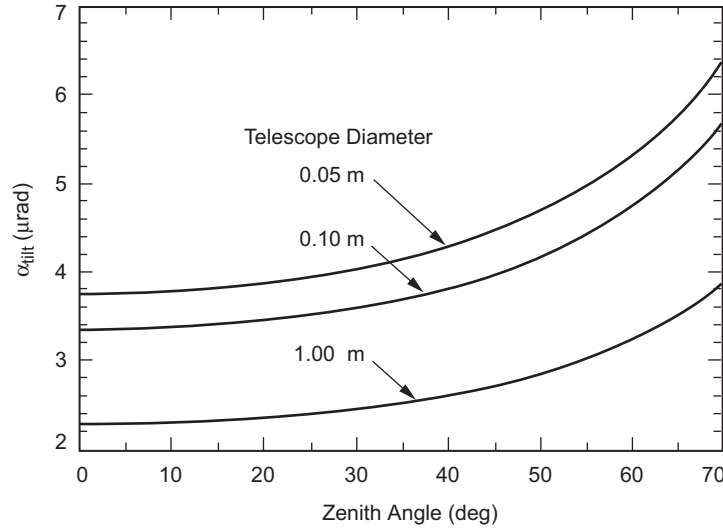
Fig. 6-11. RMS wavefront tilt as a function of zenith angle for three telescope apertures.

$$\sigma_{tilt} = 0.43 \left(\frac{\lambda}{D} \right) \left(\frac{D}{r_0} \right)^{5/6} \tag{6.1-6}$$

Although atmospheric tip/tilt affects the uplink beam pointing, the key metric of the link is how the atmosphere-induced beam jitter (dynamic tip/tilt) impacts the beam intensity on target. Specifically, what fraction of the far field beam size is due to the tip/tilt. The results in Fig. 6-11 show that the tip/tilt increases with decreasing transmitter aperture. The figure also shows that the ratio of the tip/tilt to beam size for these cases ranges from 17 percent to 30 percent of the beam size for the 5-cm beam, to 30 percent to 53 percent for the 10-cm beam; increasing with zenith angle. For the 1-m beam, the tip/tilt ranges from 2 to 3 times the beam size.

Currently, tip/tilt correction is achieved by using an exo-atmospheric beacon, such as a natural guide star or a nearby planet. For optical communications, the downlink from the spacecraft can serve as an exo-atmospheric beacon. The degree of correction achievable when using the downlink as a guide star for the uplink beam depends on the angle between the received and uplinked beams, i.e., the point-ahead angle. Figure 6-12 is a plot of the RMS wavefront tilt normalized to the 3-dB diffraction limited beam width of a 1-m telescope transmitting a 1064-nm beam. The results show that for point-ahead angles of less than 10 μrad, the RMS tilt error is less than 10 percent of the beam width for zenith angles less than 48 deg. For
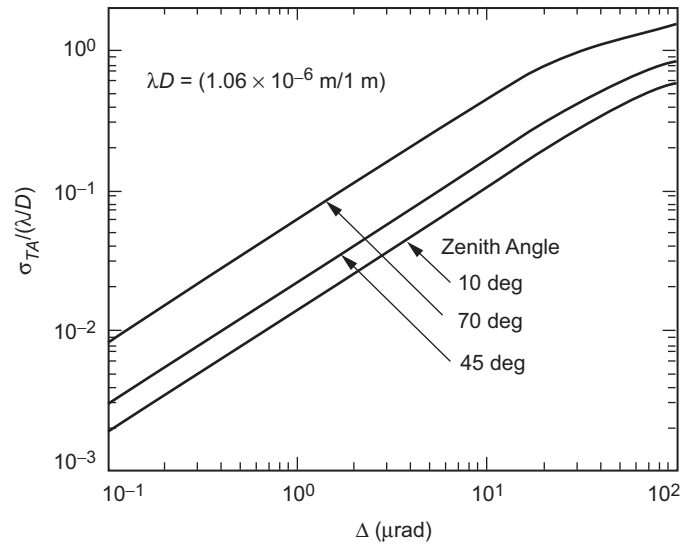
**Fig. 6-12. Normalized RMS wavefront tilt as a function
of point-ahead angle for a 1-m telescope.**

communications to geosychronous Earth orbit (GEO) and lunar spacecraft, where point-ahead angles are less than 10 µrad, the downlink can serve as an exo-atmospheric beacon to stabilize the uplink beam pointing from a 1-m aperture.

For a deep-space uplink, the point-ahead angles are on the order of hundreds of microradians. Figure 6-12 plots the normalized wavefront tilt as a function of point-ahead angle. If a planet such as Mars or the downlink from a spacecraft in deep space were used as an exo-atmospheric beacon, the residual normalized wave front tilt error would be on the order of the beam width and will degrade with increasing zenith angle.

Although the above results show that conventional adaptive optics techniques will not support uplinks to deep space probes, there are techniques under development that could mitigate the challenge. One such technique is the polychromatic laser guide star [36]. This proposed polychromatic guide star approach begins with two-photon absorption of the optical pump by the mesospheric sodium layer, and the subsequent relaxation to the ground state by a variety of fluorescence paths ranging from the UV to the near-IR. The approach uses the observed dispersion of the UV visible through IR components of the image to determine and compensate for atmospheric tip/tilt.

6.1.1.9 Multiple-Beam Propagation. An alternative method to mitigate scintillation on the uplink is to transmit multiple beams through different atmospheric spatially coherent cells. The uplink beam can be either from

different sources or from a single beam separated into multiple beams. When originating from a single source, it is desirable that the beams not be spectrally coherent to avoid interference effects when they are recombined in the far field. This can be done by introducing a path length delay among the beams that is greater than the coherence length of the source.

When the uplink beamwidth is much larger than the atmospheric seeing, the atmosphere has a negligible contribution to the beam divergence. Yet, atmospheric seeing depends on site location, atmospheric conditions, and zenith angle. For a site such as TMF with 2-arcsecond seeing, turbulence-induced beam spreading would increase the effective beamwidth of a 20-µrad transmitter beam by approximately 10 percent. To maintain the same beam intensity at the spacecraft, this would require a 20-percent increase in transmitted power.

Depending on the atmospheric conditions and the spacecraft tracking scenario, it may be necessary to transmit 4, 8, or 16 beams to reduce the intensity variance to the required level. Experimenters have reported a variety of observations when propagating any number N of beams. Reported intensity variance mitigation ranged from no effect to mitigation inversely proportional to $1/\sqrt{N}$ and to $1/N$ [37,38,39]. Results from a limited data set in the JPL Ground-to-Orbiter Lasercomm Demonstration is shown in Fig. 6-13. Although inconclusive, the data shows that the normalized variance in the intensity is approximately proportional to $1/\sqrt{N}$ for two beams, and to $1/N$ for four beams.

Based on these experimental results, we have plotted in Fig. 6-14 the normalized intensity variance given by Eq. (6.1-7) as a function of zenith angle
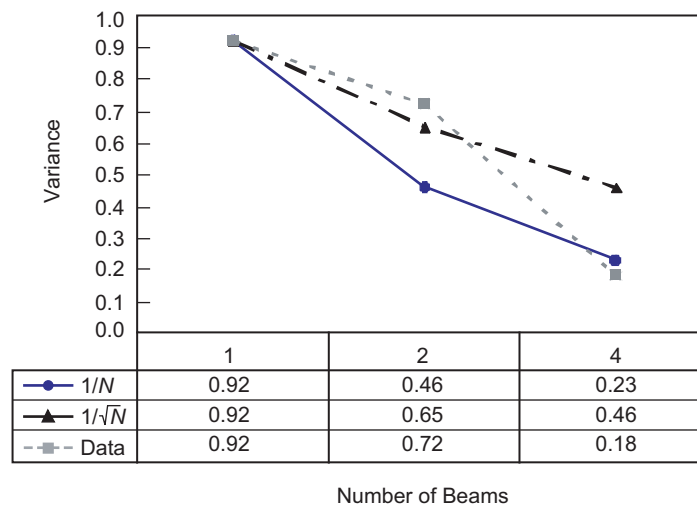

	1	2	4
$1/N$	0.92	0.46	0.23
$1/\sqrt{N}$	0.92	0.65	0.46
Data	0.92	0.72	0.18

Number of Beams

Fig. 6-13. Comparison of normalized intensity variance data for 1-, 2-, and 4-beam transmissions compared to 1/N and 1/$\sqrt{N}$.
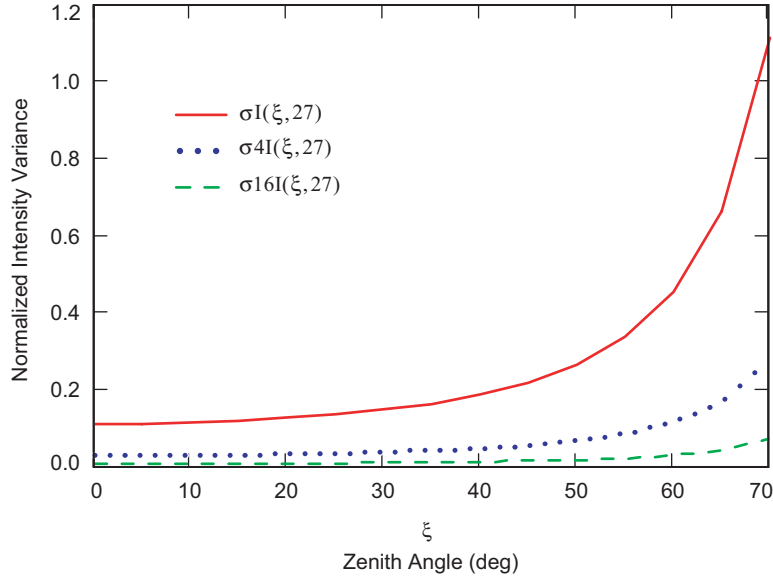
Fig. 6-14. Normalized intensity variance versus zenith angle for 1-, 4-, and 16-beam uplinks (wind speed is 27 m/s).

for 1, 4 and 16 beams [40]. These results were used in Eq. (6.1-8) to calculate the probability $F(\sigma^2,\zeta)$ that the signal fades depths are less than ζ for normalized intensity variance σ^2. Figure 6-14 plots the results for the normalized intensity variance corresponding to 1-, 4-, and 16-beam uplinks and fade depths less than 3 dB [41].

$$\sigma^2_{I/I_0} = \left(\exp\left[2.24 k^{7/6} \sec(\xi)^{11/6} \int_{h_1}^{h_2} C_n^2(h,V) h^{5/6} dh \right] - 1 \right) \quad (6.1\text{-}7)$$

$$F(\sigma^2,\zeta) = 0.5 \left[1 + erf\left(\frac{-0.23\zeta + 0.5\sigma^2}{\sqrt{2\sigma^2}} \right) \right] \quad (6.1\text{-}8)$$

In the final analysis, the uplink beacon transmitter design will be based on an optimization of the trade space of available uplink power, the site's atmospheric seeing conditions and transmitter gain, and the spacecraft's acquisition pointing and tracking strategy.

6.1.1.10 Safe Laser Beam Propagation into Space. Propagation of high-powered laser beams from the ground to space can put piloted aircraft and sensitive space assets at risk. JPL has developed a three-tiered system for safe ground-to-space laser beam propagation. The concept is shown in Fig. 6-15
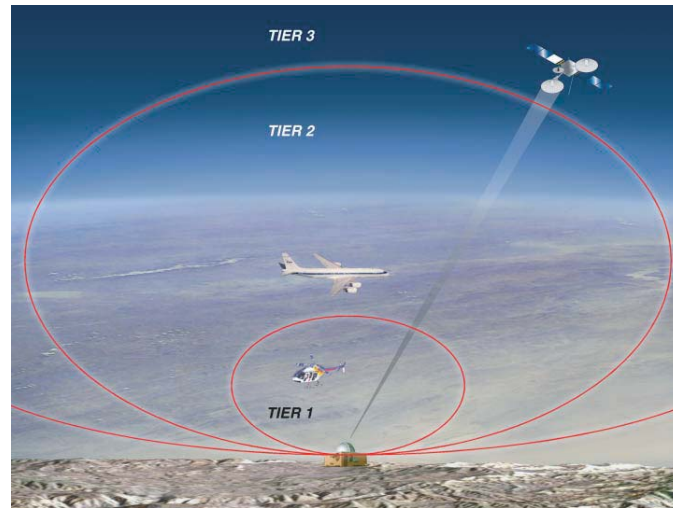
Fig. 6-15. Three-tiered system for safe laser beam propagation into space.

[42]. The objective is to demonstrate an electronic detection system that will eliminate the need for ground observers and lead the way to the implementation of autonomously operating ground stations.

Tier-1 extends from the telescope aperture to a range of approximately 4 km, and it consists of a pair of high-sensitivity long wave infrared (LWIR) cameras—the first wide field with 35 deg × 46 deg FOV, and the second narrow field with approximately 9 deg × 12 deg—for detecting small, low, and fast-moving aircraft approaching the beam. The system shown in Fig. 6-16 was developed for JPL by Image Labs International (ILI) Corporation of Bozeman, Montana.

Tier-2 overlaps with the outer range of Tier-1 and extends to the edge of space. Aircraft in Tier-2 are detected by radar. Two different radar schemes are implemented in this tier. The first, a radar display interface (RDI) is applicable to areas with controlled airspace and uses a radar feed from the controlling agency—the FAA for the United States and its territories and the corresponding air traffic control agencies for foreign stations—to alert laser beam operators to aircraft that are at risk. Such a system is used at the Air Force Research Laboratory's (AFRL's) Starfire Optical Range and the Air Force Maui Space Surveillance System (MSSS). Aircraft detected by the Air Traffic Control (ATC) radar systems in Honolulu CERAP (Combined Center Approach Control) that are in a prescribed area around MSSS are displayed at the MSSS on a direct feed from the ATC. A picture of such a display centered on Maui is shown in Fig. 6-17. In the figure the status of the RF link to the FAA is shown here on the display as "up." The exclusion zone and the laser beam pointing direction are also shown.

Fig. 6-16. Image Labs Tier-1 aircraft avoidance system consists of two long wave infrared (LWIR) cameras (wide-field 35 deg × 46 deg and narrow-field 12 deg × 9 deg).
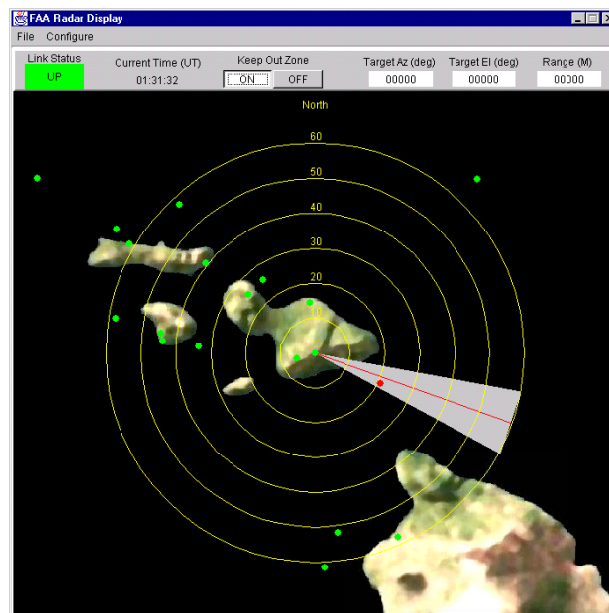

Fig. 6-17. RDI system developed by Boeing Technical Services for the AMOS. The system shows aircraft positions superimposed on a topographic map of the Hawaiian Islands. (The picture is courtesy of Capt. J. Snodgrass, Maui Space Surveillance Center, USAF.)

The second radar approach is that used during the Ground to Orbit Lasercomm Demonstration (GOLD) project [43]. An X-band radar system bore sighted with the telescope was used to detect aircraft at risk. The 60-mrad radar beam is much wider than the nominal 0.03-mrad laser beam. The radar detects aircraft at risk of entering the laser beam and triggers the laser beam shutter to interrupt lasing before the aircraft enters the laser beam. Depending on the location of the ground station, operating such a radar system may require frequency allocation by regulatory agencies and coordination with other users. The station may be assigned an operating frequency and bandwidth, and allowed to transmit up to a maximum radiated power. The performance specifications of the Primus-40 radar system that will be installed at JPL's OCTL are given in Table 6-3. A picture of the system is shown in Fig. 6-18.

The ability of the Primus-40 system to detect aircraft can be estimated from the manufacturer's specification and the radar Eq. (6.1-9) [45].

$$R_{\max} = \left[\frac{P_T G A_e \sigma}{(4\pi)^2 S_{\min}} \right]^{1/4} \qquad (6.1\text{-}9)$$

In Eq. (6.1-9), PT is the power transmitted, G is the transmitter antenna gain, A_e is the effective receiver area, σ is the target cross-section, and $S_{\min}$ is the minimum detectable signal. The radar cross section is a function of the radar wavelength and the aspect angle of the target with respect to the incident beam. Reference [45] gives nominal cross sections at microwave frequencies for various objects at normal incidence. These are: 1 m^2 for a small single-engine craft, 40 m^2 for a large jet airliner, and 100 m^2 for a large jumbo jet. It should be noted that the cross section, and hence the radar return signal, varies with aspect angle. Notwithstanding this, the above cross sections do provide a guideline for bounding the radar detection capabilities.

Table 6-3. Primus-40 radar system parameters [44]

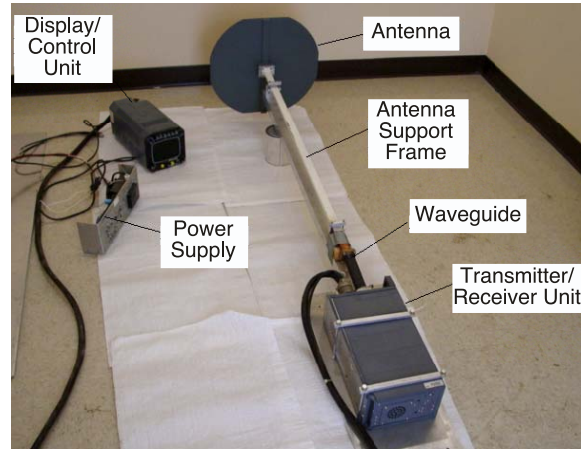| Parameter	Value
Average power, W	3
Peak power, kW	7
Pulse width, μs	1
Repetition rate, Hz	121
Operating frequency, MHz	9345
Bandwidth, kHz	375
Antenna diameter, m	0.45
Minimum detectable signal, dBm	−108

Fig. 6-18. Honeywell Primus-40 weather radar used for aircraft detection during the 1996 GOLD optical communications experiments.

From the target cross sections above and the data from Table 6-3, the maximum detection ranges for these targets are 26 km, 65 km, and 82 km, respectively. For mean sea level service ceilings of 7.6 km (20,000 ft), 12.2 km (40,000 ft), 13.7 km (45,000 ft) for these aircraft, the Primus-40 will detect these aircraft when operating at their service ceilings at ranges of 15 km, 29 km, and 34 km, respectively. The estimated radar returns for the three types of aircraft are 9, 14, and 15 dB above the minimum detectable signal, $S_{\min}$.

Tier-3 covers transmission in space and extends over the range covered by Earth-orbiting satellites. At this time, coordination of laser transmission with the LCH is not required for civilian agencies. For sites required to coordinate their transmissions, the procedure begins with the registration of the site and the laser. Key information includes:

- Laser site geodetics (latitude, longitude, and altitude)
- Laser output power peak and average
- Laser wavelength
- Beam divergence
- Operating aperture diameter
- Jitter angle

Based on the laser characteristics, the LCH would either issue a waiver stating that no coordination is needed for transmission or require that all laser transmission be coordinated. If coordination were required, the station would submit the details of the laser transmission for each operation, identifying the target satellites and pointing directions and times. The LCH would then respond with a listing of intervals when laser beam propagation is permitted. Civilian

agencies, such as NASA, although not required to coordinate with the LCH, may opt to do so for high-power laser beam transmission.

6.1.1.11 Concept Validation Experiments Supporting Future Deep-Space Optical Links. Ground-to-space optical beam propagation experiments began shortly after the invention of the laser, and several of the key challenges were identified in the early beam propagation experiments. Among these were: (i) reliably pointing narrow laser beams at spacecraft, (ii) effects of atmospheric scintillation on laser beam propagation, and (iii) effects of cloud cover. Experiments performed by JPL over the years have highlighted the challenges of propagating laser beams through the atmosphere. In some cases, these experiments have also demonstrated strategies to mitigate these deleterious effects. the difficulties of the challenge have been highlighted, and strategies to mitigate the effects have been demonstrated. In this section we discuss the JPL experiments from the Surveyor VII experiments through the GOPEX, Compensated Earth-Moon-Earth Retro-Reflected Laser Link (CEMERLL), and GOLD demonstrations, their results, and their contribution to the body of knowledge of laser communications.

In May 1962, Smullin and Fiocco demonstrated the first detection of a laser beam reflected from the lunar surface. They coupled a 50 joule per pulse ruby laser to a 30-cm telescope and transmitted the laser beam to the Albategnius, Copernicus Tycho, Longomontanaus regions of the Moon dark during the first quarter. The beam reflected from the lunar surface was detected by a photomultiplier at the Cassegrain focus of a 1.2-m telescope [46]. This lunar bounce experiment was followed by a series of retro-reflecting experiments to Earth-orbiting satellites. Yet, the effects of atmospheric seeing on a deep space optical link was not observed until 1968 when experimenters at Table Mountain (Wrightwood, California) and at Kitt Peak (Arizona) transmitted laser beams to the Surveyor VII lunar lander [47].

A 2.25-W continuous wave (CW) Ar:ion laser coupled through the full 0.6-m TMO[1] telescope was shuttered 30 s on and 30 s off. Losses (4.2 dB) in the telescope optical train resulted in 0.9-W optical power being transmitted in the 2–3 arc second atmosphere-seeing-limited beam. The 2-day long experiment was conducted during 08:15–09:26 and 10:30–11:10 Greenwich mean time (GMT) and on January 20, and during 08:30–8:41 GMT on January 21. The laser beams were detected by the vidicon on the spacecraft, and the images relayed back to Earth in real time. Figure 6-19 shows the picture of the uplink laser beams from the two stations in the non-Sun-illuminated area of the planet. The record shows that the detected uplink was sporadic. The TMF

---

[1] The Table Mountain Observatory (TMO) was renamed Table Mountain Facility (TMF) in the mid 1990s. Documents of different dates reflect these two terms for the same location.
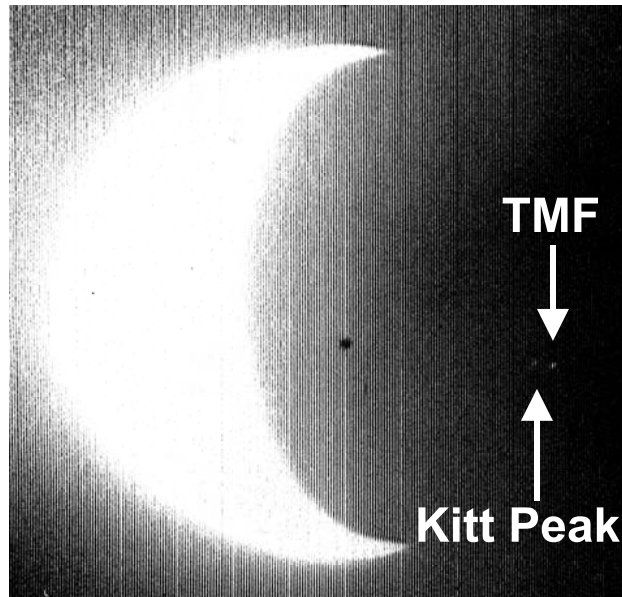
Fig. 6-19. Laser beams transmitted from Kitt Peak and Table Mountain detected by Surveyor VII vidicon camera on the Moon.

records of the experiment reported that the link was severely affected by the wind and seeing conditions at the site.

6.1.1.11.1 Galileo Optical Experiment (GOPEX). With the development of high power lasers and sensitive detectors, laser ranging experiments to Earth-orbiting satellites and to lunar retro-reflectors became more prevalent. Yet, the low percentage of returns from space-based retro-reflectors provided little experimental data to differentiate between tracking and scintillation-induced signal fades. What had not been demonstrated was reliable open-loop pointing of a narrow laser beam to a deep space probe. By 1992, there was enough uncertainty in precision pointing of laser beams to space that the opportunity provided by Galileo's VEEGA (Venus, Earth, Earth, Gravity Assist) trajectory (Fig. 6-20) was recognized as a unique chance to demonstrate an optical communications link to a spacecraft in deep space.

GOPEX was the first demonstration of open loop pointing of a laser beam from Earth to a deep space probe [48]. Uplink beams were transmitted from ground stations at the JPL Table Mountain Facility, Wrightwood, California and the Air Force Starfire Optical Range, Albuquerque, New Mexico to the Galileo spacecraft beginning at a range of 600,000 km out to 6,000,000 km [49]. The SOR provided cloud cover site diversity for the uplink. The experiment was conducted over the eight-day period December 9 through

December 16, 1992 during the second Earth Gravity assist segment of Galileo's trajectory, Fig. 6-20. The spacecraft's solid state imaging camera, Fig. 6-21, was used to detect the doubled Nd:YAG (532-nm) uplink laser transmission. The experiment's objectives were to:

- Demonstrate laser beam transmission to a spacecraft at deep-space distances.
- Verify laser-beam pointing strategies applicable to an optical uplink based solely on spacecraft ephemeris predicts.
- Validate models developed to predict the performance of the optical link.

The 90-deg Sun–Earth–spacecraft phase angle during the second Galileo flyby allowed nighttime laser transmission from the ground, providing excellent
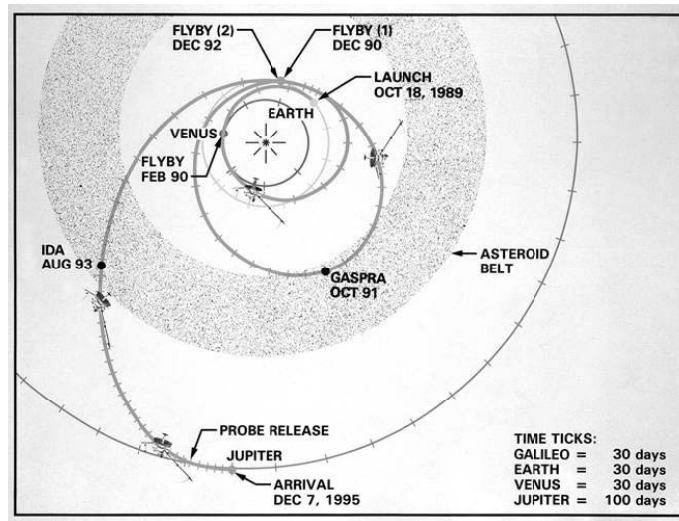

Fig. 6-20. The GOPEX demonstration was performed on the second Earth flyby of Galileo's VEEGA trajectory.
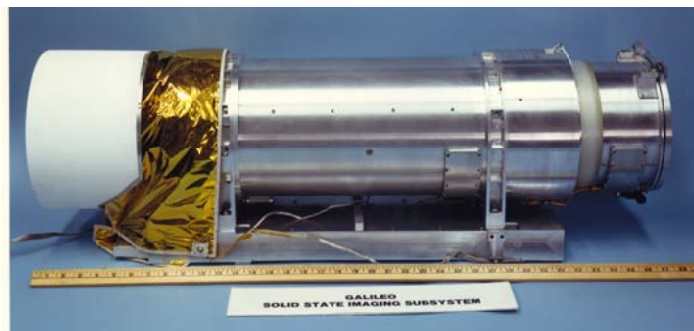

Fig. 6-21. Galileo solid-state imaging camera.

contrast of the uplink laser against a dark Earth background. The experiment was conducted between the hours of 3:00 a.m. and 6:00 a.m. Pacific Standard Time. Camera shutter exposure times were held to less than 800 ms to prevent saturation of the signal pixels by blooming of pixels imaging the sunlit part of the Earth.

The spacecraft instrument platform with the solid-state imaging (SSI) camera was scanned across the Earth, parallel to the Earth's terminator during each exposure, Fig. 6-22(a) and the pulsed uplink laser beams were imaged as a series of evenly spaced bright dots in the frame, Fig. 6-22(b). The laser pulse repetition rates from the two uplink facilities were set at 10 Hz for the SOR and 15 Hz for TMF.

The laser transmitters at both sites were frequency-doubled Nd:YAG lasers emitting at 532 nm coupled to a telescope through the coudé focus. The characteristics of both the SOR and TMF transmitters are given in Table 6-4.

At TMF, the telescope was the 0.6-m equatorial-mount astronomical telescope that had been used in 1968 to perform the laser transmission to the Surveyor VII spacecraft on the Moon. However, unlike in the Surveyor VII experiment, the laser beam illuminated a subaperture of the 0.6-m telescope. The telescope is f/36 at the coudé focus, and the appropriate beam-forming lens set was inserted into the coudé optical train to achieve the required laser beam divergence. From the coudé optical bench, the laser beam was reflected from a turning flat and through two turning mirrors before being incident on the 0.2-m secondary mirror. The beam then illuminated a 12-cm subaperture on the
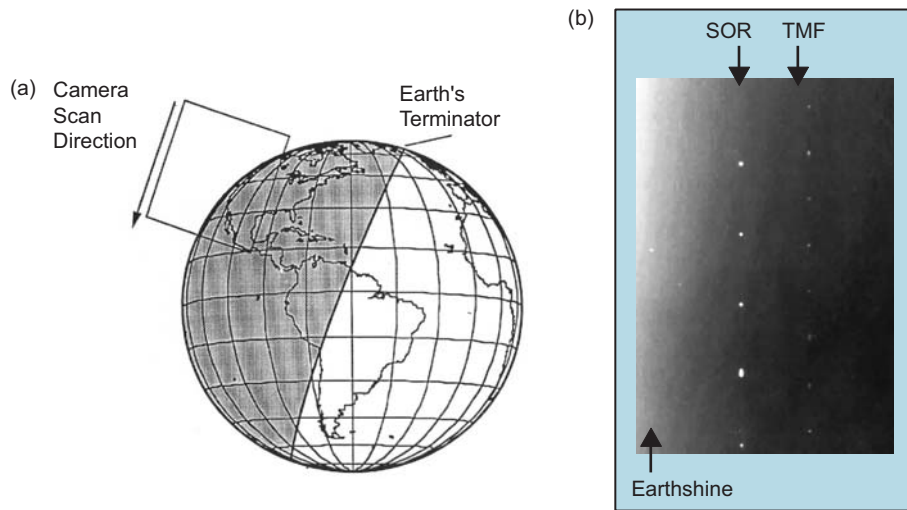

Fig. 6-22. SSI camera: (a) schematic showing how Galileo's SSI camera was scanned parallel to the Earth's terminator to capture SOR and TMF laser transmissions and (b) an SSI camera frame showing both the SOR and TMF laser beam transmissions.

Table 6-4. GOPEX laser transmitter characteristics.

Item	Table Mountain Observatory	Starfire Optical Range
Wavelength, nm	532	532
Pulse energy, mJ	250	350
Repetition rate, Hz	15–30	10
Pulse width, ns	12	15
Beam divergence, μrad		
Days 1–4	110	80
Days 6–8	60	40
Telescope mirror diameter		
Primary, m	0.6	1.5
Secondary, m	0.2	0.1
Optical train transmission	60 percent	43 percent

telescope primary. Subaperture illumination eliminated the power loss of a full-aperture illuminated system and allowed the propagation of the wide beam divergences needed to compensate for pointing errors and atmospheric beam wander effects. The full 0.6-m aperture of the telescope was used to collect light from the reference stars that were used to point the telescope to the spacecraft.

Two beam-forming lens sets, one for 110-μrad divergence and another for 60-μrad divergence, were designed to bring the laser beam to a focus at 1.3 km with the telescope focused at infinity. These wide-uplink beam divergences were several times atmospheric seeing, and thereby mitigated the effects of atmospheric tilt on pointing.

At the SOR, the flat-top laser beam was transmitted through the full 1.5-m telescope aperture with less than 10-percent loss from the secondary mirror obscuration. At both facilities, the requisite beam divergence was achieved by focusing the laser in the atmosphere. A thin-film-plate polarizer served as the aperture-sharing element, and coupled the laser output to the coudé optical train while allowing reference stars to be observed by the CCD camera positioned in the orthogonal leg of the optical train. The required laser beam divergence was achieved by focusing the outgoing laser beam at ranges of 40 km and 20 km, corresponding to 40-μrad and 80-μrad beam divergence, respectively.

Blind-pointing the telescope to Galileo was accomplished by implementing the following sequence of steps:

1) Point the telescope to a reference star located within 0.5 deg and northwest of the spacecraft.

2) Reset the telescope's right ascension (RA) and declination (Dec) readings to match the star's catalogued coordinates.

3) Two minutes and thirty seconds before transmission, center the star in the eyepiece at the telescope's coudé focus.

4) Ten seconds before transmission, point the telescope to Galileo and set the telescope to sidereal tracking for the next thirteen seconds.

This procedure was repeated during the 3-minute to 6-minute intervals between the laser transmissions to mitigate the effects of atmospheric refraction on the uplink beam pointing. Because the telescope calibration was performed just before transmission, the pointing errors introduced by mount sag were small [50]. In contrast, mount calibration at the SOR was performed only once per night, just prior to the night's experiment. Over the 8-day period, six reference stars of magnitudes 6 to 10 were used to point the telescopes to Galileo.

A summary of the detected laser detections over the 6-day GOPEX demonstration is given in Table 6-5. The uplink was detected on 56 of the 156 frames returned from the spacecraft. The uplink was detected on 82 percent (45 of the 67) of the frames with exposure times greater than 400 ms, and on only one of the 89 frames with exposures of less than 400 ms. Post-demonstration analysis showed that the loss in detection on these frames was due to an unanticipated bias in the scan platform direction. The loss of signal on the remaining 12 frames was due to a variety of causes including denial of laser beam transmission by the LCH, poor RF downlink, denial of opportunity by the Galileo Project office, and attenuation due to cirrus clouds. The large number of frames that were received with images of the uplink signal validated both the pointing strategies and the selection of uplink beam divergences.

Inclement weather, aborted transmissions, and restrictions imposed by regulatory agencies and by the Project Galileo team, temporary signal-to-noise anomalies on the RF downlink data transmission, and an unexpected camera-pointing bias error accounted for the loss of data on the remaining frames. The weather at TMF and SOR in the last 4 days of the demonstration validated the need for ground-station site diversity in optical communications. A Pacific storm dropped snow at TMF on the fourth day of the experiment precluding transmission from that location. The storm moved eastward and precluded transmission from the SOR for the remainder of the demonstration.

Analysis of the pulse strengths in the GOPEX frames showed the effects of scintillation fades. Calculations of scintillation variance from these and other GOPEX data showed that for both sites the data fit the strong turbulence theoretical models on all but the second day [51]. Figure 6-23 shows a 3-D image of one of the GOPEX frames. The fluctuations in the detected signal caused by atmospheric scintillation at TMF are clearly shown, and signal strength variations would clearly affect the quality of a command uplink to a

Table 6-5. Summary of laser signals detected during GOPEX.

Day	Shutter Speed (ms)	Frames Received	Frames with Detections
1	133	9 of 10	0
	200	24 of 25	0
	400	19 of 20	11[b]
	800	5 of 5	5
2	200	5 of 5	0
	267	15 of 15	0
	533	15 of 15	13
	800	5 of 5	5
3	200	5 of 5	0
	267	10 of 10	0
	533	5 of 5	5[c]
4	200	3 of 3	1[b,c]
	267	4 of 4	0
	533	3 of 3	1[c]
5		No GOPEX transmissions	
6[a]	133	3 of 3	0
	267	6 of 6	0
	533	3 of 3	3
7[a]	200	3 of 3	0
	400	3 of 4	3
	800	3 of 3	3
8[a]	267	2 of 2	0
	533	4 of 4	4
	800	2 of 2	2

[a] Adverse weather at SOR precluded laser transmission.

[b] Detection on some of the frames was based on one to three possible spots in the frame.

[c] Adverse weather at TMF precluded laser transmission; cloudy at SOR.

deep space probe. Subsequent JPL experiments would explore strategies to mitigate the effects of scintillation on the optical uplink.

6.1.1.11.2 Compensated Earth-Moon-Earth Retro-Reflected Laser Link (CEMERLL). The objective of the 1994 CEMERLL experiment was to evaluate the use of adaptive optics techniques in mitigating the effects of atmospheric turbulence on the uplink laser transmission [52]. The experiment was conducted jointly by JPL and the Air Force Research Laboratory's SOR

from March through September 1994 and transmitted both atmosphere-compensated and uncompensated laser beams to the retro-reflectors on the Moon [52].The target was the 300-element lunar Apollo-15 corner cube array located near Hadley Rille [53,54] (see Fig. 6-24).

The experiment was conducted during the first and last quarter phases of the Moon when the retro-reflectors were on the dark side of the lunar landscape [55]. This prevented saturation of the detectors by the sunlit lunar surface. The
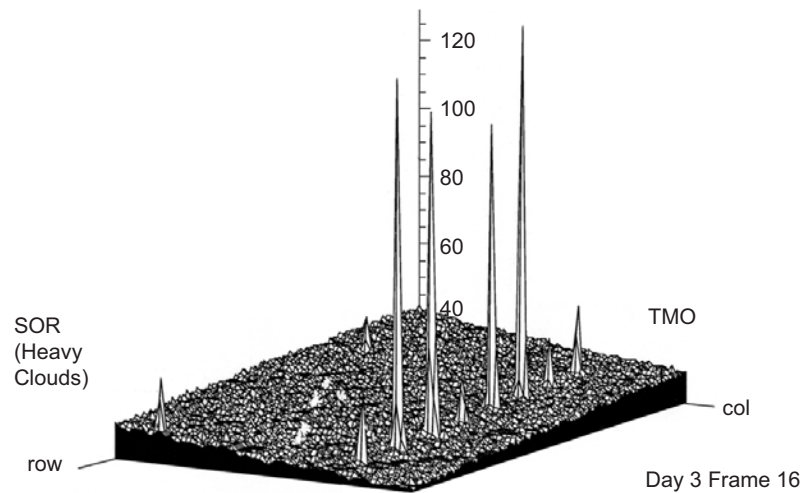

Fig. 6-23. Plot of received GOPEX uplink signal strength over a 400-ms interval.
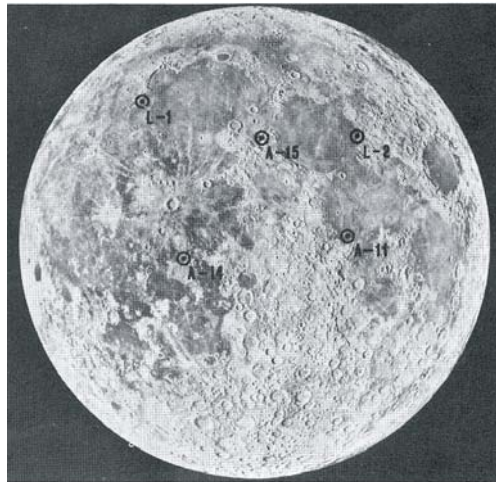

Fig. 6-24. Locations of Apollo 11, 14, and 15 and Lunakod 1 and 2 retroflectors on the moon [1].

retro-reflected laser pulses were detected at the 3.5-m SOR telescope over the three nights September 27, 28, and 29. In excess of 100 retro-reflected photons per pulse were detected when the beam was compensated. No returns were detected with the uncompensated beam.

The Rayleigh backscatter from a copper vapor laser (CVL) focused 10 km above the observatory created the laser guide star (LGS) for adaptive optics wavefront correction. Because the angular separation between the retro-reflectors and the closest exo-atmospheric guide star was well beyond the 12-μrad isoplanatic angle, tip/tilt compensation was not feasible. As seen from Earth, the closest stars passing by the edge of the Moon were approximately 3 mrad from the retro-reflectors. A Shack-Hartman wavefront sensor at the transmitter facility detected the wavefront aberrations of the CVL beam, and the wavefront reconstructor generated the commands to the deformable mirror (DM).

The Q-switched 1064-nm Nd:YAG scoring beam emitted 15-ns pulses at a 20-Hz pulse repetition rate. The laser uplink was coupled through the telescope's coudé optical path. The energy per pulse transmitted from the telescope to the Moon was 340 mJ. The scoring beam was made incident on the DM, pre-distorting the beam's wavefront so that it was well corrected at 10 km above the telescope. Under typical conditions, the seeing-limited divergence of the 1064-nm laser was typically 17 μrad. With the higher order adaptive optics loop closed, the uplink beam divergence decreased to less than 3 μrad.

The receiver was a Rockwell Science Center solid-state photomultiplier (SSPM) detector in the focal plane of the 3.5-m SOR telescope was the receiver. The detector quantum efficiency was 6–8 percent at 1.06 μm, and its 800 × 800 μm active area corresponded to a 70-μrad FOV at the f/5.6 Nasmyth focus. The detector was integrated to a high-bandwidth trans-impedance amplifier, and the assembly was enclosed in an Infrared Laboratories liquid-helium dewar cooled to 11 K. A 10-nm and a 1-nm optical filter were inserted in front of the detector to suppress the infrared signature from the dark side of the Moon.

The round trip light time between Earth and the lunar array is approximately 2.7 s; a value that continuously changes as the Moon transits the sky. The detector electronics were range gated to protect the SSPM from saturating. The sequence for initiating the detection window began with a trigger signal generated by the outgoing Nd:YAG laser at the 1.5-m telescope. The SOR calculated the expected time of arrival of the return signal at the 3.5-m telescope was calculated from the ephemeris predicts and the timing mark generated by the outgoing laser pulse. A time interval counter kept track of the delay at the 1.5-m facility. At the appropriate time, the counter sent a trigger signal to the scalar averager at the 3.5-m facility to initiate the detection window on a dedicated line between the facilities of known transmission delay. The detector trigger delay was adjusted to accommodate for the finite transit

time of the electronic signal between the 1.5-m and 3.5-m facilities. In addition, the delay was continuously adjusted to correct for the changing RTLT to the retro-reflectors as the Moon transited the sky.

Figure 6-25 is a scalar averager display of the return signals in an 82-ms interval. The vertical scale is 2 counts/division. The detection threshold was set at 210 mV, corresponding to 30 photons. This reduced the probability of false alarms while still retaining the ability to detect retro-reflected returns. The figure clearly shows the returns occurring 50 ms apart, an interval corresponding to the 20-Hz laser pulse repetition rate.

Of the more than 200,000 pulses transmitted, approximately 30 returns were detected all over the three-day period September 27 through September 29. Transmission strategies included (i) direct pointing and (ii) scanning the beam in 1-μrad increments over a 15-μrad × 15-μrad space around the location of the retro-reflectors. Although the highest percentage of returns (0.1 percent) was observed when scanning on September 28, this approach did not yield the same degree of success on September 29. The low and erratic frequency of returns was attributed to the uncompensated wavefront tip/tilt in the transmitted beam.

6.1.1.11.3 Ground to Orbit Lasercomm Demonstration (GOLD). The ETS-VI satellite was launched by Japan's NASDA on August 28, 1994 as a test bed to assess a variety of telecommunications scenarios over a wide range of frequencies. The satellite payload included the laser communications equipment (LCE) to demonstrate space-to-ground laser communications [56]. Failure of the apogee kick motor prevented geostationary positioning and left the satellite in a geo-transfer orbit with the spacecraft visible from ground facilities around the globe. NASDA transferred the satellite into a 3-day sub-recurrent orbit in November 1994 to facilitate the performance of communication experiments around the globe. Figure 6-26 shows the ground track of the satellite. The GOLD experiments with TMF were conducted during the section of the apogee pass when the satellite was over Central America [57,58].

The experiments were conducted from November 1995 to May 1996, except for a one-month break in January 1996 when the spacecraft went into eclipse and lasercom activities were shut down to conserve power. The experiment objectives were to:

- Demonstrate two-way spatial acquisition/tracking of laser beams with a spacecraft
- Accomplish one-way and two-way optical data transfer to a spacecraft and measure bit error rates
- Accumulate 10 elapsed hours of transmission/reception experience and 30 GB over a 6 month period

- Compare downlink atmospheric transmission losses with similar data from the Table Mountain Facility's Atmospheric Visibility Monitoring (AVM) observatory
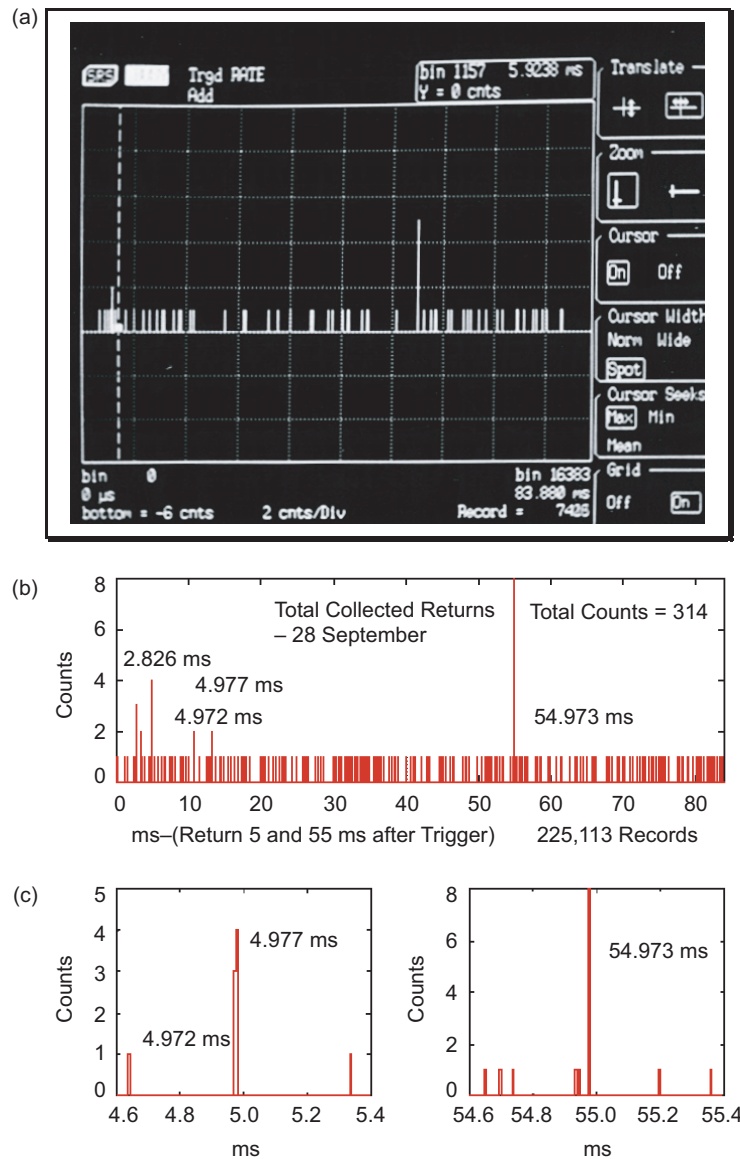
(a)

(b)

(c)

Fig. 6-25. (a) photo of scalar average output from September 28 transmission showing "hits" approximately 5 and 55 ms after trigger, (b) typical laser returns window covers 82 ms with 16,000 bins 5.12-μs wide, and (c) expanded views showing two areas of interest.
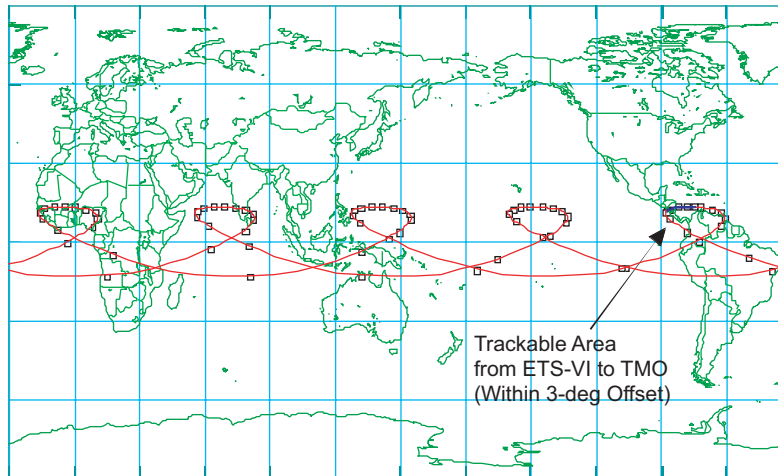

Fig. 6-26. Ground track of ETS-VI satellite showing trackable area from TMF.

The experiment was highly successful and accomplished of the following firsts:

- Bi-directional optical link between a ground station and a spacecraft at geostationary ranges.
- Demonstration of mitigation of atmospheric scintillation by using a multi-beam uplink.
- Demonstration of regeneration of an optical uplink signal to a spacecraft.
- Demonstration of the return of real data on an optical space-to-ground link.

Designed for a GEO-to-ground link, the LCE terminal was body-fixed to the ETS-VI satellite with limited coarse tracking of the LCE's gimbaled flat mirror. A combination of satellite attitude control and LCE gimbal mirror pointing was required to point the LCE to the ground. An involved and time-consuming process, communications opportunities were limited to apogee passes above the ground stations. Figure 6-27 shows the control region of the satellite attitude control system (ACS) and the LCE gimbal and the elevation and azimuth orientation of TMF in the spacecraft coordinate system. Markers are separated by 1 hour, and the trace shows approximately a 5-hour experiment window. Because the LCE was designed for geostationary operation over Japan, in a geo-transfer orbit, and at the higher latitude TMF ground station, the LCE could not center TMF in its region of control even with the assistance of the satellite ACS.

The ETS-VI satellite had limited onboard memory, and the LCE and satellite ACS control had to be updated in real time to keep TMF in the LCE's FOV. This was done by commands originating at the Communications

Research Laboratory (CRL) in Tokyo, Japan. The satellite ephemeris for pointing the telescopes to the ETS-VI were prepared from NASDA-generated orbit solutions that were sent to JPL twice weekly [59]. Figure 6-28 shows this command and data flow chain during the experiment. The procedure in chronological order was:
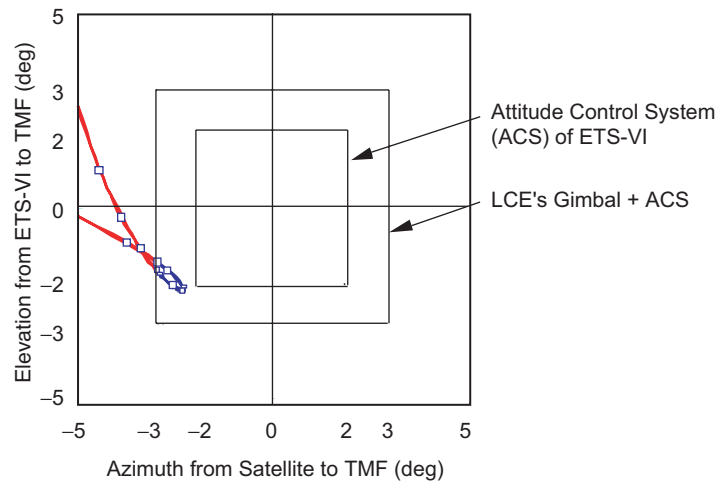

Fig. 6-27. Plot of control region of combined ACS and LCE gimbal for November 26, 1995, pass over TMF, after the first orbit maneuver.
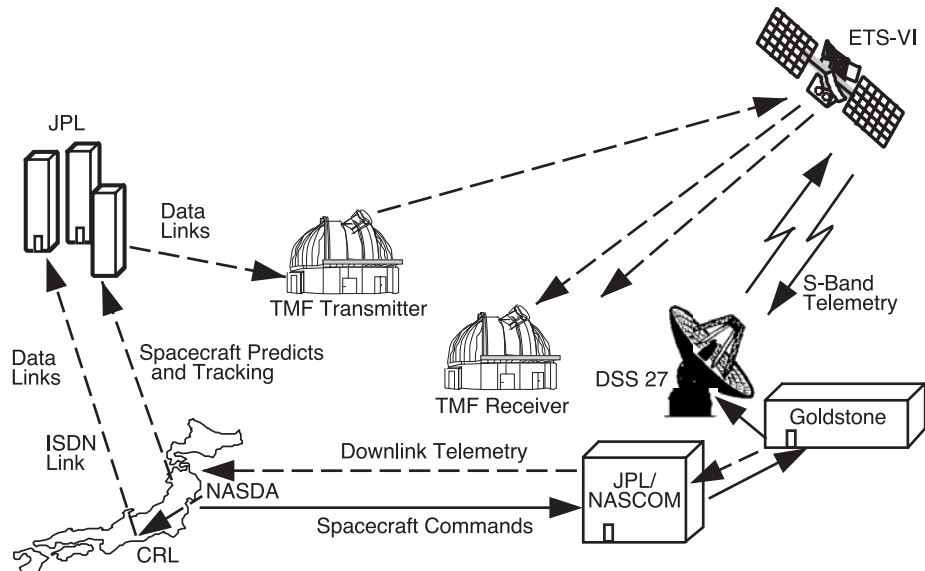

Fig. 6-28. Operations approach for GOLD: TT&C are sent from NASDA to ETS-VI via JPL/NASCOM; DSS 27 at Goldstone commands ETS-VI.

1) CRL generated LCE and spacecraft attitude pointing commands and transmitted them to NASDA.

2) NASDA relayed the commands to the JPL NASCOM and on to Goldstone, California.

3) Deep Space Station 27 (DSS 27) uplinked the commands to the ETS-VI on an S-Band link.

4) DSS 27 received the satellite telemetry and data and routed it to NASDA.

5) NASDA transferred the attitude control system (ACS) and the LCE coarse pointing and other related GOLD data to the CRL.

6) CRL immediately processed ACS and LCE data to confirm that the commands were positioning the LCE to point to TMF. This process was iterated incrementally until the combination of satellite attitude and LCE pointing placed TMF in the LCE FOV [60].

7) CRL transmitted the CCD data to TMF on a TMF-to-CRL Integrated Services Data Network (ISDN) link to allow TMF operators at TMF to validate the acquisition of the uplink laser beam.

The acquisition of the uplink was further confirmed by the direct optical downlink from the satellite.

GOLD Transmission Record. The GOLD transmission record is shown in Fig. 6-29 and Fig. 6-30. There were 22 opportunities to transmit to the satellite in each of the two GOLD demonstration phases. Phase-1 transmissions extended from October 30 to January 13 when the satellite went into eclipse and NASDA precluded all but critical satellite support to conserve battery power. In Phase 1, there were 12 two-way transmissions, 1 one-way transmission, 5 cancellations due to bad weather, 2 cancellations due to hardware failures, and 2 non-detections. Phase-2 transmissions began on March 21, 1996, shortly after the satellite had emerged from the apogee eclipse and continued to May 26, 1996. During this phase, there were 12 successful two-way
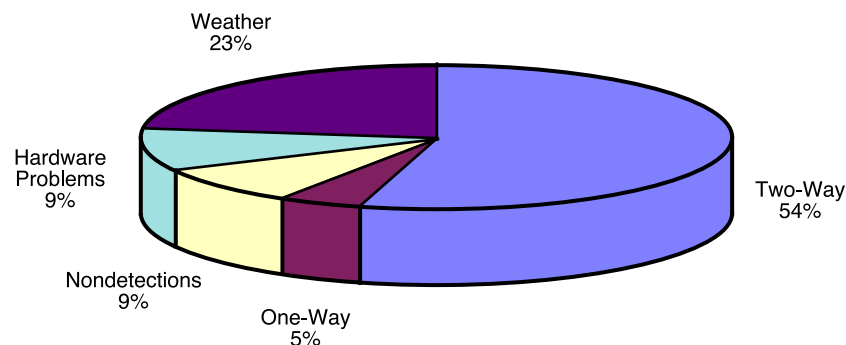

Fig. 6-29. Pie chart of the GOLD Phase-1 transmission record from October 30, 1995, to January 13, 1996.
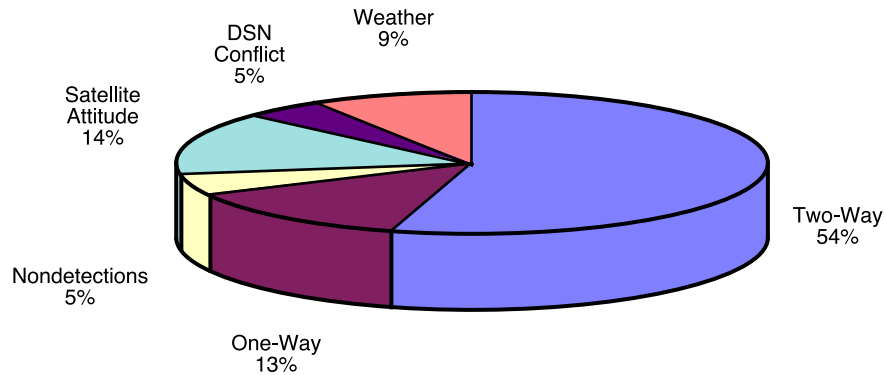
Fig. 6-30. Pie chart of the GOLD Phase-2 transmission record from March 21, 1996, to May 26, 1996.

transmissions, 3 one-way transmissions, 1 non-detection, 2 cancellations due to bad weather, and 3 cancellations due to satellite attitude-control problems.

GOLD Uplink. The TMF transmitter and receiver for GOLD were designed and developed over the 4-month period from July to November 1995. Figure 6-31 (a) is a schematic of the transmitter optical train. The transmitter telescope was the 0.6-m that had previously been used for Surveyor-7 and GOPEX demonstrations. The Ar-ion laser seen in Fig. 6-31 (b) was operated on the 514.5-nm line with 13-W continuous wave (CW) output, and was coupled to the telescope through its coudé path. The laser beam was modulated at 50-percent duty cycle to provide the required discriminant for the LCE tracking loop. The modulator consisted of four potassium dideuterium phosphate (KD*P) crystals and a polarizer. A 6000-bit error rate tester (BERT)—was used to generate a basic data pattern of 0 to 1 V square wave modulation that was amplified to the modulator's half-wave voltage in the driver, with zero volts corresponding to maximum transmission through the modulator. After modulation, the beam was incident on a concave/convex lens pair that set the beam divergence from the telescope; nominally set at 20 μrad.

A multi-beam uplink approach was used to mitigate the effects of atmospheric turbulence [61]. Here, the laser output was divided into two or four beams, and the beams kept spatially and temporally incoherent. Spatial incoherence was accomplished by separating the beams at the telescope aperture by a distance greater than the coherence cell of the atmosphere. Temporal incoherence was achieved by delaying the path length difference between the beams so that it exceeded the coherence length of the laser.

For the two-beam transmission, the beam splitter separated the beam into two equal parts; one that went through a 25-cm optical delay line with a path length difference greater than the laser's coherence length ($\lambda^2 / \lambda\Delta \sim 10\,\text{cm}$).
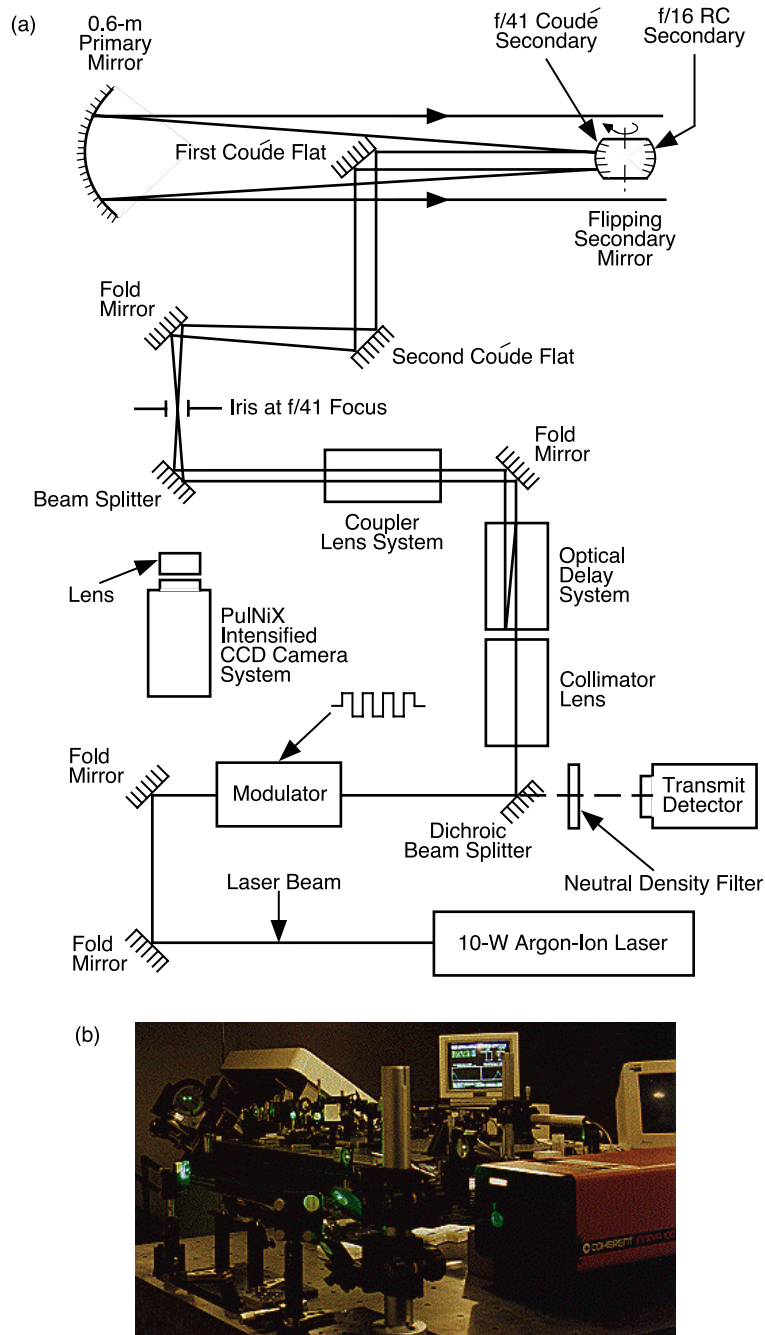
(a)

(b)

Fig. 6-31. GOLD: (a) schematic of the uplink optical train and (b) photograph of the transmitter optical train, showing the argon-ion laser Conoptics modulator and, to the far left, the M5 coudé mirror.

Both beams were reflected from a high power dichroic beam splitter and were brought to a focus at the iris located at the f/41 focus of the telescope. From there, the beams diverged and were reflected by the third coudé flat and into the telescope. The beams were made incident on opposite sides of the 0.6-m telescope's primary mirror; a distance greater than the size of an atmospheric coherence cell. See Figs. 6-32(a) two-beam and 6-32(b) four-beam transmissions. The use of spatial and temporal incoherent beams resulted in a more uniform and constant intensity profile at the satellite.

Figures 6-33, 6-34, and 6-35 show the signal strength detected by the LCE for the one-, two-, and four-beam uplink transmissions along with histograms showing the frequency of detection of a given signal strength [61]. These data clearly show the advantage of multi-beam uplink beacon. For the single-beam uplink, the median signal strength detected was 1.38 V, and the mean was 1.35 V. The data show surges of 5.7 dB and fades –12.3 dB from the mean. The histogram shows a distribution with the most frequent signal detected at 0.08 V, almost zero. The two–beam uplink showed a significant improvement in surge reduction but marginal improvement in reducing fade depth. The data did show a significant reduction in fade frequency, however. The median received signal strength for the two-beam uplink was 2.4 V. The mean was 2.19 V. Signal surges were 1.9 dB above the mean, and signal fades were –10.4 dB from the mean. For the four-beam uplink, the median signal strength was 3.08 V, and the mean was 2.93 V. Signal surges were 1 dB above the mean, and fades were –4.2 dB below the mean; a significant reduction in fade depth and fade frequency over two-beam propagation.

GOLD Downlink. The LCE aluminum gallium arsenide (AlGaAs) laser on board the ETS-VI transmitted 14-mW, average power at 830-nm current modulated. The 1.024-Mbps downlink signal was Manchester coded and
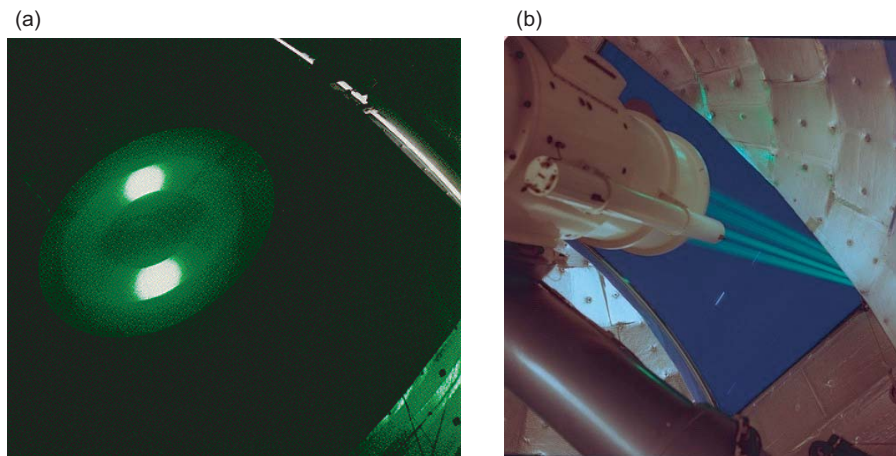
(a) (b)

Fig. 6-32. GOLD uplink: (a) two-beam laser output projected onto a scoring board in the dome of the 0.6-m telescope and (b) four beams transmitted through the dome.
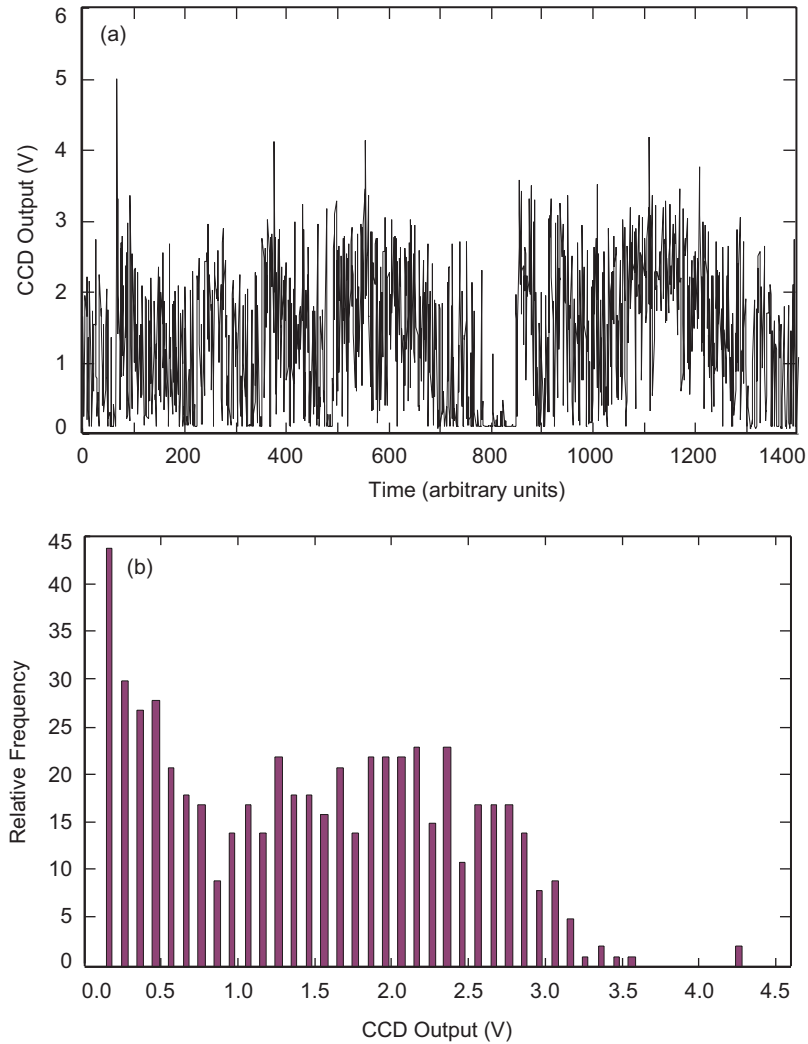
Fig. 6-33. (a) uplink signal strength detected by LCE CCD camera with single beam transmitted to ETS-VI spacecraft and (b) histogram of signal strength detected for single-beam uplink.

transmitted through a 7.5-cm aperture telescope. A schematic of the receiver optical train is shown in Fig. 6-36 (a). The receiving telescope was a 1.2-m bent Cassegrain located approximately 60 m from the 0.6-m transmitter [62]. The downlink signal reflected from the telescope was reflected onto the optical bench attached to a flange at the telescope Cassegrain focus. See Fig. 6-36 (b). The satellite downlink was reflected from a dielectric mirror and through a notch filter to separate the signal from the solar illuminated satellite image. The signal was then made incident on the APD detector. Light from the Sun-

illuminated satellite was evenly split between the tracking and seeing cameras. A red-filter was introduced into the optical path to suppress the sky background during daytime experiments.
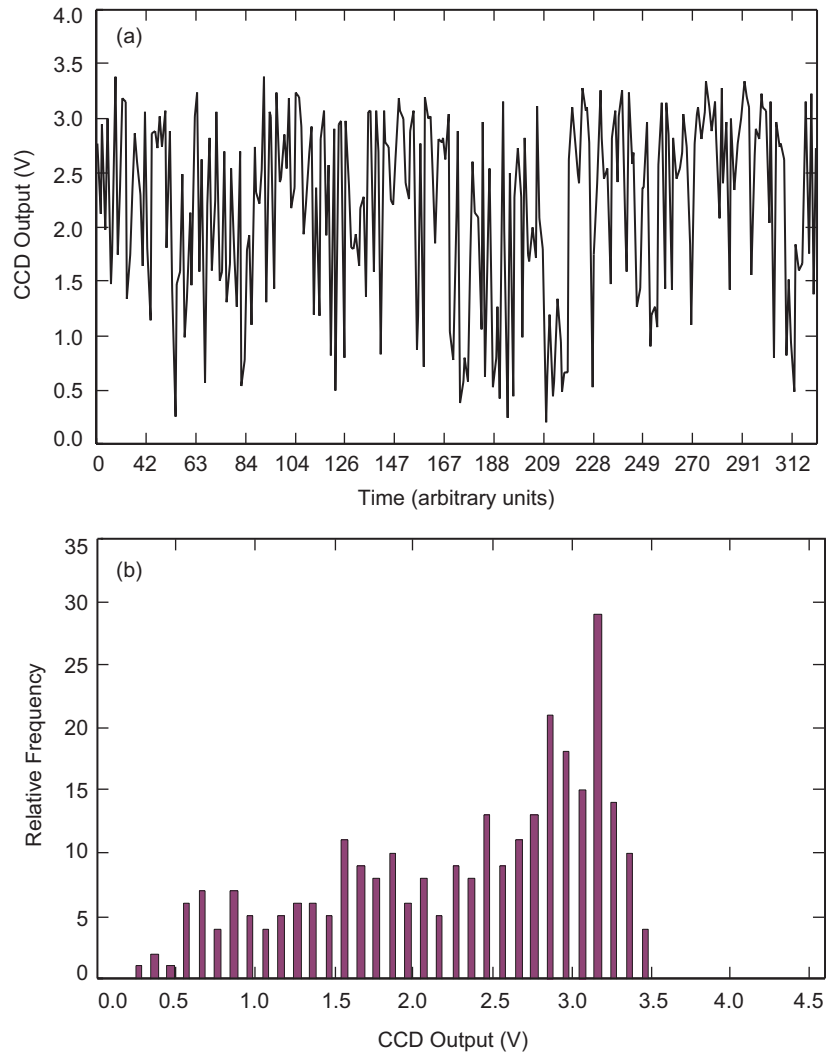

Fig. 6-34. (a) signal strength detected by CCD for two-beam uplink and (b) histogram of detected signal for two-beam uplink.
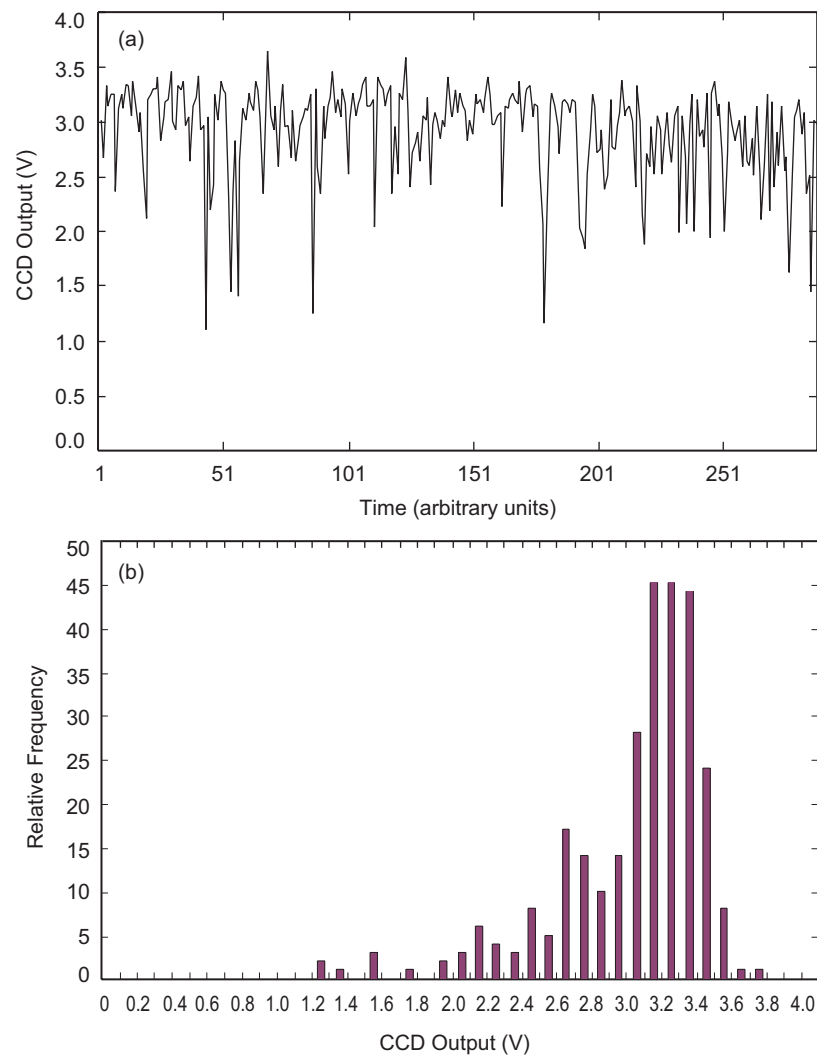
Fig. 6-35. (a) signal strength detected by CCD for four-beam uplink and (b) histogram of detected signal for four-beam uplink.

(a)

Cassegrain
Secondary

Neutral
Density
Filter

Bandpass
Beam Splitter
(514 nm)

Lowpass
Beam Splitter
(750-nm Cutoff)

Video
Camera

50%

10%

400 nm < λ < 750 nm

50%

90%

Tertiary

Seeing
Camera

λ > 750 nm

APD

1.2-m
Primary

GOLD Optics Module ◄——► 1.2-m Telescope

(b)

Fig. 6-36. Receiver optical train: (a) schematic of the 1.2-m receiver telescope at TMF, showing tracking, seeing, and receiver detectors, and (b) photograph of the optical train, with detectors and cameras, that was attached to the Cassegrain focus flange of the 1.2-m telescope.

Figure 6-37 shows a block diagram of the GOLD receiver. The signal detected by the APD was amplified, and the output simultaneously sent to a Tektronix 802-A digital oscill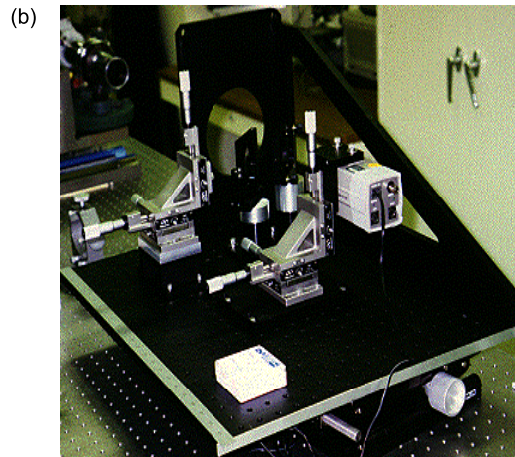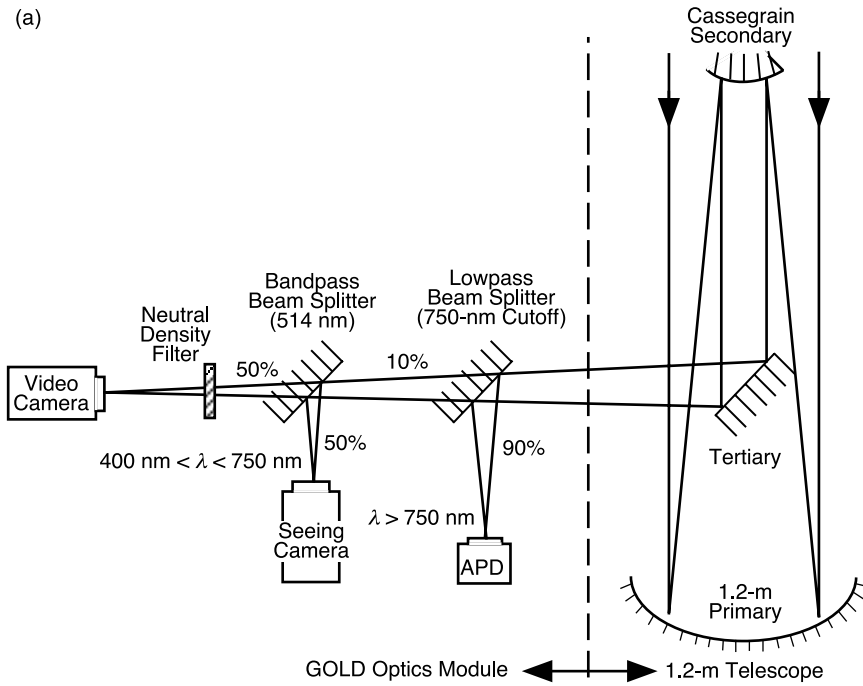oscope (that recorded the downlink signal waveform) and to a bit-error rate tester for the PN code downlink. The BERT's 1-Hz output was recorded on a PC. A bit synchronizer and a PCM recorder were used to recover the downlink telemetry [63].

The three data types received at the ground are shown in Figs. 6-38, 6-39, and 6-40. Figure 6-38 is a representative sample of the PN-coded 1.024-Mbps data stream that was used to measure the performance of the optical link. The 128-kbps spacecraft instrument data stream repeated eight times to fill the 1.024-Mbps downlink channel, as shown in Fig. 6-39. Figure 6-40 shows the 1-MHz square wave data stream that was regenerated on the spacecraft and retransmitted to the ground. The dropouts in the regenerated signal are most likely caused by atmosphere-induced signal fades on the uplink. In addition to the square-wave pattern, a 1.024-Mbps Manchester-coded 511-bit-long PN sequence was transmitted on a two-beam uplink to the satellite. The recorded atmospheric seeing during the experiment was 2 arc-sec, and the measured BER ranged from 3×10^{-4} to 2.5×10^{-3} over the forty-minute measurement interval.

6.1.1.12 Conclusion. JPL has performed a series of free space-optical communications demonstrations and has developed strategies both for safe ground-to-space laser beam propagation and for mitigating the effects of atmospheric scintillation.

To meet the needs of continuous coverage of the deep-space optical communications mission, we have studied a variety of single-aperture ground receiver options to support the link. Recognizing the need for site diversity to mitigate the effects of cloud cover, we have explored approaches to reduce the cost of large 10-m class single apertures that range from the RF Leighton dishes to lightweight glasses. While some of these approaches show promise, the challenge is to reduce scattering and to achieve the requisite performance during the daytime at small Sun angles. Our preliminary adaptive-optics
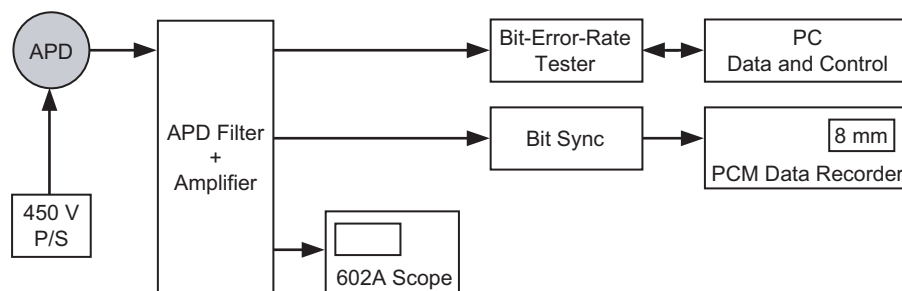
Fig. 6-37. GOLD receiver block diagram.
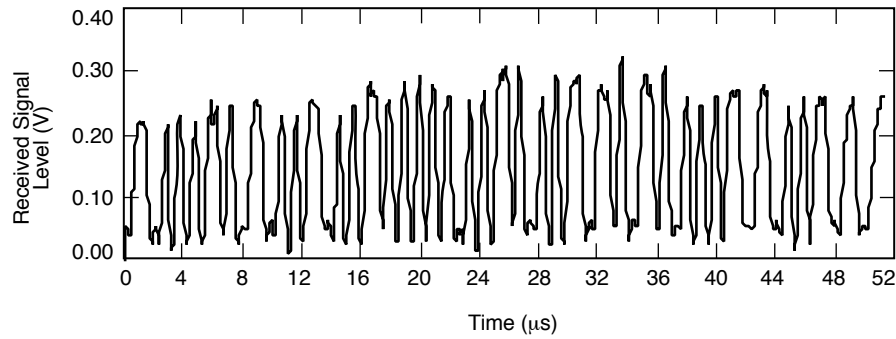
Fig. 6-38. Sample of 1.024-Mbps Manchester-coded PN sequence downlink telemetry from the LCE showing random bit flips.
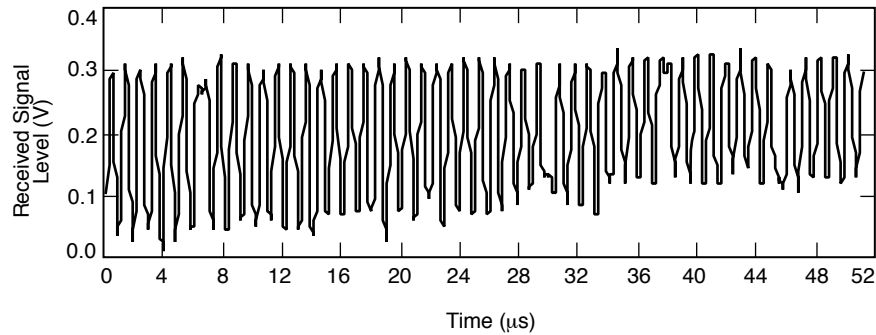
Fig. 6-39. Downlinked satellite telemetry at 128 kbps. The data show bit flips in multiples of eight consistent with 8X repetition of the bit pattern.
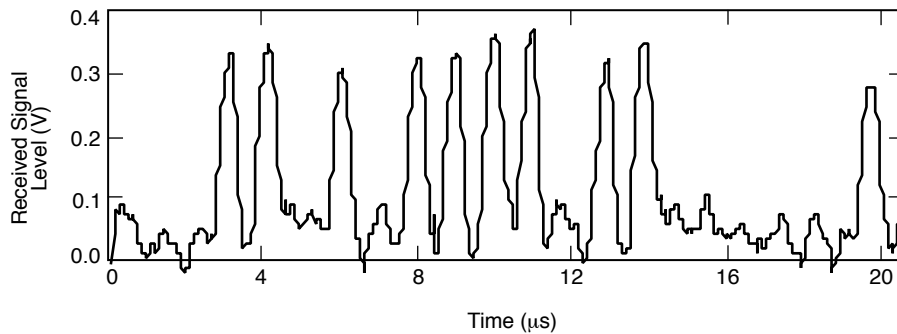
Fig. 6-40. Section of a 1-MHz square-wave regenerated from a 1-MHz uplink to the satellite.

analysis suggests that an actuator density of 900 actuators per square meter can enable FOV reduction at the deep-space receiver and background suppression, both of which can increase the capability to allow pointing at small Sun angles.

On the uplink, JPL has demonstrated the benefit of multi-beam propagation in the 1995–1996 GOLD demonstration. Yet, although this approach mitigates

uplink scintillation and supports blind pointing to the deep-space probe, its atmosphere-limited beam divergence restricts the range of application to spacecraft at Mars for reasonable uplink laser powers. In the CEMERLL demonstration, JPL and the AFRL showed that using adaptive-optics techniques on the uplink will require tip/tilt in addition to higher-order wave front correction. Yet, because the point-ahead angles for deep-space missions exceed the isoplanatic angle, using the downlink for uplink tip/tilt correction is not feasible. Polychromatic laser guide star techniques offer the possibility of tip/.tilt correction across the sky without the need for a natural guide star. This technology is currently under development.

6.1.2 Optical-Array Receivers for Deep-Space Communication
Victor A. Vilnrotter, Chi-Wung Lau, and Meera Srinivasan

6.1.2.1 Introduction. Earth-based reception of deep-space optical signals using an array of relatively small telescopes together with high-speed digital signal processing is a viable alternative to large-aperture telescopes for receiving deep-space optical signals. Large-aperture telescopes are costly to build and operate, and inherently suffer from single-point failure in case of malfunction, thus jeopardizing precious data. Performance of a properly designed array tends to degrade gracefully in case of element failures, even without replacement, but the array approach also provides the option to switch in spare telescopes in case of failure, without a significant increase in cost.

In addition to a favorable cost and risk trade-off, the optical-array receiver approach has advantages in terms of implementation complexity and performance for several key communications functions that need to be clarified and evaluated. These characteristics can best be explained in terms of an array-receiver model that emphasizes the communications aspects of the optical array. We begin by developing the underlying concepts governing the behavior of optical arrays. Next, similarities and differences between single-aperture and array telescopes designed for reception of deep-space telemetry are explored, followed by a detailed investigation of communications performance. We conclude with a comparison of array receivers with the more conventional large-aperture optical receiver under realistic operating conditions.

6.1.2.2 The Optical-Array Receiver Concept. The essential difference between a single-aperture optical communications receiver and an optical-array receiver is that a single aperture focuses all of the light energy it collects onto the surface of an optical detector before detection, whereas an array receiver focuses portions of the total collected energy onto separate detectors, optically detects each fractional energy component, and then combines the electrical signal from the array of detector outputs to form the observable, or "decision statistic" used to decode the telemetry signal. A single-aperture receiver need

not be constructed from a single monolithic glass lens or reflector element; large modern telescopes generally are constructed from hexagonal segments with each surface placed near its neighbors and monitored to form a single parabolic surface. If the image of a point source is formed using every segment of the surface and then detected, that collection of segments would be considered a single-aperture receiver. However, if the focal spot of each segment were separated from the rest and detected with a separate detector element or focal-plane detector array, that would constitute an array receiver in the framework of our definition. Note that a focal-plane array in a single telescope might be construed as an optical-array receiver under this definition, but the intent is for there to be multiple apertures. This construction serves as a convenient conceptual vehicle to illustrate the similarities and differences between single-aperture and multi-aperture array receivers.

A conceptual block diagram of an optical array receiver suitable for deep-space telemetry reception is shown in Fig. 6-41, intended to identify the key components required for array receiver operation. The most conspicuous feature of an optical array receiver is a large number of small- to medium-sized telescopes, with the individual apertures and number of telescopes designed to make up the desired total collecting area. This array of telescopes is envisioned to be fully computer controlled via the user interface and predict-driven to achieve rough pointing and tracking of the desired spacecraft. Fine-pointing and tracking functions then take over to keep each telescope pointed towards the source despite imperfect pointing predicts, telescope drive errors, and vibration caused by light wind.

The optical signal collected by each telescope is focused onto a detector array located in the focal plane, designated as the focal-plane array (FPA). Despite atmospheric turbulence degrading, the coherence of the received signal fields and interfering background radiation entering the receiver along with the signal within the passband of the optical pre-detection filter, the FPA and associated digital signal-processing electronics extract real-time pointing information, keeping the centroid of the turbulent time-varying signal centered over the FPA. This is accomplished in two steps: first, large accumulated pointing errors are fed back to the telescope drive assembly, repointing the entire instrument; and second, small excursions of the signal distribution from the center of the array are corrected via a fast-response tip-tilt mirror that responds to real-time pointing updates generated by the FPA electronics. In addition, the short-term average signal energy over each detector element is measured and used to implement various adaptive background-suppression algorithms to improve or optimize the communications performance of the entire array.

The electrical signals generated at each telescope by the FPA signal-processing assembly are collected at a central array signal-processing station, where the final operations necessary for data decoding are performed. The

FPA Signal Processing:

Real-Time Tracking Updates
Drive Correction
Tip-Tilt Mirror Assembly
Adaptive Subarrays

Telescope Array

User Interface:
Predicts
DSP Control

Array Signal Processing

Real-Time Delay Compensation

Array Combining, Sync, Tracking

Symbol Detection, Decoding

Decoded Data

Feedback
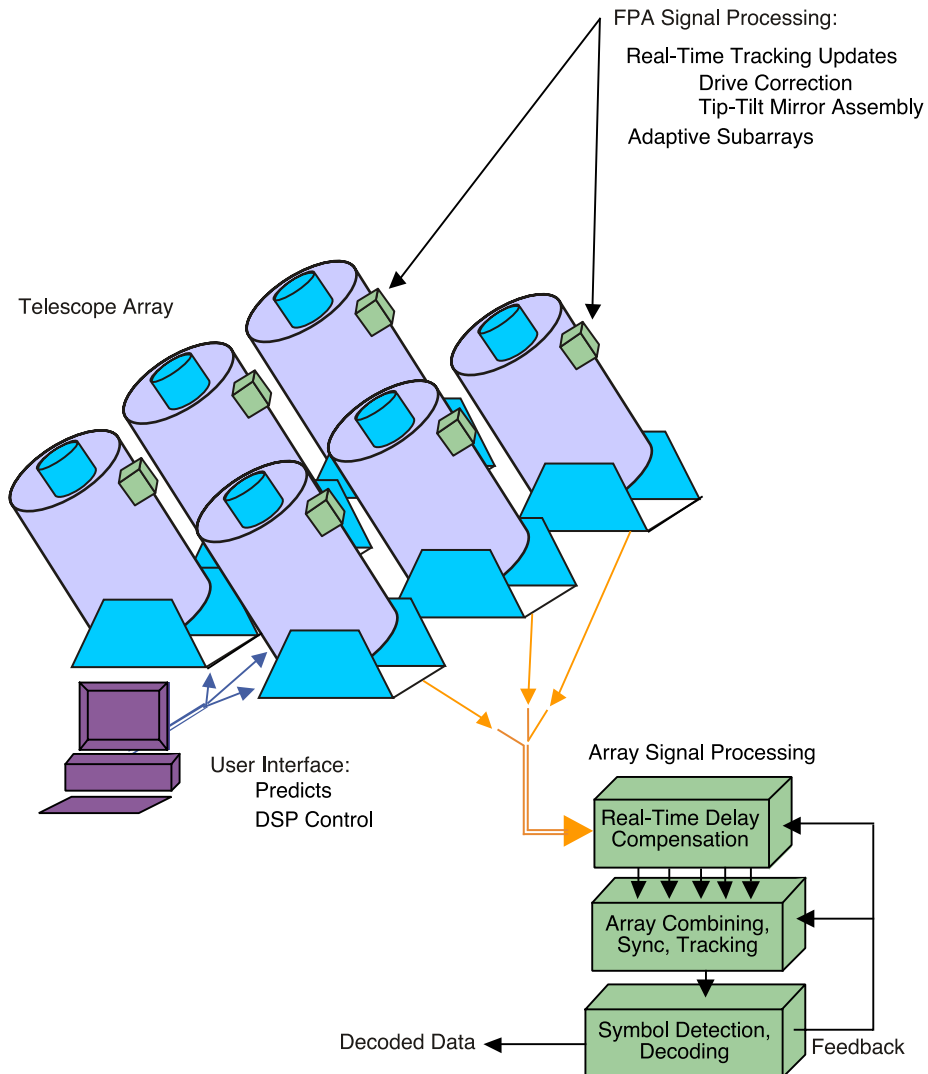
Fig. 6-41. Conceptual design of an optical array receiver, illustrating key functions required for array reception: the telescope array; focal-plane pre-processing of the signal at each telescope; and the additional array processing needed to combine the pre-processed signals and decode the received data.

relative time delay between signals from various telescopes is measured and removed, effectively aligning each signal stream in time before further processing is carried out. The delay-compensated signals then are combined in a manner to optimize array performance, and further processed to affect symbol synchronization, frame synchronization, Doppler compensation, and maintain lock between the combined signal and the receiver time frame. At this point,

the transmitted channel symbols are detected, and the decoding operation begins. The detected channel symbols now could be handed over to a hard-decision decoder, or various forms of soft-decision decoding could be implemented through the use of additional side information along with the detected symbols. The channel symbols detected by the array receiver also may be used to aid the delay compensation, array combining, and synchronization operations.

6.1.2.3 Aperture-Plane Expansions. It is common practice in the optical communications literature to expand random fields at the telescope aperture into spatial modes that are closely related to diffraction-limited fields of view, clustered to form a complete orthonormal set of functions that essentially samples the field of view (FOV) of the receiver. This concept is illustrated in Fig. 6-42, where a cluster of diffraction-limited FOVs (denoted Ω_{dl}) is shown collecting light energy from both signal and background radiation with slightly different angles of arrival. If it can be shown that each element of the set of spatial modes satisfies an integral equation whose kernel is the field coherence function over the aperture, then each sample function of the field can be expanded into an orthonormal series with uncorrelated coefficients, also known as a Karhounen-Loeve expansion [64].

When applying this model to the array receiver, it is more appropriate to view the received turbulence-degraded optical fields as "frozen" over time scales of milliseconds, the characteristic time scale of turbulence, during which time a great many optical data symbols are received. It is advantageous to view
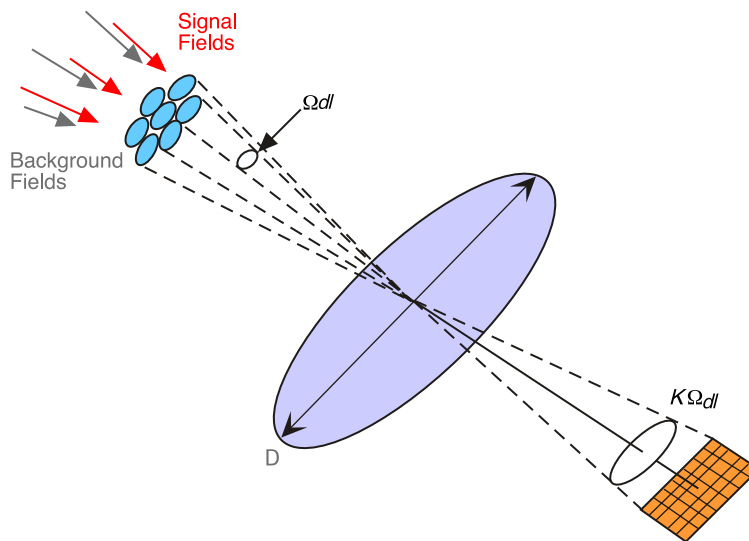

Fig. 6-42. Plane-wave expansion of aperture-plane fields: diffraction-limited FOV interpretation.

each sample function of the received field as a frozen realization of a two-dimensional field, representing a certain epoch in time over which the stationary model applies, as a deterministic two-dimensional function defined over the aperture plane of the receiver. This enables the application of well-known sampling theory to the fields, resulting in a model that clarifies the array receiver concept and contributes to the development of a useful engineering model.

Plane-wave expansions are especially useful for characterizing the effects of background radiation. In Fig. 6-42, both signal and background power are shown entering the receiver through each diffraction-limited FOV. If the diameter of the receiver is smaller than the coherence length of the signal field (a condition that can be met in the vacuum of space or even on the ground with very small apertures), then all of the signal energy is concentrated into a diffraction-limited point-spread function (PSF) in the focal plane. In effect, the signal appears to originate from a point source an infinite distance from the receiver. For the case of receiving spatially coherent signal fields, the signal power collected by a diffraction-limited telescope under ideal conditions is therefore proportional to the collecting area. The model for background radiation is somewhat more complicated, since background radiation is an extended source with respect to the narrow FOV of typical optical receivers. Surprisingly, the background power collected by a diffraction-limited telescope does not depend on the collecting area, but instead is a constant that depends only on the brightness of the source and the bandwidth of the optical filter at the wavelength of interest, λ. This can be shown by examining the units of the spectral radiance function, $N(\lambda)$, used to quantify background radiation: the units of the spectral radiance functions are power (microwatts) per receiver area (square meters), FOV (steradians), and optical filter bandwidth (angstroms or nanometers). The background power collected by a diffraction-limited receiver is given by [65]

$$P_b = N(\lambda)\Delta\lambda\Omega_{dl}A_r$$

where $\Delta\lambda$ is the optical filter bandwidth and A_r is the collecting area. Since the diffraction-limited FOV is inversely related to area, i.e., $\Omega_{dl} \approx \lambda^2/A_r$, we have

$$P_b^* = \frac{\pi^2}{16}N(\lambda)\Delta\lambda\lambda^2$$

and therefore, the background power collected by a diffraction-limited receiver, P_b^*, is independent of receiver area. Hence, all diffraction-limited receivers of

whatever size collect the same background power when observing a given background distribution, independent of receiver collecting area.

The distorted optical fields resulting from atmospheric turbulence are necessarily band limited, since the "image" of a point source observed through turbulence is of finite extent. This conclusion is based on the observation that any complex field distribution over the aperture plane is the Fourier transform of the complex "image" function generated in the focal plane [66,67], which therefore represents the wavenumber space of the aperture. In order to determine the extent of significant wavenumbers of representative optical field distributions, sample functions generated from Kolmogorov phase screens were analyzed. For the case of 10-cm atmospheric coherence length, or $r_0 = 0.1\,\text{m}$, Fig. 6-43 shows representative examples of the resulting aperture-plane coherence function, and Fig. 6-44 shows its Fourier transform, representing the two-dimensional power spectrum of the field in wavenumber space.

If we can show that the received fields over the aperture are wavenumber-limited two-dimensional functions, then we can invoke a two-dimensional version of the sampling theorem, as described in [67]. This enables the expansion of the received fields using two-dimensional sampling functions, analogous to the time-domain expansion of band-limited time sequences. The canonical sampling functions described in [67] for two-dimensional functions are closely related to the "sinc" function familiar from one-dimensional sampling theory, but functionally depend on the first-order Bessel function
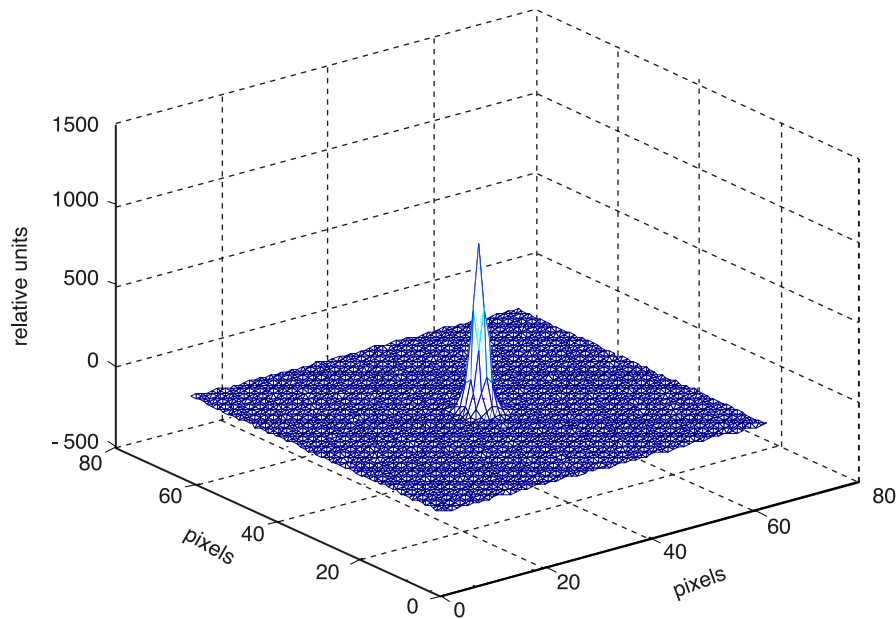

Fig. 6-43. Two-dimensional sample autocorrelation function over the aperture plane: r_0 = 10 cm.
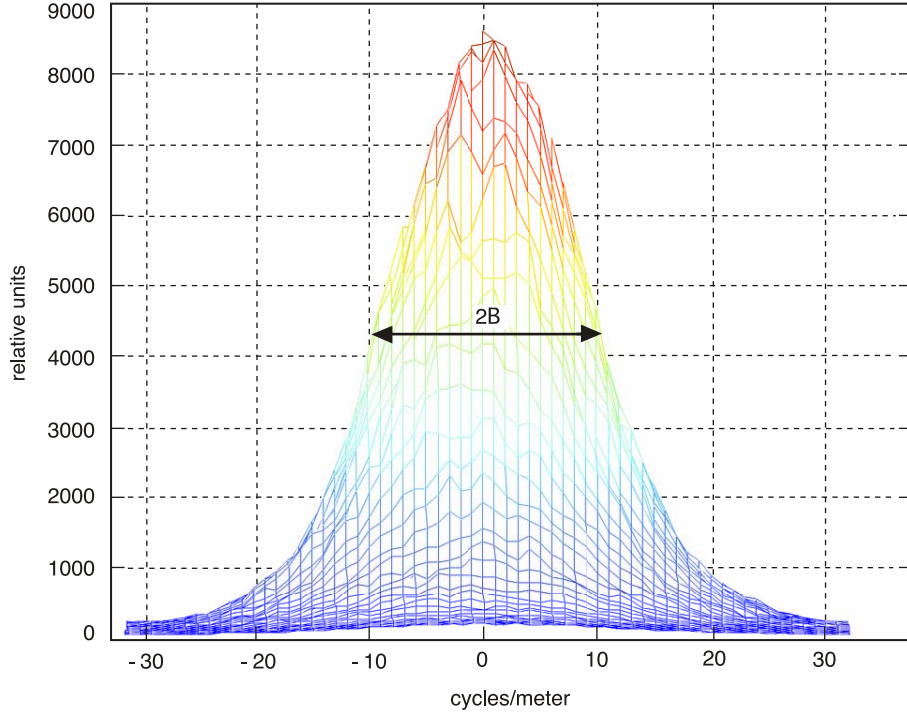
Fig. 6-44. Power spectrum of the sample field in wave-number space: r_0 = 10 cm.

$J_1(r)$, where $r = \sqrt{x^2 + y^2}$ is the radial variable along any direction in the aperture plane. If the two-dimensional optical field is limited in wavenumber space to $B = \omega/2\pi$ radians, where ω represents the angle of arrival measured from the normal to the aperture plane, then the appropriate sampling functions are of the form

$$\varphi(x,y) = C \frac{J_1\left(2\pi B\sqrt{x^2 + y^2}\right)}{2\pi B\sqrt{x^2 + y^2}} \tag{6.1-10}$$

where the normalization C is chosen to ensure that $\iint dxdy\, \varphi^2(x,y) = 1$.

We observe from Fig. 6-44 that the effective two-sided bandwidth, $2B$, of the field is about 20 cycles per meter in wavenumber space at the 3-dB point, implying that the bandwidth is approximately given by $B = 10$ cycles per meter; this implies a sample-function spacing of 0.1 m, or 10 cm, consistent with the assumed coherence length of the field.

The two-dimensional expansion functions defined in Eq. (6.1-10) can be placed on a regular grid of points corresponding to the first zero-crossing

distance of the Bessel function, forming cells of equilateral triangles as shown in Fig. 6-45. The first three functions so placed are orthogonal, but subsequent functions at various distances from a given grid point are not exactly orthogonal; however, no two functions have greater than a few percent overlap, as shown in [68]. In principle, the set of sampling functions needed to represent any realization of a wavenumber-limited optical field over the aperture can be orthogonalized using the Gram-Schmidt procedure [67], resulting in a complete orthonormal set. This complete set of sampling functions then serves as the basis for expanding arbitrary received optical fields over the aperture, with the interpretation that the coefficients are complex samples of the field at the appropriate points in the sampling lattice.

The sampling expansion illustrated in Fig. 6-45 enables the representation of the instantaneous, or frozen, received optical field, $f(x, y)$, in terms of complex samples $\alpha_{i,j}$ over a grid of points defined by the vertices of equilateral triangles, whose separation is determined by the turbulence-induced atmospheric coherence length over the aperture plane:

$$f(x,y) = \sum_{(ij) \in A_{rec}} \alpha_{ij} \varphi_{ij}(x,y) = \sum_{(ij) \in A_1} \alpha_{ij} \varphi_{ij}(x,y) + \cdots + \sum_{(ij) \in A_K} \alpha_{ij} \varphi_{ij}(x,y) \quad (6.1\text{-}11)$$
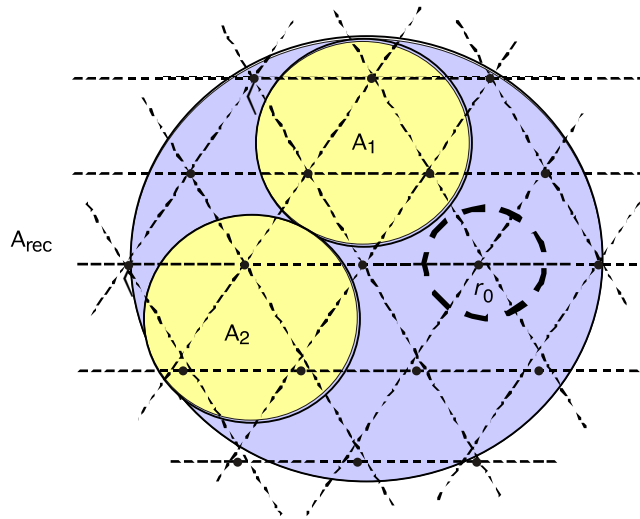

Fig. 6-45. Sampling grid over the receiver aperture defining placement of sampling functions and illustrating the interpretation of the field as samples over the entire aperture and over two subapertures.

Here,

$$\alpha_{ij} = \iint_{A_{rec}} f(x,y)\,\varphi_{ij}(x,y)\,dxdy \tag{6.1-12}$$

and the sampling functions are given by

$$\varphi_{ij}(x,y) = C \frac{J_1\left(2\pi B\sqrt{(x-x_i)^2 + (y-y_j)^2}\right)}{2\pi B\sqrt{(x-x_i)^2 + (y-y_j)^2}}$$

where x_i and y_j are the sampling point coordinates. These sampling functions are approximately orthonormal, i.e.,

$$\iint_{A_{rec}} \varphi_{ij}(x,y)\,dxdy \approx 1$$

and

$$\iint_{A_{rec}} \varphi_{ij}(x,y)\varphi_{kl}(x,y)\,dxdy \approx 0, \quad i \neq k, j \neq l$$

As shown in Fig. 6-45, the coefficients α_{ij} represent samples of the field over the (i, j)-th grid point. Due to the circular symmetry and unimodal nature of the two-dimensional sampling functions defined in Eq. (6.1-10), these samples may be interpreted as effective coherent areas of radius r_0 centered over each grid point shown by the dashed circle in Fig. 6-45. Note that we have not taken into account boundary conditions at the edge of the aperture; nor have we formally applied the Gram-Schmidt procedure to fully orthogonalize the basis functions. Therefore, this representation is somewhat approximate, but it is sufficiently accurate to motivate the development of optical array receiver theory starting with a single large aperture.

If we take the magnitude squared of the complex received field and integrate it spatially over the entire aperture, we obtain the power of the signal field through the aperture. Applying this operation to both sides of Eq. (6.1-11) yields

$$\iint_{A_{rec}} dx\,dy\,|f(x,y)|^2 = \iint_{A_{rec}} dx\,dy\left|\sum_{(i,j)\in A_{rec}} \alpha_{ij}\,\varphi_{ij}(x,y)\right|^2 \tag{6.1-13}$$

$$\cong \sum_{(i,j)\in A_{rec}} |\alpha_{ij}|^2$$

where the last expression follows from the approximate orthonormality of the sampling functions. Since the left side of Eq. (6.1-13) represents the total power of the signal, so does the right-hand side, with the interpretation that the signal power over the receiver aperture can be built up from the sum of the individual sample powers. Equivalently, the total power through the aperture can be viewed as the sum of powers collected by small effective apertures centered over each grid point. Note that if the field coherence length is equal to or greater than the diameter of the receiver aperture, then a single sampling function suffices to represent the field: in this case, there is only one coefficient in the expansion, and the total signal power through the aperture equals the squared magnitude of the sample representing the entire received optical field.

Summarizing the key features of the array model, we conclude the following:

1) The amount of background power collected by any diffraction-limited receiver aperture is a constant independent of the aperture dimensions, because the diffraction-limited FOV (steradians) is inversely related to the receiver area.

2) The amount of coherent signal power collected by a diffraction-limited receiver is directly proportional to the collecting area. For the case of free-space (not turbulent) reception, the signal is in the form of a plane wave that represents a uniform power density in units of power per unit area. For the turbulent case, the plane wave is broken up into small coherence areas over the collecting aperture, but the total average signal power collected by the receiver remains the same.

Based on the above model, the following general conclusion follows:

3) A necessary condition to ensure that total signal and noise powers collected by an array of subapertures of the same total area as a single large receiver is that each subaperture contain at least one sampling coefficient.

This conclusion follows from the interpretation of the sample coefficients as small coherence areas surrounding the center of each sampling function, with effectively constant (complex) value throughout. This model effectively replaces the continuous-field model with a discrete representation, where now the total power through the aperture is the sum of the squares of the coefficients. In effect, we have replaced integration over a continuous area with a sum of discrete terms, where each coefficient represents power flowing through a small area over the aperture; these equivalent areas are disjoint and cover the entire aperture. Subapertures containing more than one sample of the field can be constructed in a similar manner, as shown in Fig. 6-45, conserving energy since the total power flowing through a given subaperture can be estimated by counting the number of discrete signal-field samples it contains.

Whereas the signal energy per sample collected by a coherence area can be estimated directly from the coefficients, the background power cannot, since it is not coherent over the same area as the turbulence-degraded signal field; the background energy is more easily estimated from the conventional plane-wave decomposition illustrated in Fig. 6-42. However, since the total background power collected by any diffraction-limited receiver is the same, it follows that each coherence area represented by an aperture-plane sample collects P_b^* microwatts of background power. Therefore, according to this model, the total signal power collected by a subaperture containing K samples is proportional to $\sum_{k=1}^{K} |\alpha_k|^2$, whereas the total background power is proportional to $K P_b^*$. This conclusion is correct for any subaperture containing at least one sample, from the smallest area with diameter equal to a coherence length to the largest single-aperture receiver containing a great many coherence areas. We conclude that, as long as each subaperture contains at least one signal sample, the total amount of signal and background energy can be built up from the primitive coherence-area samples, and therefore a single large aperture can be constructed as the sum of non-overlapping subapertures with an equivalent collecting area. This model holds over any region on the ground where the turbulence parameters are constant, typically on the order of hundreds of meters or more, and hence over areas much greater than any single-aperture receiver under consideration. Therefore, the centers of the subapertures can be separated by relatively large distances, creating an array from the single large aperture receiver, without affecting the collected signal power and the collected background power. Arrays of receivers therefore are equivalent to a single-aperture receiver of the same collecting area in the sense that both collect the same total signal and background power, as asserted in conclusion (3), stated above.

However, these conclusions do not extend to the case where the diameters of the array elements become smaller than the atmospheric coherence length. The reason is that, as the coherence area is subdivided into smaller apertures while holding the total area constant, creating in effect subsample apertures, the signal power flowing through each subsample aperture remains proportional to the subsample area, thus conserving signal power, but the background noise power flowing into each subsample aperture is a constant independent of collecting area. This means that each subsample aperture collects less signal power while collecting the same background power; therefore, receiver performance suffers. Alternatively, the total signal power collected by a full-sample aperture and the equivalent array of subsample apertures remains constant as the number of array elements increases, but the total noise power increases proportionally with the number of array elements. A direct consequence of this behavior is the observation that in the absence of turbulence, so that the field coherence length is equal to or greater than the collecting area, subdividing the single aperture into subapertures results in

degraded performance when background noise is present. This, of course, is merely a restatement of the fact that coherence areas cannot be subdivided without collecting more noise power than signal power and so incurring a performance loss. We may conclude, therefore, that single-aperture receivers of any diameter can be subdivided into arrays of smaller apertures only if the number of array elements remains smaller than the number of signal samples needed to represent the signal field over the receiver aperture. The above concepts can be restated in terms of the largest single receiver aperture diameter, D, and atmospheric coherence length r_0:

4) The performance of an array of small telescopes is equivalent to that of a single-aperture receiver of the same collecting area, provided the number of array elements obeys the condition $N \leq (D/r_0)^2 \equiv N*$.

Since the only cause of performance degradation is background radiation, it follows that in the absence of background radiation the total number of array elements, N, is not constrained to be less than $N*$. Therefore, in situations where the background radiation is not significant—such as might be the case at night with appropriate narrowband optical filtering—any number of elements could be used to construct an array without suffering performance degradation. However, as a practical matter, the constraint on the number of array elements is not a serious impediment to array design, as the following example illustrates.

Example. It is generally accepted that even under the best possible seeing conditions on the ground, the Fried parameter typically does not exceed 20 cm at an operating wavelength of 1 μm during the day. If a 10-m aperture is needed to communicate from deep space, then the maximum number of elements permissible for an array receiver is $N \leq (D/r_0)^2 = (10/0.2)^2 = 2500$. This number is far greater than what is needed to synthesize a 10-m aperture with reasonably sized telescopes; in fact, with 1-m apertures, only 100 telescopes would be needed.

We may conclude from this example that, since turbulence is always present during ground reception, an array of telescopes can be constructed with a reasonable number of elements to synthesize a single large-aperture receiver for communications applications.

6.1.2.4 Array Receiver Performance. In the following analyses, we assume that the optical bandwidth of the receiver is great compared to its electrical bandwidth, so that a multimode assumption can be applied to both the signal and background fields. It has been shown that multimode Gaussian fields with suitably small average modal noise count generate approximately Poisson-distributed random-point processes at the output of an ideal photon-counting detector [69]. This model is reasonable for communications systems operating

even at gigabit-per-second rates, and it justifies the use of the relatively simple Poisson model which, in turn, often leads to mathematically tractable solutions.

6.1.2.4.1 Array Detector Model. Consider an array of detectors consisting of $K \times L$ detector elements, representing K detector elements per telescope (FPA) and L telescopes. Assuming a frozen-atmosphere model, the sample-function density of the array of count observables from a particular focal-plane detector element of a given telescope can be written as $p[N_{mn}(t) \,|\, \lambda_{mn}(t); 0 \le t < T]$, where $\lambda_{mn}(t)$ and $N_{mn}(t)$ represent the Poisson count intensity and number of counts, respectively, over the mn-th detector element, and where m indexes a detector element in the focal plane of the n-th telescope [69]. This represents the output of a particular element of the array. Note that if the spatial intensity distribution is known, and the location and size of each detector element are also known, then conditioning on the spatial intensity distribution is equivalent to conditioning on the array of intensity components, each of which is still a function of time. Assuming that each detector element observes the sum of a signal field plus multimode Gaussian noise field, the array outputs can be modeled as conditionally independent Poisson processes, conditioned on the average signal intensity over each detector element. The joint conditional sample-function density over the entire array can be expressed in terms of the KL dimensional vector $\mathbf{N}(t)$ as

$$p\big[\mathbf{N}(t) \,|\, \lambda(t); 0 \le t \le T\big] = \prod_{m=1}^{K} \prod_{n=1}^{L} p\big[N_{mn}(t) \,|\, \lambda_{mn}(t); 0 \le t < T\big] \qquad (6.1\text{-}14)$$

where $\mathbf{N}(t) \equiv (N_{11}(t), N_{12}(t), \ldots, N_{KL}(t))$. This detection model can be used as a starting point for problems involving hypothesis testing and parameter estimation where the desired information is contained in the intensity distribution, but only the array of count accumulator functions can be observed.

6.1.2.4.2 Hypothesis Testing with Poisson Processes. Consider M-ary pulse-position modulation (PPM) in which one of M intensity functions is received, and the receiver attempts to determine the correct symbol based on observations of the array of count accumulator functions over each of M time slots. It is assumed that the symbol boundaries are known and that the arrival time of each detected photon and the total number of detected photons can be stored for a limited duration of time necessary for processing.

With M-ary PPM modulation, a signal pulse of duration τ seconds is transmitted in one of M consecutive time slots, resulting in a PPM symbol of duration $T = \tau M$ seconds. As shown in [69], the log-likelihood function can be expressed as

$$\Lambda_i(T) = \sum_{m=1}^{K} \sum_{n=1}^{L} \left\{ \sum_{w_{j,mn} \in ((i-1)\tau, i\tau]} \ln\left(1 + \frac{\lambda_{s,mn}\left(w_{j,mn}\right)}{\lambda_b}\right) \right\}$$

$$= \sum_{m=1}^{K} \sum_{n=1}^{L} \ln\left(1 + \frac{\lambda_{s,mn}}{\lambda_b}\right) N_{mn}^{(i)} \qquad (6.1\text{-}15)$$

where $w_{j,mn}$ is the occurrence time of the j-th photon over the mn-th detector element within the i-th time slot, $N_{mn}^{(i)}$ is defined as the total number of photons occurring over the m-th detector element in the focal plane of the n-th telescope during the i-th time slot, $\lambda_{s,mn}$ is the count intensity due to signal over the mn-th detector element, and λ_b is the count intensity due to background noise. Note that with constant signal intensities, the actual arrival times of photons within each slot do not contribute to the decision; hence, only the total number of detected photons, $N_{mn}^{(i)}$, matters. Given that we know the intensity over each detector element, the i-th log-likelihood function consists of the sum of a logarithmic function of the ratio of signal and background intensities from all detector elements over the i-th pulse interval, multiplied by the total number of detected photons; the optimum detection strategy is to select the symbol corresponding to the greatest log-likelihood function.

6.1.2.4.3 Performance of the Optimum Detector-Array Receiver. The probability of a correct decision is the probability that the log-likelihood function associated with the transmitted symbol exceeds all other log-likelihood functions. Thus, when the q-th symbol is sent, then a correct decision is made if $\Lambda_q(T) > \Lambda_i(T)$ *for all $i \neq q$*. Denoting the logarithmic functions, or weights, in Eq. (6.1-15) by u_{mn}, the log-likelihood function can be rewritten as

$$\Lambda_i(T) = \sum_{m=1}^{K} \sum_{n=1}^{L} u_{mn} N_{mn}^{(i)} \qquad (6.1\text{-}16)$$

In this form, we can see that the log-likelihood function is composed of sums of a random number of weights from each detector element; for example, the m-th detector element in the n-th telescope contributes an integer number of its own weight to the sum. Note that detectors containing much more background than signal intensity do not contribute significantly to the error probability, since the outputs of these detector elements are multiplied by weights that are close to zero. This observation suggests the following suboptimum decoder concept with greatly simplified structure: list the detector elements from all telescopes

simultaneously, starting with the one containing the most signal energy, followed by every other detector ordered according to decreasing signal intensities. The logarithmic weights are partitioned into two classes: large weights are assigned the value one, while small weights are assigned the value zero. It was shown previously that this simple partitioning achieves near-optimum performance in low-to-moderate-background environments, but with greatly reduced decoder complexity.

The processing to determine which detector elements to use from the array to achieve best performance can be explained as follows: compute the probability of error for the first detector element plus background, then form the sum of signal energies from the first two detector elements (plus background for two detector elements), and so on, until the minimum error probability is reached. The set of detector elements over all telescopes that minimizes the probability of error for the entire array is selected, as this set achieves best performance. However, this straightforward process of performing the optimization is not practical for an array of telescopes, since the output of each detector element must be sent to a central processing assembly, where the computations are performed. While this is conceptually straightforward, the complexity required to achieve this processing with a large number of wideband channels quickly becomes prohibitive.

For the adaptively synthesized array detector, the probability of correct decision given hypothesis q, or H_q, can be obtained by assuming constant signal and background intensities over each time slot, yielding the conditional Poisson densities

$$p_q\left(k \mid H_q\right) = \frac{\left(\lambda_s \tau + \lambda_b \tau\right)^k}{k!} e^{-\left(\lambda_s \tau + \lambda_b \tau\right)}$$

$$p_i\left(k \mid H_q\right) = \frac{\left(\lambda_b \tau\right)^k}{k!} e^{-\lambda_b \tau}$$

Here we interpret $\lambda_s \tau$ as the total average signal count per PPM slot over the selected set of detector elements when a signal is present, and $\lambda_b \tau$ as the total average background count over the same set of detector elements, per PPM slot. As shown in [69], the probability of correct symbol decision is given by

$$P_M(C) = \left\{ \sum_{r=0}^{M-1} \left(\frac{1}{r+1} \right) \binom{M-1}{r} \sum_{k=1}^{\infty} \frac{(\lambda_s \tau + \lambda_b \tau)^k}{k!} e^{-(\lambda_s \tau + \lambda_b \tau)} \left[\frac{(\lambda_b \tau)^k}{k!} e^{-\lambda_b \tau} \right]^r \right.$$

$$\left. \times \left[\sum_{j=0}^{k-1} \frac{(\lambda_b \tau)^j}{j!} e^{-\lambda_b \tau} \right]^{M-1-r} \right\} + M^{-1} e^{-(\lambda_s + M\lambda_b)\tau}$$

(6.1-17)

and the probability of symbol error follows as $P_M(E) = 1 - P_M(C)$.

Performance of the array receiver was evaluated via simulated phase disturbances over each telescope of the array, using Kolmogorov phase screens as described in [70]. A sample field was generated using the distorted phase distribution, resulting in a matrix of complex signal amplitudes over each aperture. For these simulations, an atmospheric correlation length of $r_0 = 10$ cm was assumed. The field intensity generated in the detector plane of each telescope was integrated over the elements of a 128- × 128-pixel detector array, which is assumed to encompass the extent of the signal distribution in the focal plane of each telescope.

The performance of an entire sequence of arrays, starting with one large element representing the single-element receiver implementation and subdividing it into 4, 16, and 64 smaller elements of constant total collecting area, was evaluated in the following manner. Error probability was computed for both ideal turbulence-free conditions and for turbulence characterized by a Fried parameter (or coherence length) of $r_0 = 10$ cm and an outer scale of turbulence corresponding to 64 m. In a typical computation, the $128 \times 128 = 16,384$ pixel energies representing the output of a single 4-m aperture were sorted in decreasing order of average signal energy, and M-ary PPM symbol-error probabilities were calculated for increasing numbers of detectors, starting with the first detector. Let K_s denote the average number of signal photons per PPM slot collected by the entire array aperture when a signal is present, and let k_b denote the average number of background photons per PPM slot collected by a diffraction-limited detector element (generally made up from several contiguous pixels). We also define the total average number of background photons collected by the entire array aperture as $K_b = (D/r_0)^2 k_b$ where D is the diameter of the large single-aperture receiver. However, we should keep in mind that the adaptively synthesized focal-plane detector array typically rejects most of the background radiation, collecting background photons selectively from those detector elements that contain significant signal energy. Figure 6-46 shows the symbol-error probability for 16-dimensional PPM ($M = 16$) as a function of the number of detector elements used, for the case $K_s = 10$ photons per slot and $k_b = 0.01$ photon per slot per diffraction-limited FOV or,
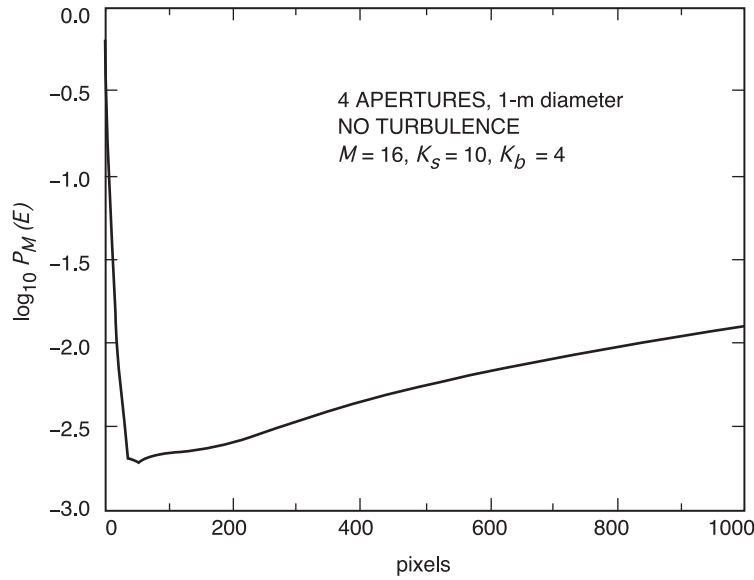
Fig. 6-46. Probability of error as a function of the number of sorted pixels: no turbulence.

equivalently, $K_b = 4$. It can be seen that for this case the smallest error probability of $10^{-2.7} \approx 0.002$ is achieved by assigning unity weight to the first 50 pixels containing the greatest signal intensities and zero to all the rest.

The same approach was used to determine array receiver performance in the presence turbulence, as shown in Fig. 6-47. However, in this case the minimum-error probability is obtained with 1200 pixels sorted according to signal energy, instead of 50 as for the diffraction-limited case. In the presence of noise, this means that performance suffers, because 1200 pixels collect approximately 24 times as much background noise as the 50 sorted pixels that attained the minimum-error probability in the absence of turbulence.

The performance of the optical arrays was evaluated using the procedure described above to determine the error probability of the adaptive "1-0" receiver. Arrays of various sizes, consisting of increasing numbers of telescopes with proportionally smaller apertures to keep the total collecting area constant, were evaluated. Independent samples of Kolmogorov phase screens were generated for each telescope, and the signal intensity distributions in the focal plane were determined for each sample function, using two-dimensional Fourier transforms. The focal plane of each telescope was assumed to contain a focal-plane array, of dimensions consistent with the telescope diameter and the expected level of turbulence.

In a typical simulation, a large telescope is analyzed first, by determining its performance according to the sorting procedure described above. The
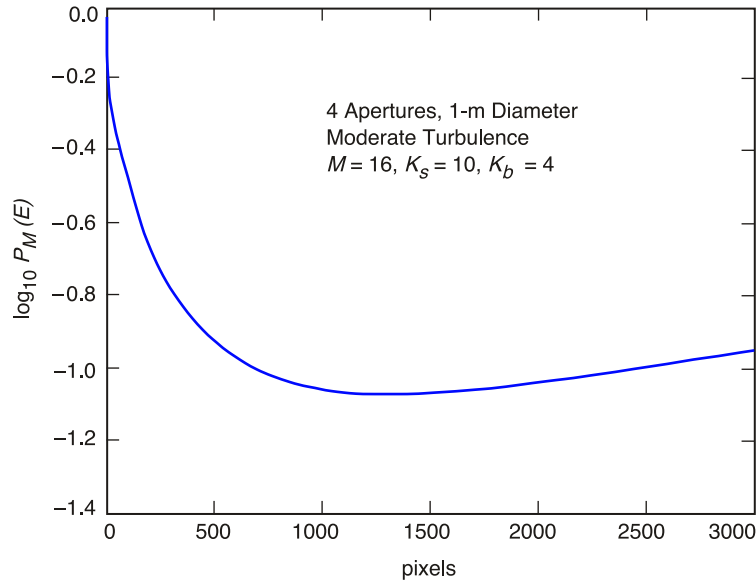
Fig. 6-47. Probability of error as a function of the number of sorted pixels: moderate turbulence, r_0 = 10 cm.

probability of error is calculated for increasing amounts of signal energy passing through the aperture, and distributed in the focal plane according to the two-dimensional Fourier transform of the aperture-field distribution generated using the Kolmogorov phase-screen program. Next, the diameter of each telescope was divided by two, generating four smaller telescopes with the same total area as the previous array, and the performance of the new larger array was computed as before. The process of dividing telescope diameters by a factor of two in order to generate the next larger array was continued four times, generating arrays of 4, 16, and 64 elements from a single large telescope. Different realizations of the signal intensity distribution were generated for each element of the new array; thus, a single telescope used a single phase-screen realization over the aperture plane, whereas an array of $N \times N$ telescopes of the same area as the single telescope used a total of N^2 different phase-screen realizations. The intensity distributions were then scaled such that the total signal energy entering the single large-aperture receiver and the array were equal.

An example of the phase distributions generated for analyzing array performance is shown in Figs. 6-48(a) and 6-48(b). The variation of optical phase over each telescope, when operating in turbulence with a Fried parameter of $r_0 = 0.1$ m (or 10 cm) and an outer scale of turbulence of 64 m, is shown in Fig. 6-48(a); the corresponding focal-plane signal distribution is shown in Fig. 6-48(b). Note that, because the 1-m telescope aperture is large compared to
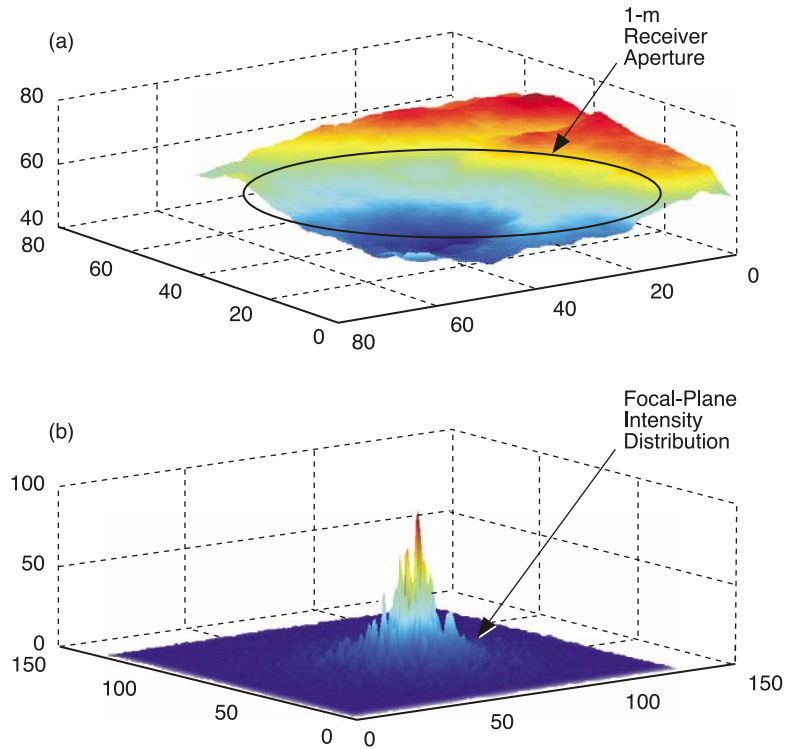
Fig. 6-48. A single 1-m-diameter telescope, 10-cm atmospheric-coherence length: (a) aperture-plane phase distribution and (b) corresponding focal-plane intensity distribution .

the 10-cm Fried parameter, there are a great many spatial modes excited by the signal field, and therefore the PSF is significantly distorted with numerous intensity peaks. This implies that a correspondingly large number of detector elements must be used to collect the signal, inadvertently collecting background radiation as well.

Aperture-plane and focal-plane distributions for two out of the four half-diameter telescopes comprising the first-level array are shown in Fig. 6-49. Note that with the smaller apertures and moderate turbulence as before, the PSF remains peaked and highly concentrated in the focal plane, suggesting that most of the signal energy is now localized in each telescope. However, due to the larger number of telescopes in the array, the same number of modes is observed as with the single large-aperture telescope, and therefore the same amount of background radiation is collected.

The process of dividing each telescope diameter to create larger arrays can be continued indefinitely in principle, yielding second-, third-, and higher-generation arrays, each containing four times as many elements as the previous configuration. However, continuing this process makes sense only as long as
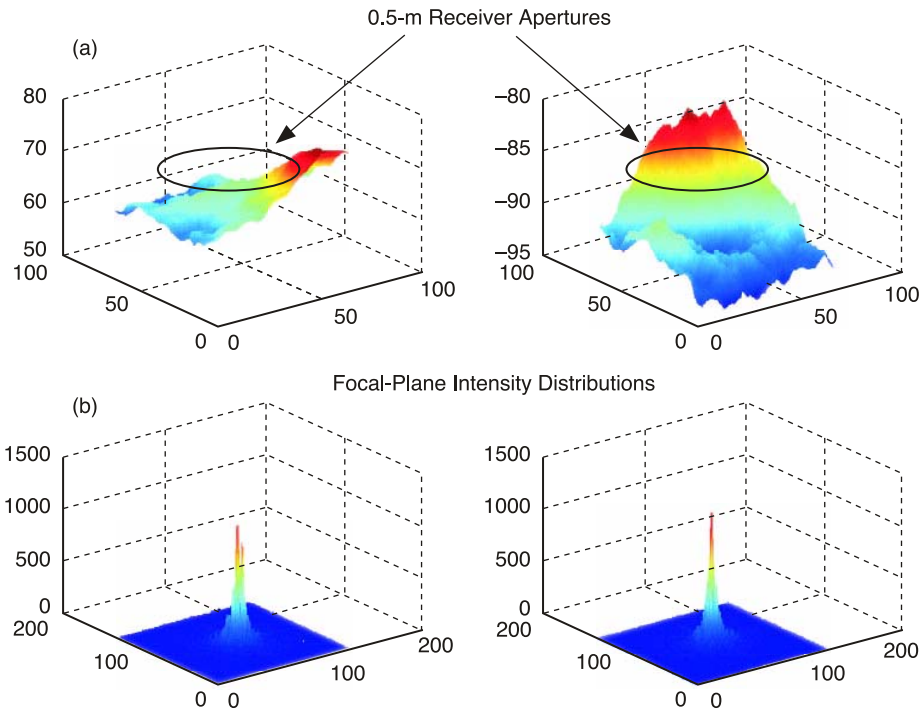
Fig. 6-49. Two telescopes of a larger array, 0.5-m diameter and 10-cm atmospheric-coherence length: (a) aperture-plane phase distributions and (b) corresponding focal-plane intensity distributions.

the telescope diameters exceed the Fried parameter; after that point, further reductions in telescope size lead to degraded performance for the reason described in 6.1.2.3. As the total number of telescopes in the array begins to exceed the total number of signal modes, it is no longer possible to distribute the signal power over more telescopes without incurring additional penalties due to the excess background radiation collected by the array. This behavior is illustrated by the performance curves in Fig. 6-50, which show the performance of a single 2-m aperture, together with arrays of 4, 16, and 64 elements of diameter 1 m, 0.5 m, and 0.25 m, respectively, under two scenarios: first, the performance of the array is determined under negligible-turbulence conditions (as might be the case for a space-borne array); and second, the performance with turbulence of 10-cm coherence length was determined for 16-PPM signals. Background radiation of 0.01 photon per diffraction-limited FOV per slot was assumed for these calculations.

Figure 6-50 shows that with little or no turbulence, such that $r_0 > D$, the single large receiver performs best. However, with significant turbulence, $r_0 << D$, the array performance is comparable to that of a single large receiver.
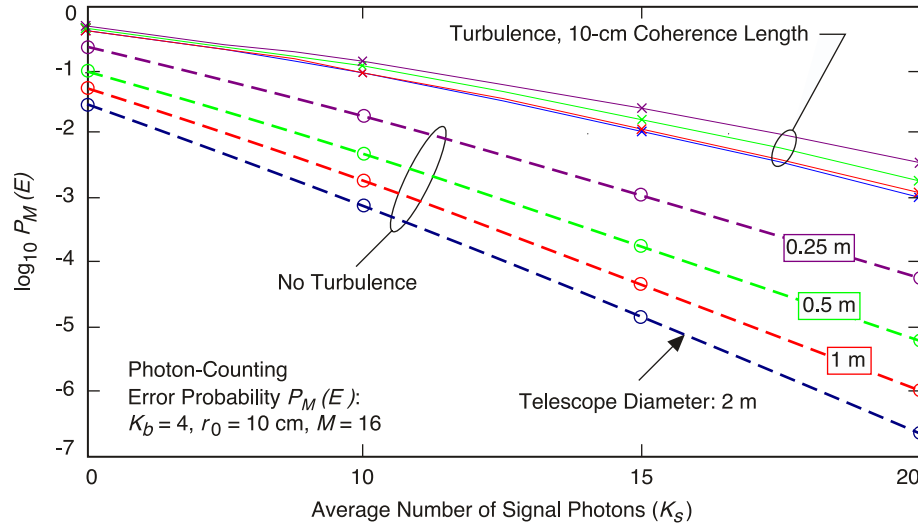
Fig. 6-50. Performance of a single 2-m telescope and an equivalent-aperture array receiver, with and without turbulence.

Note that in the absence of turbulence a single large-aperture receiver performs best because the signal is in the form of an undistorted plane wave, and therefore, a single detector element with diffraction-limited FOV suffices to collect essentially all of the signal energy. At the same time, background radiation entering the receiver from all directions within the FOV can be maximally suppressed, only the minimal amount within the small diffraction-limited cone of angles contributing to background interference within the receiver. Since diffraction-limited FOV and collecting area are inversely related, the amount of background radiation in a diffraction-limited FOV is independent of receiver aperture; this means that N diffraction-limited receivers collect N times as much background energy as a single receiver, regardless of telescope diameter. Therefore, arrays of diffraction-limited receivers collect background energy proportional to the number of elements, not proportional to the total collecting area. The performance of diffraction-limited arrays observing a signal in the absence of turbulence but with moderate background radiation in the diffraction-limited FOV of each telescope is illustrated in Fig. 6-50; note that performance degrades significantly as the number of array elements increases from a single 2-m-diameter telescope to 4 telescopes of 1-m aperture, then to 16, and finally to 64 telescopes of 0.25-m diameter.

However, turbulence is ever present; even in good seeing (corresponding to a Fried parameter of 10 cm or more), the performance of the first-generation array (of four telescopes) is virtually indistinguishable from the performance of the single aperture, as the performance curves corresponding to turbulent conditions indicate. This occurs because in the presence of turbulence the single

telescope must increase its FOV well beyond the diffraction limit to collect sufficient signal energy to minimize the probability of symbol error, and in the process collects more background energy as well. In effect, the single-aperture receiver must observe more than one (typically, a great many) spatial modes, each mode approximated by a diffraction-limited FOV collecting both signal and background energy from slightly different directions. The array of small telescopes observes the same total number of spatial modes, and hence collects the same amount of background energy by the above argument. Since the total collecting area of the array is the same as that of the single receiver, it also collects the same amount of signal energy; therefore, the performance of the array is essentially the same as that of the single-aperture receiver. Small variations in the array performance curves with turbulence are due to slight variations of the random phase distributions generated by the Kolmogorov phase-screen program.

6.1.2.4.4 Extrapolating to Determine the Performance of Large Arrays. In order to determine if there is a "best" array telescope diameter, array performance was evaluated for a given value of total signal energy, background intensity, and turbulence parameter for a large number of arrays. As originally developed, computations for array performance can be carried out in a reasonable amount of time (approximately 1 hour per run) for arrays of no more than 64 elements. This allows analysis of arrays consisting of as many as four different telescope sizes (for example, 2 m, 1 m, 0.5 m, and 0.25 m). It was found that increasing the array size beyond 64 elements, with each array containing its own focal-plane array of detectors, began to incur unacceptably great computational burdens. Therefore, an approach was developed to evaluate the performance of a large array by modifying the input noise parameters of smaller arrays, and then "connecting" the results in order to estimate performance over a much larger range of array diameters.

This technique was first applied to arrays of telescopes with diameters ranging from a single telescope of 4-m diameter to an array of 0.125-m telescopes, creating arrays of 1, 4, 16, 64, 256, and 1024 elements. These arrays were split into two sets: the first set consisted of 4-m, 2-m, 1-m, and 0.5-m telescopes, while the second set consisted of 1-m, 0.5-m, 0.25-m, and 0.125-m telescopes. The noise parameters of the second set were increased by a factor of four to account for the total noise power collected by an array with four times the number of elements, and the performances of the two sets computed using the initial program. Three different test cases were run with an average of 20 signal photons and moderate background noise of 0.01 photon per PPM slot per diffraction-limited FOV. This implies that the average number of background photons collected by the entire array aperture is $K_b = 16$, which represents an extremely high background environment. The results of the individual runs shown in Fig. 6-51 indicate that the two sets could indeed be connected,
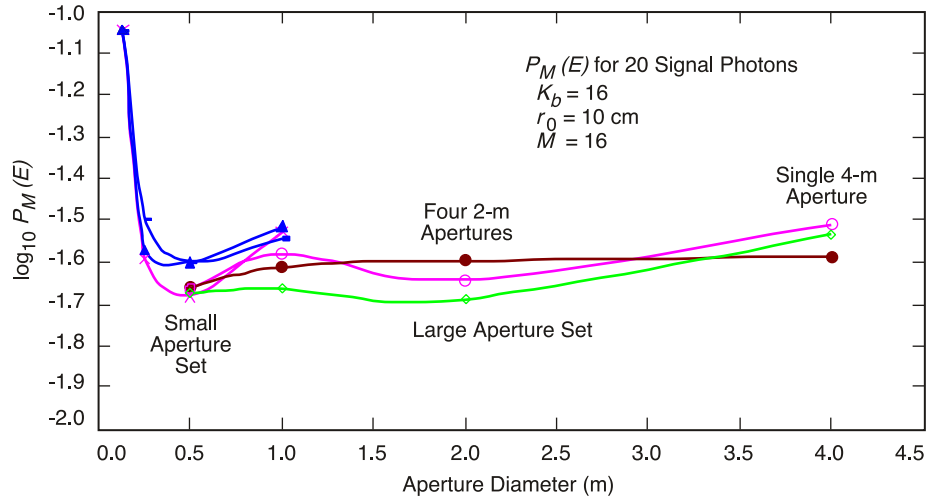
Fig. 6-51. Results of three simulation cases for evaluating the connectivity of small arrays.

resulting in greatly simplified computations. Small differences in the performance of the two sets at aperture diameters of 0.5 meter and 1 meter are attributed to variations in the sample functions of the focal-plane signal energy distributions generated by the phase-screen programs. Note that as the telescope diameters approach the Fried parameter performance deteriorates in all cases. The modal analysis presented in 6.1.2.3 predicted this performance degradation for apertures smaller than the coherence length; however, it is actually observed for somewhat larger collecting areas in Fig. 6-51. This behavior is attributed to the fact that the modal analysis was only approximate, and did not take into account edge effects that start to become significant under these conditions.

Taking the average of the performance curves of Fig. 6-51 at each telescope diameter yields the averaged performance curve of Fig. 6-52, which shows a smooth continuous curve through the entire range of diameters from 4 meters to 0.125 m, supporting the validity of the approach. Fig. 6-52 also shows the hypothetical performance of the diffraction-limited receiver, corresponding to turbulence-free conditions, but observing the same background radiation (a condition that can only be approached in free space for large apertures). Since without turbulence a single field sample suffices to represent the aperture-plane field, and hence only one diffraction-limited unit of background power is collected, the performance of the arrays is always better in the absence of turbulence.

Finally, these results were extended to cover a range of telescope diameters from 8 m to 0.125 m, again using the connected-set approach and averaging a large number of runs to obtain the final results. The results for arrays with the 8-m collecting area are shown in Fig. 6-53. These results are similar to the

previous 4-m case shown in Fig. 6-52, except that performance is uniformly worse for the following reason: with atmospheric coherence length, signal energy, and background intensity held constant for both cases, the total number of signal modes is four times as great for the 8-m equivalent aperture as for the 4-m aperture. This means the larger 8-m array collects four times as much background energy while collecting the same signal energy as the 4-m array,
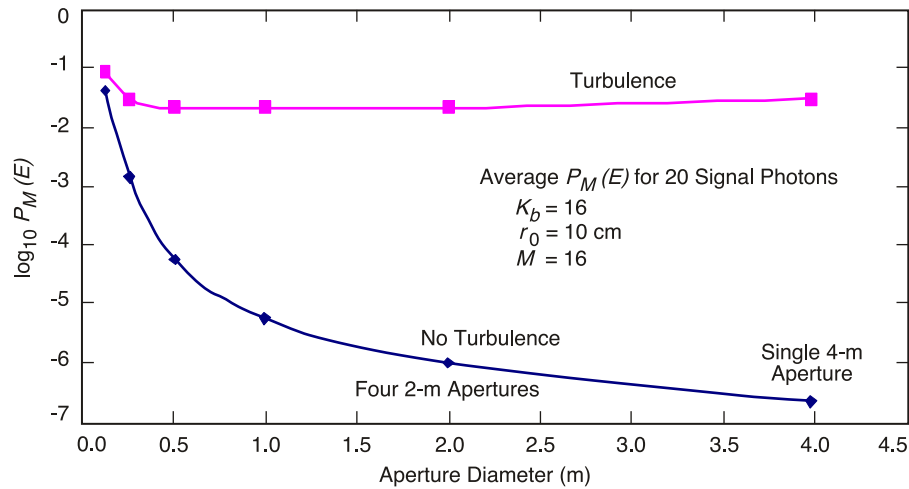

Fig. 6-52. Averaged performance of 4-m-equivalent arrays, 20 signal photons, 0.01 noise photon per slot.
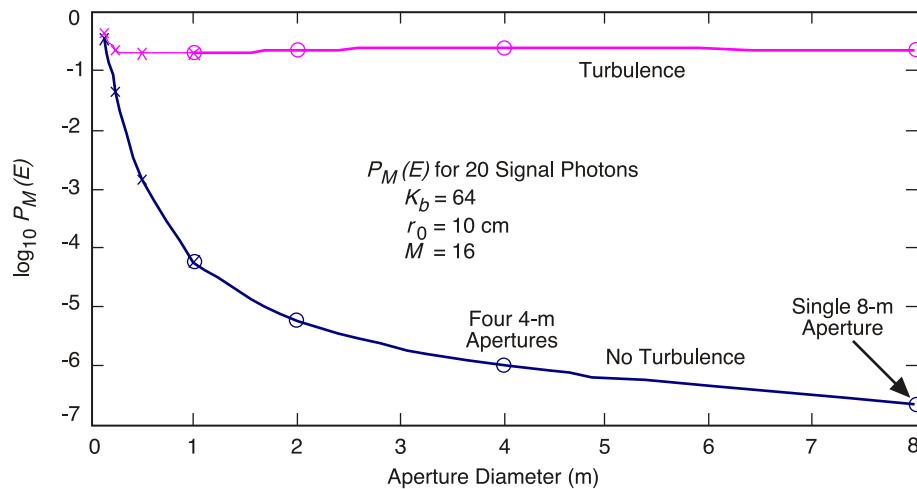

Fig. 6-53. Averaged performance of 8-m-equivalent arrays, 20 signal photons, 64 noise photons per slot. Note the degraded performance relative to the 4-m array, due to increased background noise while keeping the average signal energy the same.

and hence appears to suffer degraded performance. Similar performance would be achieved by the larger array if the signal energy were increased proportionally to the area.

In the above examples, the total number of focal-plane pixels at each telescope was not limited to any specific value a priori; in fact, every attempt was made to make sure that enough detector elements were used to collect all of the signal energy for each sample function of the phase distribution. This approach is not practical, however, since in a physical realization the number of pixels will be limited due to complexity and implementation considerations.

6.1.2.5 Conclusions. The concept of an optical array receiver suitable for deep-space communications has been defined, and the theoretical foundations of optical array receiver operation and performance have been established. The necessary mathematical models for representing aperture-plane and focal-plane fields have been developed, and detection theory has been applied to determine the performance of an optical-array receiver under realistic operating conditions. In particular, the performance of multi-element telescope arrays observing pulse-position modulated optical signals in the presence of atmospheric turbulence and background interference has been investigated, and conditions have been determined under which array performance and single-aperture receiver performance were identical. The performances of various array configurations have been determined and shown to be equivalent to the performance of the large single-aperture receiver, thus demonstrating that the array approach does not incur any losses relative to the single-aperture approach under operating conditions of interest.

Based on the above results, we conclude that the array-receiver concept represents a viable alternative to the more conventional approach of using a single large-aperture telescope to collect the optical signal energy, particularly since high-data-rate reception from the depths of space demands ever increasing collecting areas to achieve the desired performance. Large-aperture telescopes are difficult to construct and maintain, require massive support structures and drive assemblies, and pose the risk of jeopardizing the mission in case of failure. In addition, once constructed, the collecting area of a single telescope cannot be easily expanded to meet demands for increased performance. An array of small telescopes, on the other hand, provides a robust, scalable, parallel receiver architecture that can easily be expanded to meet greater demands with relative ease.

6.2 Photodetectors

6.2.1   Single-Element Detectors
Abhijit Biswas and William H. Farr

6.2.1.1 Deep-Space Detector Requirements and Challenges. This section presents discussions on detectors used for ground-based reception of optical communications transmitted from deep space. Detectors convert received signal photons into an electronic signal that is processed in order to extract information. Laser signals in the near infrared region, specifically at wavelengths close to 1.06 µm or 1.55 µm of the optical spectrum are presumed in the discussion that follows. This choice of wavelengths is dictated by the availability of high peak-to-average power laser transmitters (neodymium: yttrium aluminum garnet [Nd:YAG], neodymium: yttrium vanadium oxide [Nd:YVO$_4$], neodymium: yttrium lithium fluoride [Nd:YLF] crystal and ytterbium- or erbium-doped fiber amplifier lasers) required for achieving photon-efficient communications [71] over inter-planetary distances. Typically the signals incident on the detector are faint, not only because of the huge distances and associated losses, but also due to constraints on spacecraft power and laser electrical-to-optical-conversion efficiency. Therefore, single photon counting sensitivity combined with high photo-detection efficiency at wavelengths of interest, is highly sought after.

Photo-detection efficiency (PDE) is the product of the probability of absorption and the probability that the primary photoelectrons resulting from absorption are converted to a sensible photoelectron signal at the detector output. For most photon-sensitive detectors, this involves an internal gain or multiplication process. In addition to high PDE, detectors must also possess high bandwidth. This allows a faithful measurement of the time-of-arrival of faint photon pulses that are typically a few nanoseconds in duration. Finally, high performance for detectors demands low dark noise and gain variance or excess noise.

Detector technology drivers are further influenced by the environment in which they must operate. Ground based reception is currently being considered by NASA for near-future technology demonstrations [72] with likely follow-on distributed optical receiving networks deployed on the ground, and/or above the Earth's atmosphere in suborbital or orbital platforms. For receivers located above the atmosphere, coherent communications and near-diffraction limited reception expand the scope of useable detectors. However, the present discussion will be limited to detectors for ground-based receivers.

Deploying ground-based receiving systems adds to the detector challenge. Since the laser beam must propagate through the atmosphere prior to being collected and detected, all the effects described in Chapter 3 gain relevance.

Foremost among these is atmospheric "blurring" [73]. In order to cope with this effect, the detector field-of-view (FOV) must be enlarged. This in turn has the undesirable effect of "viewing" a larger angular region of the sky and proportionately increasing the collected background light scattered from the sky and other celestial sources. Daytime links that are of significant duration for deep space missions must contend with the increased background light. The added background for daytime links of course increases as the angular separation of the spacecraft from the sun decreases. Current thinking demands that optical links be operated at small (2–10 deg) Sun-Earth probe (SEP) angles. Under these circumstances, in addition to the formidable increase in sky background, stray light due to off-axis sunlight scattering into the detector FOV also becomes significant. Note that the penalty associated with background is two-fold. First, signal-to-noise ratio suffers as a consequence of the large additive component of background. Second, the large incident background photon flux that can be orders of magnitude larger than the average signal power can drive the detector into saturation. The latter condition can necessitate spreading the aggregate photon flux over multiple detector elements.

A general observation from the foregoing discussion is that the ability to handle faint signals in the presence of large background is a design requirement. This condition prevails for significant durations when receiving communications from planetary probes. For example, two-thirds of the optical link opportunities to a spacecraft orbiting Mars are in the daytime while for the distant outer planets this is reduced to half. Therefore, the limiting condition for detector selection is the ability to support viable daytime links. Significantly improved performance is expected with the 3–6 order-of-magnitude reduction when night time backgrounds are encountered.

Deep space optical links are rendered viable by reducing the duty cycle of the laser transmitter so that the peak power of the laser pulse can overcome the huge space loss, as well as associated system and channel losses, so that a few signal photons arrive at the detector. This calls for temporally narrow pulses typically 1–10 ns long. Additionally, modulation strategies like pulse position modulation (PPM) [71,72,73] offer temporal discrimination so that precise measurement of the time of arrival of the laser pulse can be used to transmit information. The channel capacity for idealized photon counting can be shown to offer the best performance in terms of bits per photon [74] that can be transmitted, compared to the traditional on-off key (OOK) modulation used by the telecom industry. Even with the penalty for additive background noise and imperfect devices that deviate from idealized photon-counting, the channel capacity for direct detection with photon counting is expected to be superior to alternate schemes. Of course in addition to photon counting sensitivity, a key to making deep space optical links viable is the availability of powerful codes [75] that can approach within 0.5–1.5 dB of capacity.

Therefore, ground-based optical detectors must provide efficient photon counting together with high bandwidth capable of precisely sensing photon arrivals. Additionally, the contributions of thermal or dark noise and gain variance or excess noise that cause device performance to deviate from ideal Poisson detection must be minimized through materials selection and good detector design.

Figure 6-54 provides an example of the data rates achievable from deep space optical links. Data rate is presented as a function of the background photon flux in photons/second incident on the detector. In this example, incident average signal photon fluxes (λ_s) of 1×10^6 and 5×10^6 photons/second were assumed. For each value of λ_s data rates were estimated for PDEs of 0.3 and 1.0. Various combinations of system and channel parameters can give rise to the operating points shown in Fig. 6-54. A PPM-order of 128 with the slot width allowed to vary in discrete steps and with a fixed code rate of 0.5 was chosen for deriving the results plotted in Fig. 6-54. In addition a 3-dB link margin and a 2-dB loss to account for the electronic and hardware implementation were assumed. The data rates flatten out with reduced background because of the constraints imposed by the combination of the assumptions made. These constraints are realistic since relaxing them in order to overcome the data rate limit will entail added complexity to the laser transmitter. Typical mass, power, and complexity limitations on a state-of-the-
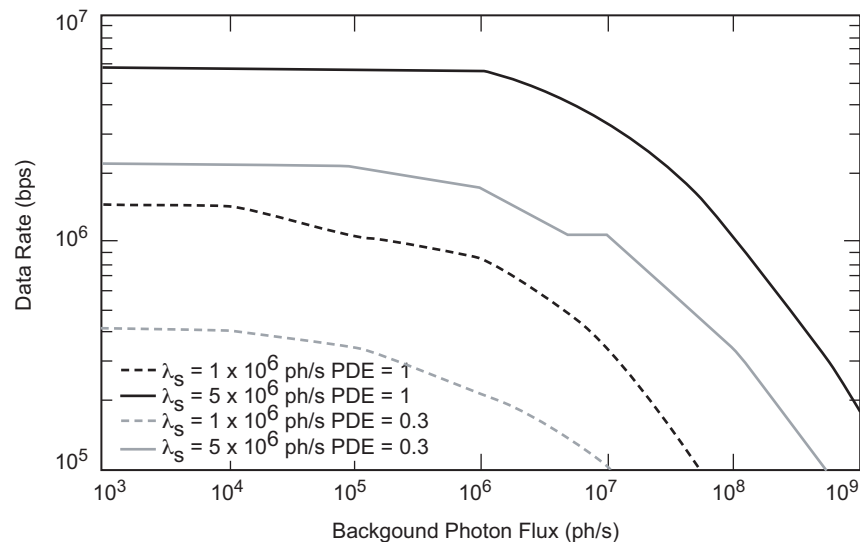

Fig. 6-54. Data rate versus average background photon flux incident on the detector shown for two mean flux levels of 1 and 5×10^6 photons/second and for two PDEs of 0.3 and 1. A PPM order of 128 is assumed, and data rates have a 3-dB link margin and a 2-dB implementation loss.

art spacecraft laser transmitter will result in performance similar to that depicted in Fig. 6-54. Data rates below 100 kbps are not plotted. A detailed description of how these data rates can be derived is given in references [75] and [76]. The intent here was to emphasize the influence of the detector on the link performance.

6.2.1.2 Detector System Dependencies. Critical dependencies for a detector embedded in a deep-space optical communications system are briefly pointed out in this section.

Foremost among these detector dependencies is the ability to collect sufficient signal photons to satisfy the required data rates, in the presence of additive background. Fig. 6-54 is an example of how viable operating points for a set of coding and modulation constraints such as the code rate, PPM-order and slot width can be computed. Large effective collection areas are invariably required to achieve viable operating points. Large effective collection areas can be achieved by using large-diameter single monolithic photon collectors or alternatively, through the use of an array of smaller apertures. Studies and research on both these approaches show considerable promise [77,78,79]. The specific approach chosen for implementing large effective apertures will influence the selection of detectors. Firstly, the coupling of light from relatively smaller diameter versus larger diameter apertures on to the detector surface must be accounted for. Secondly, arrays involve combining the output from a large number of detectors. Therefore, in the latter case, low-noise or noiseless photon counting is desired in order to prevent an additive dark noise contribution when combining the outputs from the elements of the array. Finally, signal combination in arrays is complicated by the requirement to maintain precise temporal alignment between the incoming pulse streams. Either the ability to precisely distribute a clock to an extended array of receivers must be met, or local clock synchronization at each array element must be implemented. Note that for the latter to occur, the signal-to-noise ratio must be 1/N that for an N-element array compared to an equivalent single aperture.

Because detectors are expected to operate in harsh background light environments, every effort is made to reject or suppress background photons. Polarization discrimination and optical filtering are both utilized. Thus, transmitting circularly polarized laser light can in principal afford a 3-dB reduction in unpolarized background that reaches the detector. Narrow-band optical filtering is a highly desirable means of suppressing background as well.

The use of powerful near capacity achieving codes has been pointed out before. In order to implement these codes, the detected signal must be temporally synchronized, and suitable high speed hardware and software are needed to accomplish this.

Early in this discussion the laser transmitter wavelength was presumed to be in the near infrared, specifically near 1060 or 1550 nm. This deserves a brief

mention since the argument can be made that laser wavelengths be chosen for compatibility with available high efficiency detectors. From a detector standpoint, this would of course be attractive; however, optical communications systems design issues do not favor this rather complex trade. Selecting shorter wavelengths entails larger background contributions since the solar flux increases towards the visible; moreover, the optical tolerances at shorter wavelengths become tighter. Atmospheric turbulence also is more severe at shorter wavelengths. On the other hand the option of going to longer wavelengths that would favor background, turbulence and optical tolerances, is limited by the lack of lasers and efficient high-bandwidth detectors.

6.2.1.3 Detectors for Deep-Space Communications. In this section a brief description of potential photon counting devices is presented. It should be stated at the outset that at the time of writing this text, photon counting devices with desired characteristics for supporting deep space optical links were not commercially available. A number of efforts are underway to develop perhaps the first generation of deep-space optical detectors for ground-based receivers.

As shown in Fig. 6-54, the data rate required for an optical link will largely dictate the PDE of the detector. Other detector parameters (such as dark and excess noise) perturb the performance and are important, but PDE will prove to be the biggest driver in developing detectors. For example, increasing dark noise will shift the operating point in Fig. 6-54 towards the right on the abscissa, while an increase in excess noise may render the 2-dB implementation loss assumed in Fig. 6-54 inadequate, or it may require novel signal processing to achieve timing synchronization and decoding.

Photon-counting detectors can be subdivided into two categories, proportional or linear photon counters and Geiger mode photon counters. Linear photon counters output voltage pulses in response to single-photon incidence. Moreover, the voltage pulse height is proportional to the mean number of incident photons. Typically in these devices, a fraction of the incident photons is absorbed depending on the quantum efficiency. The absorbed photons result in primary photoelectrons that undergo internal gain or multiplication resulting in a secondary photoelectron current flow across a resistor that is sensed as a voltage pulse. The efficiency with which primary photoelectrons are converted to a sensible output signal contributes to a multiplicative term that determines the PDE. For an ideal proportional photon counter, the output pulse height would uniquely identify the number of absorbed photons. Practical device constraints (such as thermal noise and gain variance or excess noise) smear out the measured voltage response so that a distribution of voltages results from the incidence of a given number of photons. If the output voltage variance is narrow, the number of absorbed photons can still be uniquely determined. This usually occurs when the gain variance or excess noise is sufficiently low. Proportional photon counters

operating in this mode are sometimes referred to as photon-number detectors. On the other hand, if the excess noise is large, a unique relation between the output voltage and the number of absorbed photons ceases to exist. Fig. 6-55 shows a conceptual schematic of the different modes of operation of proportional photon counters relative to an ideal photon counter.

The temporal response of proportional photon-counters is limited by the ability to resolve photon time of arrivals, also referred to as detector bandwidth. Detector bandwidth limitations can reside in the detector or be introduced by post-detection analog conditioning electronics. Photon arrival time separations exceeding the detection bandwidth causes variance in the pulse shape output by the detector. For pulse position modulation, this pulse-shape variance can give rise to inter-symbol interference effects. Examples of proportional photon counters are photomultiplier tubes and avalanche photodiodes.

Geiger mode avalanche photodiodes (GMAPDs) are operated biased close to breakdown, so that incidence of a single photon triggers an avalanche or breakdown resulting in a gigantic output pulse. In this mode, detectors do not instantaneously recover from breakdown. Active and passive quenching circuits are implemented on the backend of GMAPDs that determine the dead time and after-pulsing characteristics. After-pulsing results from trapped charge that is emitted at a delay following breakdown. Thus, GMAPDs provide infinite gain (or virtually noiseless performance) but cannot provide a photon-number response since the dead times vary from tens to thousands of nanoseconds.
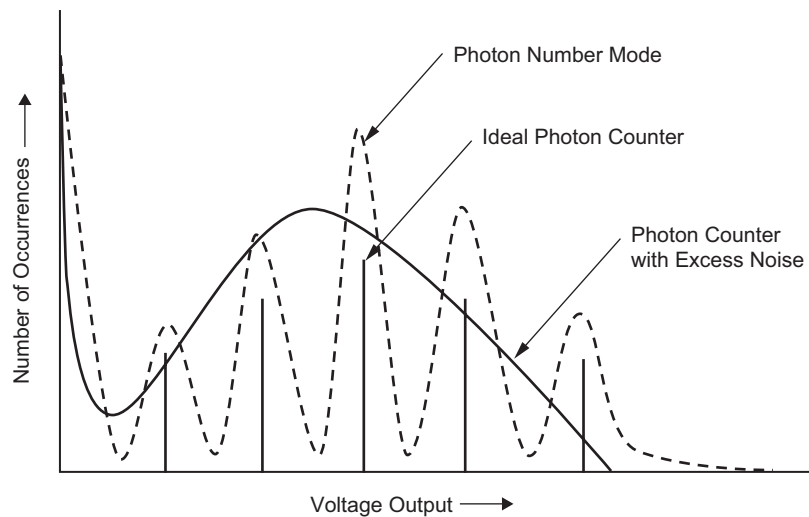

Fig. 6-55. A conceptual view comparing the histograms expected for the output of a linear mode proportional photon-counting detector for an ideal photon counter, a photon-number mode detector, and a photon counter with excess noise.

For pulse position modulation, the detector should count photon arrivals with temporal precision that is a small fraction of the slot width and generate output voltages proportional to the number of photons counted. Uncertainty in the number of counted photons and time of arrival will result in link performance degradation. A photon-number mode detector can meet these requirements if it (i) does not saturate due to the incidence of high photon fluxes, (ii) has low excess noise to count the number of photons over a slot interval accurately, (iii) has adequate bandwidth, and (iv) has a low dark noise. Provided the detector can meet these requirements, backend processing electronics in the receiver can perform the synchronization and likelihood estimation that are subsequently fed to the decoder for extracting bits of information. Given most available proportional photon counters, the fluxes typically encountered in day-time near-Sun links will tend to drive a single detector to saturation, and the use of a small array of detectors is required to handle the highest photon fluxes expected when operating close to the Sun. The array element outputs are processed in parallel and combined prior to processing. Provided two to four detector elements are used, the additive dark noise penalty is not excessive. For example, if a detector has 300 thousand counts per second (kcps) of dark counts then four of these will contribute to 1 million counts per second (Mcps), but this is still a small fraction of the 10^8–10^9 cps of background photons.

As pointed out in [74], GMAPD photon counters can be used with an extended array of receiving apertures. The photons arriving at the focal plane of each collection aperture are proportional to the diameter. A suitably sized array of GMAPDs at the focal plane of each aperture will ensure that the mean number of photon arrivals per detector dead time does not exceed 1. If this condition can be met, there will be no blockage loss. In reality, depending upon the link design, some blockage loss can be allocated.

Given the brief discussion on some very general approaches toward implementing photon counting schemes for deep-space optical links a few specific detectors will be briefly described.

6.2.1.3.1 Photomultiplier Tubes (PMT). Photomultiplier tubes (PMTs) for free-space optical communications were laboratory tested in the early 1980s at JPL [80,81]. It was shown in this early work that the photon counting channel capacity could indeed be validated through laboratory measurements. A laboratory link at 2.5 bits/photon was demonstrated using a photon-counting PMT with a quantum efficiency of 15 percent at 850 nm. Pulse widths of 100 ns were used, and both uncoded and coded (Reed-Solomon coding) bit-error rate performance matched that predicted by channel-capacity computations. Unfortunately, a big bottleneck to adapting PMTs has been the detection efficiency limitations at the wavelengths of interest.

   More recently, commercial liquid-nitrogen-cooled PMTs with quantum efficiencies as high as 8 percent at 1064 nm have become available. Laboratory testing of such a device manufactured by Hammatsu Corporation, Hammatsu, Japan (Model Number R5509-42) was conducted [82] in the laboratory. The PMT was shown to behave like a proportional photon counter with the measured pulse height being proportional to incident photons per pulse, as suggested by the plot in Fig. 6-56. Figure 6-57 shows a 1064-nm laser pulse train measured in the laboratory using this PMT. The upper trace was generated by splitting a fraction of the incident laser pulse train onto a high speed photodiode in order to provide a reliable timing reference. The delay between the pulses in the upper trace and the PMT output represents the difference in light-travel time for the laser beam to reach the photodiode and PMT. A comparison of the traces in Fig. 6-57 illustrates the bandwidth limitations of the PMT. The temporal width of the high-speed photodiode output is far more representative of the laser pulse duration than the PMT bandwidth-limited pulse shapes in the lower traces. Furthermore, relatively larger fluctuations in pulse-height response of the PMT, associated with its gain variance are apparent from a comparison of the two traces. The gain variance causes the probability distribution function of the output to deviate from an ideal Poisson distribution. In this case a Polya-distribution function shows a reasonable fit to the measured data as shown in Fig. 6-58. In this plot, the parameter b is a free-fitting parameter that represents the uniformity of the photocathode and the subsequent dynode stages. Thus $b = 0.1$, 0.25, 1, 0.01, 0.01, 0.01 denotes a figure of merit with respect to uniformity for the photocathode and the
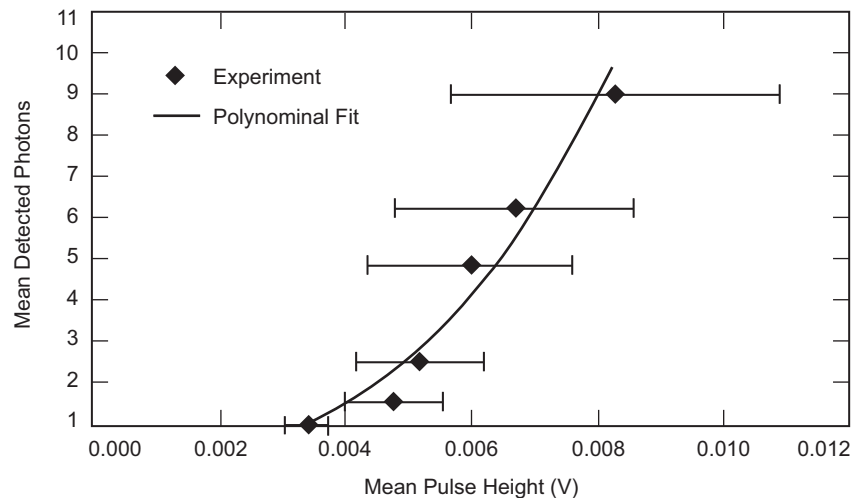

Fig. 6-56. A laboratory measured plot of output voltage versus mean number of incident photons for a photon-counting photomultiplier tube.
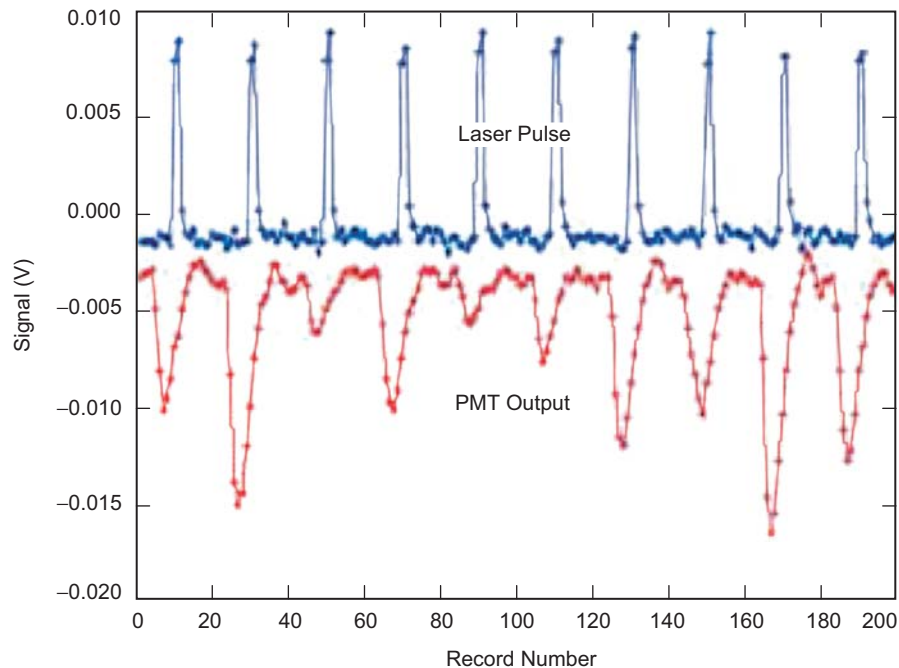
Fig. 6-57. An example of the output from a photon-counting photomultiplier tube shown in the lower trace. The upper trace is a time reference generated by splitting a fraction of the light incident on the PMT onto a high-speed photodiode. The delay between the pulses in the upper trace and lower trace is due to optical path differences.

subsequent dynode stages of the PMT. The higher numbers of 0.1 to 1 indicate a large degree of non-uniformity resulting in photoelectron emission deviating significantly from Poisson, while the smaller values for the subsequent stages is much more Poisson like.

While the PMT provides a reasonable example of a photon counter, its deficiencies in supporting a deep-space link are many. The bandwidth of the PMT would limit the minimum PPM slot width to ~ 9 ns while less than 1–2 ns are required to support the space-qualifiable lasers that are being considered. The anode current limit on these detectors is 2 microamperes (µA), equivalent to an incident photon flux of approximately 3×10^8 photons/second. In order to use such a device under severe background noise would require a small array (for example, 2×2) of devices. The largest drawback is the PDE, which is of the order of 8 percent.

Hybrid PMTs [83,84] are newly emerging photon counting detectors that hold considerable promise for providing efficient photon counting at 1060 and 1550 nm. Here a transmission-mode photocathode is used with a gallium arsenide (GaAs) Schottky avalanche photodiode that serves as the anode. These devices have bandwidths in excess of 1 GHz and excess noise as low as 1.023.
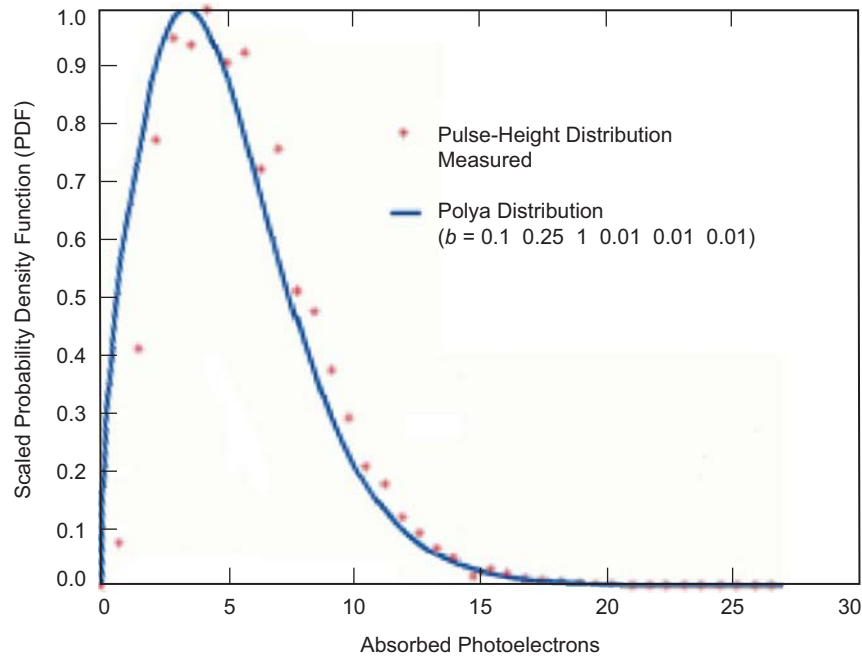
Fig. 6-58. A Polya-distribution function fitted to a measured PMT histogram. The parameter *b* is a free-fitting parameter representing a figure of merit of the uniformity of emission from the photocathode and subsequent dynode surfaces. A *b* of 0 would represent nearly perfect Poisson emission characteristics; deviation from *b* = 0 represents non-uniformity.

The internal gain occurs in two steps. The primary photoelectrons are accelerated by a high voltage (8 kV) and produce secondary photoelectrons by impact ionization with a gain of approximately 1000–1500. Subsequently, the anode provides an avalanche photodiode (APD) gain stage of about 10. These internal gains are sufficient to provide photon-counting sensitivities. The dark current can be reduced by cooling of the device. These devices are manufactured by Intevac Inc., Santa Clara California. They hold considerable promise of providing PDEs in the range of 30–40 percent at 1064 nm with the use of an InGaAsP photocathode.

6.2.1.3.2 Avalanche Photodiodes (APDs). Avalanche photodiodes are mature devices for many applications and typically operate under a bias voltage to provide high internal gain. The underlying device theory for APDs is treated in several text books [85,86] and is not treated here. Experimental work relevant to the use of APDs for deep space communications links has been reported [87]. These devices were limited by the Webb + Gaussian model and fall short of providing photon counting sensitivities.

More recently, visible light photon counters (VLPCs, manufactured by DRS Inc. of Anaheim, California) [87] have emerged as very high PDE photon-number devices that would be ideally suited for supporting deep space optical links. The only drawback of these devices is that their spectral response is very poor at 1064 nm. One drawback of these detectors is that they have to operate at cryogenic temperatures ranging from 6 to 8 K. Notwithstanding this drawback, if the spectral response could be extended into the near-infrared, they would prove attractive.

A GMAPD tailored for use with an array of smaller diameter (80 cm) apertures is underway at Lincoln Laboratories [88]. These detectors have PDEs of 45 percent and dark currents of the order of 50 kilocounts per second (kcps) at 290 K. The dead time on these detector elements is of the order of 1.6 µs. The planned implementation of these GMAPDs will utilize an array optically coupled to the collecting aperture with a lenslet array [74]. Refresh times of the order of 1 µs are considered possible for these detectors.

6.2.1.3.3 Detector Summary. In summary, it is appropriate to report that the planned upcoming deep space optical communications demonstration [72] has spurred the development of photon counting detectors [89,90] for deep space optical communications. In the next few years reports of progress on these developments should become available. Furthermore, the developments are expected to be ongoing since detectors that meet all the requirements discussed above will go a long way toward rendering optical communications links from deep space reliable and robust under the severe background contamination conditions that are expected to prevail for significant durations. These detectors will also be able to provide very high performance during the remaining duration when significantly reduced backgrounds are encountered.

6.2.2 Focal-Plane Detector Arrays for Communication Through Turbulence
Victor A. Vilnrotter and Meera Srinivasan

6.2.2.1 Introduction. Ground-based reception of optical signals from space suffers from degradation of the optical phase-front caused by atmospheric turbulence. This leads to a reduction in the effective diameter of the receiving telescope, and to random fluctuations of the receiver's "point-spread function" (PSF) in the focal plane. For example, the diffraction-limited FOV of a receiving telescope can be taken to be approximately $\theta_{dl} \cong \lambda / D_R$ which, for a 3-m aperture and 1-µm wavelength translates to 0.33 µrad. If the effective focal length of the telescope is 6 m, then a diffraction-limited PSF of 2 µm diameter, or 0.002 mm, will be produced in the focal plane. Thus, under ideal conditions, a very small detector could be used to collect virtually all of the signal energy, while at the same time spatially filtering out most of the background radiation.

However, atmospheric conditions rarely permit diffraction-limited operation of large telescopes. Even under "good" seeing conditions, the phase of the received signal field tends to become uncorrelated over distances greater than 20 cm, deteriorating to as little as 2–4 cm during the day [91]. Under these conditions, the dimensions of the PSF in the focal-plane tend to increase inversely with coherence length, as if the diameter of the collecting aperture were correspondingly reduced: the telescope still collects all of the signal energy propagating through its physical aperture, but the collected signal energy is now re-distributed onto a much larger spot in the focal-plane. An example of the increase in the effective dimensions of the receiver's PSF over its diffraction-limited value is shown in the contour plots of Fig. 6-59, obtained from a simulation using Kolmogorov phase-screens corresponding to 1-m telescope diameter and 4-cm atmospheric coherence length. For this example, the dimensions of the diffraction-limited PSF correspond roughly to a single pixel of the 16×16 detector array shown superimposed on the signal distribution.

In order to collect all of the signal energy, the dimensions of a single optical detector must be made large enough to encompass the degraded PSF as well as its random excursions in the focal-plane, which tend to change on time-
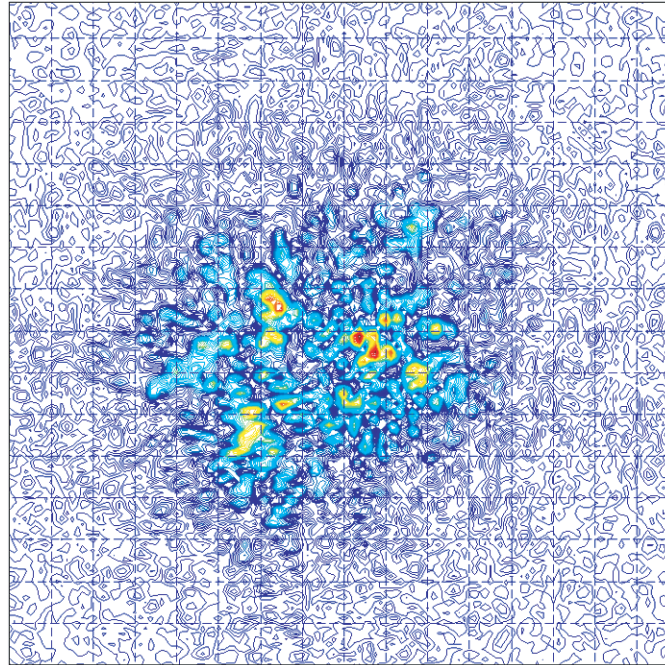

Fig. 6-59. Contour plot of instantaneous focal-plane signal distribution (covering 16×16 detector array) due to atmospheric turbulence, 4-cm coherence length, 45×45 μrad FOV.

scales of 10–100 ms. However, a large detector implies a large receiver FOV, which in turn implies a corresponding increase in the amount of background radiation admitted into the receiver. That, in turn, degrades communications performance. These problems are effectively mitigated by the use of a photon-counting detector array together with high-speed digital electronics capable of performing the signal-processing functions required for optimum or near-optimum detection.

6.2.2.2 Optical Direct Detection with Focal-Plane Arrays. In the following analyses we shall assume that a "multimode" assumption can be applied to both the signal and background fields. It has been shown that multimode Gaussian fields with suitably small average modal noise count generate approximately Poisson-distributed random point processes at the output of an ideal "photon-counting" detector [64]. This model is reasonable for communications systems operating even at mega-bit per second (Mbps) rates, and it justifies the use of the relatively simple Poisson model which, in turn, often leads to mathematically tractable solutions.

6.2.2.2.1 Single-Detector Model. Suppose that a single-detector element "measures" the number of photons contained in the received field by producing a stream of free electrons at its output terminal in response to the absorbed photons. If the occurrence-time of each pulse can be measured, and if the amplitude of each pulse is normalized to unity, then we can define a count accumulator function $N(t)$, consisting of positive integer-valued jumps occurring each time a photon is detected. As in [92], we can associate a conditional sample-function density with the detected process, conditioned on the intensity function $\lambda(t)$, defined as

$$
p[N(t)\,|\,\lambda(t); 0 \le t < T] = \begin{cases} \exp\left(-\int_0^T \lambda(t)\,dt\right); & N(T) = 0 \\[2em] \left[\displaystyle\prod_{i=0}^{N} \lambda(w_i)\right] \exp\left(-\int_0^T \lambda(t)\,dt\right); & N(T) \ge 1 \end{cases}
\tag{6.2-1}
$$

where the set $\{w_i\}$ is the occurrence times of the detected photons, and $N(t)$ is the count accumulator function of the process over the time-interval [0,T). If instead of just a single detector, an array of detectors were used to detect the optical fields, then the notation must be suitably generalized to enable unambiguous description of the output of each detector element.

6.2.2.2.2 Array Detector Model. Consider a rectangular array of detectors consisting of $K \times L$ detector elements. For some applications, such as finding the "center" of the signal intensity distribution, it is important to know the

location of each detector element within the array; therefore, we include the subscripts mn, $1 \leq m \leq K$, $1 \leq n \leq L$, to denote the position of the detector element within the array. Thus, the sample function density defined in Eq. (6.2-1) can be written as $p[N_{mn}(t) | \lambda_{mn}(t); 0 \leq t < T]$, which now represents the output of a particular element of the array. Assuming that each array element observes the sum of a signal-field plus multimode Gaussian noise-field with average noise-count per mode much less than one, the array outputs can be modeled as conditionally independent Poisson processes, conditioned on the average signal intensity over each detector element [64,93]. Hence, we denote the joint conditional sample function density of the array as

$$p\left[\mathbf{N}(t) | \lambda(t); 0 \leq t \leq T\right] = \prod_{m=1}^{K} \prod_{n=1}^{L} p\left[N_{mn}(t) | \lambda_{mn}(t); 0 \leq t < T\right] \quad (6.2\text{-}2)$$

where $\mathbf{N}(t) \equiv (N_{11}(t), N_{12}(t), \ldots, N_{KL}(t))$, and each component on the right-hand-side is of the form defined in Eq. (6.2-1).

6.2.2.2.3 Hypothesis Testing for Poisson Processes. Consider M-ary pulse-position modulation (PPM), in which a signal pulse of duration τ seconds is transmitted in one of M time-slots, resulting in a PPM symbol of duration $T = \tau M$ seconds, after which the receiver attempts to determine the correct symbol based on observations of the array of count accumulator functions over each of the M time slots. It is assumed that the symbol boundaries are known and that the arrival time of each detected photon and total number of detected photons can be stored for a limited duration of time necessary for processing. Under the i-th hypothesis, the integrated intensity over the mn-th detector element is given by

$$\lambda_{mn}^{(i)}(t) = \begin{cases} \lambda_{s,mn}(t) + \lambda_b & (i-1)\tau \leq t < i\tau \\ \lambda_b & \text{else} \end{cases} \quad (6.2\text{-}3)$$

where $\lambda_{s,mn}(t)$ is the received signal intensity function for the mn-th detector element, often assumed to be constant over the i-th slot duration, and λ_b is the background intensity per detector element. Suppose that each of the M messages is equally likely to be transmitted with probability M^{-1}, and that each message generates a unique vector of detector array intensities at the receiver, denoted by $\boldsymbol{\lambda}^{(i)}(t) = \left(\lambda_{11}^{(i)}(t), \lambda_{12}^{(i)}(t), \ldots, \lambda_{KL}^{(i)}(t)\right)$. At the end of T seconds, the post-detection processor selects that message corresponding to the greatest probability of having been received. Equivalently, the decoder selects the

message corresponding to the greatest "log-likelihood" function, $\Lambda_i(T)$, conditioned upon the signal occurring in the i-th time-slot:

$$
\begin{aligned}
\Lambda_i(T) &= \ln\left\{ p\left[\mathbf{N}(t) \mid \boldsymbol{\lambda}^{(i)}(t); 0 \le t < T \right] \right\} \\
&= \sum_{m=1}^{K} \sum_{n=1}^{L} \ln\left\{ p\left[N_{mn}(t) \mid \lambda_{mn}^{(i)}(t); 0 \le t < T \right] \right\} \\
&= \sum_{m=1}^{K} \sum_{n=1}^{L} \left(-\int_{(i-1)\tau}^{i\tau} \lambda_{mn}^{(i)}(t)\, dt + \sum_{w_{j,mn} \in ((i-1)\tau, i\tau]} \ln \lambda_{mn}^{(i)}\left(w_{j,mn} \right) \right) \\
&\quad + \left(\text{terms that depend only on } \lambda_b \right)
\end{aligned}
\tag{6.2-4}
$$

where $w_{j,mn}$ is the occurrence time of the j-th photon over the mn-th detector element within the same time-slot. By expressing the total intensity over the i-th time-slot as

$$
\lambda_{mn}^{(i)}(t) = \lambda_b \left(1 + \frac{\lambda_{s,mn}(t)}{\lambda_b} \right) = \ln(\lambda_b) + \ln\left(1 + \frac{\lambda_{s,mn}(t)}{\lambda_b} \right) \quad (i-1)\tau \le t < i\tau \tag{6.2-5}
$$

assuming constant signal intensity over the i-th time-slot, independent of the value of i, and ignoring terms that do not convey any information about the transmitted symbol, the log-likelihood function reduces to

$$
\begin{aligned}
\Lambda_i(T) &= \sum_{m=1}^{K} \sum_{n=1}^{L} \left\{ \sum_{w_{j,mn} \in ((i-1)\tau, i\tau]} \ln\left(1 + \frac{\lambda_{s,mn}\left(w_{j,mn} \right)}{\lambda_b} \right) \right\} \\
&= \sum_{m=1}^{K} \sum_{n=1}^{L} \ln\left(1 + \frac{\lambda_{s,mn}}{\lambda_b} \right) N_{mn}^{(i)}
\end{aligned}
\tag{6.2-6}
$$

where $N_{mn}^{(i)}$ is defined as the total number of photons occurring over the mn-th detector element during the i-th time-slot. Note that with constant signal intensities the actual arrival-times of photons within each slot do not contribute to the decision; hence, only the total number of detected photons, $N_{mn}^{(i)}$, matters. The optimum detection strategy is to select the symbol corresponding to the greatest log-likelihood function.

6.2.2.2.4 Performance of the Optimum Detector-Array Receiver. The probability of a correct decision is just the probability that the log-likelihood function associated with the transmitted symbol exceeds all other log-likelihood functions, i.e., when the q-th symbol is sent, a correct decision is made if $\Lambda_q(T) > \Lambda_i(T)$ *for all $i \neq q$*. Denoting the logarithmic functions, or "weights," in Eq. (6.2-5) by u_{mn}, the log-likelihood function can be rewritten as

$$\Lambda_i(T) = \sum_{m=1}^{K} \sum_{n=1}^{L} u_{mn} \, N_{mn}^{(i)} \qquad (6.2\text{-}7)$$

In this form, we can see that the log likelihood function is composed of sums of a random number of weights from each detector element. The probability density of the log likelihood function is the convolution of the probability densities from each detector element, and therefore all possible combinations of sums are represented. This means that the probability masses in the convolved density are defined over all possible sums of weights from every detector element, and the probability over each point is the product of the individual probabilities contributing to that point.

Define the set of ordered numbers over which the probability density of the i-th log likelihood function takes on values as $\{\alpha_0 = 0, \alpha_1, \alpha_2, ...\}$ and let $\Pr[\Lambda_i(T) = \alpha_k \mid H_q] \equiv p_i(\alpha_k \mid H_q)$. The received symbol is decoded correctly if the sum of weights from all detector elements over the signal-slot exceed the sum of weights from every other (non-signal) slot. Taking all cases into account as in [64], and assuming equiprobable signals, the probability of correctly decoding the received symbol is given by

$$P_M(C) = P_M(C \mid H_q) = \left\{ \sum_{r=0}^{M-1} \left(\frac{1}{r+1} \right) \binom{M-1}{r} \sum_{k=1}^{\infty} p_q(\alpha_k \mid H_q) \left[p_i(\alpha_k \mid H_q) \right]_{i \neq q}^{r} \right.$$

$$\times \left[\sum_{j=0}^{k-1} p_i(\alpha_j \mid H_q) \right]_{i \neq q}^{M-1-r} \Bigg\}$$

$$\left. + M^{-1} \left\{ p_q(\alpha_0 \mid H_q) \left[p_i(\alpha_0 \mid H_q) \right]^{M-1} \right\} \right.$$

$$(6.2\text{-}8)$$

where $p_q(-)$ and $p_i(-), i \neq q$, refer to the probability densities corresponding to the signal and null hypotheses, respectively. The probability of a symbol error

is simply $P_M(E) = 1 - P_M(C)$. Note that by counting all ties as errors in Eq. (6.2-8) a lower bound on the probability of correct detection, $P_M^l(C)$, is obtained that is much easier to compute, namely

$$
\begin{aligned}
P_M(C) \geq P_M^l(C) \equiv & \sum_{k=1}^{\infty} p_q(\alpha_k | H_q) \left[\sum_{\substack{j=0 \\ i \neq q}}^{k-1} p_i(\alpha_j | H_q) \right]^{M-1} \\
& + M^{-1} \left\{ p_q(\alpha_0 | H_q) \left[p_i(\alpha_0 | H_q) \right]^{M-1} \right\}
\end{aligned}
\tag{6.2-9}
$$

leading to the following upper bound on the error probability:

$$
P_M^u(E) \equiv 1 - P_M^l(C) \geq P_M(E)
$$

6.2.2.2.5 The "Adaptive Synthesized Detector" Receiver. We observe from the preceding analysis that detectors containing much more background than signal intensity do not contribute significantly to the error probability, since the outputs of these detector elements are multiplied by weights that are close to zero. This observation suggests the following suboptimum decoder concept with greatly simplified structure:

1) List the detector elements in decreasing order of signal intensity.

2) Compute the probability of error for the first detector element plus background.

3) Compute the probability of error for the sum of signal energies from the first two detector elements (plus background for two detector elements).

4) Continue this process until the minimum error probability is reached.

Each set of detectors may be effectively considered to be a single detector, so that no weighting is applied to account for variations in the signal distribution over the detector elements included in that set. The set of detector elements that achieves the minimum probability of error is the best "synthesized single detector" matched to the signal intensity distribution. Note that this straightforward process of performing the optimization by actually calculating the error probabilities for each partial sum of detectors is not practical. Later in this paper we shall describe some practical methods for approximating this procedure.

In effect, we have partitioned the logarithmic weights into two classes: "large" weights were assigned the value one, while "small" weights were assigned the value "zero." We shall show that this simple partitioning achieves near-optimum performance in low to moderate background environments, but with greatly reduced decoder complexity.

For the "adaptive synthesized single detector," the probability of correct decision can be obtained directly from Eq. (6.2-8), by setting $\alpha_k = k$ in the probability densities, and assuming constant signal and background intensities over each time-slot, yielding

$$p_q\left(k \mid H_q\right) = \frac{\left(\lambda_s \tau + \lambda_b \tau\right)^k}{k!} e^{-\left(\lambda_s \tau + \lambda_b \tau\right)} \text{ and } p_l\left(k \mid H_q\right) = \frac{\left(\lambda_b \tau\right)^k}{k!} e^{-\lambda_b \tau} \quad (6.2\text{-}10)$$

Direct substitution of these Poisson densities into Eq. (6.2-8) yields

$$
\begin{aligned}
P_M(C) = & \left\{ \sum_{r=0}^{M-1} \left(\frac{1}{r+1}\right) \binom{M-1}{r} \sum_{k=1}^{\infty} \frac{\left(\lambda_s \tau + \lambda_b \tau\right)^k}{k!} e^{-\left(\lambda_s \tau + \lambda_b \tau\right)} \left[\frac{\left(\lambda_b \tau\right)^k}{k!} e^{-\lambda_b \tau}\right]^r \right. \\
& \left. \times \left[\sum_{j=0}^{k-1} \frac{\left(\lambda_b \tau\right)^j}{j!} e^{-\lambda_b \tau}\right]^{M-1-r} \right\} \\
& + M^{-1} e^{-\left(\lambda_s + M\lambda_b\right)\tau}
\end{aligned}
$$

$$(6.2\text{-}11)$$

where, again, $P_M(E) = 1 - P_M(C)$.

6.2.2.2.6 The Gaussian Approximation. When the array contains a large number of detector elements, the computation of the probability density of the weighted sum of Poisson random variables becomes prohibitively difficult. It is shown in reference [94] that a useful Gaussian approximation to the discrete density of the weighted sum of Poisson random variables may be derived from the characteristic function of the discrete density, leading to the following approximation:

$$
\begin{aligned}
P_M(E) = & 1 - P_M(C) \\
& \cong 1 - \int_{-\infty}^{\infty} dy \, \frac{e^{-y^2/2}}{\sqrt{2\pi}} \left\{1 - \frac{1}{2} Erfc\left(\frac{\sigma_{sb}}{\sigma_b} y + \frac{\eta_{sb} - \eta_b}{\sigma_b}\right)\right\}^{(M-1)} \quad (6.2\text{-}12)
\end{aligned}
$$

where the mean and variance of the approximating continuous random variables for signal and non-signal slots is η_{sb}, σ_{sb}^2, and η_b, σ_b^2, respectively, and where $Erfc(x) = 1/\sqrt{2\pi} \int_x^{\infty} e^{-y^2/2} dy$. In terms of the weighted signal intensities, the mean and variance are defined as

$$\eta = \sum_{m=1}^{K} \sum_{n=1}^{L} u_{mn} \, \lambda_{mn} \, \tau \ \text{and} \ \sigma^2 = \sum_{m=1}^{K} \sum_{n=1}^{L} u_{mn}^2 \, \lambda_{mn} \, \tau \qquad (6.2\text{-}13)$$

We expect this approximation to be accurate when either of two conditions are satisfied: when the average photon energies over each detector element are so high that the Poisson distribution can be well approximated by a Gaussian density (this would occur with intense background radiation), or when the conditions for the central limit theorem are satisfied. The central limit theorem applies if the average photon energies over the entire array are sufficiently similar, so that a large number of detector outputs can be considered identically distributed random variables, or when the array outputs can be partitioned into several groups of random variables, each containing a large enough number of random variables to justify the Gaussian model.

6.2.2.2.7 Performance Bounds for Poisson Detection. For the special case of binary PPM signaling, $M = 2$, the following useful form has been obtained by Hubbard [94]:

$$P_2(E) = \exp\left(-\Delta^2\right) \left\{ \sum_{k=0}^{\infty} \left(\frac{\sqrt{\lambda_b \, \tau}}{\Delta + \sqrt{\lambda_b \, \tau}} \right)^k F_k(\psi) - \tfrac{1}{2} F_0(\psi) \right\} \qquad (6.2\text{-}14)$$

where $\Delta = \sqrt{(\lambda_s + \lambda_b) \, \tau} - \sqrt{\lambda_b \, \tau}$, $\psi = 2\tau \sqrt{(\lambda_s + \lambda_b) \, \lambda_b}$, $F_k(\psi) = e^{-\psi} I_k(\psi)$, and $I_k(\psi)$ is the modified Bessel function of order k. Since for any $\psi \geq 0$ and $k \geq 0$, $I_k(\psi) \leq I_0(\psi)$, a useful upper bound to Eq. (6.2-14) can be easily constructed as

$$P_2(E) \leq \exp\left(-\Delta^2\right) \left\{ \sum_{k=0}^{\infty} \left(\frac{\sqrt{\lambda_b \, \tau}}{\Delta + \sqrt{\lambda_b \, \tau}} \right)^k - \tfrac{1}{2} \right\} F_0(\psi)$$

$$= \exp\left(-\Delta^2\right) \left(\frac{\sqrt{\lambda_b \, \tau}}{\Delta} + \tfrac{1}{2} \right) F_0(\psi) \equiv P_2(UB)$$

$$(6.2\text{-}15)$$

This upper bound on the binary PPM error probability can be further approximated in the limit of very small and very large background energies as

$$P_2(UB) \cong \begin{cases} \frac{1}{2}\exp\left(-\Delta^2\right) & \lambda_b\,\tau \ll 1 \\[4mm] \left(\dfrac{\sqrt{\lambda_b\,\tau}}{\Delta}+\dfrac{1}{2}\right)\dfrac{\exp\left(-\Delta^2\right)}{\sqrt{2\pi\psi}} & \lambda_b\,\tau \gg 1 \end{cases}$$

(6.2-16)

The binary PPM error probability and its upper bound can also be used to further bound M-ary PPM performance for the single detector case, in a manner similar to the "union bound" familiar from the "additive Gaussian noise" problem. The result is an expression of the form $P_M(E) \le (M-1)P_2(E)$. The proof, presented in [95, Appendix B], is somewhat complicated by the fact that for the optical problem the probability of committing an error when attempting to resolve ties among maximal counts must also be taken into account.

6.2.2.2.8 Comparison of Exact and Approximate Performance Calculations.
A performance comparison of the optimally weighted array receiver and the "adaptive synthesized single detector" receiver (also referred to as the "0-1" subarray in the figures) has been carried out for average background energies of $K_b \equiv \lambda_b\tau = 0.1$ and 1.0. Two different signal models were used: a simple "test" model where only 5 of the $16 \times 16 = 256$ total detector elements were assumed to contain signal energy while the rest are assumed to contain no signal, and a more realistic 16×16 detector array model where the signal distribution over the array was simulated using a Kolmogorov turbulence model as described in [96], and all 256 detector elements may contain some signal.

For the test model the proportions of the total average absorbed signal energy $K_s \equiv \lambda_s\tau$ over the five detector elements were assumed to be (1.0, 0.3, 0.2, 0.05, and 0.02). Equation (6.2-8) was evaluated using this model, and compared with results obtained via Monte-Carlo simulations. The results are shown in Fig. 6-60 as a function of the total average absorbed signal energy K_s. It is evident that optimal weighting (represented by large squares) yields somewhat better performance than the suboptimum "0-1 subarray" computed according to Eq. (6.2-11), and that greater improvements occur at greater background intensities: however, the improvements due to the significantly more complicated optimally weighted array are only about 0.3 dB at an error probability of 0.001 for the high background case.

The reason for using only five detectors in the examples of Fig. 6-60 is that convolving more than five weighted Poisson densities rapidly becomes prohibitively difficult due to excessive demands on computer memory. Therefore, only this "five-detector" example could be evaluated computationally through the use of the bound on the probability of correct
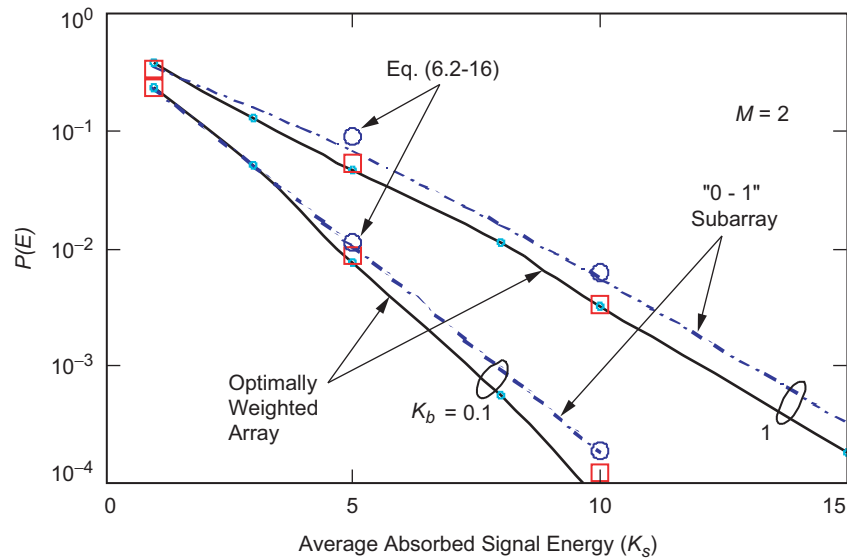
Fig. 6-60. Performance of optimally weighted array and adaptive "zero-one" subarray, binary PPM.

detection defined in Eq. (6.2-9), and only for background intensities not exceeding an average of 2 photons per detector per slot. Note the excellent agreement between the calculated error probabilities for the "0-1" subarray case and the approximate upper-bound of Eq. (6.2-16), represented by the large circles in Fig. 6-60 at average signal energies of 5 and 10 photons.

In Fig. 6-61, a realistic spatial distribution of the signal intensity over the focal-plane was generated using Kolmogorov phase-screens. Monte-Carlo simulations were performed to evaluate the error probability for the optimally weighted array. The "Gaussian" approximation to the error probability defined in Eq. (6.2-12) has also been evaluated for the binary PPM case, $M = 2$, with average background energies (per detector element) of $K_b \equiv \lambda_b \tau$ equal to 0.1, 1, and 5 photons/time-slot, as a function of the total average signal energy. It can be seen that the Gaussian approximation is close to the exact values obtained from Monte-Carlo simulation, and that good agreement is obtained even for small background energies per detector element, as direct comparison with the simulation results (large diamonds) indicates. In fact, it appears that this Gaussian approximation provides useful results over the entire range of background and signal energies represented in Fig. 6-61. The performance of the "0-1" subarray is also shown as the dashed curves: as expected, performance is somewhat worse than that of the optimally weighted array, but not significantly so.
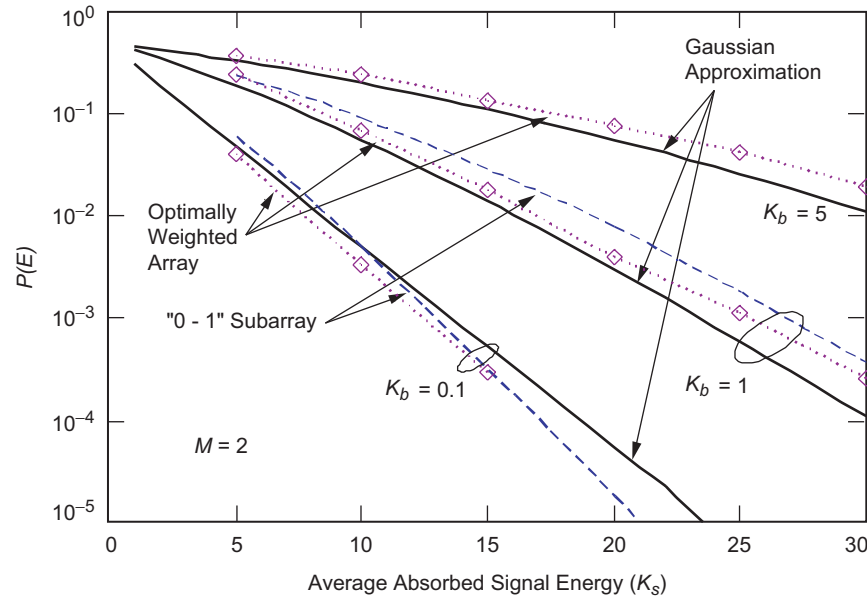
Fig. 6-61. Exact error probabilities, Gaussian approximations to the weighted sum, and simulation results for the "realistic" signal distribution described in 6.2.2.3 Numerical Results.

6.2.2.3 Numerical Results

6.2.2.3.1 Performance of Optimally Weighted Array. Both analytical calculations and Monte-Carlo simulations were performed in order to obtain PPM error probabilities for the "adaptive synthesized single detector" subarray. Performance of the optimally weighted array receiver was obtained from simulations: for each PPM symbol, M Poisson random variables with the proper statistics were generated, the optimum weights were applied, and the symbol corresponding to the largest observable selected. Simulated turbulence-degraded signal distributions were generated over the 16×16 detector array for all subsequent results. With no loss in generality, the transmitted symbol was always assumed to be the one corresponding to a signal pulse in the first slot. The detection process was repeated a large number of times (until 100 errors were accumulated) and repeated for increasing average signal energy with various background levels. Figure 6-62 shows the results of this simulation for $M = 2$, 16, and 256. The probability of bit error is shown as a function of the receiver's "photon efficiency," ρ, which is a measure of the average number of bits of information carried by each absorbed photon. It can be seen that with background levels of 0.1–1.0 photons per slot, $\rho = 0.3 - 0.5$ bits/photon can be
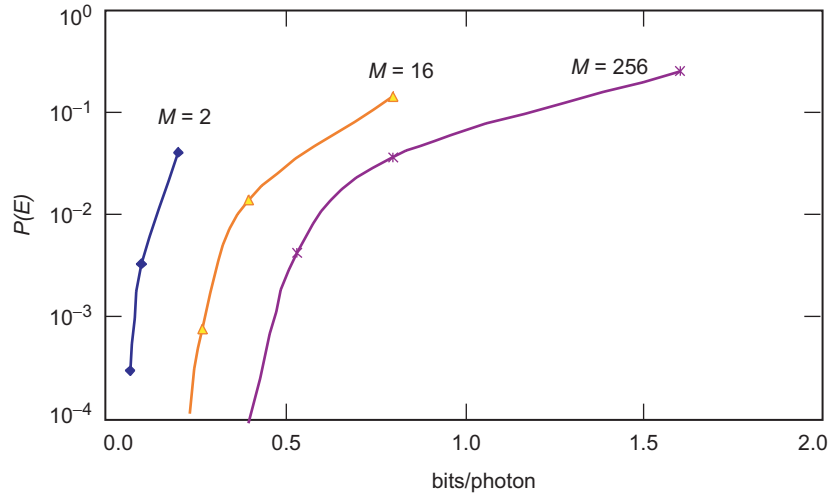
Fig. 6-62. Simulated PPM bit-error probability of optimum array receiver as a function of "photon efficiency" ρ (bits/photon), $K_b = 0.1$.

achieved with 256 PPM signaling at uncoded symbol error probabilities around 0.001–0.01.

6.2.2.3.2 Performance of "Adaptive Synthesized Single Detector" Receiver.
In order to generate a spatial distribution of the signal incident upon the detector plane, a sample field was generated using a "Kolmogorov phase-screen" program [96], resulting in a matrix of complex signal amplitudes. For the simulation, an atmospheric correlation length of $r_0 = 4$ cm was assumed, which implies that the results should apply to any receiving aperture that is much greater than this correlation length [91]. The field intensity generated in the detector plane by the simulation is then integrated over the elements of a 16×16 detector array, which is assumed to encompass the extent of the signal distribution in the detector plane. Detector signal intensities are normalized so that for the *mn*-th detector we obtain an average number of absorbed signal photons of $\lambda_{s,mn}\tau$. A constant average background photon energy of $\lambda_b\tau$ is assumed over each detector element.

For a given sample function of the intensity distribution, the $16 \times 16 = 256$ detector elements were sorted in decreasing order of average signal energy, and *M*-ary PPM symbol error probabilities were calculated for increasing numbers of detectors, starting with the first detector, using Eq. (6.2-11). The lowest curve in Fig. 6-63 shows the symbol error probability for binary PPM ($M = 2$) as a function of the number of detector elements used, for the case $K_s = 10$ and $K_b = 0.1$ (that is, total average signal photons absorbed by the entire array is 10, and the average number of background photons *per detector element* is 0.1).
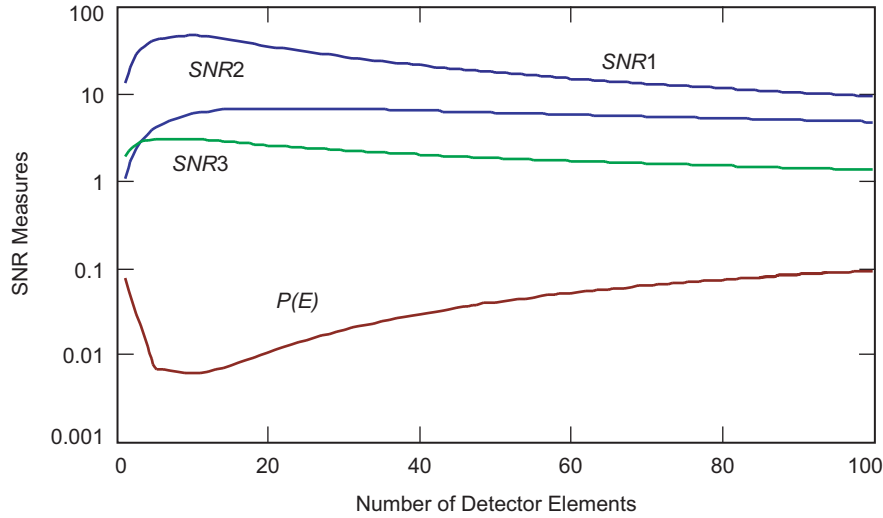
**Fig. 6-63.   Comparison of the optimum number of detector elements
predicted by the three SNR measures.**

It can be seen that for this case the smallest error probability of 0.0049 is achieved by assigning unity weight to the first 15 detector elements containing the greatest signal intensities, and zero to all the rest.

In Figs. 6-64 and 6-65, binary PPM symbol error probabilities are shown as a function of total average number of absorbed signal photons for four cases:

1)   When the optimum number of "0–1" weighted detector elements are used,

2)   When simulating the optimally weighted array,

3)   When all 256 detector elements are given unity weight (synthesizing a large, nonadaptive single detector element), and

4)   When an ideal "adaptive optics" system succeeds in concentrating all of the available signal energy into a single detector element, which then is the only detector element that is observed.

Using the same focal-plane signal distribution as before, error probabilities were computed for average background photon counts of 0.1 and 1.0, shown in Figs. 6-64 and 6-65, indicating performance gains by the "adaptive synthesized single detector" over a single "large" non-adaptive detector of 2 and 2.8, respectively, at an error probability of 0.001, corresponding to 3 dB and 4.5 dB of performance improvement. Note the excellent agreement of the approximation of Eq. (6.2-16) (large circles) with the computed values. When compared to the ideal "adaptive optics" receiver that concentrates all of the collected signal energy in a single element of the array, the gains are 3.8 and 8.2, corresponding to 5.9 dB and 9.1 dB of improvement. Note that the optimal weighted array yields only about 0.3 dB improvement over the optimized "0–1"

subarray at a symbol error probability of 0.001, even with relatively high background energy of $K_b = 1$.

Fig. 6-64. Binary error probability of "large single detector," optimally weighted array, optimized "0–1" subarray, and single detector element with ideal adaptive optics: $M = 2$, $K_b = 0.1$.
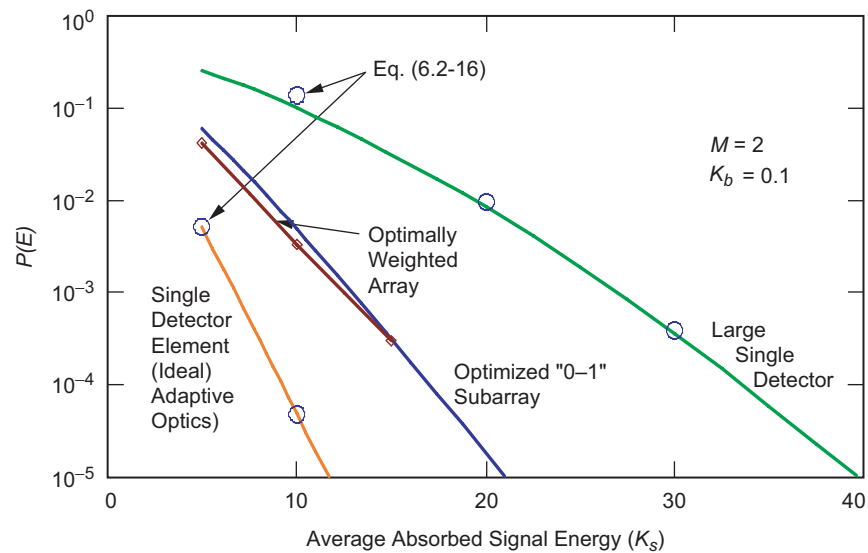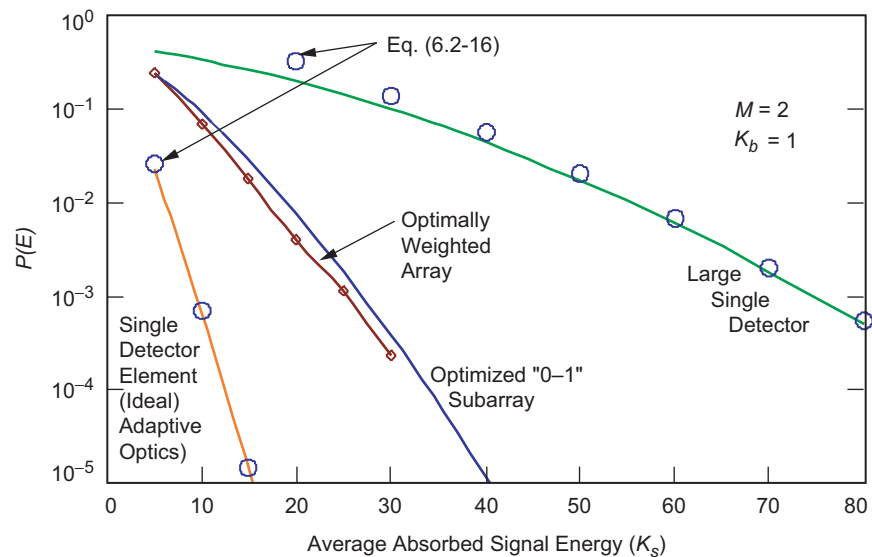

Fig. 6-65. Binary error probability of "large single detector," optimally weighted array, optimized "0–1" subarray, and single detector element with ideal adaptive optics: $M = 2$, $K_b = 1$.

Similar gains are evident in Fig. 6-66, which represent the symbol error probability, $P(SE)$, of the optimized subarray observing 16-dimensional ($M = 16$) PPM. The accuracy of the "union bound" evaluated for the case $\lambda_b \tau \gg 1$ is evident (large circles), especially at the lower error probabilities.

Performance improvements were also obtained for several different focal-plane distributions at an average background energy of one photon per detector per slot, in order to verify that the above results were typical. Numerical results have shown that three out of four simulations yielded performance comparable to that of Fig. 6-65, requiring approximately 26 signal photons to achieve an error probability of 0.001 while utilizing 9 to 13 elements of the array in the region of error probabilities examined. One of the phase-screen simulations yielded an unusually favorable signal distribution that achieved optimum performance with only 4 detector elements, but still needed roughly 22 signal photons for 0.001 error probability. We can conclude, therefore, that for different distributions generated using the same atmospheric and receiver parameters, similar receiver performance is obtained; hence it is reasonable to use a "representative" signal distribution for the subsequent numerical analysis. Note that as more detector elements are used the performance tends to deteriorate, since a greater amount of background energy is collected by the receiver.

6.2.2.4 Summary and Conclusions. The problem of improving the performance of ground-based optical receivers through the use of photon-
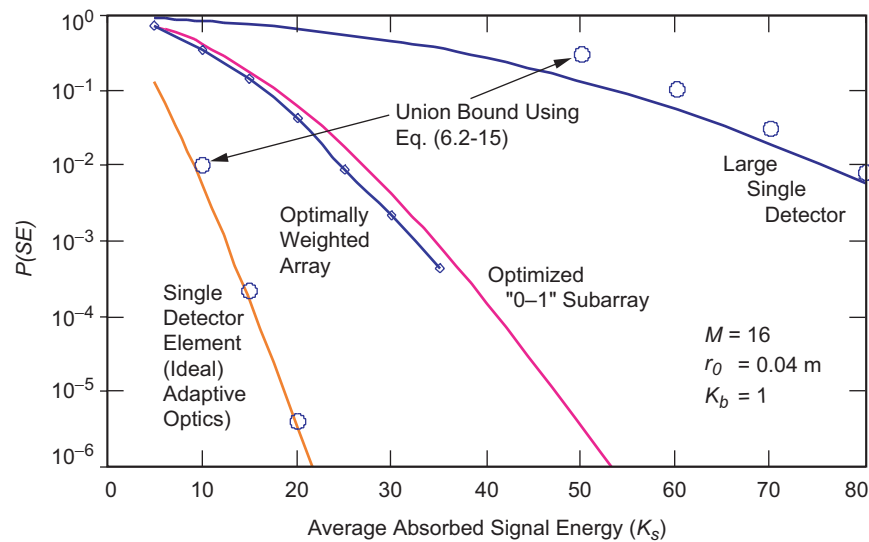

Fig. 6-66. Error probability of "large single detector," optimally weighted array, optimized "0–1" subarray, and single detector element with ideal adaptive optics: $M = 16$, $K_b = 1$.

counting detector arrays together with optimum signal processing algorithms has been addressed. The optimum array detection algorithm was derived, and a simpler suboptimum structure based on the optimum algorithm was also defined. Exact and approximate expressions for the error-probability performance of these structures were derived, and simulations were carried out to verify the analytic performance calculations. Realistic sample-functions of turbulence-degraded focal-plane signal distributions were generated using the Kolmogorov phase-screen algorithms described in [96], corresponding to moderate daytime turbulence (coherence-length of 4 cm), and used to evaluate the performance of optimum and suboptimum array detection algorithms designed for PPM signals. Performance improvements of up to 5 dB were demonstrated over a single "large" detector designed to collect most of the turbulent signal, when operating in the presence of moderate to strong background radiation. The use of "ideal adaptive optics" in front of the detector, which concentrates most of the signal energy into a single detector element, was evaluated and found to provide approximately 3 dB of additional improvement at an error probability of 0.001. It was shown that in cases of interest, the simpler suboptimum detector array algorithm performs nearly as well as the optimal array, with considerable savings in computational complexity.

6.3 Receiver Electronics

Andrew A. Gray, Victor A. Vilnrotter, and Meera Srinivasan

6.3.1 Introduction

The objective of this chapter is to describe discrete-time demodulator architectures for broadband optical pulse-position modulation (PPM) that are capable of processing Nyquist or near-Nyquist data rates. These architectures can provide numerous advantages for realizing communications demodulators in digital very large scale integrated (VLSI) circuits. The architectures are developed within a framework that encompasses a large body of work in optical communications, synchronization, and multirate discrete-time signal processing and are constrained by the limitations of the state-of-the art in digital hardware. This chapter attempts to create a bridge between theoretical communication algorithms and analysis for deep-space optical PPM and modern digital VLSI. The primary focus of this work is on the synthesis of discrete-time processing architectures for accomplishing the most fundamental functions required in PPM demodulators, post-detection filtering, synchronization, and decision processing. The architectures derived are capable of closely approximating theoretical performance of the continuous-time algorithms from which they are derived. The work concludes with an outline of the development path that leads to hardware.

This work builds on a large body of previous work in optical communications in particular *Optical Communications* by Gagliardi and Karp [97], "Design and Analysis of a First-Generation Optical Pulse-Position Modulation Receiver" by Vilnrotter and Srinivasan [98], and many others that are referenced later in this work. The focus in this work is not on the analysis of performance of optical communications systems but rather synthesis of discrete-time architectures suitable for realizing the functions of certain continuous-time processing using modern digital VLSI. The primary discrete-time signal processing building blocks are presented in this work along with preliminary performance results; the tasks required for synthesizing more complete demodulator architectures and analyzing their performance are outlined in the conclusion.

Figure 6-67 illustrates a block diagram of the optical transmitter and ground receiver system. The development path of the digital demodulator is also indicated from an oversimplified high level; a more complete description of this process is presented in the conclusion. The work presented here is one step in the development process starting from theoretical formulation and ending with implementation of the digital demodulator. Many elements of the discrete-time architectures developed here are fundamental and remain valid independent of whether or not the communications channel is radio frequency or optical, and some of these elements are derived with the intent to overcome limitations of state-of-the-art digital hardware.

The architectures are parameterized to utilize the tremendous flexibility achievable with modern digital hardware and to satisfy a large range of system requirements. System requirements play an increasingly critical role in the development as the steps in the process of Fig. 6-67 get closer to implemented hardware. Many system requirements may be met with numerous variations on discrete-time architectures developed herein. The final determination of which architecture is to be fully developed to implementation and the determination of numerous parameters are determined from specific requirements, and constrained by implementation considerations such as commercially available high-speed chips and board technology.

Next, a brief overview highlighting the objective of each section is given. Section 6.3.2 is an introduction to discrete-time architectures. The motivation for their development is discussed and includes the many advantages of implementation of signal processing using digital VLSI circuits.

Section 6.3.3 introduces discrete-time synchronization and slot filtering, and it introduces the impact of signal dynamics with fixed sample rate systems employing this processing. The motivation for fixed-phase analog-to-digital (A/D) sampling and the time-varying slot or interpolation filter is presented.

Section 6.3.4 extends the results of Section 6.3.3 to more complete demodulator models. Simplified models of demodulators are presented here, and these are extended throughout the remaining sections.
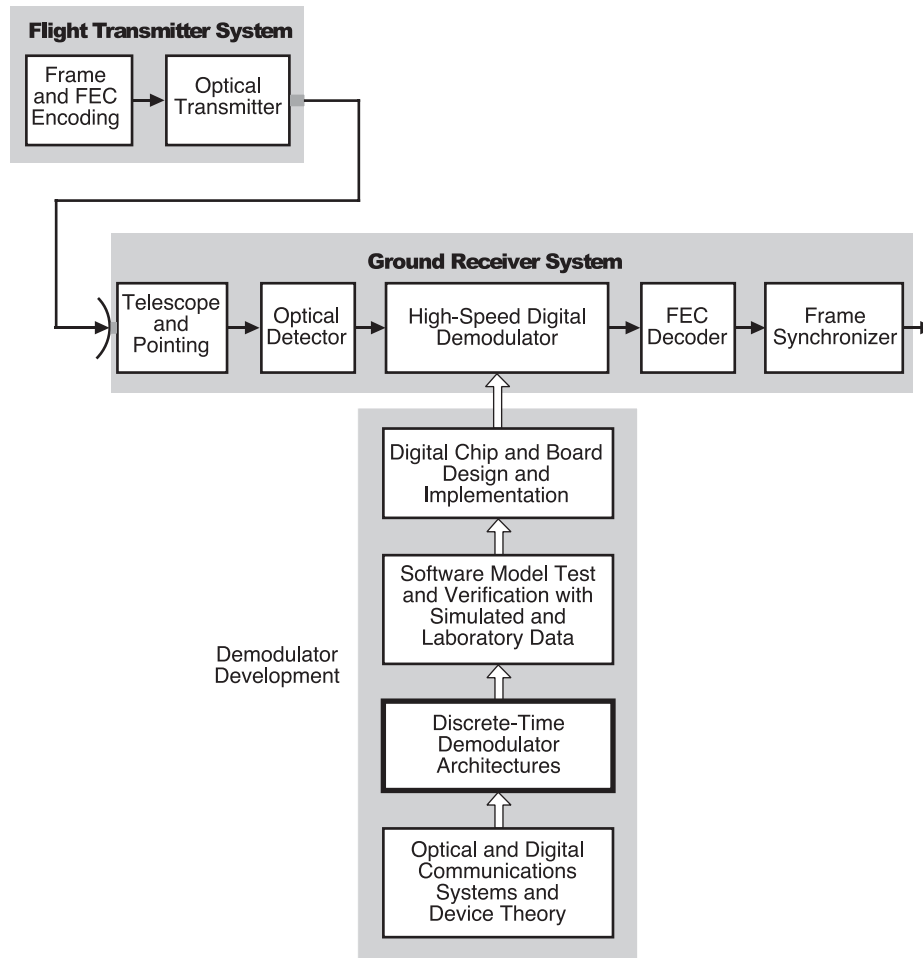
Flight Transmitter System

Frame and FEC Encoding → Optical Transmitter

Ground Receiver System

Telescope and Pointing → Optical Detector → High-Speed Digital Demodulator → FEC Decoder → Frame Synchronizer

Demodulator Development

Digital Chip and Board Design and Implementation

Software Model Test and Verification with Simulated and Laboratory Data

Discrete-Time Demodulator Architectures

Optical and Digital Communications Systems and Device Theory

Fig. 6-67. Block diagram of the system and simplified development path for the digital demodulator.

In Section 6.3.5 problems identified in Sections 6.3.3 and 6.3.4 are addressed by various signal processing methods including non-linear processing. The methods for combining post-detection filtering and correction of synchronization errors are addressed with the time-varying post-detection or interpolation filters.

Section 6.3.6 presents parallel discrete-time demodulator architectures. The serial processing results are extended to parallel or vector processing which is required to achieve the processing necessary for broadband pulses requiring very high sample rates. This parallelization is performed on the core processing of slot synchronization and post-detection filtering. Symbol synchronization

and other demodulator algorithms are not explicitly addressed here but are considered much more straightforward to design in discrete-time.

In Section 6.3.7 asynchronous discrete-time processing is addressed. The fixed-rate processing of a signal that contains modulated data with a rate that is asynchronous to the sample and system clocks creates significant challenges, specifically asynchronous digital design and implementation. The asynchronous processing is shown to create particular challenges for the parallel architectures.

Section 6.3.8 introduces representative discrete-time architectures derived using the methods, framework, and signal processing designs developed herein. In this section we use generic parallel discrete-time algorithms and methods developed earlier and existing in the literature to synthesize specific designs that incorporate capability for trading processing rate with complexity. The performance of a software model of a receiver architecture is given that includes a simplified model of the optical channel. While the demodulator architectures presented are not complete, they encompass many required functions, and the evolution to more complete architectures is presented in brief.

Section 6.3.9 presents system models along with certain design/ implementation equations. Frequency and digital transmission line models are presented. The parallel discrete-time demodulator is described in terms of bandwidth and clock rates. This model is useful in establishing specific design parameters of the parallel digital demodulator and implementation platform from requirements such as data rates, PPM pulse bandwidth, and other requirements. The transmission line model is useful for high-speed digital platform design by establishing the primary input/output (I/O) requirements on the implementation platform.

In Section 6.3.10 the conclusion is presented that provides an overview of the work presented and indicates the next steps in the development of a broadband hardware implementation. These steps encompass discrete-time design and analysis, extensive software modeling and simulation, and hardware design tools and methods and realization. The conclusion includes an overview of the state-of-the art processes that lead to implementation in modern VLSI platforms and devices. Parts of this process are derived from targeting VLSI implementation in field programmable gate arrays (FPGAs). These devices have in many instances enabled improved development strategies of complex VLSI systems, reducing development risk while facilitating more aggressive schedules and development processes. The development process proposed incorporates extensive use of a variety of software models and tools, some of which are generic and used for system and subsystem validation and others that are device specific. Modern communications systems, such as the one developed here, are generally beyond any type of comprehensive closed-form analytical analysis or performance evaluation and rely extensively on Monte-

Carlo simulation. However, as part of the process, illustrated analytical models and bounds are used extensively to validate various subsystem performances.

6.3.2 Introduction to Discrete-Time Demodulator Architectures

Receivers are arguably the most complicated processing element (hardware or software) in a communications system. Modern digital receivers must be flexible enough to process parameterized modulation schemes, pulse shapes, and data rates. Receiver complexity is directly related, although not necessarily linearly, to the complexity of the modulation type used in the system. Many modulations developed for optical communication are complex, with some so complicated that it may be impractical to implement them in hardware. The PPM modulation was selected for this monograph because it appears to be the modulation of choice for most future deep-space optical satellite communications systems. In addition, the demodulator architectures developed are based on the assumption of single-symbol decision processing, as opposed to symbol decisions that are based on maximum-likelihood sequence detection [99,100]. However, the demodulator may process input signals to generate soft symbols at the output of the post-detection filter that may be further processed by a forward error correction decoder (maximum-likelihood sequence decision processing).

With the availability of VLSI technology, coupled with the flexibility of discrete-time signal processing algorithms, it is very desirable to implement receivers with as much digital processing capability as possible [101]. Dynamic range in filter bandwidths of greater than 8 orders of magnitude is feasible, and similar flexibility exists with other processing functions when implemented in modern digital circuits. In addition, an all-digital demodulator implemented using complementary metal oxide semiconductor (CMOS) technology has great advantages in size and reliability and greatly reduced reproduction costs over analog demodulators as well as other digital technologies [102,103]. The number of options for realizing digital VLSI circuits is extensive, and ranges from many FPGAs, commercially available digital signal processors (DSPs), and applications specific circuits (ASICs). FPGAs in particular have increased the flexibility of high speed digital processing, with large scale reconfiguration of VLSI possible with relatively rapid design cycles.

Often the only true limitation to the data rates an all-digital demodulator can process is the A/D converter. However, conventional CMOS digital demodulators currently have substantially lower clock rates than the fastest commercially available A/D converters. In such a high rate system, the minimum number of samples required for discrete-time processing, the Nyquist rate, is required to process the maximum data rate possible, the Nyquist data rate. Because commercially available CMOS hardware generally has lower clock rates than the fastest A/D converters, CMOS digital demodulators using

traditional serial algorithms for digital communications process data rates many times lower than the maximum Nyquist data rate. The rate difference motivates the development of parallel processing architectures.

It should be noted that, strictly speaking, there is no such thing as an all-digital receiver. There is always some analog processing for the optical-to-digital conversion, typically accomplished by optical-to-electrical (analog) and then conversion to a digital signal. For the purposes of this work, the definition of an *all-digital demodulator* is such that the modulated optical waveform is detected and converted to an analog current and then voltage signal. This voltage is sampled, and then the demodulator functions of post-detection filtering, symbol-decision processing, synchronization (including slot-timing and symbol recovery for PPM), and symbol-to-bit conversion are performed using exclusively digital processing. The continuous-time A/D clock phase and frequency are not adjusted using feedback from the digital demodulator. There are many other functions of a demodulator that, although necessary, will prove more trivial to implement and are not dealt with in this work. These functions include slot and symbol-synchronizer lock detection, power estimation, error-control decoder preprocessing, and others. Here we derive discrete-time architectures for realizing the primary demodulator functions using known continuous-time processing, acknowledging that the processing utilized in a demodulator and the performance obtained are highly dependant on the optical channel used in the system. In the architecture development, we place particular emphasis on the two greatest and related challenges of a Nyquist data rate digital implementation, Nyquist rate sampling of communications signals and very high rate (bandwidth) processing.

6.3.3   Discrete-Time Synchronization and Post-Detection Filtering Overview

The PPM slot and symbol synchronization, post-detection filtering of the input signal, and symbol decision processing form the core of the optical PPM satellite-communications receiver. Synchronization and post-detection filtering are often thought of as separate operations; however, we shall demonstrate here that they may be combined in an intuitive way to create time-varying discrete-time filter architectures. Furthermore, these architectures are well suited for and motivated by all-digital implementation.

The post-detection filter is a specified operation that is used to process the received signal in a precise time-synchronized fashion. The incoming waveform or received signal is often convolved with the post-detection filter, although there are other types of processing employed depending on the system [97]. In the development of the discrete-time architecture here we assume that the incoming sampled waveform is convolved with a post-detection filter. The waveform analysis is greatly simplified and ignores the statistical nature of the

signal at the output of the optical detector. This simplified analysis should be thought of as a conceptual tool to reveal many fundamental elements of the parallel processing discrete-time architecture design that are largely independent of the statistical nature of the input signal even if the channel is radio frequency or optical. This approach results in a general architecture for accomplishing time-synchronized processing that encompasses or is readily extended to other processing that does incorporate the detailed nature of the input signal. Regardless of the post-detection filter coefficients (or even if it is not a linear filter/convolution, e.g., threshold processing), precise time synchronization of the required signal processing in the presence of signal dynamics is generally required. Understanding the implications and properties of this precise time synchronization with Nyquist or near-Nyquist sampling motivates much of the discussion and analysis here; this understanding is critical in developing discrete-time demodulator architectures for Nyquist data rates. The results of this section are used in Section 6.3.8 to develop architectures with generalized slot-synchronization and post-detection filtering.

6.3.3.1 Discrete-Time Post-Detection Filtering. In the generic digital communications transmitter, baseband bits are mapped to modulation symbols, A_k. The transmit pulse shape is give by $p(t)$. The output of the transmitter is then

$$Q(t) = \sum_{k=-\infty}^{\infty} r_k p\left(t - kT_{sym} - A_k T_{slot} + \phi_k\right) \qquad (6.3-1)$$

Here T_{sym} is the symbol period, T_{slot} is the slot period, r_k represents the intensity variations, and ϕ_k is a timing jitter sequence [104]. The timing jitter and intensity variation terms will be excluded from the simplified analysis and discussion here. As example, consider the 8-PPM signal set in Fig. 6-68:
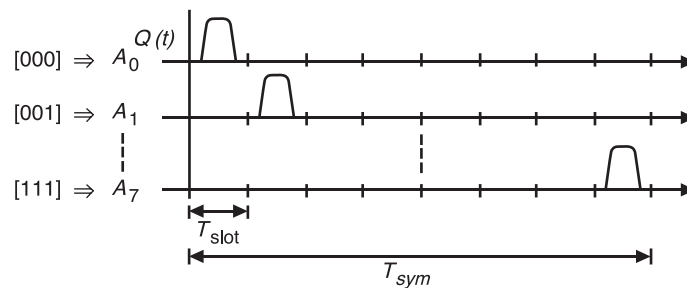

Fig. 6-68. Example PPM symbol set.

Transmitting the signal $Q(t)$ through a linear noiseless channel with impulse response, $b(t)$, will result in a received signal

$$R(t) = \int_{-\infty}^{\infty} b(\tau) \sum_{k=-\infty}^{\infty} p\Big(t - kT_{sym} - A_k T_{slot} - \tau\Big) d\tau \qquad (6.3\text{-}2)$$

This can be rewritten as

$$R(t) = \sum_{k=-\infty}^{\infty} h\Big(t - kT_{sym} + A_k T_{slot}\Big), \quad h(t) = \int_{-\infty}^{\infty} b(\tau) p(t-\tau) d\tau \quad (6.3\text{-}3)$$

where $h(t)$ is the received pulse. The result of the continuous-time input filtered with some post-detection filter is then

$$y(t) = \int_{-\infty}^{\infty} R(t-\tau) f(t) d\tau \qquad (6.3\text{-}4)$$

Where the filter $f(t)$ may be designed from some optimality criteria or criterion derived for the optical channel. Here we derive the time-varying slot filter assuming a classical matched filter approach common in radio-frequency communications; this derivation will illustrate fundamental problems with discrete-time synchronization for which architectures are then designed to solve. The post-detection filter peak SNR or optimal output is obtained by sampling at the slot rate,

$$y_M(n) = y\Big(T_{slot}n\Big) \quad n = 1,2,3... \qquad (6.3\text{-}5)$$

It should be noted that in an operational wireless communications system with channel noise, including timing jitter, the desired signal or sample is generally not obtained, but some estimate or approximation is. For example, with jitter ϕ_k that varies from one pulse to the next, the optimal sample estimate $\hat{y}_M(n)$ will generally not equal the true optimal sample point, $\hat{y}_M(n) \neq y_M(n)$. If the system is designed properly, the estimate of the optimum sample (or samples) will have zero average error assuming there are no other unaccounted for dynamics or signal distortions and it is an unbiased estimator [105,106,107]. We progress assuming no jitter in the input signal so as to derive necessary fundamental concepts in a simplified fashion, but it must be understood that the slot synchronization algorithm design should average the effects of jitter and other channel noise sources in such a way that an unbiased estimate of timing offset is obtained and then corrected for. For a discrete-time demodulator system with sample period T_s,

$$h_d(n) = h\left(T_s n + \Delta t_R\right) \qquad\qquad (6.3\text{-}6)$$

$$f_d(n) = h\left(-T_s n - \Delta t_M\right) \otimes K\left(T_s n\right) \qquad\qquad (6.3\text{-}7)$$

$$R_d(n) = \sum_{k=-\infty}^{\infty} h_d\left(n - kT_{sym} + A_k T_{slot}\right) \qquad\qquad (6.3\text{-}8)$$

$$y_d(n) = \sum_{k=-\infty}^{\infty} R_d(k) f_d(n-k) \qquad\qquad (6.3\text{-}9)$$

Here Δt_R is the time offset of the received signal $h_d(n)$ and Δt_M is the time offset of the post-detection filter $f_d(n)$. In general, for $f_d(n)$ to have equivalent performance to the continuous-time post-detection filter the following condition must be met, $\Delta t_M = \Delta t_R$. (Other conditions must also be met, such as band limited signals.) If this condition is not met, the discrete-time system realizing $f_d(n)$ will generally result in different (probably reduced) performance compared with the continuous-time system with $f(t) = h(-t) \otimes K(t)$ [100]. Note that $K(t)$ is a designed impulse response derived from system specific criteria, the simplified case is an impulse and could perform the same role as a constant for scaling. So $f(t)$ is a convolution of the time-reversed received pulse and a design pulse $K(t)$. The output of the discrete-time filter may be downsampled at the slot rate,

$$y_D(n) = y_d(Dn) \qquad\qquad (6.3\text{-}10)$$

Obtaining synchronized samples at the output of the post-detection filter is required to obtain the optimum filter output defined by some criterion. Obtaining this correct sample or samples (if no downsampling or another downsample rate is used) is the objective of slot synchronization. Any sampling offset [108] may result in performance degradation. This performance degradation may occur in varying degrees to the decision process and the slot-synchronization algorithm itself as some closed-loop slot-synchronization algorithms contain the post-detection filter in their feedback path [106]. Figure 6-69 illustrates a conceptual (post detected) received waveform and post-detection filter demonstrating ideal and non-ideal slot timing at some time t_0. Note that if $\Delta t_M \neq \Delta t_R$, the peak will not be represented by a discrete-time sample, but the error may be removed or minimized via a variety of discrete-time processing methods; however, these may entail significant challenges to realizable in real-time hardware with very high-rate sampled systems.
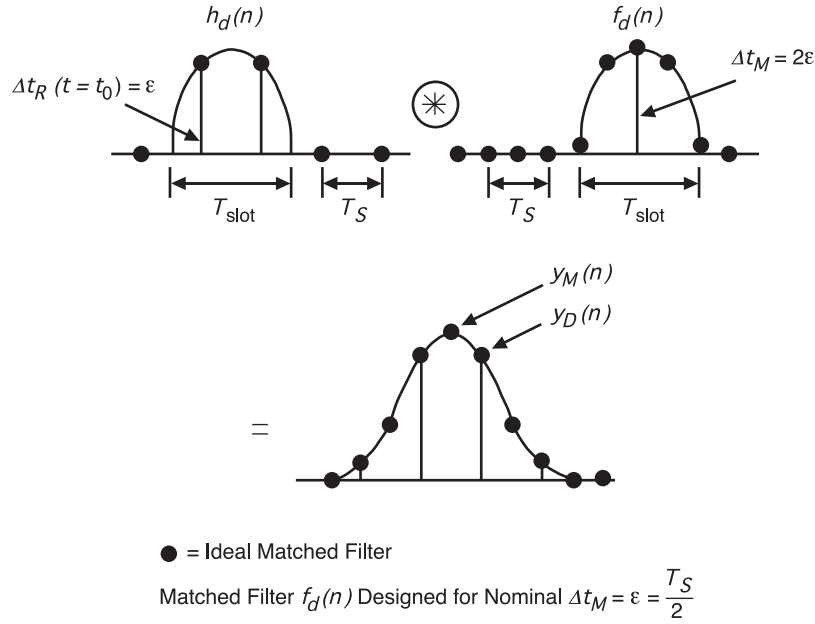
Fig. 6-69. Illustration of discrete-time post-detection filtering.

In this conceptual example, an arbitrary slot or receive filter was used. This could just as well be an integrate-and-dump filter (moving average filter with downsample); in which the signal may be synchronized before the integrate-and-dump by some time-varying interpolation filter to adjust the phase of the signal (an example of this is given in Section 6.3.7). Recall that in a discrete-time communications receiver with very high-data (sample) rates when flexibility is required or when the receiver is used for ranging, it is very desirable to fix the sample clock. In addition, adjusting the oscillator may be very difficult or impractical in near-maximum-Nyquist data rate receivers due to the very high clock rate, significantly greater than 1 GHz with modern A/Ds. However, when sampling the received signal at a constant sampling rate f_s, the sample offset Δt_R defined earlier changes with time, that is $\Delta t_R(t)$. This is due to the non-linear Doppler channel created by the relative velocity between ground stations and the transmitting satellite and the difference between the transmitter and receiver clocks. These differences are impossible to predict precisely. The difference between the discrete-time post-detection filter output and the ideal continuous-time post-detection filter output is the *fractional sampling offset*. The fractional sampling offset (or simply sampling offset) can be no larger than one half a sample period, or $T_s/2$. For the downsampled discrete-time post-detection filter output to be equal to the continuous-time matched filter sampled output, $y_D(n) = y_M(n)$, from the previous equations,

$$y_D(n) = y_d(nD)$$

$$= \sum_{k=-\infty}^{\infty} \left(\sum_{m=-\infty}^{\infty} h\left(T_s\left(k - mT_{sym} + A_m T_{slot}\right) + \Delta t_R\right) f\left(nT_S D - k\right) \right) \qquad (6.3\text{-}11)$$

$$= \int_{-\infty}^{\infty} \left(\sum_{m=-\infty}^{\infty} h\left(\left(nT_{sym} - \tau\right) - mT_{sym} + A_k T_{slot}\right) \right) f(\tau) d\tau = y_M(n)$$

This equality cannot be valid unless the following condition is met:

$$T_s nD + \Delta t_R = T_{slot} n \qquad (6.3\text{-}12)$$

Note that Δt_R is varying with time, and so is T_{slot}, but in a continuous-time processing system it is assumed that the oscillator frequency and phase are adjusted such that the matched filter output sampling time T_{slot} is optimal. Recall that T_s is fixed for the discrete-time system proposed. This fact (combined with a time-varying Δt_R with fixed Δt_M) implies that the discrete-time matched filter peak, or other optimal sample or samples if another optimality criterion is used, in general will not be represented by the discrete-time samples of the post-detection filter output. Furthermore, it should be noted that when Nyquist rate sampling is utilized, the sample period is the largest possible, making the potential sampling offset the largest possible. The A/D oscillator phase could theoretically be adjusted such that Δt_R is obtained to match Δt_M.

The slot synchronization algorithm estimates the slot time delay ($\Delta t_\varepsilon = \Delta t_M - \Delta t_R$) and frequency $1/T'_{slot}$ from the received signal $R(t)$ where the true slot frequency is $1/T_{slot}$. Slot synchronization for the optical channel may be accomplished by a number of algorithms, ranging from optimal estimators to highly sub-optimal estimators, and may be an open-loop estimator or a closed-loop estimator with feedback. It turns out that detecting or estimating the error in a discrete-time or digital implementation with Nyquist-rate sampling at very high bandwidths is often less challenging than correcting for it in real-time. While the type of estimator and its estimation performance are key considerations in any demodulator design and implementation, a nominal algorithm is chosen from [100], and the development presented here is focused primarily on how to correct for time-varying synchronization errors that the algorithms estimates. It will become apparent that most known estimation algorithms can be used in conjunction with the architecture developed with proper modification and/or discrete-time design. However, determining the performance of the resulting discrete-time system may be very challenging.

A property of the PPM demodulator is that once slot synchronization is estimated, and the slot clock determined, then the symbol clock may generally be readily derived, and hence the bit clock may also be derived. Symbol synchronization is required to determine symbol boundaries so that the slot position of the pulse in the symbol can be estimated; the estimate $\hat{A}_k$ can be made. This process is referred to as the decision process, refer to Fig. 6-70. Following this estimate, symbol-to-bit mapping is performed; this operation inverts the bit-to-symbol mapping at the transmitter. Following this processing forward error correction decoding may be performed if coding is used in the system. In modern systems the process of symbol-to-bit mapping and decoding may be performed in a coupled fashion. Figure 6-70 illustrates a simplified optical communications receiver. Note the two-step symbol process: first, slot synchronization (slot clock recovered) and pulse filtering are performed on all slots to determine $y_M(n)$; second, symbol synchronization and symbol decision processing are accomplished to form the symbol estimates $\hat{A}_k$. Other processing follows, such as forward error correction and frame synchronization.

Figure 6-71 illustrates a simplified discrete-time receiver with discrete-time post-detection filter. This system employs a constant clock rate and synchronous processing, and therefore it is a greatly simplified model. The slot
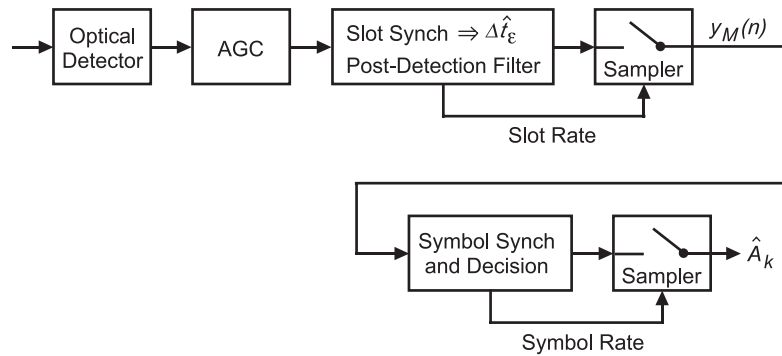

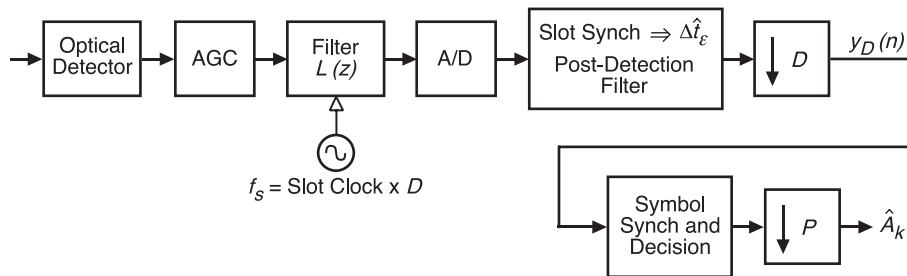Fig. 6-70. Simplified primarily continuous-time receiver.

Fig. 6-71. Simplified discrete-time receiver.

synchronization algorithm recovers the true slot clock by estimating slot phase and frequency offset from the nominal slot clock, this nominal clock frequency is $1/T_S$. By obtaining the estimate $\Delta \hat{t}_\varepsilon$ of Δt_ε the phase of the slot clock is determined and the frequency may also be estimated using successive $\Delta \hat{t}_\varepsilon$ estimates. The number of samples per slot for this signaling is $D = T_{slot}/T_S$, the slot period divided by the sample period. The number of samples per PPM symbol is $C = DP$, where P is the number of slots per symbol, that is $P = 2^m$. Next, we will analyze the critical deficiencies in this model and use the results to develop appropriate discrete-time signal processing algorithms and architectures to overcome these deficiencies.

If the Nyquist criterion is met, the peak, or any other sample(s), may be obtained or estimated using discrete-time phase delay methods [109,110]. One method for realizing the latter is to change the discrete-time slot filter, $f_d(n)$, with time to match the time-varying incoming sampled received pulse shape such that $\Delta t_\varepsilon(t) = \Delta t_R(t) - \Delta t_M(t) = 0$ or with noise sources in the system the mean estimate $\overline{\Delta t}_\varepsilon(t) = \overline{\Delta t}_R(t) - \overline{\Delta t}_M(t) < \varepsilon_0$ and the variance of the estimate $\text{var}\left\{\overline{\Delta t}_\varepsilon(t)\right\} < \varepsilon_1$ for some design parameters ε_0 and ε_1. Another method is to use a generic time-varying interpolation filter. Therefore, in a discrete-time system slot-synchronization can be thought of as having two components. The sampling offset must be removed ($\Delta t_M(t) = \Delta t_R(t)$) or minimized to ensure that one of the discrete-time sample (or samples), determined by some selection criterion, represent the slot energy in the decision process. The discrete-time architecture must minimize the fractional sampling offset in order to approximate the performance of the ideal continuous-time system.

Static timing or phase offset has been considered under the assumption the received signal phase has first and second derivatives that are zero. This is just the first step in developing effective demodulator architectures, but it should be realized that in an operational system with scenarios including Doppler, the first and second derivatives of phase are generally not zero (although higher derivatives can often be ignored [111]). There are frequency offsets and frequency rate changes. These correspond in not only a time-varying phase shift of the post-detection filter but also possibly a change in the post-detection filter impulse response itself as the pulse, slot, and symbol periods either expand or contract with Doppler. These nonlinear pulse distortion considerations are beyond the scope of this work. However, it will be become clear that once the basic framework for developing, analyzing, and implementing a discrete-time architecture with time-varying phase capability is completed, extending it to higher order dynamics is possible and is very similar to previous work in the field of synchronization.

In summary, we have demonstrated that in a discrete-time system with signal dynamics and a fixed sample-clock, slot synchronization/post-detection

filtering poses challenges to discrete-time design and implementation, particularly with Nyquist sampling. These concepts are considered further in Section 6.3.5 in the development of discrete-time architectures for accomplishing synchronization error correction for broadband pulses.

6.3.3.2 Slot and Symbol Synchronization and Decision Processing. Here a brief summary is presented of known signal processing for performing slot and symbol synchronization, post-detection filtering, and decision processing outlined in [97,99,100] for a simple optical channel model. References for previous work include [112–127]. Some of the structures presented here do not represent unique or optimal solutions but may represent good design choices based on analysis and systems presented in the references given. Figure 6-72 illustrates the conceptual continuous-time slot synch, a variation of which is analyzed in [128].

The discrete-time or sampled version of Fig. 6-72 is given in Figs. 6-73, 6-74, and 6-75. To date, performance of the discrete-time system has not been analyzed in closed form. The filter structure is the generic discrete-time version (using the impulse invariant transformation) of the continuous-time closed-loop second order loop filter used commonly in phase-locked loop, Costas loops, data-transition tracking loops, early-late gate type loops, and many other synchronization loops. The performance and loop-filter design must be determined through analysis analogous to that performed numerous times on similar synchronization loops that exist both in published research and analysis and in operational systems assuming the additive white Gaussian noise channel; examples of these derivations may be found in [129,130]. This filter structure is derived from the two-pole continuous-time loop and may be used to track both phase and frequency. Note that the loop filter $L(z,l)$ in Figs. 6-74 and 6-75 may be extended to include more poles (increasing the order of the loop) and is
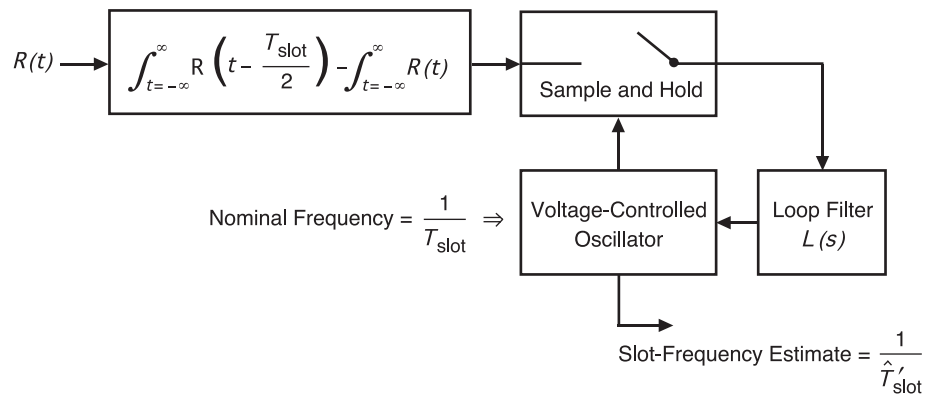

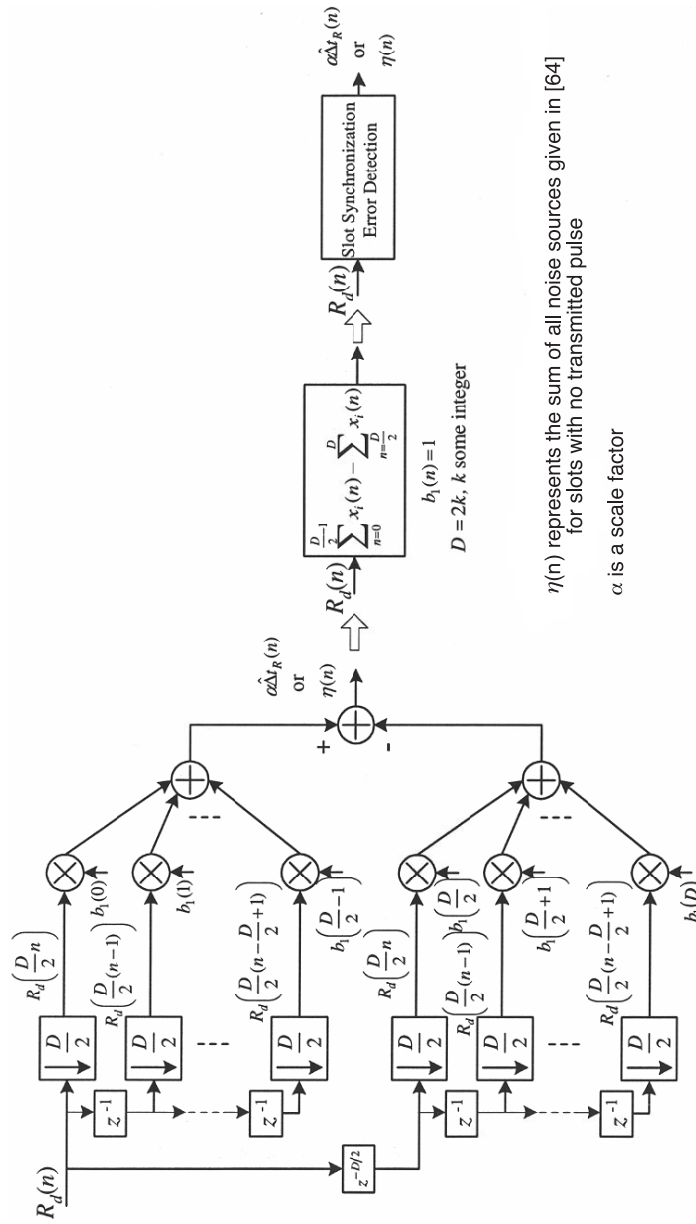Fig. 6-72. Continuous-time model of the slot-synchronization loop.

Fig. 6-73. Generalized and simplified discrete-time slot-error detection.
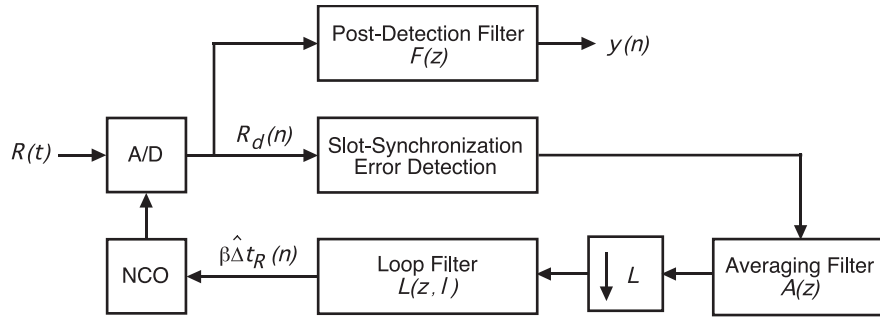
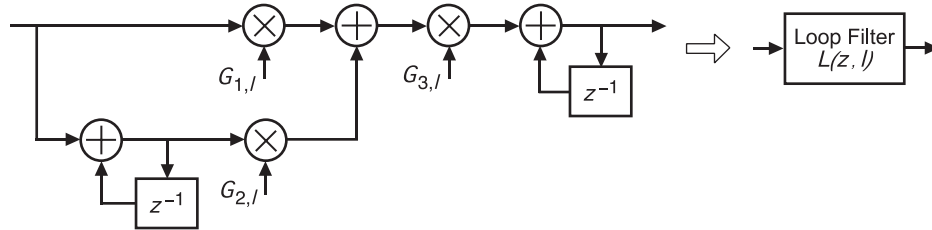Fig. 6-74. Discrete-time slot-synchronization loop.

Fig. 6-75. Discrete-time and time-varying loop filter structure.

a function of l. The latter characteristic indicates the ability to switch on-the-fly the filter bandwidth, which is commonly done in communications systems. The filter coefficients may be changed on the fly to achieve different bandwidths or damping factors and increase performance during the various regions of operation of the receiver. For example, tracking bandwidths are often different than acquisition bandwidths, and it may be desirable to change bandwidths or even tracking loop order with signal-to-noise ratio and/or signal dynamics. Obviously an intelligent controller, such as a state-machine or human-in-the loop, must be used to control such changes.

Figure 6-76 illustrates the operations of symbol synchronization and decision processing. The various algorithms fall into two general categories, those requiring a pilot sequence to acquire and track and those that operate on random data sequences, the so-called blind acquisition and tracking algorithms. There is relatively little previous work on evaluating the performance of these algorithms with the specific optical channel as described in [97,99]. It is assumed in this development that an algorithm using a periodic pilot sequence will be utilized, making the acquisition and tracking of a large range of PPM orders relatively straightforward.

From [97] the post-detection and decision processing is highly dependant on the characteristics of the optical channel and the optical detector used. Given the channel and operating scenarios outlined in [99], the slot-synchronized

decision process of choosing the slot with the greatest energy from the slots within a symbol boundary to estimate which symbol was transmitted is nearly optimum for a large range of system parameters. This is fortunate as this decision processing is readily accomplished with digital processing and may be easily parallelized. Figure 6-77 illustrates a simple example of the detection and decision process. Here ideal slot and symbol synchronization are assumed. The filter $F(z)$ is a simple moving average filter with D coefficients ($f(n)=1$), where $D = 4$ is the number of samples per slot, and the output is downsampled by D. The output of the downsampler is the sum of all the samples in a slot. These samples are then processed to decide which slot has the greatest energy. The samples in the slots other than the slot containing the transmitted pulse are non-zero due to the noise on the input signal.

Although symbol synchronization and detection/decision processing are essential processing elements, and their performance must be evaluated carefully in any theoretical or practical receiver development, they generally are
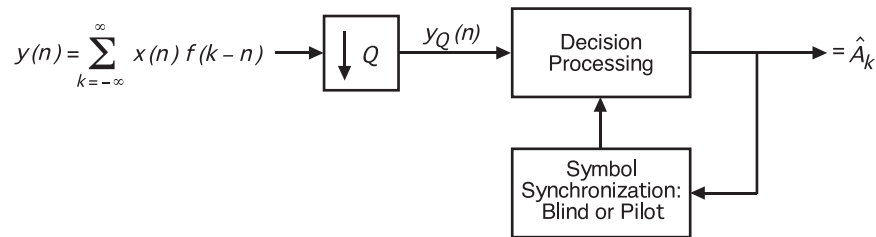

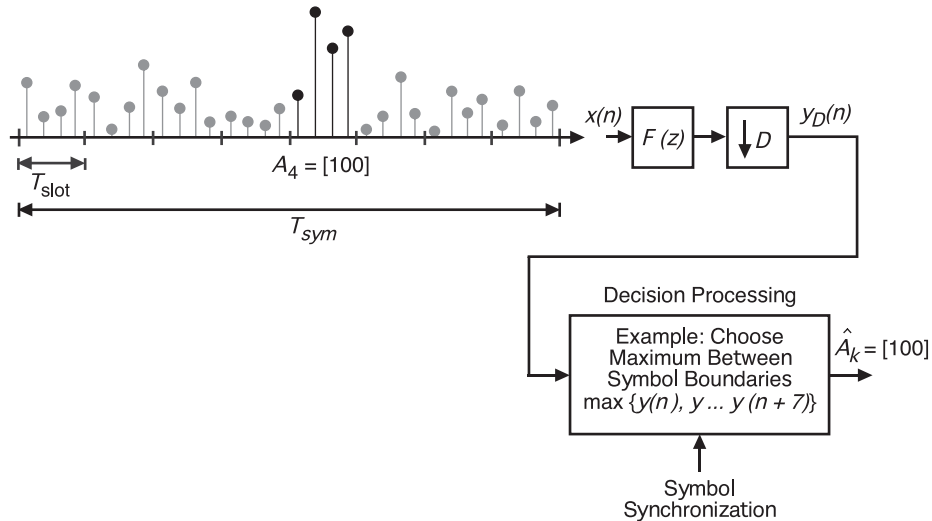**Fig. 6-76. Discrete-time symbol synchronization and decision processing.**

Fig. 6-77. Example symbol synchronization and detection,
$Q = D$ **and choose maximum detection.**

not as challenging to realize in digital VLSI as slot synchronization and post-detection filtering. These former functions are generally processed at much lower rates, depending on PPM order, than slot filtering and timing error estimation and correction processing. Of course if other types of decision algorithms that require more complex processing are needed, this may not be the case.

Finally, as stated previously, many of these algorithms are not uniquely optimum but dependant on the channel characteristics, dynamics, etc. The algorithms presented very briefly in this section are meant to be representative of the signal processing structures used for accomplishing slot timing synchronization, post-detection filtering, symbol synchronization, and decision processing. One of many possible modifications is the integrated symbol and slot synchronization algorithm that may offer increased performance particularly with high-order PPM. The structures presented may be readily modified to accommodate the feedback from symbol synchronization to slot synchronization, and an example of this type structure is given in Section 6.3.8. The optimal slot and symbol synchronization and detection are highly dependant on the optical detector and other channel characteristics. This provides motivation for highly flexible, that is parameterized and reconfigurable, discrete-time processing architectures. We now introduce demodulator variations based on these "base-line" algorithms in a more global context and identify significant design choices along with specific challenges to their realization in discrete-time or digital VLSI.

6.3.4   Discrete-Time Demodulator Variations

Figure 6-78 illustrates a discrete-time demodulator for PPM type modulation. Based on the definition of the all-discrete-time demodulator developed in this work, Fig. 6-78 is not strictly an all-discrete-time
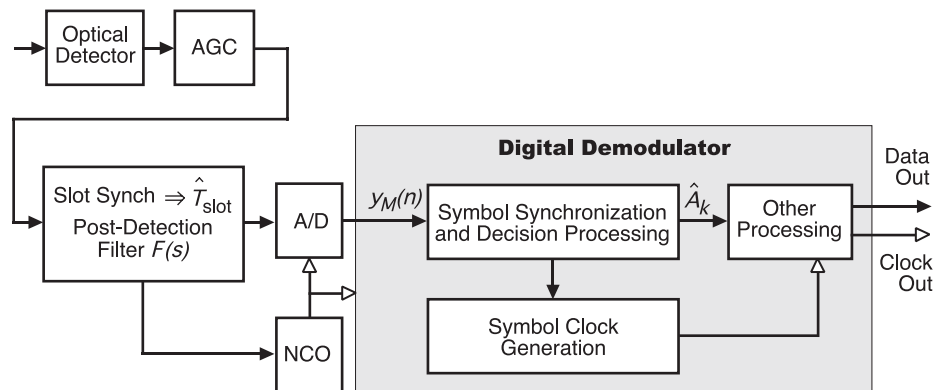

Fig. 6-78. Hybrid analog and discrete-time PPM receiver.

demodulator but a hybrid demodulator, as the slot-timing recovery is performed with continuous time processing. Figure 6-79 is a variation on this same theme but incorporates more discrete-time processing. Figure 6-80 illustrates an all-digital demodulator for a communications system with time-varying slot phase and period and may represent a reasonable design choice for some systems. For example, this demodulator may provide adequate performance in systems with many more samples per slot than required by the Nyquist rate. Nyquist rate sampling in such a system implies that some additional discrete-time signal processing is necessary to synthesize continuous-time phase adjustments of the A/D converter in order to approximate performance of the system in Fig. 6-79.

For very high sample rates, ranging applications where one desires an ultra-stable clock source, a large dynamic range in data rate, a large dynamic range of input bandwidth, or other flexibility (high parameterization or reconfigurability), the receiver in Fig. 6-80 is the desired implementation [106]. At very high sample rates ($\gg$1 GHz) adjusting the A/D oscillator phase to correct for synchronization errors as in Figs. 6-78 and 6-79 may be very difficult. The analog circuits necessary to accomplish this function are also generally very limited in dynamic range of bandwidths, signal amplitude variations, etc. The architecture in Fig. 6-80 is the base line all-discrete-time demodulator architecture which we will further develop to mitigate losses in slot synchronization performance, post-detection filtering, and decision processing due to a fixed-sample rate near Nyquist rate sampling. In addition to operate at very high sampling rates ($\gg$1 GHz) parallel processing is required given the current state-of-the art in commercial-off-the-shelf CMOS VLSI circuits.

Finally, the three receivers in Figs. 6-78 through 6-80 are greatly simplified versions of actual receivers and represent the variations of primary interest from a top level architecture development. There are many additional variations, functions (many diagnostic in nature) necessary in an operational receiver. However, Fig. 6-80 represents the core of the most challenging discrete-time processing that must be further developed to operate with Nyquist rate sampling and with processing rates 10–20 times slower than the required A/D converter rates for sampling broadband PPM ($>$500 MHz).

6.3.5 Discrete-Time Demodulator with Time-Varying Post-Detection Filter

Now we derive a serial system such as that illustrated in Fig. 6-80 with a nominal sample rate $D(1/T_{slot})$ such that with Nyquist or near-Nyquist sampling the system has the performance of a system employing a sample rate many times the Nyquist sample rate. That is to say, the system has a sample rate $D(1/T_{slot})$ that operates with identical or nearly identical performance to the system with sample rate $DN(1/T_{slot})$, where N is some large positive
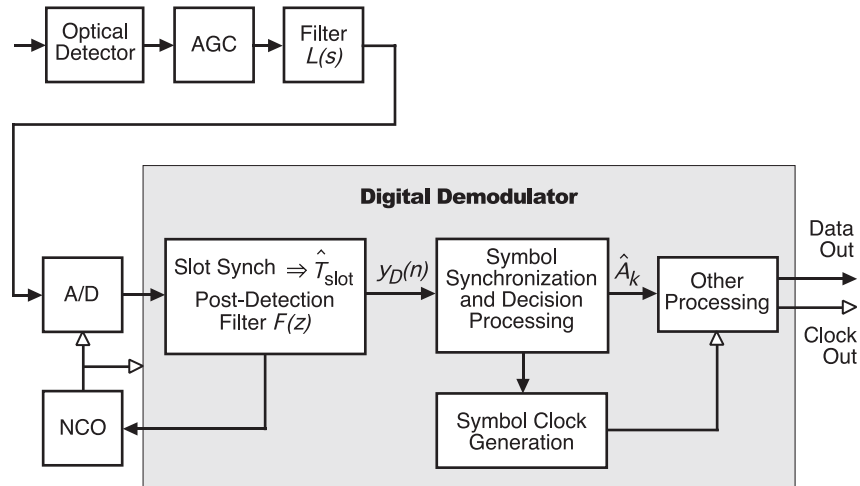
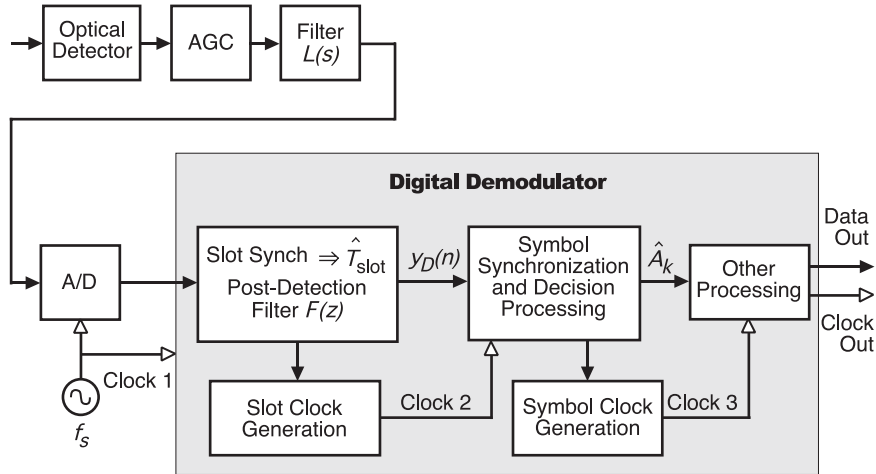**Fig. 6-79. Discrete-time demodulator with feedback to A/D.**

Fig. 6-80. All discrete-time demodulator.

integer (for example >100). Here the assumption is made that the received pulse is full-response and band-limited (which is impossible in theory but can be approximated in practice). For the scenario such that the signal is band-limited but not full-response [101] the system developed will not be identical but may be designed to be nearly equivalent. Several properties of multirate systems relevant to this development are illustrated in Figs. 6-81(a) through 6-81(e) [111].

Figure 6-81(a) illustrates some discrete-time sequence $x(n)$ convolved with another discrete-time sequence $h(n)$. Figure 6-81(b) illustrates the
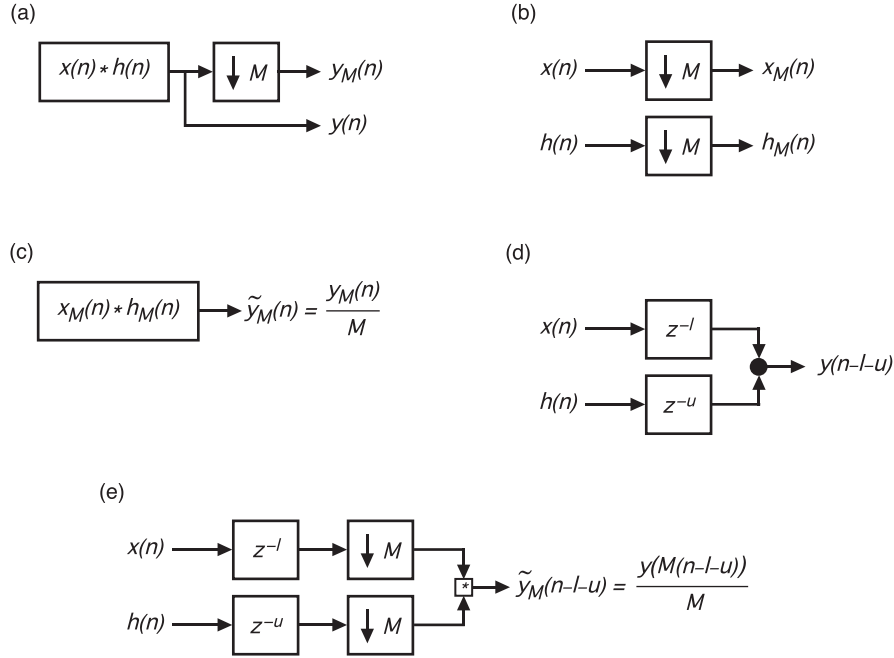
(a)

(b)

(c)

(d)

(e)

Fig. 6-81. Multirate signal processing properties: (a) downsampled convolution, (b) downsampled input, (c) convolved downsampled signals, (d) convolved time-shifted signals, and (e) convolved time-shifted and downsampled signals.

notation for the downsampled sequences. If $x(n)$ and $h(n)$ are perfectly bandlimited such that no aliasing results from this downsampling (implying infinite sequences), the result of this convolution is related to $yM(n)$ as demonstrated in Fig. 6-81(c) by a constant scale factor, M. If $x(n)$ and $h(n)$ are not infinite in time extent, convolving their downsampled versions as in Fig. 6-81(c) will result in a sequence that can be related to $yM(n)$ by some distortion function that incorporates the effects of aliasing caused by the downsampling. Under the assumption of this development, there is no aliasing. Figures 6-81(d) and 6-81(e) illustrate the effect that independent sample delays have on the convolved output and how such a delay relates to $y(n)$. As illustrated in Fig. 6-82, the sampled received pulse shape $hdN(n)$ can be approximated from $hd(n)$ as illustrated using the expander and interpolation filter. If we make the simplifying assumption that $h(t)$ is perfectly band-limited (with D samples per slot) and full-response (although theoretically not possible) and the perfect interpolation filter is used (infinite time extent) [111], then $\tilde{h}_{dN}(n) - h_{dN}(n) \approx 0$.

Now the time-variable *slot* or *post-detection filter bank* ($f_d(n,u)$) can be developed from the received pulse, $h_{dN}(n)$ (or $\tilde{h}_{dN}(n)$), as illustrated in

Fig. 6-83 [112]. The filter bank $f_d(n,u)$ may be developed from the time reversed $h_{dN}(n)$ or another filter $v(n)$. The filter $v(n)$ for example could be an interpolation filter. Each sampled filter u is shifted in time by $-T_S/N$ from u-1 (recall the sample period of T_S and D samples per slot).

It is clear from this development and the properties in Figs. 6-81(c) through 6-81(e) that the output of Fig. 6-84(b) is equivalent to the output of Fig. 6-81(a) divided by the scale factor N [112]. Assuming the delays l and u are correct, such that the output is the desired sample (possibly with residual fractional sampling offset, $\Delta t_e \leq T_S/2N$), any sample that can be obtained with the $DN(1/T_{slot})$ sampled system can now be obtained from the $DN(1/T_{slot})$ sampled system due to the bank of time-shifted filters.

These properties are combined to generate the architecture in Fig. 6-85 that utilizes primarily synchronous processing and can operate with Nyquist rate sampling while approximating the performance of a system with a much higher sample rate (N times more samples per slot).

There are many other aspects of the time-varying post-detection filter and slot-synchronizer design that require analysis and further development on the
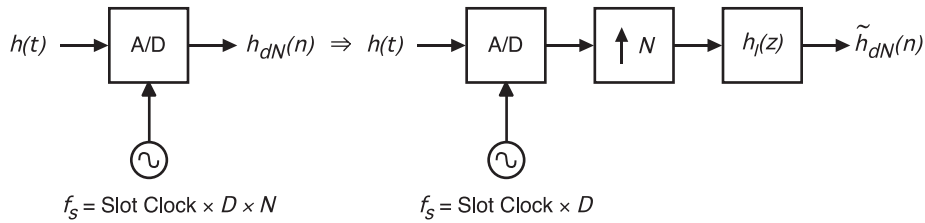

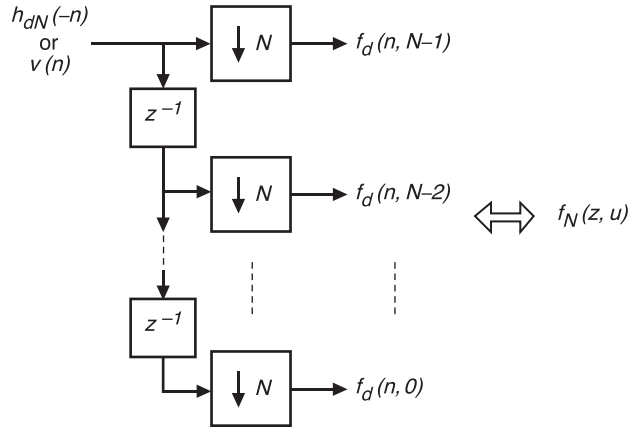**Fig. 6-82. Approximating high-sample-rate system with low-sample-rate system.**

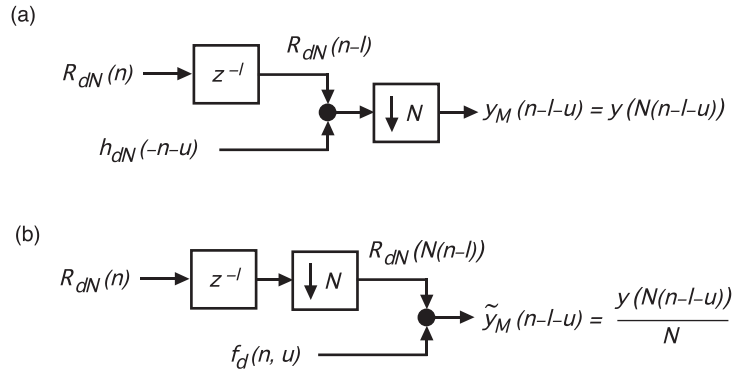**Fig. 6-83. Filter bank generation.**

(a)

(b)

Fig. 6-84. Multirate signal processing properties: (a) delay, convolution, and downsample, and (b) delay, downsample, and convolution.

path to practical implementation and to determine performance with realistic channel conditions. There is one issue in particular that requires further careful consideration in both the architecture development and hardware design and implementation. Recall that the reason that post-detection filter $F(z)$ needs to vary with time is because the transmitter and receiver are fundamentally asynchronous, and the actual received data rate will generally differ and vary with time from the expected data rate chosen to set the A/D and system clocks. Consider the design of Fig. 6-85, as part of the time-varying detection filter and slot synchronization algorithm the true slot clock is recovered. The true symbol clock is also recovered and is synchronous to the slot clock; however, both of these clocks are asynchronous to the A/D or system clock. Thus the implementation of the architecture of Fig. 6-85 requires high speed digital design with asynchronous clocks. The asynchronous nature of the processing also creates additional design challenges when a parallel- or vector-processing architecture is developed. These challenges are addressed in detail in Section 6.3.6.

Finally, of course, it is not possible to achieve perfectly band-limited pulse shapes that are also full-response or to implement perfect (infinite in time extent) interpolation filters, all of which was assumed for simplicity in the derivation of Fig. 6-85. However, these can be approximated very closely in reality, and generally such a system based on these principles results in negligible implementation losses if designed and implemented properly.

6.3.6 Parallel Discrete-Time Demodulator Architectures

Due to the very high sampling rates required by broadband optical pulses processing rate reductions of 10–20 are typically required given the current state-of-the art if the targeted processing implementation is commercially
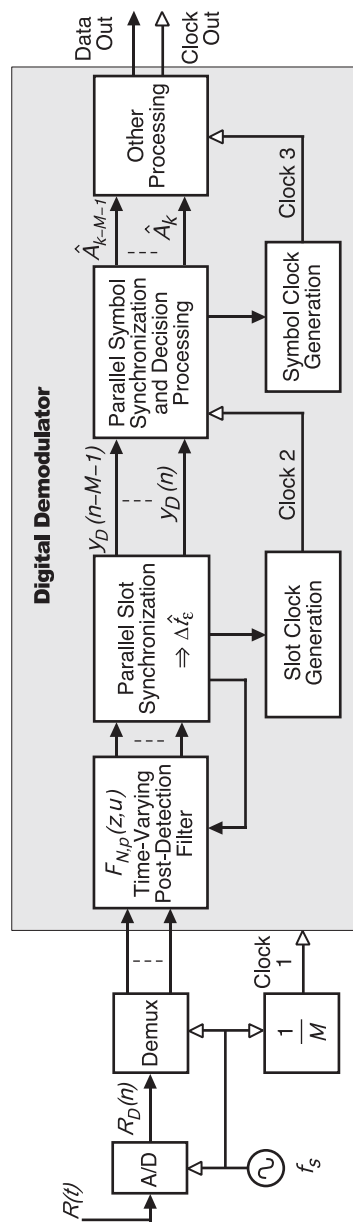
Fig. 6-85. Nyquist-rate discrete-time demodulator.

available CMOS (FPGAs for example). Some demodulator functions are trivial to parallelize, and others are not. The process of parallelization generally increases complexity; depending on the methods used, the increase in complexity may be linear or nonlinear [105,106,111,112]. There are numerous methods, many based on frequency domain or dual time-frequency domain processing, for parallelizing the convolution/correlation processing that reduce the complexity or transistor count of parallel implementations [106,111,112, 131–148]. Figure 6-86 illustrates the most straightforward time-domain method of parallelizing the FIR filter structure illustrated in Fig. 6-87.

There is a much more elegant way of representing parallel filters and filter banks that is based on multirate notation. The vector downsample operation is given in Fig. 6-88.

The parallel filter can then be represented by the structures given in Fig. 6-89, where the demultiplexer operation represents the delay and vector downsample chain (ordered serial-to-parallel conversion).

Using this notation, the parallel version of the demodulator given in Fig. 6-85 is given in Fig. 6-90. A core processing element of the demodulator is the time-varying parallel filter bank, $F_{N,p}(z,u)$. This is also the processing element that may dominate the complexity (transistor) count of the VLSI implementation. There are numerous potential simplifications to the filter structure in Fig. 6-89. For example, if the impulse response is symmetric, the multipliers and adders may be reduced by a factor of 2. In addition, as indicated earlier, there are other options for performing the parallel filtering, and many have greatly reduced multiplier requirements depending on the filter type and order.

As mentioned earlier, one of the additional challenges of realizing the architecture in Fig. 6-85 or Fig. 6-90 in digital VLSI is appropriate asynchronous clock management. Additionally, the parallel implementation is much more straightforward to realize if the number of parallel paths (vector length) remains constant throughout a given processing operation (i.e., convolution). Obviously this creates challenges as each slot clock and symbol clock represents a fixed-vector length of data samples and both of these are asynchronous with the A/D (system) clock. From a high level, the system of Fig. 6-90 is primarily composed of synchronous clocks and fixed-vector length
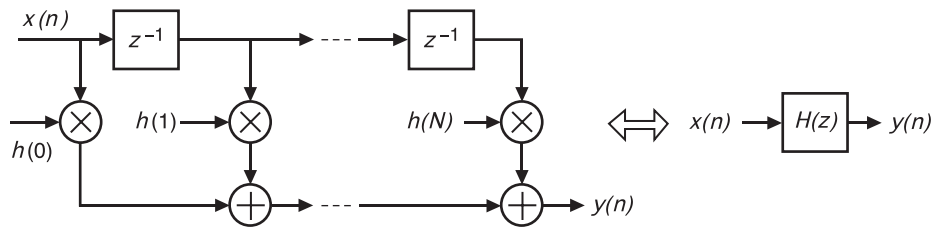

Fig. 6-86. FIR filter structure.
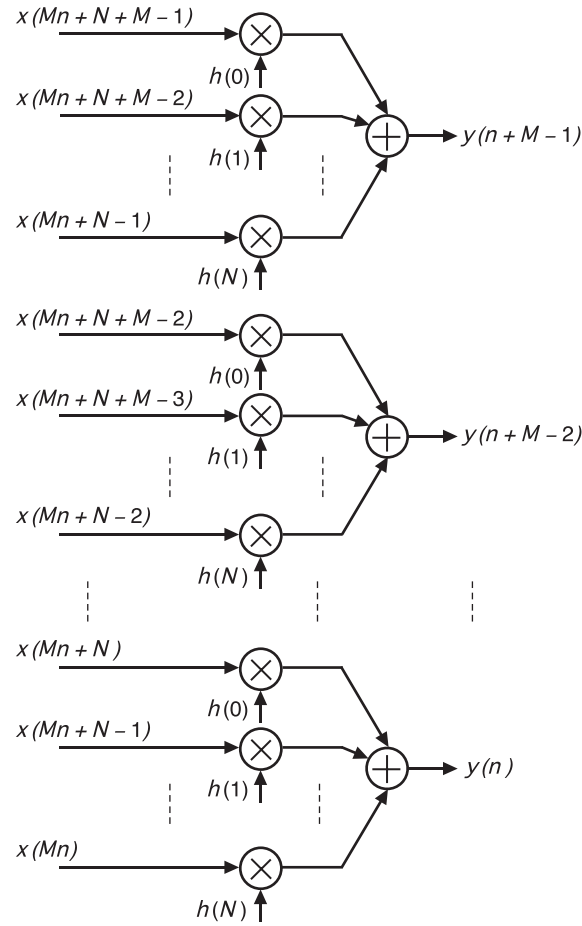
Fig. 6-87. Parallel FIR filter structure.

parallel processing. However the data symbols must be clocked out at the true symbol rate that is asynchronous to the A/D clock and the $1/M$th rate system clock. One method of re-clocking the vector of symbols at the recovered data rate is with the asynchronous first-in first-out (FIFO) circuit, and there are many ways to realize this circuit. More details of the slot and symbol clock generation and the conceptual asynchronous FIFO type circuits are presented in the next section.

6.3.7   Asynchronous Discrete-Time Processing

The input signal has a dynamic nature due to the Doppler in the channel and the absence of synchronization between the oscillators in the transmitter and receiver. As a result of this dynamic signal the error $\Delta \hat{t}_\varepsilon$ varies with time,

Fig. 6-88. Vector downsample operation.

Fig. 6-89. Parallel filter bank representations.

Fig. 6-90. Parallel discrete-time demodulator.

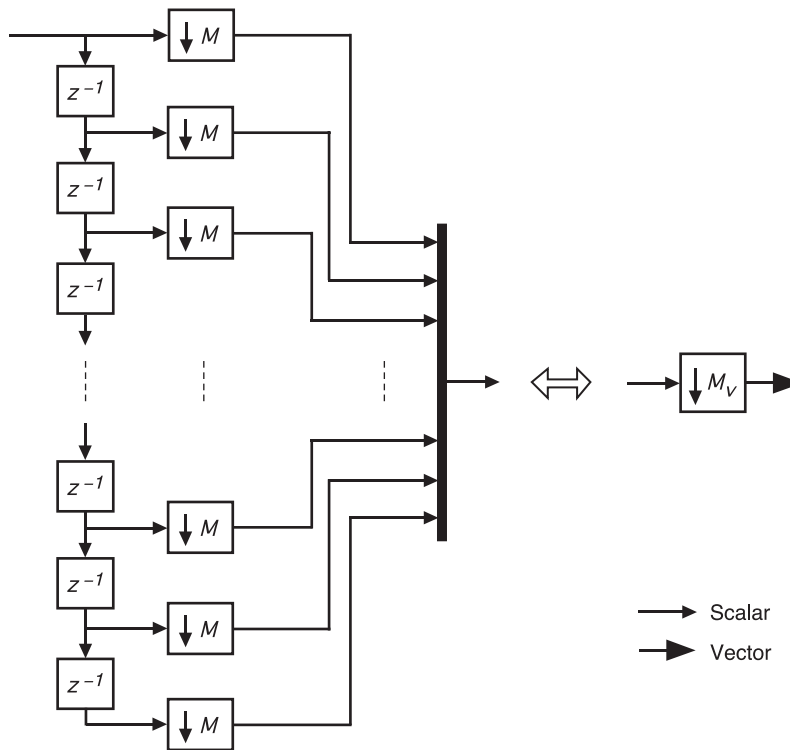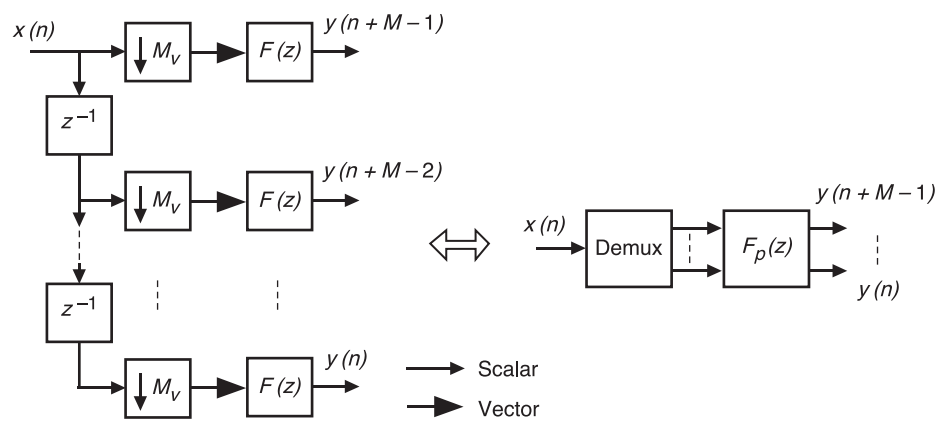and given the fixed-sample clock A/D of Fig. 6-90, this results in a discrete-time system with asynchronous sample rates and a digital implementation with asynchronous clocks. The simplified error signal model may be represented as

$$\Delta t_\varepsilon(t) = T_{slot}(t) - T'_{slot}(t) + \tau \tag{6.3-13}$$

where T'_{slot} is slot period due to Doppler, and τ is a fixed time offset. The slot period with Doppler is given by,

$$T'_{slot} = T_{slot} + T_{slot}\left(\frac{v}{c}\right) \tag{6.3-14}$$

where v is the relative velocity of the transmitter relative to the receiver and c is the speed of light. Note that the relative velocity may be positive or negative. However, for reasons that will be demonstrated, significant simplifications result if the received sample clock frequency is set such that,

$$1/T'_{slot} \leq \frac{f_{S\_nominal} + r_1}{D} = \frac{f_S}{D} \tag{6.3-15}$$

The sample frequency is set such that the nominal sample rate assuming no Doppler, $f_{S\_nominal}$ is increased by the real constant r_1 such that the true sample frequency f_S divided by the designed number of samples per symbol is greater than the maximum slot frequency the demodulator processes. The slot synchronization algorithm creates a new estimate at the nominal symbol rate,

$$\hat{\Delta t}_\varepsilon\left(nT_{sym}\right) \approx T_{slot}\left(nT_{sym}\right) - T'_{slot}\left(nT_{sym}\right) + \tau + \eta_0(n) \tag{6.3-16}$$

Here $\eta_0(n)$ is some noise on the estimate. Successive timing error estimates must be accumulated, and this accumulation is represented as

$$\sum_n \Delta\hat{t}_\varepsilon\left(nT_{sym}\right) \approx \sum_n T_{slot}\left(nT_{sym}\right) - \sum_n T'_{slot}\left(nT_{sym}\right) + \tau + \sum_n \eta_0(n) \tag{6.3-17}$$

An accumulator such as this exists in the filter given in Figure 6-75. As stated previously, the error estimate is an approximation to the difference between the nominal slot rate and the actual slot rate. This estimate is not generally equal to the actual error as many signal components and signal distortions are not included in this simple model. These include multiple jitter sources, channel and amplifier noise sources, imperfect filters, etc. Much analysis must be performed to determine actual performance of the estimator as a function of integration time or filtering and the statistical properties of the numerous random variables in the communications system. As shown in [99],

this filtering may be accomplished with a closed-loop feedback system yielding very desirable Doppler tracking capabilities. Here we continue to address the implication of asynchronous processing on the overall architecture and ignore random noise and distortions.

The accumulated error may become arbitrarily large as n becomes arbitrarily large. For practical purposes the error must be accumulated in a cyclic fashion, that is modulo some multiple of $-T_S$. Recall the system clock rate of the serial demodulator in Fig. 6-85 is $1/T_S$. It is now demonstrated that it is desirable to alter the slot clock at time increments given by the following,

$$\text{round}\left\{\sum_n \Delta \hat{t}_\varepsilon\left(nT_{sym}\right)\right\} = -\frac{L}{N}T_S \qquad (6.3\text{-}18)$$

where $L = kN$ and k is some integer greater than or equal to 1. For the demodulator in Figure 6-85, there are clocks with periods T_S, T_{slot}, and T_{sym} as illustrated in Fig. 6-91.

Recall the slot period is D times the sample period, $T_{slot} = DT_S$. Here $L/N = 1$, $L/N = D$, and $L/N + DP$ in the accumulated error estimate represents the time of one sample clock, slot clock, or symbol clock cycle, respectively. The timing error in the signal is partially corrected with the filter bank $F_{N,p}(z,u)$; the error is quantized to one of the time-shifted versions of the detection or interpolation filter. This error correction must be made modulo some time LT_S/N. Otherwise arbitrary filter lengths and complexity are required if $1/T'_{slot} < 1/T_{slot}$ and the receiver runs for an arbitrarily long time. When the accumulated error time reaches its minimum value, it must *wrap* or *roll-over*; otherwise, it will become arbitrarily large. Figure 6-92 illustrates the accumulation of the error estimate $\Delta \hat{t}_\varepsilon$ modulo $L/N \, T_S$.

While the filter bank of Fig. 6-83 indicates a time-delay of one sample period $(N(T_S/N))$ from the first filter $(u = 0)$ to the last $(u = N-1)$ it may be
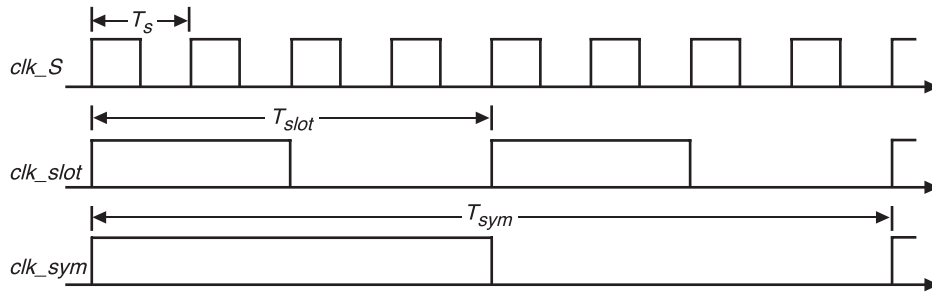

Fig. 6-91. Sample, slot, and symbol clocks.

$$\sum \Delta \hat{t}_\varepsilon = \sum_{n=0}^{\infty} \Delta \hat{t}_\varepsilon \ (nT_{sym}) \ \text{mod} - L \ (T_S/N) \Rightarrow \sum \Delta \hat{t}_\varepsilon$$
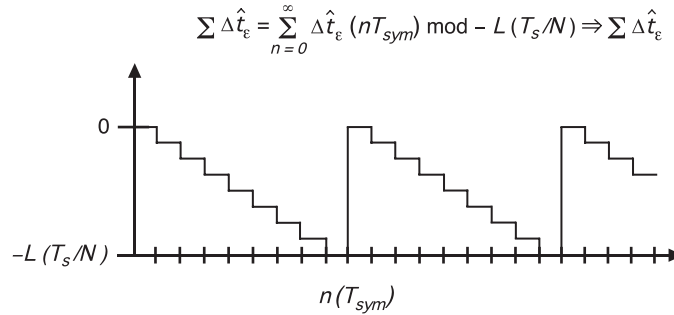

Fig. 6-92. Time delay.

designed for any delay that is a ratio of L/N times (T_S). It will be demonstrated that for certain parallel processing architectures specific delays result in much more simple overall implementations. To gain more insight into these issues consider the example in Fig. 6-93.

- Illustration (a) is a received 2-PPM signal with 4 samples per slot ($D = 4$) and no dynamics.
- Illustration (b) is a conceptual depiction of the effects of dynamics on the signal where the amount of Doppler is greatly exaggerated to illustrate key concepts. In reality, the timing error in illustration 2 would typically be thousands or millions of times smaller per slot period.
- Illustration (c) demonstrates how the error is used to change u, thus choosing a filter with different subsample timing delay. For this example, assume that the slot filter is a perfect interpolation filter, so incrementing u creates a time-quantized delay, quantized to $T_S/2$, in the signal given in illustration two of the figure. Incrementing u by one is equivalent to incrementing one-half of one sample period. The maximum timing error due to time-quantization with this filter bank is $T_S/(2N) = T_S/4$. The total delay in the filter bank is chosen to be $-DT_S - T_S$, which is one and one-quarter slot periods (recall there are $D = 4$ samples per slot). To create a process that results in repetition of an entire symbol when the filter rolls-over or wraps, the filter bank design method of Figure 6-83 had to be extended by $-4T_S$.
- In illustration (d), when the timing error wraps, it instantaneously moves the output signal back in time by $4f_S$ (one slot period). The wrapping of the filter bank index u results in samples that have already been output of the filter to be output again. These samples must be discarded, and the slot clock period associated with them must also be discarded. The period of the clock following the filter wrapping is instantaneously doubled, and the slot clock returns to its nominal period (T_{slot}). This
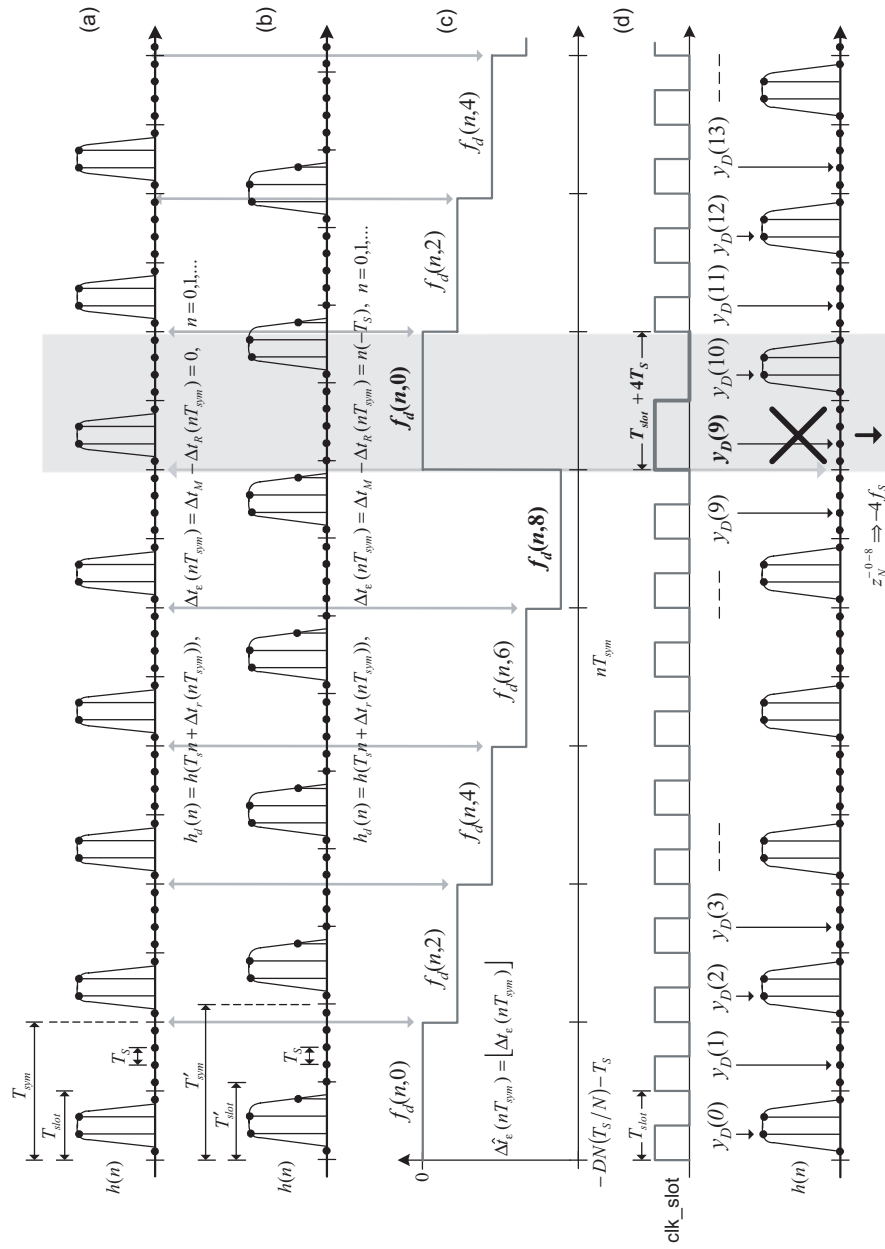
Fig. 6-93. Conceptual illustration of time-varying phase tracking and multirate processing.

processing results in a slot clock with an average frequency that is equal to the recovered slot rate. In this way the timing estimates are made and accumulated to adjust the clock period, which is readily accomplished in digital circuitry. There is obviously a need for a roll-over detector to indicate when the clock period should be adjusted; this is also readily accomplished with digital circuits. This roll-over detector may be designed to further average out or remove with thresholding the variations of the accumulated phase error estimates due to noise and other distortions on the input signal, and thereby avoid multiple roll-overs due to jitter on the error signal.

Although the memory length of the filter in Fig. 6-93 was chosen to be seemingly arbitrary to illustrate specific concepts, the number of samples that are repeated and then discarded after filter index roll-over is a significant consideration in the design of the filter bank. It will be shown that it is very desirable to create the filter bank to rollover on slot boundaries and this requires a modification to the earlier filter bank design method given in Fig. 6-83; consider Fig. 6-94.

In Figure 6-83, the prototype filter, $h_{dN}(n)$ or $v_{dN}(n)$ is zero padded, the filter is appended with a number of zero samples. The number of filters in the bank is now L, setting L equal to an integer number of slots yields:

$$\frac{L}{N} T_S = \frac{RDN}{N} T_S = RDT_S \quad \Rightarrow \quad L = RDN \qquad (6.3\text{-}19)$$

In this case the total time delay from the 0 indexed filter to the $(L-1)$ indexed filter is the number of samples per slot (D) times the number of slots (R) times the sample period, and the total number of filters is equal to RDN. Figure 6-95 illustrates a conceptual filter bank with $R = 1$.

The result is the ability to correct larger timing error before index roll-over. This increased filter memory however results in more complex filter banks, but
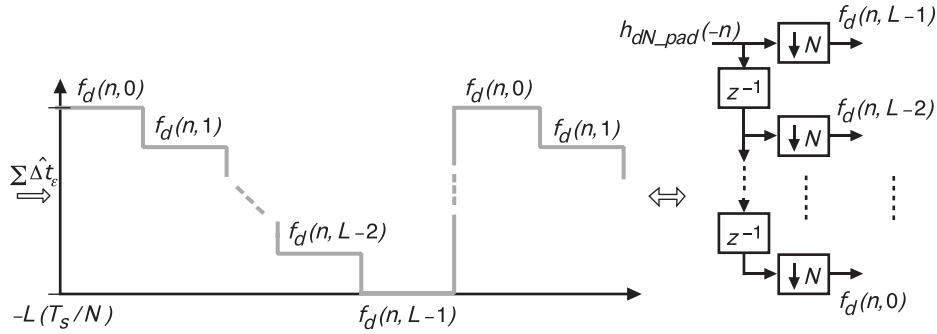

Fig. 6-94. Filter bank for correcting *R* slot times before rollover: prototype filter length $L = R \times D \times N$.

it allows control over the jump in time and corresponding number of samples discarded when the index to the filter bank rolls over. There is an equivalent multirate structure for the filter bank in Fig 6-94 that results in significant simplifications as illustrated in Fig 6-96.

The details of this simplified multirate filter bank are not presented here, but the structure incorporates a variable delay block before the filter bank. The delay is modulo $k-1$, where $L = kN$. With this structure the sub-sample errors are corrected by the filter bank while timing corrections that are integer multiples of a sample period are corrected by the variable delay. In this structure, the complexity of the filter bank is similar to that of Fig. 6-83, but it is increased by the addition of the variable delay. The error estimate $\Delta \hat{t}_\varepsilon$ is decomposed into two components, one quantized to integer sample time error that is used to control the variable delay and another component quantized to sub-sample timing error used to control the filter bank. Note that if $k = D$, then the filter bank will "roll-over" on slot boundaries.

The motivation for the filter index to roll-over on slot boundaries is provided in Fig. 6-97. Consider the filter bank of the parallel architecture of Fig. 6-90, and note that after being processed by the filter bank, the signal is input to the slot synchronization algorithm. The current synchronization algorithms introduced earlier cannot have discontinuities in their input; if the signal is instantaneously (in the discrete-time domain this is effectively possible) shifted in time, it must be done on a slot boundary or some modified slot synchronization algorithm normalizing for the time shifts in the input must be developed. Note that the phase (timing error) wrapping can only occur across the vector boundary as this is when error estimates are updated in the parallel system. Error estimates are not updated within a vector block, only across vector boundaries, and when the roll-over occurs it is known precisely
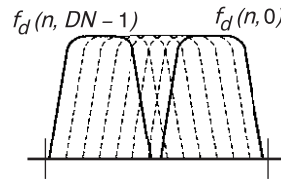

Fig. 6-95. Filter bank.
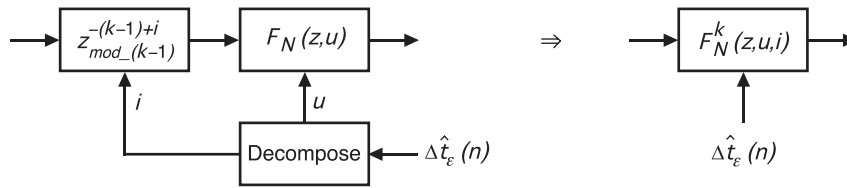
Fig. 6-96. Conceptual simplified filter bank.
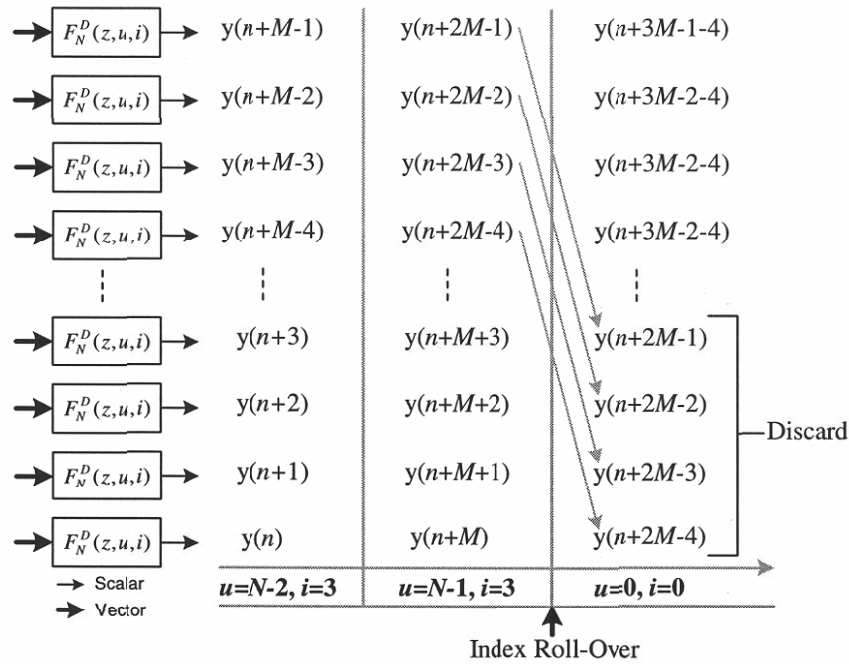
Fig. 6-97. Roll-over on slot boundaries of parallel/vector system.

which data samples are repeated due to the roll-over detector circuit, refer to Fig. 6-97.

There is another model of the time-varying filter bank that is useful for building further insight useful for formal analysis beyond the scope of this document. The filter bank may be modeled as a numerically controlled oscillator (NCO) [113,1,2,3]. The variables u and i are updated every symbol and may be thought of as the error signal to the NCO. The phase of the NCO is changed by the error $\Delta \hat{t}_R(nT_{sym})$, and frequency is determined by the derivative of this estimate.

Figure 6-98 summarizes the results of this section from a high level. The asynchronous FIFO circuit is a critical subsystem of the demodulator. The functions of this circuit are to order the parallel vector appropriately for the parallel symbol synchronization and detection in the presence of the filter bank index "roll-over" and re-clock the data out at the appropriate recovered rate. The details of the asynchronous FIFO (such as memory depth, overflow and underflow flags, and many other elements of this circuit) are not presented here. There are many possible implementations to accomplish the functions of this circuit.

Fig. 6-98. Parallel digital demodulator.

In conclusion, the elements of the architecture presented in this section are largely generic. They accommodate a time-variable post-detection filter for which the purpose is two fold: filtering and the critical operation of correcting sample and sub-sample timing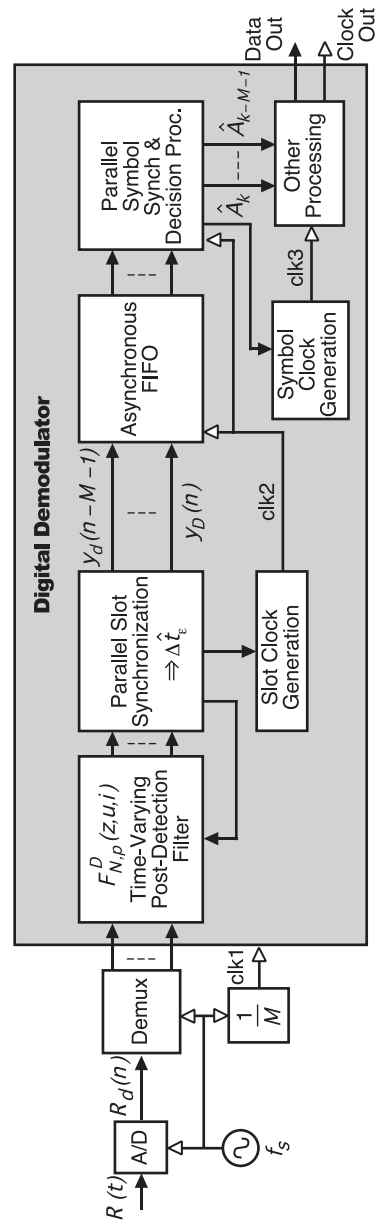 errors. This filter may be utilized with any number of slot-timing error estimation algorithms and in a closed loop system as in Fig. 6-73 through Fig. 6-75 and may approximate the high sample per slot A/D with continuous-time phase adjustments. It was inferred in this development and stated here explicitly that in addition to the challenges of designing the post-detection processing and slot-synchronization algorithms from a communications theoretical perspective, designing architectures for realizing these function in discrete-time at very high rates with Nyquist or near-Nyquist rate sampling entails many challenges. Overcoming these challenges requires developing and synthesizing discrete-time signal processing methods and algorithms for realizing the fundamental algorithms while overcoming the challenges of asynchronous and parallel digital design and implementation given the current state-of-the art in digital VLSI circuits. The discrete-time structures for realizing decision processing and symbol synchronization also pose many challenges; however, these challenges are generally more readily overcome than those for post-detection filtering and slot-synchronization, namely sub-sample and asynchronous real-time processing at the maximum sample rate (A/D rate), as such these architectures were not presented here in detail. With this as context the next section develops more complete parallel discrete-time demodulator architectures.

6.3.8 Parallel Discrete-Time Demodulator Architectures

6.3.8.1 Simple Example Architecture. The purpose of this example is to illustrate further key considerations when synthesizing concepts developed earlier. A greatly simplified list of hypothetical requirements for a communication system and hardware limitations is given as follows:

1) Slot period, $T_{slot} = 2$ ns (500 MHz bandwidth)

2) PPM pulse period = 1 ns (1 GHz bandwidth)

3) 4-64 PPM modulation

   Hardware limitations:

1) VLSI implementation in a FPGA with a maximum clock rate of 250 MHz

2) 4 giga-samples per second A/D converter

Even from this short-list of requirements numerous design parameters may be determined. First the Nyquist sampling rate of the PPM pulse bandwidth, and hence the system, must be >1 GHz $\times$ 2 = 2 GHz. It should be clear given the earlier discussions that the architectures development assume $D = 2k$, where k is some integer. Although not stated explicitly this assumption leads to

multiple simplifications in the parallel architecture development and facilitates many further simplifications in both the architecture and in the hardware design beyond the scope of this work. There is also additional motivation for sampling above the Nyquist rate, design margin. Given that the A/D can accommodate a 4-GHz sample rate, D is set equal to 4. Given that the VLSI device implementing the demodulator architecture operates at 1/16th the rate of the A/D converter, the rate reduction or number of parallel paths M is set equal to 16.

Assume that some interpolation filter is used as the prototype filter in developing the filter bank $F_N^4(z,u,i)$. Determining N, the number of time-shifted filters in the filter bank, is generally not trivial. From a hardware complexity perspective N should be made as small as possible to minimize complexity and transistor count. Yet, from a pure performance perspective, N should be made as large as possible to minimize residual sampling offset and synthesize as closely as possible the phase/time adjustments of the continuous-time system. Assume $N = 128$; the residual sampling offset is then $0.25\,\text{ns}/(2 \times 128) \cong 0.0009766$ ns or approximately 1 picosecond (ps). This number may or may not be a good design choice depending on many other characteristics in the system both in the transmitter and in other subsystems of the receiver. For example, if the A/D oscillator phase jitter is significantly greater than 1 ps, it may not make sense to have the resolution of $N = 128$. Another perspective to consider is the performance, both tracking and acquisition, of the closed-loop tracking system of Figs. 6-73 through 6-75 (or other slot synchronization algorithms) with time-quantized error correction. Much previous work exists in analyzing these and other issues; furthermore, a loop similar to that proposed has been analyzed, tested, and validated in hardware with $N = 128$ [106]. However, detailed analysis of the performance of the type of loop with the optical channel has not been completed to date. Figure 6-99 is a block diagram of a parallel architecture satisfying the simplified requirements that includes a structure for a non-time-varying pulse-equalizer $B_1(z)$.

Note that details of parallel symbol synchronization and decision processing are not given here, but are generally significantly less complex to realize than post-detection filtering and parallel slot-synchronization. The challenging aspect of these former functions lies in the fact that they are parameterized on PPM order, but with the flexibility of a digital implementation, such challenges are readily overcome. It should be noted that the number of parallel paths and the number of samples per slot in the slot synchronization processing and filter $F_N^D(z,u,i)$ is readily scalable by powers of two, and the amount of parallelization in the functions of symbol synchronization and decision processing is largely independent of these. Note
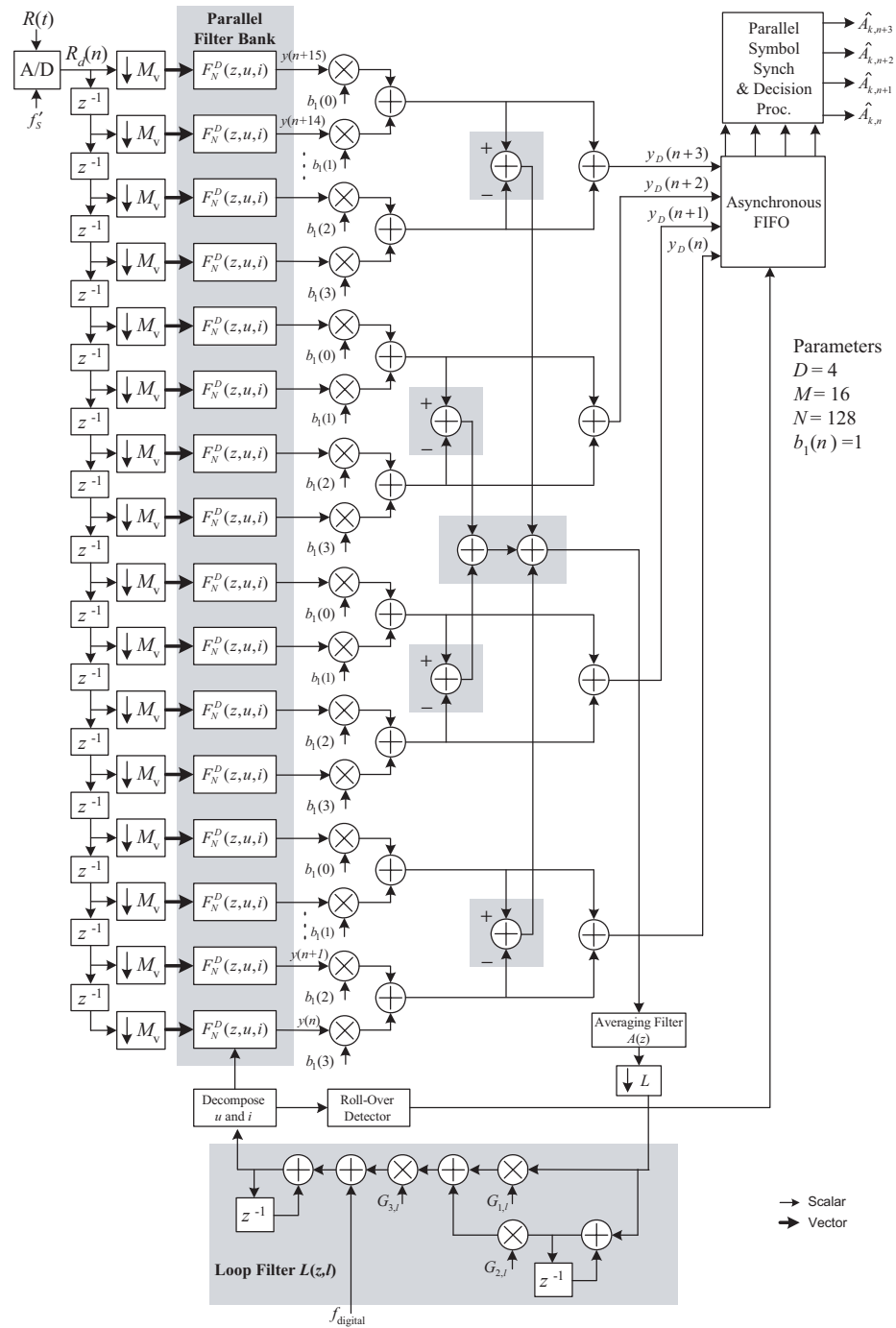
Fig. 6-99. 1/16th rate parallel architecture.

that, due to the large overlap of vectors input to the vector downsample and parallel filter banks of Fig. 6-99, significant simplifications are possible in such parallel architectures. However, derivations of such simplifications are beyond the scope of this work.

As stated earlier, determining the performance analytically or pseudo-analytically of an architecture such as that in Fig. 6-99 for most realistic communications channels is a significant undertaking. However, given that loss-less or perfect reconstruction parallelization techniques were used in its development, there is no need to determine the performance of this specific architecture. Figure 6-100 presents a serial equivalent architecture for which performance can be determined or estimated more readily although this determination is still non-trivial with realistic channel models. This serial architecture is equivalent from a communications systems performance perspective not from a processing rate or complexity perspective that has been a focus of this work. The delay Q_1 is the total delay added by the parallel architecture in the feedback. For example, to model the actual delay in the implementation Q_1 must include the pipeline delays in all multipliers and adders in the feedback path.

6.3.8.2 Performance with a Simple Optical Channel Model. A basic model of the optical PPM symbol detection uses photon-counting detection in the presence of background noise [97,98]. Thermal noise is negligible when using photon counting. This analysis assumes ideal slot and symbol synchronization. The number of photons in a coherent-state optical field generated by lasers is Poisson-distributed, i.e., the probability of detecting k photons, $k \geq 0$, is given by the expression

$$P(k) = \frac{K_s^k}{k!} e^{-K_s} \qquad (6.3\text{-}20)$$

K_s is the average number of signal photons per slot. The probability of correct detection for *M* order PPM is

$$P_M(C) = 1 - \frac{M-1}{M} e^{-K_s} \qquad (6.3\text{-}21)$$

The probability of symbol error is related to this quantity as

$$P_M(SE) = 1 - P_M(C) = \frac{M-1}{M} e^{-K_s} \qquad (6.3\text{-}22)$$
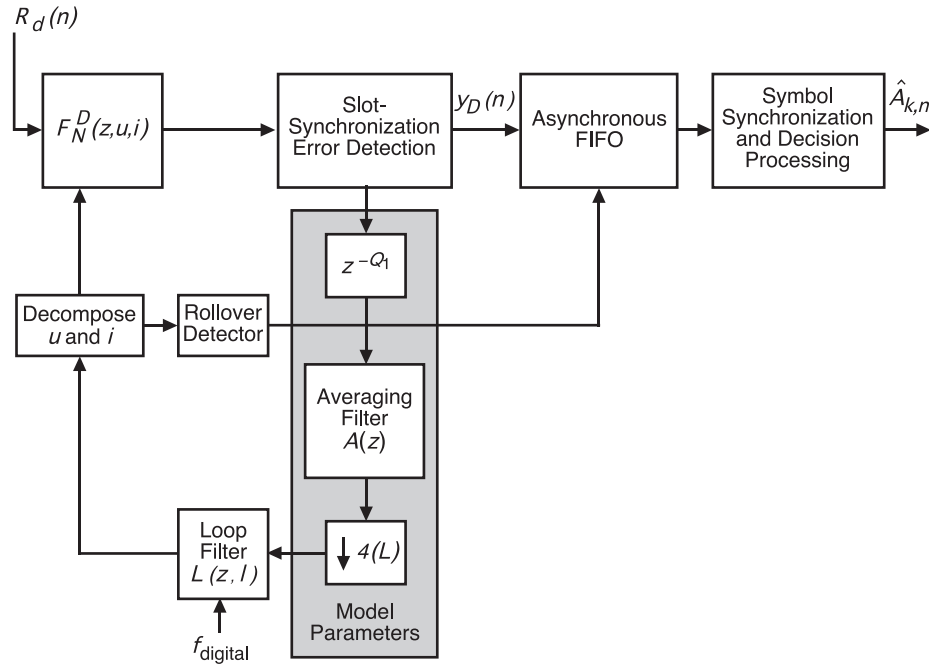
Fig. 6-100. Serial model of the parallel architecture.

When significant amounts of background light enter the receiver along with the signal, it is possible for the receiver to make an error, even if one or more signal photons are detected, because a noise slot may occasionally produce a greater count than the signal slot. Let the average number of background photons be K_b. The probability of correct detection for maximum-likelihood detection of PPM symbols in the presence of noise has been derived in [97] and shown to be:

$$P_M(C) = \left\{ \sum_{r=0}^{M-1} \left(\frac{1}{r+1} \right) \binom{M-1}{r} \sum_{k=1}^{\infty} \frac{(K_s+K_b)^k}{k!} e^{-(K_s+K_b)} \left[\frac{(K_b)^k}{k!} e^{-K_b} \right]^r \right.$$

$$\left. \times \left[\sum_{j=0}^{k-1} \frac{(K_b)^j}{j!} e^{-K_b} \right]^{M-1-r} \right\}$$

$$+ M^{-1} e^{-(K_s+MK_b)}.$$

(6.3-23)

The corresponding error probability is given by

$$P_M(E) = 1 - P_M(C) \tag{6.3-24}$$

Software simulations of the system in Fig. 6-100, with 4 PPM, $N = 128$, $D = 4$ samples/slot, and a normalized loop filter bandwidth of approximately 0.005 were performed using Matlab Simulink. Figure 6-101 is a basic block diagram of the simulation model. The simulation assumed a fixed slot phase offset, thus requiring the slot and symbol synchronization loops to acquire and then track.

Using the mathematical model described in Eq. (6.3-1), the transmitted pulse, $p(t)$, was a perfect square pulse that occupied 50 percent of the slot period. No intensity variations other than those from the photo-detector were modeled. The optical channel models only a simplified photon counting type (possibly PMT) photo-detector as described above. The output of the channel is a Poisson distribution given by,

$$y(k) = \frac{\lambda^k}{k!}e^{-\lambda}, \text{ with parameter } \lambda = \begin{cases} K_s + K_b & \text{signal slot} \\ K_b & \text{no signal slot} \end{cases} \tag{6.3-25}$$

The software utilized a Poisson channel model, and the background mean photon count (K_b) remained constant at 1. The signal mean photon count vs. signal error rate (SER) simulation results are plotted in Fig. 6-102. These simulation results vary little from the theoretically predicted results given by Eq. (6.3-24); however, it should be emphasized that this is a simplified optical channel model.

6.3.8.3 Evolved Parallel Architectures. The architecture of Fig. 6-99 is not a unique or final architecture design for the high-rate optical PPM demodulator; it is a starting point from which to evolve. A core processing element is the time-varying post-detection filter bank. This processing or some close variation is envisioned as being a key element of any all-digital demodulator; however, numerous simplifying signal processing structures for accomplishing this processing are possible. Other signal-processing algorithms might be fundamentally improved or changed depending on the optical channel and advancing detection and estimation theoretical techniques derived for that channel. For example, consider that the optimal PPM slot synchronization signal processing algorithm has currently not been derived for the optical
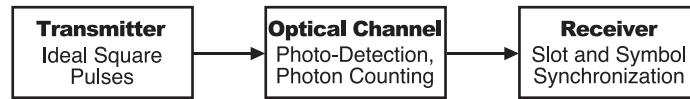

Fig. 6-101. Software model block diagram.
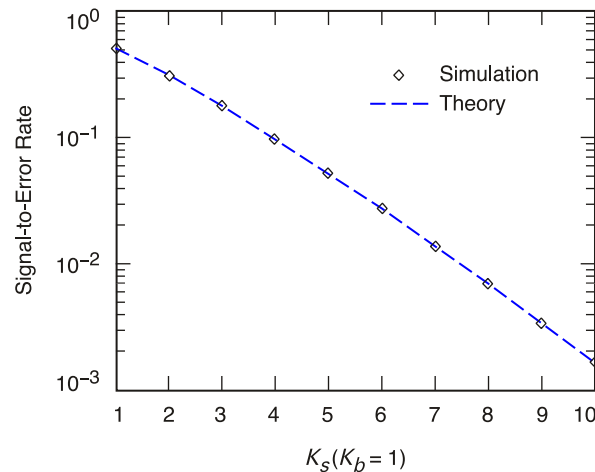
Fig. 6-102. Performance of the software model.

channel described in [99]. In addition to deriving such processing algorithms, improvements to existing synchronization algorithms might include a symbol decision-directed slot-synchronization loop for the optical channel or pulse equalization. Indeed the list of theoretical improvements or channel-specific designs for synchronization, post-detection filtering, and decision processing as well as other processing subsystems is quite long. In addition, as the state-of-the-art hardware implementation devices improve, more computationally complex signal processing may be feasibly implemented. Future algorithm improvements cannot be predicted with a high degree of accuracy. However, there is a set of architecture evolutions or improvements that are largely possible to predict. These are the signal processing functions that while not the focus of this work, are a necessary part of a ground receiver or demodulator. The demodulator architecture will evolve to contain these functions:

- Master controller (for real-time autonomous demodulator monitoring and control)
- Forward error correction preprocessing
- Power estimation and SNR estimation
- Slot synchronization and symbol synchronization lock detection
- Digital automatic gain control

Figure 6-103 illustrates an evolved parallel-demodulator architecture incorporating additional functions. Many additional functions have been added to the base-line architecture of Fig. 6-99, and the slot-synchronization loop incorporates the option of being decision directed. The base-line parallel processing and subsample timing error correction of Fig. 6-99 remains intact. Examples of other architecture improvements and alternatives are presented next. We will demonstrate advantages in having the filter bank for timing-error
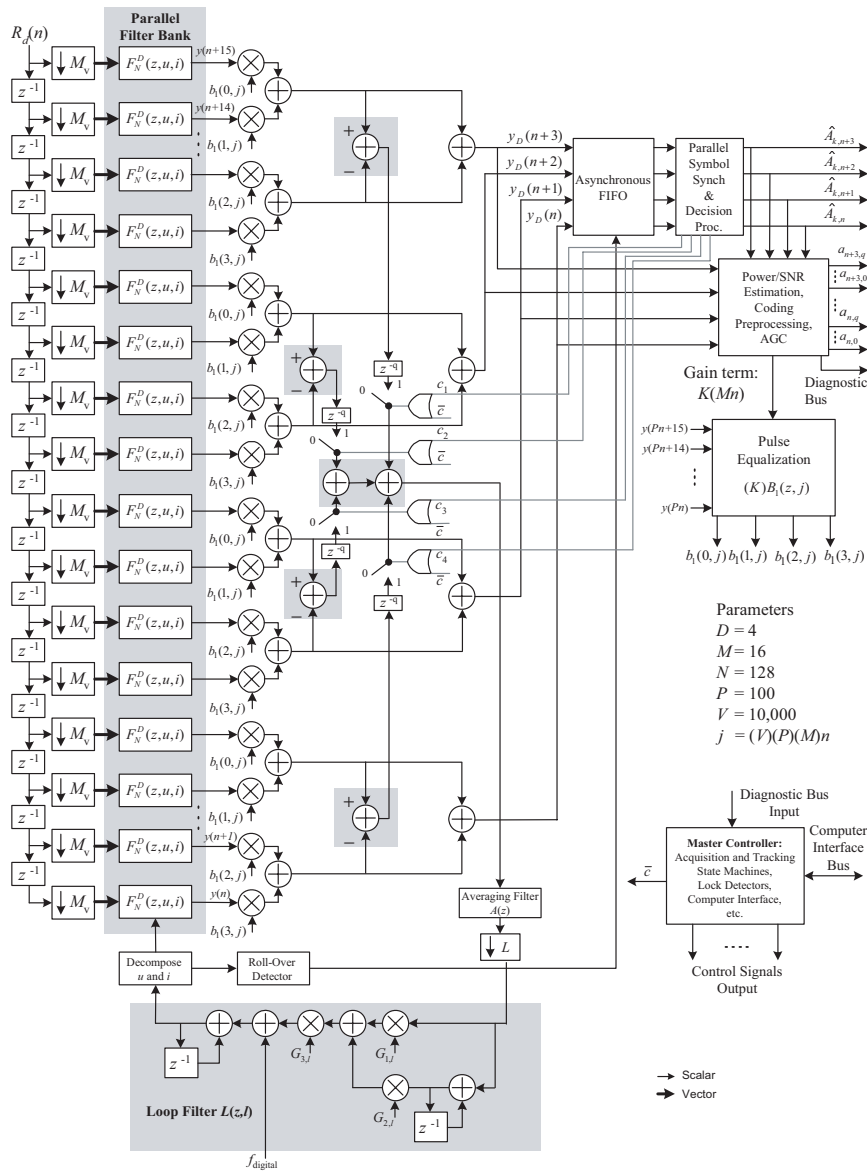
Fig. 6-103. A more comprehensive architecture; core processing of Fig. 6-101 retained.

estimation to be designed independently of the post-detection filter bank used for filtering and timing-error correction on the signal used for decision processing. The process of synchronization and post-detection filtering may be separated or deconstructed. It will become clear that there are several advantages to deconstructing the processing this way. Part of the motivation for this is that different filter-bank designs and processing rates may be used for

synchronization and post-detection filtering, and this may facilitate further advantages in the design and implementation of the synchronization filter.

Consider the architecture in Fig. 6-104; this architecture may be designed to be mathematically equivalent to the slot synchronization architecture given in Fig. 6-99.

Consider the architecture in Fig. 6-105; this architecture is a straightforward modification to that of Fig. 6-104 and incorporates a simple averaging filter with all-ones coefficients that is downsampled by a rate that is equal to the number of coefficients that are in the filter (L). Very large filter orders are possible with the simple feedback structure as illustrated in the figure. The simple averaging filter depicted is often referred to as the integrate-and-dump filter. The input to this averaging filter may be switched with control signals c_i to be either zero ($c_i = 0$) or the sampled input signal ($c_i = 1$). This is done to allow feedback control from the decision processing such that only samples estimated to contain a PPM pulse are input to the slot synchronization algorithm. Note that due to the large overlap of input vectors in Figs. 6-99 and 6-105, significant further simplifications are possible in the realization of these architectures.

Each output line of the vector downsample block in Fig. 6-105 is a vector, so there are actually a vector of switches and averaging filters operating at rate f_s, but the output of these filters is clocked at rate $f_s/(ML)$; this is the input rate to the time-varying filter bank. However, the filter bank $\overline{F}^D_{N_1,p}(z,u,i)$ operates at rate Mf_S/L, that is M times faster than its input because this one filter structure is used to process all inputs. This is referred to as *hardware reuse*. This architecture requires 1/16th the number of concurrent multipliers of that required by Fig. 6-104 for the same prototype filter order (same signal processing performance). This may result in a significant savings in concurrent multipliers but with some added complexity of register delays and other controlling logic that are required in the hardware reuse architecture. This complexity reduction may result in a filter bank design $\overline{F}^D_{N_1,p}(z,u,i)$ with more multipliers and/or more time-shifted filters (larger N) than would otherwise be feasible to implement. *This complexity reduction increases the design options of the filter $\overline{F}^D_{N_1,p}(z,u,i)$, and thus, the design and performance options of the slot-synchronization algorithm that are feasible.* It should be emphasized that a full-rate filter bank $F^D_{N,p}(z,u,i)$ is still required to filter and correct the timing error of the input signal that is then input to the decision process (recall this is the process of estimating the transmitted symbol). Figure 6-106 illustrates the architecture with deconstructed slot-synchronization (timing error estimation) and timing-error correction in the post-detection filtering with some pulse equalizer $B_2(z)$.
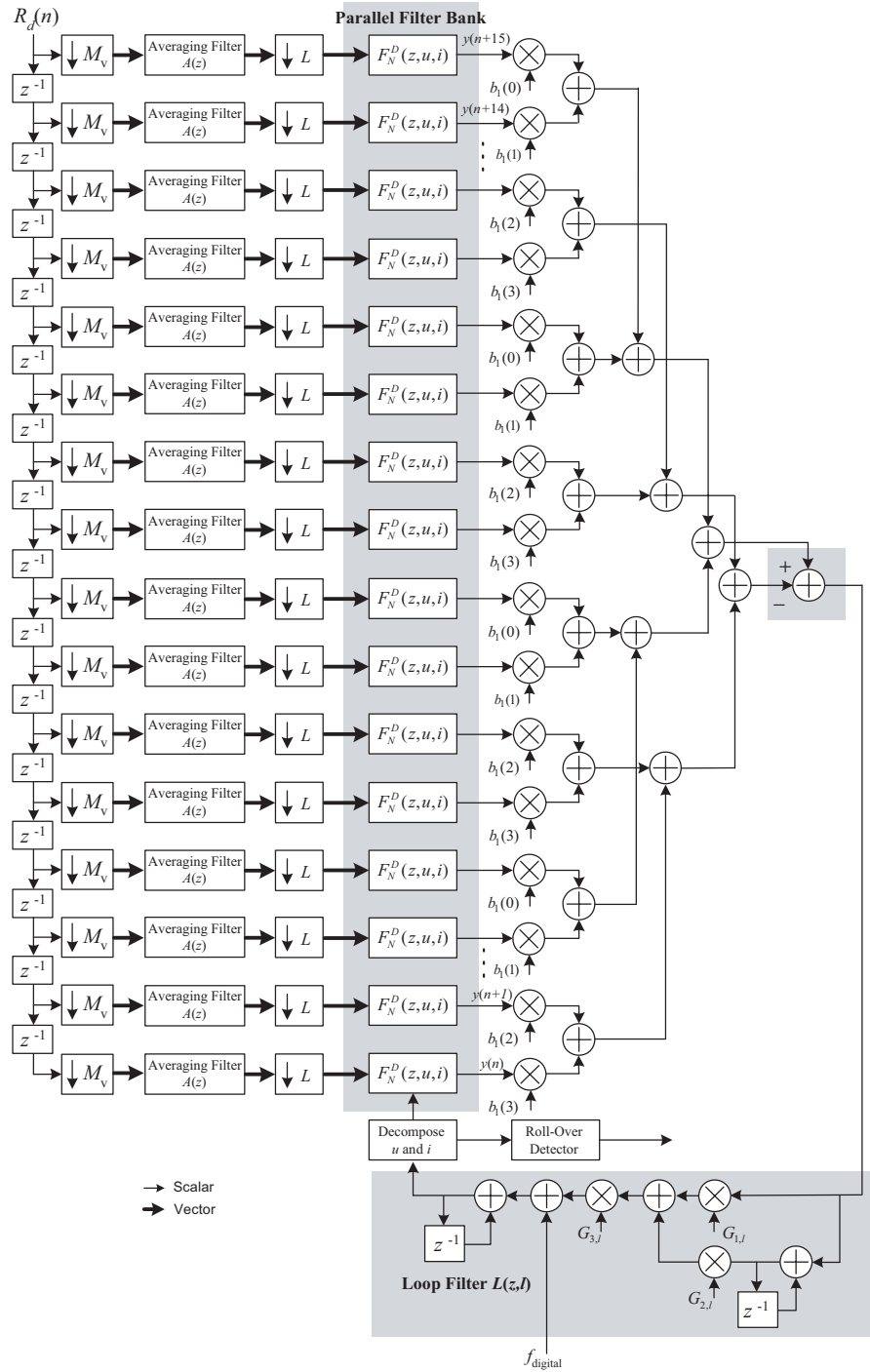
Fig. 6-104. Alternative slot-synchronization architecture equivalent to that of Fig. 6-103.
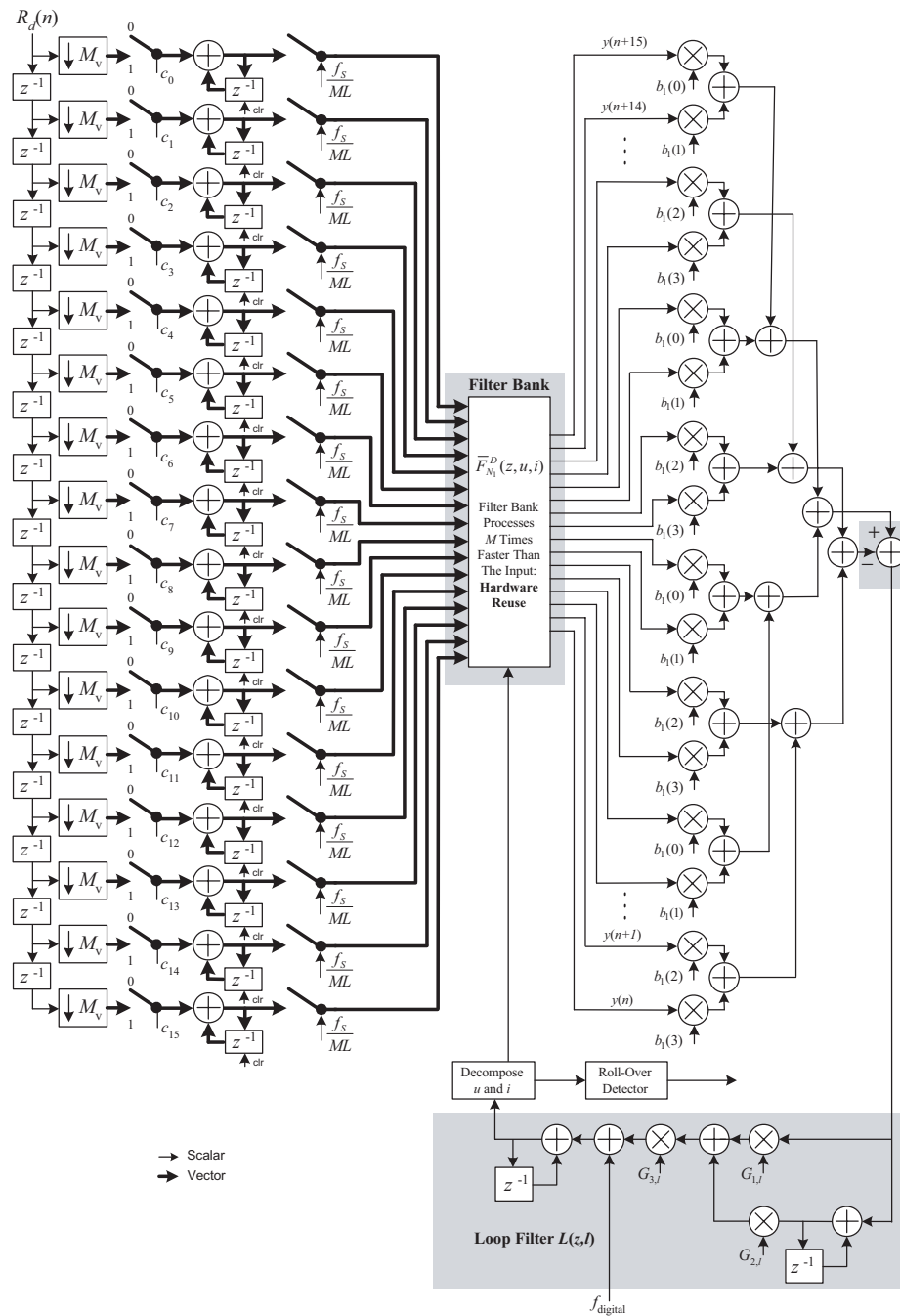
Fig. 6-105. Simplified alternative slot-synchronization architecture; filter rate = $M \times$ (the parallel input rate).
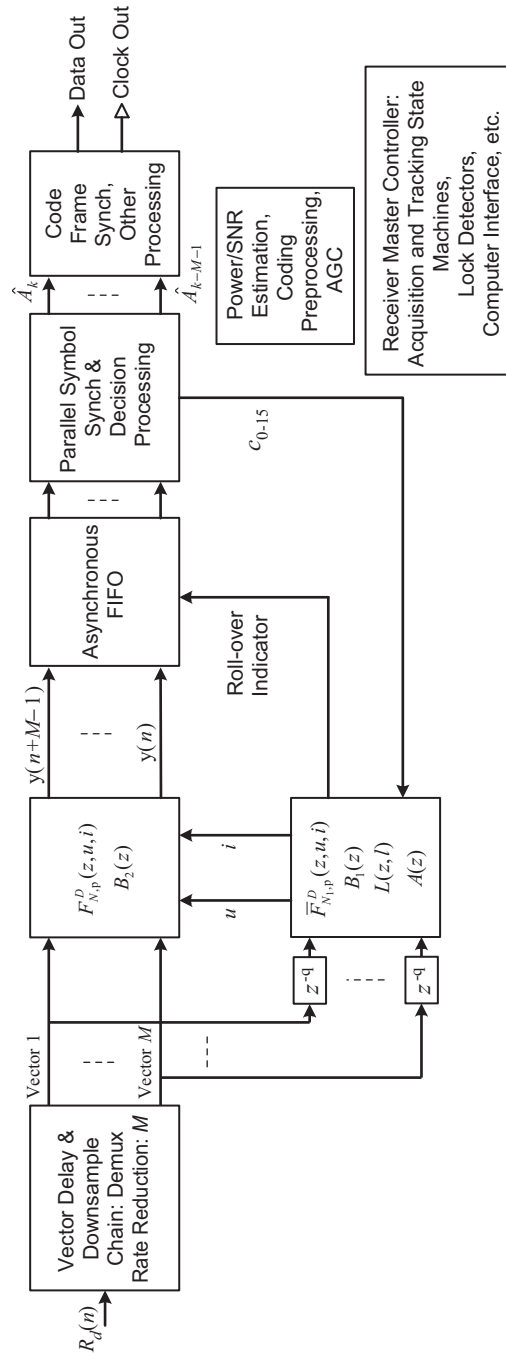
Fig. 6-106. Alternative parallel demodulator architecture: slot-synchronization error estimation with filter bank $\overline{F}_{N1,p}^{D}(z,u,i)$ and equalizer filter $B_1(z)$ separated from the post-detection filter bank $F_{N,p}^{D}(z,u,i)$ and detection equalizer $B_2(z)$; the processing rate of the filter $\overline{F}_{N1,p}^{D}(z,u,i) = M(f_s)/L$ and filter $F_{N,p}^{D}(z,u,i) = f_s/M$.

The processing rate of the filter $\overline{F}^D_{N_1,p}(z,u,i) = M(f_S)/L$, the rate of filter the $F^D_{N,p}(z,u,i)$ is f_S/M. The time-varying filter $\overline{F}^D_{N_1,p}(z,u,i)$ and pulse equalizer $B_1(z)$ for slot-timing error estimation may be designed and implemented independently of the time-varying post-detection filter $F^D_{N,p}(z,u,i)$ for filtering and signal timing error correction and the equalizer $B_2(z)$ for pulse filtering (possibly for pulse distortion mitigation). Note the signal delay (z^{-q}) between the slot-synchronization processing and the signal path containing the post-detection filter bank and the decision processing. This is to facilitate appropriate feedback from symbol synchronization to slot synchronization if such a decision-directed system is desired. This delay is not in the feedback path of the closed-loop synchronization algorithm. This is not the case for the architecture of Fig. 6-103, which required a delay in the feedback path in order to be decision-directed. This delay may be small, but any delay in the feedback has the potential to degrade synchronization performance.

Summarizing the advantages of the architecture in Fig. 6-106, first filter bank $\overline{F}^D_{N_1,p}(z,u,i)$ may be designed and optimized for synchronization estimation performance independently of the filter bank $F^D_{N,p}(z,u,i)$ used for correction timing errors and filtering for the decision process. The filter bank $\overline{F}^D_{N_1,p}(z,u,i)$ may incorporate many more design choices and may be many times more computationally intensive, that is a larger number of coefficients and/or larger resolution, and/or larger N than would otherwise be possible. The architecture of Fig. 6-106 does not require an additional delay in the synchronization feedback path in order to be decision-directed. This architecture may or may not be a good choice over the architectures of Fig. 6-99 or Fig. 6-103. Depending on the system, desired performance and regions of operation, and the resulting filter bank design(s), the architecture of Fig. 6-106 may be more or less computationally intensive than the architectures of Fig. 6-99 or Fig. 6-103.

The filter bank $F^D_{N,p}(z,u,i)$ may be designed for specific pulse shapes and jitter conditions. Although the on-chip memory requirements likely preclude one of numerous banks of filters to be chosen on-the-fly without reconfiguration, there is another solution. As an example of the flexibility of this architecture when targeting reconfigurable (FPGA) VLSI implementation multiple filter banks, k filter banks, $F^D_{k,N,p}(z,u,i)$, may be developed and stored off-line and reconfigured for field tests and experiments very rapidly (seconds or less).

Finally, the architectures presented in this section are examples of those that may be developed given the methods and framework presented in this work along with other multirate discrete-time signal processing theorems and communications demodulator algorithms found in the literature. Many further discrete-time PPM demodulator architecture variations may be developed with varying degrees of complexity and performance. The conclusion includes a discussion of the high speed digital platform suitable for implementing such architectures and the development process that facilitates an evolving architecture development incorporating software modeling and simulation, analysis, laboratory experimentation, and rapid prototyping. We now present the key design equations for understanding the architecture from a frequency (clock rate) and transmission line perspective; these are useful in understanding the complexity and challenges of the high-speed platform that is used to implement the class of architectures presented here.

6.3.9 Primary System Models and Parameters

There are several aspects of the discrete-time architecture illustrated in Fig. 6-99 that must be considered in the development of the high-speed digital platform. Two of the most significant are the frequency (clock rate) requirements and the number of required data transmission lines. These requirements are largely determined by the sample rate of the system along with the hardware limitations of the digital devices used to realize the discrete-time or digital architectures that together determine M and the number of parallel input/output signals.

The primary clock frequencies are represented in the first four illustrations in Fig. 6-107, the maximum frequencies are in the right-most shaded column. These clock relationships are critical for such things as high-speed platform design, VLSI circuit design, and floor-planning. The relationship between the clock frequency on a given axis and the clock frequency on one axis above is given in the left-most shaded column. The fastest digital clock rate is the sample frequency (also referred to as the system frequency) on the top axis; this rate is reduced by the serial-to-parallel conversion, resulting in the divide by M. The slot rate clock is represented on the second axis, the symbol frequency is given on the third axis, and the bit clock frequency is given in the fourth axis. The slot synchronization loop bandwidth is illustrated on axes as a fraction of the symbol rate.

Certain fundamental design equations of the architecture given in Fig. 6-99 are now summarized. The variables in these equations fall into two categories: *design parameters* and *operational parameters*. It is a key step in the development of complex VLSI systems to assign all parameters to one of these two categories. Such categorization is essential for establishing priorities and the associated schedule for establishing parameter values. This, in turn, allows

development resources to be focused appropriately for various development strategies; one of which is summarized in the conclusion of this work. The two categories are defined as follows.

1) Design parameters determine the physical construction of the prototype board layout and design, the VLSI device, the package, and numerous other significant elements of the design. These physical parameters are generally either not reconfigurable after manufacture or require significant redesign. These parameters should be determined before significant design work is undertaken.

(a) Frequency Equations   Maximum

$0 \quad \dfrac{f'_S}{16} \quad \dfrac{f'_S}{8} \quad \dfrac{f'_S}{M} \quad \dfrac{f'_S}{2} \quad f'_S$

Sample Frequency

(b)

$f^{8,M}_{slot} = \dfrac{1}{8}\left(\dfrac{f'_S}{M}\right) - \Delta f \quad f^{D,M}_{slot} = \dfrac{1}{D}\left(\dfrac{f'_S}{M}\right) - \Delta f \quad f^{2,M}_{slot} = \dfrac{1}{2}\left(\dfrac{f'_S}{M}\right) - \Delta f \qquad \Delta f \text{ represents} \qquad \dfrac{f'_S}{M}$

the Doppler

Slot Frequency   shift in slot

frequency

(c)

$f^{8,D,M}_{sym} = \dfrac{1}{2^8} f^{D,M}_{slot} \quad f^{k,D,M}_{sym} = \dfrac{1}{2^k} f^{D,M}_{slot} \quad f^{1,D,M}_{sym} = \dfrac{1}{2^1} f^{D,M}_{slot} \qquad f^{D,M}_{slot} = \dfrac{1}{D}\left(\dfrac{f'_S}{M}\right) - \Delta f$

Symbol Frequency

(d)

$f^{8,D,M}_{bit} = 8\left(f^{k,D,M}_{sym}\right) \quad f^{k,D,M}_{bit} = k\left(f^{k,D,M}_{sym}\right) \quad f^{1,D,M}_{bit} = 1\left(f^{k,D,M}_{sym}\right) \qquad f^{k,D,M}_{sym} = \dfrac{1}{2^k} f^{D,M}_{slot}$

Bit Frequency

(e)

$B_L = (0.0001) f^{k,D,M}_{sym} \quad B_L = (B_D) f^{k,D,M}_{sym} \quad B_L = (0.001) f^{k,D,M}_{sym} \qquad f^{k,D,M}_{sym} = \dfrac{1}{2^k} f^{D,M}_{slot}$
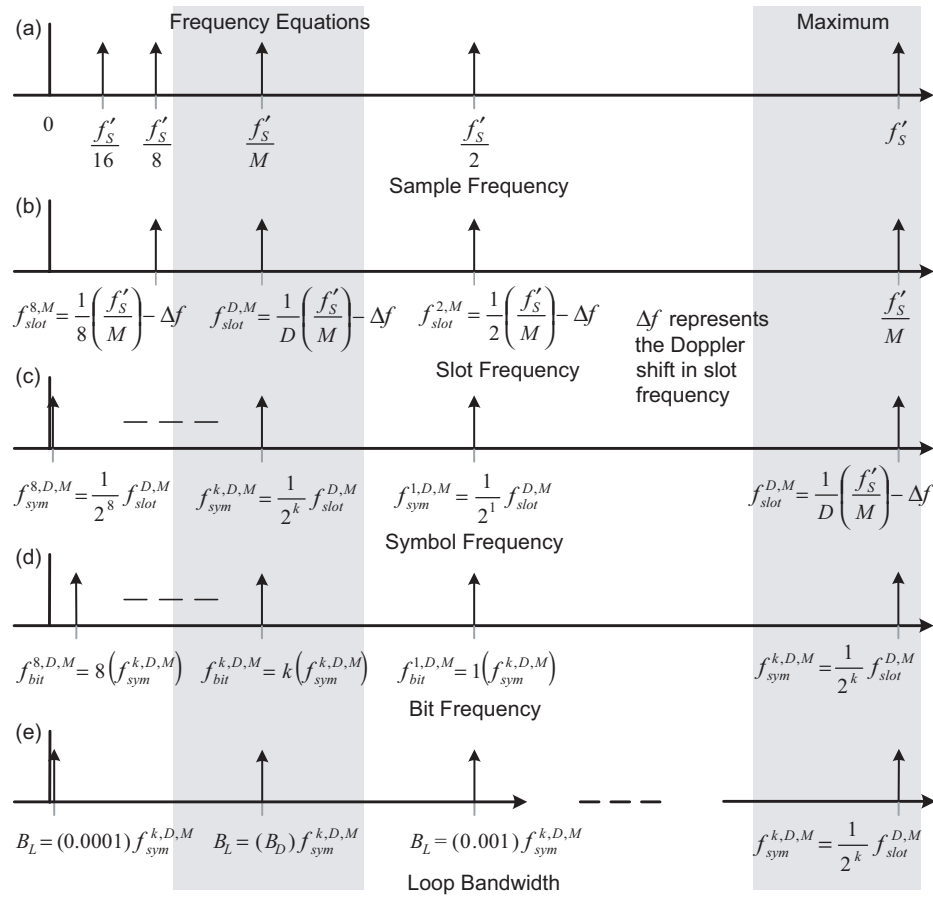
Loop Bandwidth

Fig. 6-107. Frequency model.

2) Operational parameters may take on a variety of values depending on the requirements of the system. The operational parameters are either programmable or reconfigurable without significant redesign. The values of these parameters generally do not need to be known precisely before design or even during hardware implementation and test. However, the range, the maximum and minimum values, should be established or estimated as early as possible in the development process.

The top-level design equations and parameters for the architecture in Fig. 6-99 are given in Table 6-6. This is not a comprehensive list of equations describing the digital demodulator, but the most essential ones in early phase hardware development.

Figure 6-108 illustrates a simple digital input/output model of the architecture in Fig. 6-99. This model indicates the approximate number of digital input/output transmission lines required between major signal processing sub-systems of the demodulator. Of primary concern is the number of transmission lines at the output of the parallel-to-serial converter. The number of lines cannot exceed the input capability of the device used to implement the rest of the demodulator. At the same time, the number of lines must support the rate reduction required.

6.3.10 Conclusion and Future Work

Discrete-time demodulator architectures for broadband free-space optical PPM, which are capable of Nyquist or near Nyquist data rates were presented. While these architectures do not represent unique solutions, methods, or designs, they were developed within a framework that encompasses a large body of theoretical work in optical communications, synchronization, and multirate discrete-time signal processing; and they were constrained by many of the limitations of the state-of-the-art digital hardware. The primary focus of this work was on the development of discrete-time processing of the most fundamental algorithms and processing required in PPM demodulators; those necessary for post-detection filtering, synchronization, and decision processing. Numerous other processing subsystems are required in an operational receiver. Integrated in the development and discussion were numerous considerations of modern VLSI devices as well as platform design. The most fundamental design decisions, those globally impacting platform design or fundamentally limiting performance, are summarized as follows:

- The development targets an all-digital approach as opposed to a hybrid analog-digital or primarily analog implementation.
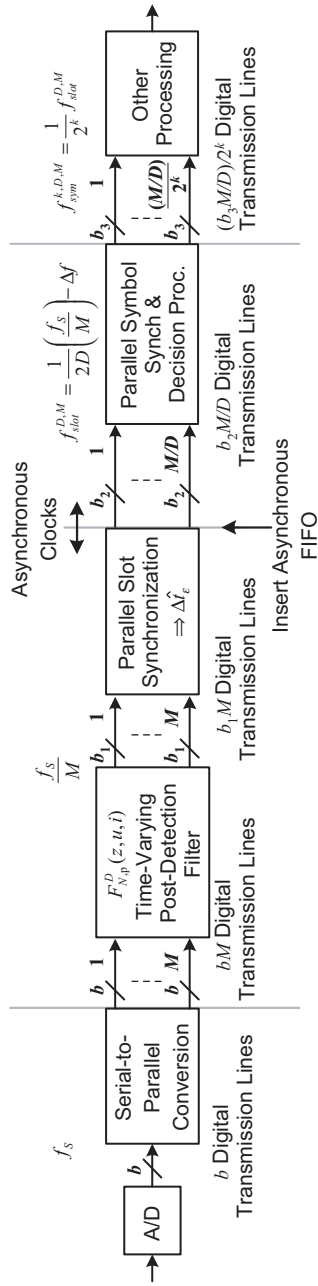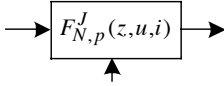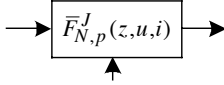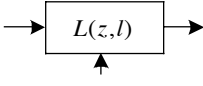
Fig. 6-108. Data I/O model.

Table 6-6. List and description of primary design functions.

Design Function	Parameter Description
$f_{bit}^{k,D,M} = \dfrac{k}{2^k DM}\left(\dfrac{f_S}{M}\right)$ $= \underbrace{\left(\dfrac{k}{2^k}\right)}_{\substack{\text{Operational}\\\text{Parameter}}} \underbrace{(f_s)\ \left(\dfrac{1}{D}\right)\ \left(\dfrac{1}{M}\right)}_{\substack{\text{Design}\\\text{Parameters}}}$	*Operational:* k = The number of bits per symbol *Design:* D = Nominal number of samples per slot M = Processing rate reduction f_S = Ideal sample rate, not actual sample rate
$f_{sym}^{k,D,M} = \dfrac{1}{2^k} f_{slot}^{D,M}$	*Operational:* k = bits per symbol 2^k = Number of slots per symbol
$\dfrac{D}{T_{slot} + T_{slot}\left(\dfrac{v_{min}}{c}\right)} \le f_S'$	*Design:* f_S' = The actual sample rate must be greater than the Doppler-shifted slot rate times D
Parallel Time-Varying Post-Detection Filter $\longrightarrow \boxed{F_{N,p}^J(z,u,i)} \longrightarrow$ $\uparrow$ i = sample index u = sub-sample index $h_{dN}(n)$ or $v(n)$ prototype filter	*Operational:* N = Prototype FIR filter oversample rate, maximum residual sample offset = $T_S/(2N)$, there are N filters in the filter bank RDN = Number of coefficients in the prototype filter $J(T_S)$ = Timing error accumulated before roll-over
Parallel Time-Varying Slot-Synch Filter $\longrightarrow \boxed{\bar{F}_{N,p}^J(z,u,i)} \longrightarrow$ $\uparrow$ i = sample index u = sub-sample index $h_{dN}(n)$ or $v(n)$ prototype filter	*Operational:* N = Prototype FIR filter oversample rate, maximum residual sample offset = $T_S/(2N)$, there are N filters in the filter bank RDN = Number of coefficients in the prototype filter $J(T_S)$ = Timing error accumulated before roll-over
Slot Synch Loop Filter $\longrightarrow \boxed{L(z,l)} \longrightarrow$ $\uparrow$ l = filter tracking/acquisition index $B_{LD} = (B_N) f_{sym}^{k,D,M}$	*Operational:* B_{LD} = Discrete-time bandwidth of IIR loop filter: $G_{1,l}$, $G_{2,l}$, $G_{3,l}$ B_N = Discrete-time bandwidth normalized as a fraction of the symbol rate (B_L = Prototype analog loop filter bandwidth)
$\dfrac{1}{T_{slot}} \le f_{\text{digital}} \dfrac{1}{T_{slot} + T_{slot}\left(\dfrac{v_{min}}{c}\right)}$	*Operational:* f_{digital} = Normalized digital slot frequency rate

- The all-digital design or lack of feedback from digital-to-analog processing results in tremendous flexibility without redesign; the many orders of magnitude (typically greater than 8 with current CMOS) possible with digital implementation can be achieved without the difficulties and limitations of the digital-to-analog feedback approach.

- The fixed-sample per slot design results in a simplified demodulator development. As the symbol rate changes, the number of samples per slot remains constant. Once one data rate has been tested and verified, a large subset of characteristics and parameters for all data rates has been verified; thus, the end result is a more simple and time-efficient development. The downside of this approach is that the anti-aliasing filter before the A/D may require a variable bandwidth, and these issues are discussed further in [105,106]. This latter is one motivation for not using this fixed number of samples per slot approach, and there are others. It should be noted that the design process and the reconfigurable platform do not fundamentally limit the choice of alternative designs for different data rates, or for a different number of samples per slot. With an FPGA approach and an appropriately designed platform, the decision to use a different number of samples per slot may be made at virtually any phase of the development, although architecture iteration would be required.

There are numerous other design decisions that were made here and even more that are yet to be made during the development. Many of these decisions require further analysis, such as precisely which slot-synchronization algorithm to use and its parameter values for various regions of operation (SNR and signal dynamics), and many are decisions made by digital designers that have no direct impact on communications performance and are not dependent on regions of operation. It must be understood that a great many of these open-design questions cannot be answered by considering and optimizing one or even a small number of factors. Answering design questions about VLSI systems as complex as those illustrated in Figs. 6-99, 6-103, and 6-106 are usually not about optimality of a criterion but trading off many criteria against one another. One of the motives of Section 6.3.8 was to illustrate some of these trades. If the core problem posed there (asynchronous parallel processing) had been done so and analyzed in purely mathematical terms, the most critical design questions would have been largely obscured. The asynchronous filter bank design is a very complex undertaking with numerous tradeoffs made between hardware complexity, rate reduction, impact of filter design on communications systems performance (synchronization and decision processing), and commercially available methods for processing asynchronous data streams (many of which are device dependent).

The focus in this work was not on the analysis of performance of optical communications systems; although the architectures presented are capable of

closely approximating theoretical performance of certain continuous-time systems. This assertion is given without mathematical proof, but basic simulation results of a software model were presented. In addition there are numerous examples of communications algorithms and theoretical constructs based on similar signal processing theories and structures [105,106]. The performance analysis of the parallel architectures presented here is a significant undertaking and must incorporate the numerous characteristics of the deep-space optical communications channel including the primary transmitter and front-end detector characteristics. Figure 6-109 illustrates the development path of a digital receiver from a high level.

Figure 6-110 illustrates the development path in greater detail. The state-of-the art hardware development process is given with emphasis on VLSI circuit realization in FPGA devices. These devices have revolutionized modern hardware design. In addition to the obvious advantages of reconfigurable hardware, the stringent risk reduction and management techniques required by historical methods of VLSI implementation (analog and digital), particularly application-specific integrated circuits, are significantly relaxed. This results in a significantly altered design process. In addition, the inclusion of a development feedback path is possible as depicted in the figure; such paths were often not feasible in VLSI design and implementation before the advent of the FPGA.

This process, if used correctly and in conjunction with a well designed hardware platform, facilitates rapid prototypes to be generated targeting specific applications. If the application changes, the design can be reiterated. *Arguably the largest advantage of this process targeting reconfigurable devices is the ability to make forward progress without a full set of requirements or without establishing values for all operational parameters. This is often the case with new or untested complex systems where a combination of analysis*
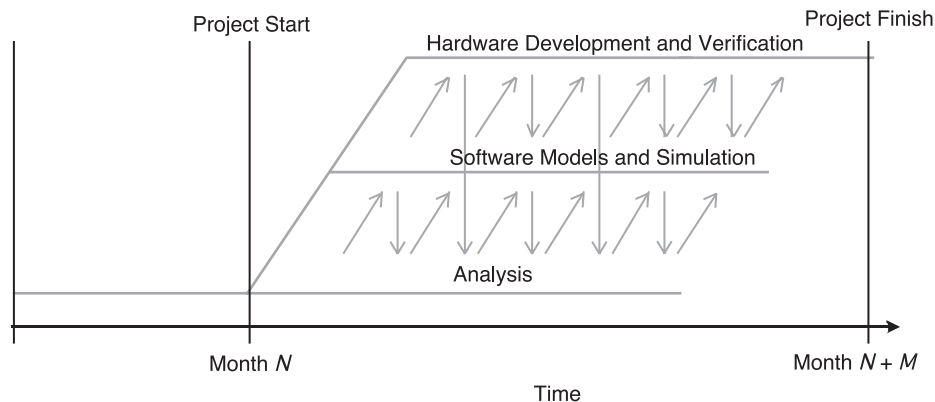
Fig. 6-109. Parallel development model.

and experimental physical work must be accomplished in conjunction to advance the state-of-the art. However, a certain set of design parameters must be established to properly design the hardware platform; if not commercially available, this platform design itself requires another design process with many steps whose description is beyond the scope of this work. Certainly such things as A/D selection, FPGA selection, determination of maximum clock rates and clock rate ranges, and a host of other parameters must be determined before the platform design and implementation or commercial purchase is made in the event that a commercial solution is available.

The development in this work was presented at a sufficiently high level to address the most significant challenges of the all-digital design and

Fig. 6-110. State-of-the-art design process: the path from concept to operational digital demodulator.

implementation. There were many omissions in the work presented here that must be addressed in the development of a complete receiver. The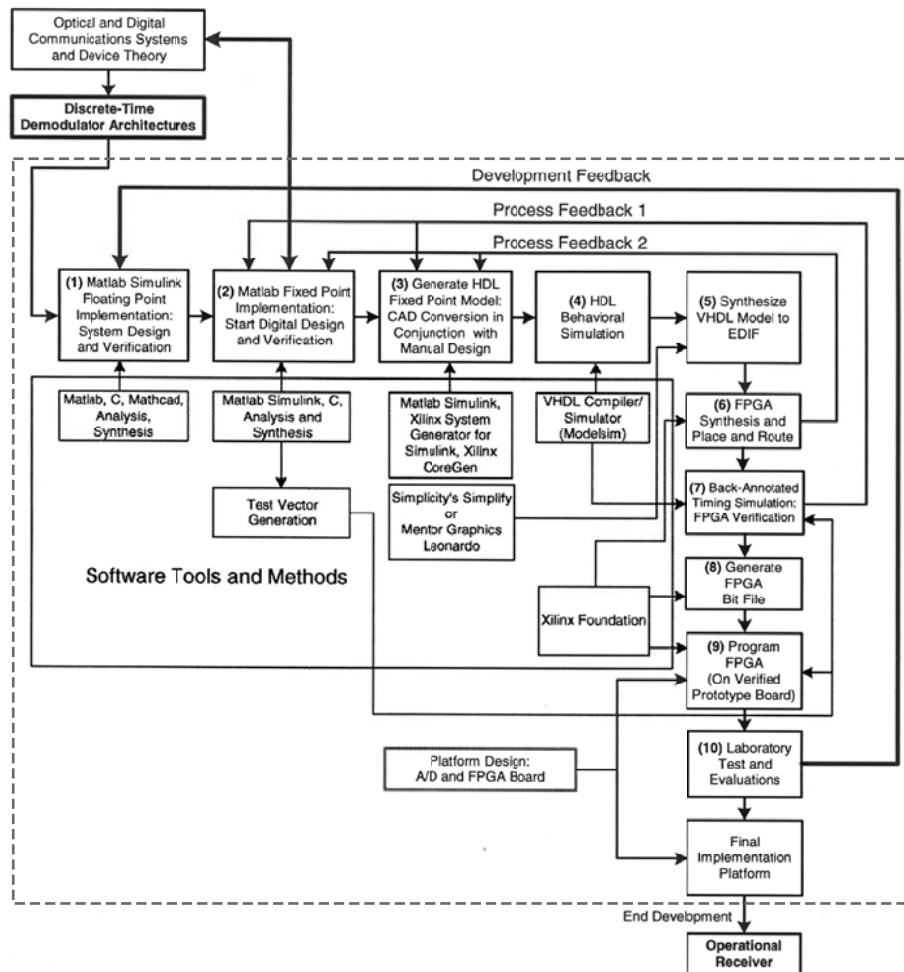 primary issues of the demodulator development in the pre-hardware laboratory test phase, many of which should be addressed targeting a specific set of requirements, are summarized below.

- The architectures presented may be further developed to incorporate numerous simplifications; many of these simplifications occur in a complex trade-space of performance and implementation device limitations. Of particular interest is minimizing the complexity of the filter bank $F_{N,p}^D(z,u,i)$.

- The function of automatic gain control (AGC) was largely ignored in this work. This circuit may be accomplished in analog or digital circuits or both. In many systems a "course" AGC circuit is used to control the amplitude of the signal input to the A/D to avoid clipping and underflow, while a "fine" AGC is implemented digitally to provide tight control of amplitude for such signal processing systems as the slot synchronization loop whose stability, bandwidth, damping factor, and overall performance depend on amplitude statistics.

- The completed discrete-time demodulator architecture must be converted to include quantized amplitude. This typically involves varying degrees of analysis and simulation.

- The performance and type, open or closed loop, of the discrete-time slot synchronization algorithm must be established for various receiver regions of operation using analysis techniques outlined in references presented in this work.

- When a closed-loop system derived from variations of Fig. 6-74 and the references given in Section 6.3.3.2 the required analysis may be broken down into a number of subtasks:
  - The discrete-time loop design equation must be established; and gain margin, bandwidth, damping factor, and many other characteristics must all be determined.
  - Characterization of synchronization performance with the large signal amplitude fluctuation characteristic of the optical channel.
  - Tracking versus acquisition performance must be established for the operational scenario or scenarios. This will include development of an acquisition algorithm. Among other things this algorithm might determine when to switch loop filter bandwidths autonomously.
  - Slot lock detection circuits and performance must be established. Probability of false-lock and false-alarm must be established for these circuits.
  - Performance in the presence of transmitter and receiver oscillator jitter must be established.

- A simple interpolation filter may be used with the system of Figs. 6-101 through 6-106. However, the slot or interpolation filter might be designed to achieve specified performance of the PPM slot synchronization loop. The design might be further refined to incorporate criteria derived from the optimal detection given the actual channel.
- Symbol synchronization performance and lock detection must be established. Blind or pilot sequence system or both may be implemented.
- Complete end-to-end system Monte-Carlo or pseudo-Monte-Carlo performance modeling and simulation of the demodulator must be performed. This type of comprehensive validation is accomplished in phases, starting with basic subsystem validation and progressively including more and more subsystems and channel parameters. This type of testing and validation accomplishes two goals, first system performance may be determined or approximated when doing so analytically is not possible or not feasible, and second cost and schedule risks of validating an operational system in the field are reduced. To first order, the resources that are spent on these end-to-end simulations is determined by the level of performance prediction required, the number of operational scenarios, and the risk tolerance of the project. As an example, before a system as complex as that of Fig. 6-103 is field tested, thousands of hours of simulations will be run to accomplish these goals even with moderate risk reduction goals over a moderate number of operational scenarios (a few dozen); many times that number may be utilized for more thorough validation across a more complex set of operating scenarios. These test and verification plans are integrated into the process of Fig. 6-108.
- More optimal slot synchronization algorithms might be developed. In addition, the decision-directed slot and symbol loops, different slot synchronization algorithms might be derived based on open-loop optimality criterion. It is envisioned that such algorithms may be implemented in the architecture given in Figs. 6-99, 6-103, or 6-106 with design evolution (it is envisioned that the majority of the architecture will remain unchanged).
- Modern forward error correction (FEC) decoders may require preprocessing; the performance of this preprocessing must be established.

This is a grossly simplified list of tasks that must be completed as part of the development of the parallel digital demodulator for free-space optical PPM. Before comprehensive laboratory testing and validation of the complete demodulator is undertaken the majority of these tasks should be completed. However, the process of Fig. 6-108 is flexible and gives project managers many

options for trading development schedule and progress with risk. It is possible and in many cases highly desirable to largely complete certain stand-alone signal processing subsystems, that is step them through the entire process of Fig. 6-108, and verify that subsystem with a laboratory hardware test. Such "front-runner" efforts serve a valuable process-risk reduction role by validating the applicability and suitability of various vendor tools and software tool upgrades, as well as hardware devices and platforms. Such "front-runner" activities also serve to demonstrate and validate the end-to-end concept-to-hardware process.

References

[1]   H. P. Stahl, G. H. Rowell, G. Reese, A. Byberg, "Multivariable Parametric Cost Model for Ground-Based Telescopes," *Proceedings of the SPIE*, vol. 5497, *Modeling and Systems Engineering for Astronomy*, S. C. Craig and M. J. Cullum, editors, pp. 173–180, September 2004.

[2]   J. E. Carey, C. H. Crouch, and E. Mazur, "Femtosecond Laser-Assisted Microstructuring of Silicon Surfaces," *Optics and Photonics News*, vol. 14, no. 2, pp. 32–36, February 2003.

[3]   D. L. Robinson and J. R. Lesh, "A Cost-Performance Model for Ground-Based Optical Communications Receiving Telescopes," *Proceedings of SPIE OE Lase*, Paper 756-20, pp. 130–134, SPIE, Bellingham, Washington, January 1987.

[4]   K. Shaik, M. Wilhelm, and R. Horttor, *Ground Based Advanced Technology Study (GBATS)*, JPL D-11000 (internal document), Jet Propulsion Laboratory, Pasadena, California, August 5, 1994.

[5]   E. L. Kerr, "Strawman Optical Reception Development Antenna (SORDA)," *The Telecommunications and Data Acquisition Progress Report 42-93, January–March 1988*, Jet Propulsion Laboratory, Pasadena, California, pp. 97–110, May 15, 1988.
      http://ipnpr.jpl.nasa.gov/progress_report/

[6]   D. Wonica, "Economical 10-m Class Ground-Based Receiver for Deep-Space Optical Communications," *Proceedings of the SPIE*, vol. 2123, *Free-Space Laser Communication Technologies VI*, G. S. Mecherle, Editor, pp. 487–497, August 1988.

[7]   C. Kramer, C. G. Degiacomi, U. U. Graf, R. E. Hills, M. Miller, R. T. Schieder, N. M. Schneider, J. Stutzki, and G. F. Winnewisser, "New KOSMA 3-m Telescope," *Proceedings of the SPIE*, vol. 3357, *Advanced Technology MMW, Radio, and Terahertz Telescopes*, T. G. Phillips, Editor, pp. 711–720, July 1998.

[8]   J. A. Booth, M. J. Wolf, J. R. Fowler, M. T. Adams, J. M. Good, P. W. Kelton, E. S. Barker, P. Palunas, F. N. Bash, L. W. Ramsey, G. J. Hill, P. J. MacQueen, M. E. Cornell, and E. L. Robinson, "The Hobby Ebberly Completion Project," *Proceedings of the SPIE*, vol. 4837, *Large Ground-based Telescopes*, J. M. Oschmann, L. M. Stepp, Editors, pp. 919–933, February 2003.

[9]   E. Kerr "An Integral Sunshade for Optical Receiving Antennas," *The Telecommunications and Data Acquisition Progress Report 42-95*, *July–September 1988*, Jet Propulsion Laboratory, Pasadena, California, pp.180–195, November 15 1988.
http://ipnpr.jpl.nasa.gov/progress_report/

[10]   E. L. Kerr and C. W. DeVore, "Shutters and Slats for the Integral Sunshade of an Optical Reception Antenna," *The Telecommunications and Data Acquisition Progress Report 42-95*, *July–September 1988*, Jet Propulsion Laboratory, Pasadena, California, pp. 196–201, November 15, 1988.

[11]   B. Clymer "Reflected Sunlight Reduction and Characterization for a Deep Space Optical Receiver Antenna (DSORA)" *The Telecommunications and Data Acquisition Progress Report 42-103, July–September 1990,* Jet Propulsion Laboratory, Pasadena, California, pp. 110–117, November 15 1990.
http://ipnpr.jpl.nasa.gov/progress_report/

[12]   K. Wilson, *Trip Repot to Duisburg, Germany and Zermatt, Switzerland*, JPL D-32056 (JPL Internal document), Jet Propulsion Laboratory, Pasadena, California, November 5, 1997.

[13]   J. V. Sandusky, D. J. Hoppe, and M. J. Britcliff, "Deep Space Optical Reception Antenna (DSORA): Aperture Versus Quality," *The Telecommunications and Mission Operations Progress Report 42-143*, *July–September 2000*, pp. 1–11, November 15, 2000.
http://ipnpr.jpl.nasa.gov/progress_report/

[14]   Hextek Corporation web site, accessed June 7, 2005.
http://www.hextek.com

[15]   S. Piazzolla and S. Slobin, "Statistics of Link Blockage Due to Cloud Cover for Free-Space Optical Communication Using NCDC Surface Weather Observation Data," SPIE Meeting, San Jose, California, 2002, *Proceedings of the SPIE*, vol. 4635, *Free-Space Laser Communication Technologies XVI*, G. Stephen Mecherle, editor, pp. 138–149, April 2002.

[16]   R. P. Link, R. J. Alliss, and M. E. Craddock, "Mitigating the Effect of Clouds on Optical Communications," *Proceedings of SPIE*, vol. 5338, *Free-Space Laser Communication Technologies XVI*, G. S. Mecherle, C. Y. Young, J. S. Stryjewski, editors, pp. 223–232, June 2004.

[17]   K. Wilson M. Troy, M. Srinivasan, B. Platt, V. Vilnrotter, M. Wright, V. Garkanian, H. Hemmati, "Daytime Adaptive Optics For Deep Space Optical Communications" *Space Activities and Cooperation Contributing to All Pacific Basin Countries: Tenth International Space Conference of Pacific Basin Countries, ISCOPS*, Tokyo, Japan, December 10–12, editors: P. M. Bainum, L. Furong, T. Nakajima, American Astronomical Society, pp. 481–492, 2003.

[18]   G. S. Mecherle, W. Akle, C. J. Starkus, J. E. Klein, and G. W. Holleman, "Coherent Detection Optical Relay Satellite for Deep-Space Communication," *Proceedings of SPIE*, vol. 2123, *Free-Space Laser Communication Technologies VI*, G. S. Mecherle, editor, pp. 218–236, August 1994.

[19]   G. S. Mecherle, W. Akle, C. J. Starkus, and J. E. Klein, "Direct Detection Optical Relay Satellite for Deep-Space Communication," *Proceedings of SPIE*, vol. 2123, *Free-Space Laser Communication Technologies VI*, G. S. Mecherle, editor, pp. 134–155, August 1994.

[20]   K.E. Wilson, K. Shea, J. Ceniceros, M. Wright, and R. Cesarone, "Cost and Performance Comparison of an Earth-Orbiting Optical-Comm Relay Transceiver and a Ground-based Optical Receiver Subnet," *The Interplanetary Network Progress Report 42-153, January–March 2003*, Jet Propulsion Laboratory, Pasadena, California, pp. 1–12, May 15, 2003. http://ipnpr.jpl.nasa.gov/progress_report/

[21]   S. C. Casey, "The SOFIA Program: Astronomers Return to the Stratosphere," *Advances in Space Research*, vol. 34, pp. 560–567, 2004.

[22]   K. Wilson, H. Hemmati, and S. Lee, *Mars Optical Communications Study Report*, JPL D-28438 (internal document), Jet Propulsion Laboratory, Pasadena, California, September 26, 2001.

[23]   *NMP ST6 Final Briefing Acquisition, Pointing and Tracking for Interplanetary Optical Communication*, Ball Aerospace and Technologies Corporation and Jet Propulsion Laboratory Optical Communications Group, Ball Aerospace, Boulder, Colorado, August 2001.

[24]   J. Berg and R. St. Piere, *Solid State Lasers OTRW Presentation to JPL, July 1, 1997*, JPL D-32057 (internal document), Jet Propulsion Laboratory, Pasadena, California, 1997.

[25]   N. Savage, "Fiber Lasers Power up," *Optical Engineering Magazine*, vol. 3, p. 53, August 2003.

[26]   N. Peyghambarian and A. Schülzen, "High Power Devices in Compact Packages," *Optics and Photonics News*, pp. 36–41, June 2005.

[27] D. L. Fried, "Aperture Averaging of Scintillation," *Journal of the Optical Society of America*, vol. 57, no. 2, pp. 169–175, 1967.

[28] J. Churnside, "Aperture Averaging of Optical Scintillations in the Turbulent Atmosphere," *Applied Optics*, vol. 30, no. 15, pp. 1982–1994, 1991.

[29] J. C. Christou, B. Ellerbroek, R. Q. Fugate, D. Bonaccini, and R. Stanga, "Rayleigh Beacon Adaptive Optics Imaging of ADS 9731: Measurements of the Isoplanatic Field of View," *Astrophysical Journal*, vol. 450, pp. 369–379, September 1, 1995.

[30] P. Wizinowich, D. S. Acton, C. Shelton, J. Gathright, K. Ho, W. Lupton, K. Tsubota, O. Lai, C. Max, J. Brase, J. An, K. Avicola, S. Olivier, D. Gavel, B. McIntosh, A. Ghez, and J. Larkin, "First Light Adaptive Optics Images from the Keck II Telescope: A New Era of Angular Resolution Imagery," *Publications of the Astronomical Society of the Pacific* (PASP), vol. 112, pp. 315–319, March 2000.

[31] J. M. Spinhirne and G. A. Ameer, "Adaptive Optics Using the 3.5-m Starfire Optical Range Telescope," Proceedings of SPIE, vol. 3126, Adaptive Optics and Applications, R. K. Tyson and R. Q. Fugate, editors, pp. 257–268, October 1997.

[32] P. M. Metzen "High Reliable Copper Vapor Lasers," *Proceedings of the ESO Workshop Laser Technology for Guide Star Adaptive Optics Astronomy*, Garching, Germany June 23–26, 1997.

[33] E. Kibblewhite, "The Design and Performance of Laser Systems for Generating Sodium Beacons," *Proceedings of NATO Advanced Studies Institute on Laser Guide Star Adaptive Optics for Astronomy*, vol. 551, September 20–October 10 , 1997, edited by N. Ageorges and C. Dainty, Kluwer Academic Publishers, pp. 67–87, 1997.

[34] S. S. Olivier, J. A. K. Avicola, H. D. Bissinger, J. M. Brase, H. W. Friedman, D. T. Gavel, C. E. Max, J. T. Salmon, and K. E. Waltjen, "Performance of Laser Guide Star Adaptive Optics at Lick Observatory," *Proceedings of the SPIE*, vol. 2534, San Diego, California, pp. 26–37, August 1995.

[35] S. S. Oliver, D. T. Gavel, "Tip-tilt Compensation for Astronomical Imaging," *Journal of the Optical Society of America* A, vol. 11, no. 1, pp. 368–374, January 1994.

[36] R. Foy, J.-P. Pique, A. Petit, P. Chevrou, V. Michau, G. Grynberg, A. Migus, N. Ageorges, V. Bellanger, F. Biraben, R. Deron, H. Fews, F. Foy, C. Högemann, M. Laubscher, D. Mül1er, C. d'Orgeville, O. Peillet, M. Redfern, M. Schöck, P. Segonds, R. Soden, M. Tallon, E. Thiébaut, A. Tokovinin, J. Vaillant, and J.-M. Weulersse, "Polychromatic Guide Star Feasibility Study," *Proceedings of the SPIE*, vol. 4065, *High-Power Laser Ablation III*, C. R. Phipps, editor, pp. 312–323, August 2000.

[37] M. Reyes, A. Comeron, A. Alonso, A. Rodriguez, J.A. Rubio,V. Fedrico Dios, S. Chueca, and S. Zodnik, "Ground-to-Satellite Bidirectional Laser Links For Validation of Atmospheric Turbulence Model," *Proceedings of the SPIE*, vol. 4821, Seattle, Washington, pp. 33–43, July 2002.

[38] C. Higgs, H. Barclay, D. Murphy, and C. A. Primmerman, "Multibeam Illumination," *Lincoln Laboratory Journal*, vol. 11, pp. 8–22, 1998.

[39] M. Jeganathan, K. E. Wilson, and J. R. Lesh, "Preliminary Analysis of Fluctuations in the Received Uplink-Beacon-Power Data Obtained From the GOLD Experiments," *The Telecommunications and Data Acquisition Progress Report 42-124, October–December 1995*, pp. 20–32, Jet Propulsion Laboratory, Pasadena, California, February 15, 1996. http://ipnpr.jpl.nasa.gov/progress_report/

[40]   K. E. Wilson, A. Biswas, S. Bloom, and V. Chan "Effect of Aperture Averaging on a 570 Mbps 42 km Horizontal Path Optical Link," *Proceedings of the SPIE*, vol. 2471, pp. 244–253, April 1995.

[41] H. T. Yura and W. G. McKinley, "Optical Scintillation Statistics for IR Ground-to-Space Laser Communications," *Applied Optics*, vol. 22, no. 21, pp. 3353–3358, November 1, 1983.

[42] K. Wilson, W. T. Roberts, V. Garkanian, F. Battle, R. Leblanc, H. Hemmati, and P. Robles "Plan for Safe Laser Beam Propagation from the Optical Communications Telescope Laboratory," *The Telecommunications and Data Acquisition Progress Report, 142-152, October–December 2002*, Jet Propulsion Laboratory, Pasadena, California, pp. 1–17, February 15, 2003.

[43] K. E. Wilson and J. R. Lesh, "An Overview of the Galileo Optical Experiment (GOPEX)," *The Telecommunications and Data Acquisition Progress Report 42-114, April–June 1993*, Jet Propulsion Laboratory, Pasadena, California, pp. 192–204, August 15, 1993. http://ipnpr.jpl.nasa.gov/progress_report/

[44] *RCA - Primus - Honeywell - Sperry Primus-40 WXD Digital Radar Maintenance Manual*, IB8029050, Rev-3, p. 4-3, October 1978.

[45] M. Skolnik, *Introduction to Radar Systems*, Second Edition, McGraw–Hill (New York, St. Louis), p. 15, 1980.

[46] L. D. Smullin and G. Fiocco, "Project Luna See," Institute of Electrical and Electronics Engineers Proceedings, vol. 50, pp. 1703–1704, 1962.

[47] L. H. Allen, M. S. Schumate, and J. W. Young, *The Surveyor-VII Laser Pointing Experiment Table Mountain Station Description*, JPL D-32055 (internal document), Jet Propulsion Laboratory, Pasadena, California, 1968.

[48] K. E. Wilson and J. R. Lesh, "An Overview of the Galileo Optical Experiment (GOPEX)," *The Telecommunications and Data Acquisition Progress Report 42-114, April–June 1993*, pp. 192–204, August 15, 1993. http://ipnpr.jpl.nasa.gov/progress_report/

[49] R. Q. Fugate, "GOPEX at the Starfire Optical Range," *The Telecommunications and Data Acquisition Progress Report 42-114, April–June 1993*, Jet Propulsion Laboratory, Pasadena, California, pp. 255–279, August 15, 1993. http://ipnpr.jpl.nasa.gov/progress_report/

[50] W. M. Owen, Jr., "Telescope Pointing for GOPEX," *The Telecommunications and Data Acquisition Progress Report 42-114, April–June 1993*, Jet Propulsion Laboratory, Pasadena, California, pp. 230–235, August 15, 1993. http://ipnpr.jpl.nasa.gov/progress_report/

[51] B. M. Levine, K. S. Shaik, and T.-Y. Yan, "Data Analysis for GOPEX Image Frames," *The Telecommunications and Data Acquisition Progress Report 42-114, April–June 1993*, Jet Propulsion Laboratory, Pasadena, California, pp. 213–229, August 15, 1993.

[52] B. M. Levine and K. Kiasaleh, "Intensity Fluctuations in the Compensated Earth-Moon-Earth Laser Link (CEMERLL) Experiment," *Proceedings of the SPIE*, vol. 2123, *Free-Space Laser Communication Technologies VI*, G. S. Mecherle, editor**,** pp. 409-422, January 1994.

[53] P. J. Shelus, "MLRS: a Lunar/Artificial Satellite Laser Ranging Facility at the McDonald Observatory," *IEEE Transactions on Geoscience and Remote Sensing*, vol. GE-234, pp. 385–390, 1985.

[54] J. E. Faller, "The Apollo Retroreflector Arrays and A New Multi-lensed Receiver Telescope," *Space Research XII*, Akademie-Verlag, Berlin, pp. 235–246, 1972.

[55] K. E. Wilson, P. R. Leatherman, R. Cleis, J. Spinhirne, and R. Q. Fugate, "Results of the Compensated Earth-Moon-Earth Retroreflector Laser Link (CEMERLL Experiment," *The Telecommunications and Data Acquisition Progress Report 42-131, July–September 1997*, Jet Propulsion Laboratory, Pasadena, California, pp. 1–13, November 15, 1997.

[56]   K. Araki, Y. Arimoto, M. Toyoda, M. Toyoshima, M. Shikatani, T. Takahaski, T. Fukuzawa, H. Okazawa, Y. Suzuki, and T. Aruga, "Laser Communications Experiment Using ETS-VI Satellite," *CRL International Topical Workshop on Space Laser Communications*, March 10–11, 1997 Communications Research Laboratory, Tokyo, Japan, pp. 34–47, 1997.

[57]   K. Wilson, J. R. Lesh, K. Araki, and Y. Arimoto, "Preliminary Results of the Ground/Orbiter Lasercom Demonstration Experiment Between Table Mountain and the ETS-VI Satellite," *Proceedings of the SPIE*, vol. 2699, *Free-Space Laser Communication Technologies VIII*, G. S. Mecherle, editor**,** pp. 121–132, April 1996.

[58]   K. Wilson, M. Jeganathan, J. Lesh, J. James, and G. Xu, "Results for Phase 1 and Phase 2 GOLD Experiments," *The Telecommunications and Data Acquisition Progress Report 142-128, October–December 1996*, Jet Propulsion Laboratory Pasadena, California, pp. 1–11, February 15, 1997. http://ipnpr.jpl.nasa.gov/progress_report/

[59]   M. Owen, S. D. Gillam, J. W. Young, and D. Mayes, "Ephemeris Generation for the ETS-VI and Its Effects on Pointing Strategies Adopted for Daytime Acquisition and Tracking," *The Telecommunications and Data Acquisition Progress Report 142-128, October–December 1996*, Jet Propulsion Laboratory, Pasadena, California, pp. 1–11, February 15, 1997. http://ipnpr.jpl.nasa.gov/progress_report/

[60]   M. Toyoshima, K. Araki, Y. Arimoto, M.Toyoda, M. Jeganathan, K. Wilson, and J. Lesh, "Reduction of ETS-VI laser Communication Equipment Optical-Downlink Telemetry Collected During GOLD," *The Telecommunications and Data Acquisition Progress Report 142-128, October–December 1996,* Jet Propulsion Laboratory, Pasadena, California, pp. 1–9, February 15, 1997.
http://ipnpr.jpl.nasa.gov/progress_report/

[61]   M. Jeganathan, M., K. E. Wilson, and J. R. Lesh, "Preliminary Analysis of Fluctuations in the Received Uplink-Beacon-Power Data Obtained From the GOLD Experiments," *The Telecommunications and Data Acquisition Progress Report PR 42-124, October–December 1995*, Jet Propulsion Laboratory, Pasadena, California, pp. 20–32, February 15, 1996. http://ipnpr.jpl.nasa.gov/progress_report/

[62]   S. D. Gillam, J. W. Young, and D. R. Sidwell, "JPL Table Mountain Facility Support of the Ground/Orbiter Lasercomm Demonstration," *The Telecommunications and Data Acquisition Progress Report 42-125, January–March 1996*, Jet Propulsion Laboratory, Pasadena, California, pp. 1–11, May 15, 1996. http://ipnpr.jpl.nasa.gov/progress_report/

[63] C. Pasqualino "Characterization of Avalanche Photo Diode Detector Used for Optical Communications Experiments with the Japanese ETS-VI" *The Telecommunications and Data Acquisition Progress Report 142-128, October–December 1996,* Jet Propulsion Laboratory Pasadena, California, pp. 1–8, February 15, 1997. http://ipnpr.jpl.nasa.gov/progress_report/

[64] R. Gagliardi and S. Karp, *Optical Communications*, New York: John Wiley and Sons, 1976.

[65] W. Pratt, *Laser Communications Systems*, New York: John Wiley and Sons, 1969.

[66] J. W. Goodman, *Introduction to Fourier Optics*, New York: McGraw-Hill, 1968.

[67] D. Petersen and D. Middleton, "Sampling and Reconstruction of Wavenumber-Limited Functions in N-Dimensional Euclidian Spaces," *Information and Control*, vol.5, pp. 279–323, 1962.

[68] V.Vilnrotter, *Focal-Plane Processing for Scattered Optical Fields*, Ph.D. Dissertation, University of Southern California, Los Angeles, California, June 1978.

[69] V. Vilnrotter and M. Srinivasan, "Adaptive Detector Arrays for Optical Communications Receivers," *IEEE Transactions on Communications*, vol. 50, no. 7, pp. 1091–1097, July 2002.

[70] P. Negrete-Regagnon, "Practical Aspects of Image Recovery by Means of the Bispectrum," *Journal of the Optical Society of America*, vol. 13, no. 7, pp.1557–1576, July 1996.

[71] C.-C. Chen, *"Figure of Merit for Direct-Detection Optical Channels," The Telecommunications and Data Acquisition Progress Report 42-109, January–March 1992*, Jet Propulsion Laboratory, California Institute of Technology, Pasadena, California, pp. 136–151, May 15, 1992. http://ipnpr.jpl.nasa.gov/progress_report/

[72] D. Boroson, A. Biswas, and B. L. Edwards, "MLCD: Overview of NASA's Mars Laser Communications Demonstration System," *Proceedings of SPIE: Free-Space Laser Communication Technologies XVI*, [Ed. S. Mecherle], vol. 5338, pp. 16–28, 2004.

[73] G. G. Ortiz, J. V. Sandusky, and A. Biswas, "Design of an Opto-Electronic Receiver for Deep-Space Optical Communications," *The Telecommunications and Mission Operations Progress Report 42-142, April–June 2002*, Jet Propulsion Laboratory, Pasadena, California, pp. 136–151, August 15, 2000. http://ipnpr.jpl.nasa.gov/progress_report/

[74]   D. M. Boroson, R. S. Bondurant, and J. J. Scozzafava, "Overview of High Rate Deep Space Laser communications Options," *Proceedings of SPIE: Free-Space Laser Communication Technologies XVI*, [Ed. S. Mecherle], vol. 5338, pp. 37–49, 2004.

[75]   B. Moision and J. Hamkins, "Deep-Space Optical Communications Downlink Budget: Modulation and Coding," *The Interplanetary Network Progress Report 42-154*, *April–June 2003*, Jet Propulsion Laboratory, Pasadena, California, pp. 1–28, August 15, 2003. http://ipnpr.jpl.nasa.gov/progress_report/

[76]   A. Biswas and S. Piazzolla, "Deep-Space Optical Communications Downlink Budget from Mars: System Parameters," *The Interplanetary Network Progress Report 42-154, April–June 2003*, Jet Propulsion Laboratory, Pasadena, California, pp. 1–38, August 15, 2003. http://ipnpr.jpl.nasa.gov/progress_report/

[77]   M. Britcliffe, D. Hoppe, W. Roberts, and N. Page, "A ten-meter Ground-Station Telescope for Deep-Space Optical Communications: A Preliminary Design," *The Interplanetary Network Progress Report 42-147, July–September 2001*, Jet Propulsion Laboratory, California Institute of Technology, Pasadena, California, pp. 1–17, November 15, 2001. http://ipnpr.jpl.nasa.gov/progress_report/

[78]   V. Vilnrotter, C.-W. Lau, M. Srinivasan, R. Mukai, and K. Andrews, "An Optical Array Receiver for Deep-Space Communication through Atmospheric Turbulence," *The Interplanetary Network Progress Report 42-154, April–June 2003*, Jet Propulsion Laboratory, Pasadena, California, pp. 1–21, August 15, 2003. http://ipnpr.jpl.nasa.gov/progress_report/

[79]   D. M. Boroson, R. S. Bondurant, and D.V. Murphy, "LDORA: A Novel Laser Communications Receiver Array Architecture," *Proceedings of SPIE: Free-Space Laser Communication Technologies XVI*, [Ed. S. Mecherle], vol. 5338, pp. 56–64, 2004.

[80]   J. R. Lesh, J. Katz, H. H. Tan, and D. Zwillinger, "2.5-Bit/detected Photon Demonstration Program: Description, Analysis and Phase I Results," *The Telecommunications and Data Acquisition Progress Report 42-66, September–October 1981*, Jet Propulsion Laboratory, Pasadena, California, pp. 115-132, December 15, 1981. http://ipnpr.jpl.nasa.gov/progress_report/

[81]   J. Katz, "2.5 Bit/Detected Photon Demonstration Program: Phase II and III Experimental Results," *The Telecommunications and Data Acquisition Progress report 42-70 May–June 1982*, Jet Propulsion Laboratory, Pasadena, California, pp. 95–104, August 15, 1982. http://ipnpr.jpl.nasa.gov/progress_report/

[82] A. Biswas and W. H. Farr, "Laboratory Characterization and Modeling of a Near-Infrared Enhanced Photomultiplier Tube," *The Interplanetary Network Progress Report 42-152, October–December 2002*, Jet Propulsion Laboratory, Pasadena, California, pp.1–14, February 2003. http://ipnpr.jpl.nasa.gov/progress_report/

[83] R. A. Larue, K. A. Costello, G. A. Davis, J. P. Edgecumbe, and V. W. Aebi, "Photon Counting III-V Hybrid Photomultipliers Using Transmission Mode Cathodes," *IEEE Transactions on Electronic Devices*, vol. 44, pp. 672–678, 1997.

[84] R. A. Larue, G. A. Davis, D. Pudvay, K. A. Costello, and V. W. Aebi, "Photon Counting 1060 nm Hybrid Photomultiplier with High Quantum Efficiency," *IEEE Electron Device Letters*, vol. 20, pp. 126–128, 1999.

[85] B. E. A. Saleh and M. C. Teich, *Fundamentals of Photonics,* J. Wiley and Sons, Inc. (New York, New York), pp. 666–673, 1991.

[86] S. B. Alexander, *Optical Communication Receiver Design,* International Society for Optical Engineers (Bellingham, Washington) and The Institution of Electrical Engineers, pp. 102–109, 1997.

[87] A. Biswas, B. Madden-Woods, M. Srinivasan, V. A. Vilnrotter, and W. H. Farr, "Ground Detectors for Optical Communications from Deep Space," *Proceedings of SPIE: Free-Space Laser Communication Technologies XIV*, [Ed. S. Mecherle], vol. 4635, pp. 72–83, 2002.

[88] S. Takeuchi, J. Kim, Y. Yamamato, and H. Hoag, "Development of a High-Quantum Efficiency Single-photon Counting System, "*Applied Physics Letters*, vol. 74, pp. 1063–1065, 1999.

[89] K. A. McIntosh, J. P. Donnelly, D. C. Oakley, A. Napoleone, S. D. Calawa, L. J. Mahoney, K. M. Molvar, E. K. Duerr, S. H. Groves, and D. C. Shaver, "InGaAsP/InP Avalanche Photodiodes for Photon Counting at 1.06 μm," *Applied Physics Letters*, vol. 81, pp. 2505–2507, 2002.

[90] A. Biswas and W. H. Farr, "Detectors for Ground-Based Reception of Optical Communications from Mars," Paper MH3, IEEE Lasers and Electro-Optics Society (LEOS) Annual Meeting, November 7–11, 2004, Rio Grande, Puerto Rico, United States, 2004.

[91] L. C. Andrews and R. L. Phillips, *Laser Beam Propagation through Random Media*, SPIE Optical Engineering Press, Bellingham, Washington, 1998.

[92] D. L. Snyder, *Random Point Processes*, John Wiley & Sons, New York, New York, 1975.

[93] E. V. Hoversten, R. O. Harger, and S. J. Halme, "Communications Theory for the Turbulent Atmosphere," *Proceedings of the IEEE*, pp. 1626–1650, October 1970.

[94] W. M. Hubbard, "Binary Detection in an Optical Twin Channel Receiver," *IEEE Transactions on Communications Technology*, vol. 19, pp. 221–223, April 1971.

[95] V. A. Vilnrotter, *Optical Receivers Using Rough Reflectors*, JPL Publication 85-25, Jet Propulsion Laboratory, Pasadena, California, May 1, 1985.

[96] P. Negrete-Regagnon, "Practical Aspects of Image Recovery by Means of the Bispectrum," *Journal of the Optical Society of America*, vol. 13, no. 7, July 1996.

[97] R. Gagliardi and S. Karp, Optical Communications, Second Edition, John Wiley & Sons, Inc., (New York, New York), 1995.

[98] V. Vilnrotter and N. Srinivasin, "Adaptive Detector Array for Optical Communication Receivers," *Telecommunications and Mission Operations Progress Report 42-141, January–March 2000*, Jet Propulsion Laboratory, Pasadena, California, pp. 1–22, May 15, 2000. http://ipnpr.jpl.nasa.gov/progress_report/

[99] J. Proakis, *Digital Communications*, McGraw-Hill, Inc., New York, New York, 1995.

[100] M. Simon, S. Hinedi, and W. Lindsey, *Digital Communication Techniques*, PTR Prentice Hall, Englewood Cliffs, New Jersey, 1995.

[101] N. H. E. Weste and K. Eshraghian, *Principles of CMOS VLSI Design*, Addison-Wesley Publishing Company, Reading, Massachusetts, 1993.

[102] R. Sadr, P. P. Vaidyanathan, D. Raphaeli, and S. Hinedi, *Parallel Digital Modem Using Multirate Filter Banks*, JPL Publication 94-20, Jet Propulsion Laboratory, Pasadena, California, August 1994.

[103] A. Gray, *Very Large Scale Integration Architecture for Nyquist Rate Digital Communications Receivers*, Ph. D. Dissertation, University of Southern California, Los Angles, California, May 2000.

[104] V. Vilnrotter, A. Biswas, W. Farr, D. Fort, and E. Sigman, "Design and Analysis of a First Generation Optical Pulse-Position Modulation Receiver," *The Interplanetary Network Progress Report 42-148, October–December 2001*, Jet Propulsion Laboratory, Pasadena, California, pp. 1–20, February 15, 2002. http://ipnpr.jpl.nasa.gov/progress_report/

[105] R. McDonough and A. Whalen, *Detection of Signals in Noise*, Academic Press, New York, 1995.

[106] C. W. Helstrom, *Elements of Signal Detection and Estimation*, PTR Prentice Hall, Englewood Cliffs, New Jersey, 1995.

[107] H. L. Van Trees, *Detection, Estimation, and Modulation Theory*, Part I, John Wiley and Sons, Inc., New York, 1968.

[108] R. Sadr and W. J. Hurd, "Detection of Signals by the Digital Integrate-and-dump Filter With Offset Sampling," *The Telecommunications and Data Acquisition Progress Report 42-91*, July–September *1987*, Jet Propulsion Laboratory, Pasadena, California, pp. 158–173, November 15, 1987. http://ipnpr.jpl.nasa.gov/progress_report/

[109] A. V. Oppenheim and R. W. Schafer, *Discrete-Time Signal Processing*, Prentice-Hall, Englewood Cliffs, New Jersey, 1989.

[110] P. P. Vaidyanathan, *Multirate Systems and Filter Banks*, Prentice-Hall, Englewood Cliffs, New Jersey, 1993.

[111] H. Meyr and G. Ascheid, *Synchronization in Digital Communications*, Wiley Series in Telecommunications, John Wiley and Sons, New York, New York, 1990.

[112] C. N. Georghiades, "Detecting Random PPM Sequences in the Absence of Sequences in the Absence of Synchronization," *Proceedings of the 22nd Conference on Information Science Syst*ems, Princeton, New Jersey, pp. 159–163, March 1988.

[113] X. Sun and F. Davidson, "Timing Recovery in Free Space Direct Detection Optical Communication Systems with PPM Signaling," Communications, 1989. *ICC 89, BOSTONICC/89, IEEE International Conference on World Prosperity Through Communications*, vol. 1, pp. 428–432, June 1989.

[114] F. Davidson and X. Sun, "Slot Clock Recovery in Optical PPM Communication Systems with Avalanche Photodiode Photodetectors," *IEEE Transactions on Communications*, vol. 37, no. 11, pp. 1164–1172, November 1989.

[115] X. Sun and F. Davidson, "Word Timing Recovery in Direct Detection Optical PPM Communication Systems with Avalanche Photodiodes Using a Phase Lock Loop," *IEEE Transactions on Communications*, vol. 38, no. 5, pp. 666–673 May 1990.

[116] S. Chauchin, L.-Y. Huang, J.-J. Lee, and C.-K. Wang, "A Frame-Based Symbol Timing Recovery for Large Pull-in Range and Small Steady State Variation," *The First IEEE Asia Pacific Conference on ASICs, AP-ASIC '99*, pp. 75–78, August 1999.

[117] G. L. Lui, "PPM Symbol Synchronization in Random Data," *IEEE Military Communications Conference, MILCOM '91, Military Communications in a Changing World,* vol. 3, pp 1047–1053, November 1991.

[118] C. N. Georghiades, "On the Synchronizability and Detectability of Random PPM Sequences," *IEEE Transactions on Information Theory*, vol. 35, no. 1, pp. 146–156, January 1989.

[119] C. N. Georghiades, "On PPM Sequences with Good Autocorrelation Properties," *IEEE Transactions on Information Theory*, vol. 34, no. 3, pp. 571–576, May 1988.

[120] R, Velidi and C. N. Georghiades, "Symbol Synchronization for Optical Multi-Pulse Pulse Position Modulation Systems," *IEEE International Conference on Personal Wireless Communications*, pp. 182–184, August 1994.

[121] R, Velidi and C. N. Georghiades, "Optimal and Suboptimal Frame Synchronizers for Optical Multi-Pulse PPM," *IEEE International Symposium on Information Theory*, p. 79, July 1994.

[122] K. Sato, T. Ohtsuki, I. Sasase, and S. Mori, "Performance Analysis of (m, 2) MPPM with Imperfect Slot Synchronization," *IEEE Pacific Rim Conference on Communications, Computers and Signal Processing*, vol. 2, pp. 765–768, May 1993.

[123] M. Asano, T. Ohtsuki, H. Uehara, and I. Sasase, "A Novel Frame Synchronization Rule for Optical DPPM Systems with Restriction of Frame Length," *IEEE Global Telecommunications Conference, Communications: The Key to Global Prosperity*, vol. 2, pp. 923–927, November 1996.

[124] D. Jinsong, I. Oka, and C. Fujiwara, "Symbol Error Probability of Time Spread PPM Signals in the Presence of Interference," *IEEE Pacific Rim Conference on Communications, Computers and Signal Processing, '10 Years PACRIM 1987-1997 - Networking the Pacific Rim*, vol. 1, pp. 1–4, August 1997.

[125] C. Georghiades, "Optimum Joint Slot and Symbol Synchronization for the Optical PPM Channel," *IEEE Transactions on Communications*, vol. 35, no. 6, pp. 632–636, June 1987.

[126] K. Sato, T. Ohtsuki, H. Uehara, and I. Sasase, "Communication Systems with PPM Signaling Lightwave Technology," *Journal of Lightwave Technology*, vol. 14, no. 9, pp. 1963–1969, September 1996.

[127] J. M. H. Elmirghani and R. A. Cryan, "Jitter Implications on Optical Fibre PPM Performance," *ICC 94, SUPERCOMM/ICC '94, Conference Record, IEEE International Conference on Serving Humanity Through Communications*, vol. 2, pp. 665–669, May 1994.

[128] V. A. Vilnrotter, E. R. Rodemich, and H. H. Tan, "A Synchronization Technique for Optical PPM Signals," *The Telecommunications and Data Acquisition Progress Report 42-86*, *July–September 1986*, Jet Propulsion Laboratory, Pasadena, California, pp. 24–31, November 15, 1986. http://ipnpr.jpl.nasa.gov/progress_report/

[129] S. Aguirre, W. J. Hurd, R. Kumar, and J. Statman, "A Comparison of Methods for DPLL Loop Filter Design," *The Telecommunications and Data Acquisition Progress Report 42-86, July–September 1986*, Jet Propulsion Laboratory, Pasadena, California, pp. 114–124, November 15, 1986. http://ipnpr.jpl.nasa.gov/progress_report/

[130] S. A. Stephens and J. B. Thomas, "Controlled-Root Formulation for Digital Phase-Locked Loops," *IEEE Transactions on Aerospace and Electronic Systems*, vol. 31, no. 1, January 1995.

[131] A. Gray, "Parallel Sub-Convolution Filter Bank Architectures," *IEEE International Symposium on Circuits and Systems*, Bangkok, Thailand, May 2003, vol. 4, pp. IV-528–IV-531, 2003.

[132] W. Zhuo and E. Micheli-Tzanakou, "A High Performance Continuous Data Flow Filter Using Sliding Discrete Fourier Transform (DFT) and One Point Inverse DFT," *IEEE International Conference on Information Technology Applications in Biomedicine*, pp. 51–56, May 1998.

[133] J. J. Shynk, "Frequency-Domain and Multirate Adaptive Filtering," *IEEE Signal Processing Magazine*, vol. 9, pp. 14–37, January 1992.

[134] M. A. Soderstrand and R. J. Miller, "High-Speed Convolution Using GQRNS Arithmetic Hardware," *IEEE International Symposium on Circuits and Systems,* vol. 3, pp. 1556–1558, 1989.

[135] W. S. Gan and Y. K. Chong, "Parallel Implementation of the Frequency Bin Adaptive Filter for Acoustical Echo Cancellation," *International Conference on Information, Communications and Signal Processing*, vol. 2, pp. 754–757, September 1997.

[136] G. E. Johnson, R. A. Muir, J. M. Scanlan, and W. M. Steedly, "The Sliding Frequency-Domain Adaptive Filter Algorithm Amenable to Parallel Implementation," *IEEE Proceedings of ASILOMAR*-29 (Asilomar, California), vol. 2, pp. 1126–1130, 1996.

[137] M. E. Deisher and A. S. Spanias "Real-Time Implementation of a Frequency-Domain Adaptive Filter on a Fixed-Point Signal Processor," *International Conference on Acoustics, Speech, and Signal Processing*, vol. 3, pp. 2013–2016, 1991.

[138] K. Eneman, and M. Moonen, "Filter bank Constraints for Subband and Frequency-Domain Adaptive Filters," *IEEE ASSP Workshop on Applications of Signal Processing to Audio and Acoustics*, p. 4, October 1997.

[139] D. R. Bungard, L. Lau, and T. L. Rorabaugh, "Programmable FFT Processors for Wide-Bandwidth HF Spread-Spectrum Communications and Radar Signal Processing," *IEEE International Conference on Acoustics, Speech, and Signal Processing*, vol. 2, pp. 1357–1359, 1989.

[140] Y. Elcherif, S. Mashali, and M. El-Serif, "Semi-Systolic Bit Level Arrays for High Speed Convolution," *IEEE International Conference on Systems Engineering*, pp. 391–394, 1989.

[141] H. A. Chow, H. Alnuweiri, and S. Casselman, "FPGA-Based Transformable Computer for Fast Digital Signal Processing," *IEEE Symposium on FPGAs for Custom Computing Machines*, pp. 197–203, 1995.

[142] Yuan-Pei Lin and P. P. Vaidyanathan, "Application of DFT Filter Banks and Cosine Modulated Filter Banks in Filtering," *IEEE Asia-Pacific Conference on Circuits and Systems*, pp. 254–259, 1994.

[143] Y. C. Lim, and B. Farhang-Boroujeny, "Fast Filter Bank (FFB)," *IEEE Transactions on Circuits and Systems-II: Analog and Digital Signal Processing*, vol. 39, no. 5, pp. 316–318, May 1992.

[144] A. Klouche-Djedid, "IIR Stable, Causal and Perfect Reconstruction Uniform DFT Filter Banks with a Real or Complex Prototype Filter," *IEEE Colloquium on Digital Filters: An Enabling Technology*, pp. 13/1–13/6, 1998.

[145] N. Fliege, "Polyphase FFT Filter Bank for QAM Data Transmission," *IEEE International Symposium on Circuits and Systems*, vol. 1, pp. 654–657, May 1990.

[146] S. Weiss, L. Lampe, and R. W. Stewart, "Efficient Subband Adaptive Filtering with Oversampled GDFT Filter Banks," *IEEE Colloquium on Adaptive Signal Processing for Mobile Communication Systems*, pp. 411–419, October 1997.

[147] A. P. R. Rodrigues, M. R. Petraglia, and J. Szezupak, "An Adaptive Filtering Subband Structure with Critical Sampling," *IEEE International Symposium on Circuits and Systems*, *ISCAS '96*, vol. 2, pp. 368–371, 1996.

[148] K. Eneman and M. Moonen, "A Relation Between Subband and Frequency-Domain Adaptive Filtering," *13th International Conference on Digital Signal Processing Proceedings*, vol. 1, pp. 25–28, July 1997.

[149] J. Vollmer, "Analysis and Design of Numerically Controlled Oscillators Based on Linear Time-Variant Systems," *Proceedings of the IEEE-SP International Symposium on Time-Frequency and Time-Scale Analysis*, pp. 453–456, October 1998.

[150] M. M. Al-Ibrahim, "A Multifrequency Range Digital Sinusoidal Oscillator with High Resolution and Uniform Frequency Spacing," *IEEE Transactions on Circuits and Systems II: Analog and Digital Signal Processing*, vol. 48 no. 9, pp. 872–876, September 2001.

[151] M. M. Al-Ibrahim, "A Simple Recursive Digital Sinusoidal Oscillator with Uniform Frequency Spacing," *IEEE International Symposium on Circuits and Systems*, vol. 2, pp. 689–692, May 2001.